Molecular-Frame Angularly-Resolved Photoelectron Spectroscopy

Molecular-Frame Angularly-Resolved Photoelectron Spectroscopy

Dissertation

zur Erlangung des Doktorgrades an der Fakultät für Mathematik, Informatik und Naturwissenschaften
Fachbereich Physik
der Universität Hamburg

vorgelegt von

Evangelos Thomas Karamatskos

Hamburg
2019

Gutachter der Dissertation:	Prof. Dr. Jochen Küpper Prof. Dr. Robin Santra
Zusammensetzung der Prüfungskommission:	Prof. Dr. Jochen Küpper Prof. Dr. Robin Santra Prof. Dr. Henry Chapman Prof. Dr. Markus Drescher Prof. Dr. Daniela Pfannkuche
Datum der Disputation:	19.09.2019
Vorsitzende der Prüfungskommission:	Prof. Dr. Daniela Pfannkuche
Vorsitzender des Fach-Promotionsausschusses Physik:	Prof. Dr. Michael Potthoff
Leiter des Fachbereichs Physik:	Prof. Dr. Wolfgang Hansen
Dekan der Fakultät MIN:	Prof. Dr. Heinrich Graener

to my father

Eidesstattliche Versicherung

Hiermit versichere ich an Eides statt, die vorliegende Dissertationsschrift selbst verfasst und keine anderen als die angegebenen Hilfsmittel und Quellen benutzt zu haben. Die eingereichte schriftliche Fassung entspricht der auf dem elektronischen Speichermedium. Die Dissertation wurde in der vorgelegten oder einer ähnlichen Form nicht schon einmal in einem früheren Promotionsverfahren angenommen oder als ungenügend beurteilt.

Hamburg, den 10. Oktober 2019

Evangelos Thomas Karamatskos

Niels Bohr and Wolfgang Pauli
observing a spinning top.
(Lund 1951)

Zusammenfassung

Eine der größten wissenschaftlichen und technischen Herausforderungen der heutigen Zeit ist es, chemische Reaktionen mit atomarer räumlicher und zeitlicher Auflösung zu messen und dadurch den sogenannten „Molecular Movie“, den molekularen Film, aufzunehmen. Wichtige Vorraussetzungen, um diesem ultimativen Ziel näher zu kommen, sind einerseits Methoden, um kalte, kontrollierte Moleküle zu präparieren, und andererseits Abbildungstechniken, die die erforderliche räumliche und zeitliche Auflösung vereinen. In den letzten Jahren sind, vor allem aufgrund der rasanten Entwicklung von Laser- und Elektronenquellen, verschiedene verfeinerte Abbildungsmethoden zugänglich geworden. Eine Kombination aus Methoden, um Moleküle in verschiedenen Quantenzuständen zu separieren und diese dann mithilfe von gepulsten Lasern feldfrei auszurichten, erlaubt es, Moleküle mit hoher Präzision zu manipulieren und zu präparieren, bevor diese mit Abbildungsmethoden vermessen werden. Der Einsatz von gepulsten Starkfeldlasern mit extrem kurzen Pulsdauern im mittleren Infrarotbereich hat Selbstabbildungsmethoden, wie die Methode "Laser-Induced Electron Diffraction (LIED)", hervorgebracht, die heute soweit ausgereift ist, dass ihr Potential zur Messung von statischen Strukturen und der Dynamik von Molekülen mit atomarer räumlicher und zeitlicher Auflösung genutzt werden kann.

Diese Arbeit kann im Wesentlichen in zwei Teile gegliedert werden, die Kontrolle von Molekülen und deren Abbildung mittels Elektronendiffraktion zur Strukturbestimmung.

Im ersten Teil liegt der Fokus in der Optimierung von Methoden zur feldfreien Ausrichtung von Molekülen mithilfe von optimal geformten Laserfeldern. Starke feldfreie Ausrichtung wird für drei Moleküle gezeigt, beginnend mit dem relativ simplen linearen Molekül Carbonylsulfid (OCS) bis hin zum komplexen, asymmetrischen Kreisel Indol, der keine Rotationssymmetrien aufweist und keine Markeratome enthält. Verschiedene experimentelle und numerische Verfahren steigender Komplexität werden vorgestellt, die jeweilig von der Komplexität des auszurichtenden Moleküls abhängen und eine starke, feldfreie Ausrichtung der Moleküle und den Zugang zum moleküleigenen Inertialsystem ermöglichen.

Im zweiten Teil wird die "Laser-Induced Electron Diffraction (LIED)" Methode genutzt, um die statische Struktur von Molekülen mit atomarer Auflösung zu bestimmen, und am Beispiel von OCS angewendet. Die starke, feldfreie Ausrichtung, die im ersten Teil vorgestellt wird, wird genutzt, um winkelaufgelöste Impulsverteilungen von Photoelektronen direkt im Molekülsystem (MF-ARPES) zu messen. Dies wird für verschiedene Ausrichtungen der Molekülachse bezüglich der Polarisation des ionisierenden Lasers durchgeführt. Die gemessenen MF-ARPES zeigen große Unterschiede, die auf die Struktur des höchsten populierten Molekülorbitals zurückzuführen sind. Die niederenergetischen Elektronen in den winkelaufgelösten Impulsverteilungen weisen holographische Interferenzmuster auf, deren Struktur von der Ausrichtung der Moleküle abhängt. Desweiteren werden winkelabhängige Ionisationraten für direkte, niederenergetische, sowie gestreute, hochenergetische Elektronen präsentiert, die eine klare Abhängigkeit von der Ausrichtung der Moleküle zeigen. Die oben beschriebenen Beobachtungen erlauben Schlußflogerungen über den Einfluss des zugrundeliegenden Molekülorbitals auf die Starkfeldionisation und feldgetriebene Rekollisionen zu ziehen.

Abstract

One of the big technical and scientific challenges today is to accomplish the ultimate dream of filming chemical reactions with atomic spatial and temporal resolution and recording the molecular movie. Important prerequisites toward this goal are, on the one hand, methods to create cold, controlled molecular samples and, on the other hand, imaging techniques that combine the required spatial and temporal resolution. In recent years, especially due to the fast progress in the development of laser and electron sources, more and more refined imaging techniques have become accessible. The combination of quantum state selection with laser-induced field-free alignment and orientation, allow to precisely control and prepare the molecules under study, before being imaged. Using ultrafast, high-intensity laser sources in the mid-infrared spectral range, self-imaging methods, such as laser-induced electron diffraction (LIED), have emerged and their full potential can be explored today to image the structure and dynamics of molecules with atomic spatio-temporal resolution.

This work can be divided into two major parts, the control and the imaging part.

In the control part, the focus lies on the optimization of field-free alignment using tailored light fields. Strong field-free alignment will be presented for three different molecules, ranging from the relatively simple linear molecule carbonyl sulfide (OCS) up to the complex asymmetric top rotor indole, which lacks rotational symmetries and marker atoms. Different experimental and numerical schemes of increasing complexity will be presented, depending on the complexity of the molecule under study, that allow to achieve strong field-free alignment and to access the molecule-fixed frame (MFF).

In the imaging part, the LIED method will be employed to image and to retrieve the static structure of molecules with atomic resolution, applied on the example of OCS. The unprecedented degree of field-free alignment of OCS, achieved in the control part, is employed to record angularly-resolved photoelectron momentum distributions (PEMDs) for different rotational wavepackets and for different orientations of the molecular axis with respect to the ionizing laser polarization. These molecular-frame angularly-resolved photoelectron spectra (MF-ARPES) exhibit large differences, indicating a dependence of the emitted electron continuum wavepacket and its dynamics on the shape of the highest occupied molecular orbital (HOMO). In the low-energy region of the PEMDs, strong-field photoelectron holography (SFPH) is observed, revealing diverse interference patterns for different molecular orientations. Moreover, measurements of angle-dependent ionization yields of direct, low-energy electrons and of rescattered, high-energy electrons will be presented, showing clear alignment-dependent features. From these aforementioned observations, conclusions will be drawn about the impact of the underlying molecular orbital on strong-field ionization and field-driven recollisions.

Contents

1 Introduction

Scientific knowledge and scientific progress are strongly driven by observation. Most scientist would agree with this simple but far-reaching statement, which constituted a central driving force for the development of ever more elaborate observation methods over the centuries. A major breakthrough in this evolution was the invention of the photographic camera and photographic plates in the 19th century, as it allowed for the first time to record images and store them permanently. The information stored in such images is integrated over the exposure time, defined by the shutter speed, and the information itself is carried by the light that ultimately blackens the plates. Since in the early days only low-intensity light sources existed, taking a sharp picture required long exposure times within which people were requested to stay motionless in order not to blur the image and decrease its quality. Technological progress enabled the acquisition of images on ever faster time scales with shorter and shorter exposure times. It soon was recognized that taking consecutive images could capture motion, which was beautifully demonstrated by Eadweard Muybridge in 1878 who imaged the motion of a galopping horse and proved that at certain times none of its four feet was on the ground but all were simultaneously in the air.

These developments proved to be of major significance for science and were shortly after their invention used in laboratories around the world to observe physical phenomena. Later, with the development of pulsed light and electron sources, time-resolved atomic and molecular imaging became accessible. In particular, the so called pump-probe scheme emerged as an important tool to probe the structure and dynamics of matter. In a pump-probe experiment a certain physical or chemical process is initiated by a short pump pulse, whose arrival time defines time zero, and subsequently the progress of the reaction is monitored by a second short probe pulse for a sequence of time delays between these two pulses. The time resolution is limited by the pulse duration and the spatial resolution is limited by the wavelength of the probe pulse. In order to obtain high-resolution images with higher temporal and spatial resolution, probe pulses with shorter wavelengths, i. e., higher energy, shorter pulse durations and higher peak intensities are required. Again, as before in the history of science, these requirements triggered vast technological progress and the development of more and more refined imaging methods continuing to this very day.

1.1. Imaging Chemical Dynamics

Atoms and molecules are the building blocks of matter, where molecules consist of two or more atoms bound together through chemical bonding. The molecular equilibrium structure, i. e., the spatial distribution of its atomic constituents is characterized through

the bond lengths, typically on the order of ∼100 pm (1 pm = 10^{-12} m), the bond angles and the torsion angles, arranged in such a way as to minimize the total internal energy. The microscopic structure of a molecule defines its physical and chemical properties, known as the structure-function relationship [1]. The most conventional methods to image the structure of molecules are electron and x-ray diffraction. In both methods diffraction patterns of elastically scattered particles are recorded in momentum space, which need to be inverted in order to extract the molecular structure in real space. The spatial resolution in all imaging methods is either limited by the wavelength of the light or the de Broglie wavelength when matter waves are utilized. In order to reach a spatial resolution of 100 pm, photons with energies of 12.4 keV or more are needed, which is already in the hard x-ray range. Electrons can reach such a resolution already with a kinetic energy of 150 eV, because they possess mass. Furthermore, the scattering cross sections are typically 5-6 orders higher for electron scattering compared to x-ray scattering, because electrons possess charge [2]. This difference in the magnitude of the scattering cross sections makes conventional electron diffraction (CED) methods more suitable for application to surfaces or small molecules in the gas phase, i. e., gas-phase electron diffraction (GED), reaching a spatial resolution as high as 0.1 pm [2]. On the other hand, x-rays are due to their longer mean-free path more suitable for the study of large macromolecules, proteins and bulk samples, such as crystals, reaching a spatial resolution on the order of 1 pm [3]. Today there exist many new microscopy methods that are far superior in terms of spatial resolution compared to optical microscopy, such as transmission electron microscopy (TEM) [4], allowing to image non-crystallized samples, and the later developed cryo-TEM [5] in which samples are cryogenically cooled, thereby allowing to image proteins and viruses with a few hundred picometer spatial resolution. The Nobel Prize in Chemistry 2017 was awarded jointly to Jacques Dubochet, Joachim Frank and Richard Henderson "for developing cryo-electron microscopy for the high-resolution structure determination of biomolecules in solution".

However, the determination of the static equilibrium structure of molecules provides only a small fraction of the overall framework. Nature is not static and continuously subject to change. Molecules may interact with each other or with electrons and photons and far-off-equilibrium dynamics can be initiated. Today we know that chemical bonding and chemical reactions are mediated by the valence electrons in atoms and molecules. Atomic motion within molecules takes place in the femtosecond time domain (1 fs = 10^{-15} s), thus defining the natural timescale for chemical bond making and bond breaking. Pure electronic motion is even faster, reaching down to the attosecond time domain (1 as = 10^{-18} s) [6], which can be understood by considering that the orbit period for the 1s-electron in hydrogen is 152 as according to the Bohr model and the unit of time in atomic units is 24.2 as, defined as the time an electron in the first Bohr orbit needs to travel a distance a_0 = 52.9 pm, i. e., the Bohr radius, which is the natural unit of length.

One of the biggest scientific and technological challenges today is to record the so called 'molecular movie'. The main idea is to initiate some physical process or chemical reaction in a molecule and to follow the reaction in real time. The ability to record such a movie would lead to a completely new and deeper understanding of how chemical reactions take place, the possibility to control and steer chemical reactions with an unprecedented

degree of control and to test physical models with the highest possible accuracy. This objective poses many requirements on the light and particle sources used for imaging, such as spatio-temporal atomic resolution, high coherence, high flux and source stability, but at the same time there are also strong requirements on the targets under study. In the following we will briefly introduce the most important and state-of-the-art imaging techniques that are available today, their strengths and disadvantages, and in how far the recording of the molecular movie is feasible.

Milestones in the development of light sources were the MASER by Gordon et al. in 1954 [7] and the LASER in 1960 by Maiman et al. [8]. Shortly after their development many different lasing media were discovered, generating light at different wavelengths. Combined with new techniques such as mode-locking, employing the non-linear Kerr effect, and pulse compression, ultrashort pulses were routinely produced ranging from ns down to fs. Today the working horse of laboratory-based research is the Ti:Sapphire laser with a central wavelength of about 800 nm, routinely delivering pulses in the fs domain. The Nobel prize in physics in 2018 was jointly awarded to Arthur Ashkin, Gérard Mourou and Donna Strickland for their groundbreaking contributions in the field of laser physics, the latter two in particular for methods in generating high-intensity, ultra-short optical pulses. The technological progress in laser science opened up new research fields, such as femtochemistry, whose pioneer Ahmed H. Zewail was awarded the Nobel prize in Chemistry in 1999 for his studies of the transition states of chemical reactions using femtosecond spectroscopy [9, 10]. Despite their big success and many important insights that these time-resolved spectroscopies offer, structure determination is only possible in an indirect way and they lack the spatial resolution required for the molecular movie.

Time-resolved x-ray diffraction has become available with the advent of synchrotron light sources providing up to 10^{12} photons per pulse. The time resolution is limited to typically $\sim$100 ps, which is not sufficient to resolve electronic and vibrational motion in molecules and the photon flux is low for gas phase applications. Only with the development of free-electron lasers (FELs) [11], which deliver high-flux, femtosecond-short laser pulses with photon energies ranging from the XUV to the hard x-ray range, time-resolved x-ray diffraction of gas-phase samples became possible. Powerful imaging approaches, such as coherent diffractive imaging (CDI) [12–15], have emerged with the ultimate goal to achieve single particle imaging [16, 17] and the filming of the molecular movie [18–20]. First proof-of-principle experiments have already been carried out, showing that single-shot diffraction from nanoscale-sized objects is possible [21] and that the diffraction-before-destruction principle applies [22]. However, these imaging methods still do not reach atomic resolution on the order of the bond lengths. Furthermore, since most FELs are based on the self-amplified spontaneous emission (SASE) principle, they suffer from having random pulse profiles from shot to shot, short coherence times as well as time jitter in the range of a few to a few hundred femtoseconds. This is a disadvantage, in particular for pump-probe experiments, because from shot to shot the synchronization between the pump and the probe pulse changes and a high timing uncertainty is introduced. A possible resolution of this problem was proposed by using well stabilized seed lasers to initiate the lasing process using stimulated emission instead of spontaneous emission [23]. Another drawback is that these light sources are only

available in big facilities, which are costly to build and to maintain. In addition, one must apply for beamtime and access is limited in time. Therefore, parallel to the development of accelerator-based light sources, huge efforts are undertaken to create laboratory-based sources, which are cheaper, easier to maintain and accessible on a daily basis.

Through the progress in laser science and the development of ultrafast laser sources many new time-resolved laboratory-based imaging methods have emerged over the past decades. In ultrafast electron diffraction (UED), electron pulses are generated by illuminating a photocathode with a femtosecond-short laser pulse leading to electron emission through the photoelectric effect. Today, typically electron pulses with pulse durations of few ps and up to 10^6 - 10^7 electrons per pulse can be produced [24]. The temporal resolution is limited through space charge effects where due to the mutual Coulomb repulsion between the electrons spatial and temporal broadening of the electron pulses occurs. In order to increase the temporal resolution and to reach the fs domain either the number of electrons per pulse must be reduced [25] or electron beams at relativistic velocities are utilized [26]. The latter method has the disadvantage that at these kinetic energies cross sections decrease significantly and that these relativistic electron sources are again operated at big facilities [27].

In laser-induced Coulomb-explosion imaging (CEI), which was extensively used in the present work, a femtosecond-short high-intensity laser is used to multiply ionize molecules and subsequently its ionic fragments are recorded. Recording the velocity components of these fragments allows to reconstruct the molecular structure at the time of ionization if the dissociation occurs rapidly and the axial recoil approximation holds. Using this method, the structure and dynamics of nuclear wavepackets in I_2 could be imaged with $\sim$200 pm spatial resolution and 80 fs temporal resolution [28]. Later, even sub-100 pm spatial resolution and sub-5 fs temporal resolution was achieved with CEI when imaging vibrating D_2^+ ions and dissociating SO_2^{2+} ions [29].

A promising approach for the creation of ultrashort pulse VUV and XUV radiation is to utilize high harmonic generation (HHG). In HHG, a laser is focused into an atomic or molecular target gas. The target, consisting typically of rare-gas atoms in most experiments, is strong-field ionized and a fraction of the released electrons returns after some propagation in the laser field, where they are accelerated, to their parent ion. Upon recombination the electrons emit the kinetic energy they gained in the laser field as high-energy photons. This is also the mechanism leading to XUV attosecond pulses, first demonstrated in 2001 by the groups of Pierre Agostini [30] and Ferenc Krausz [31]. Advantages of these light sources are that for both, the pump and the probe pulse, the same laser can be used such that synchronization between the two is extremely stable and can be controlled to a high degree. Furthermore, the emitted radiation is highly coherent. Although HHG and attosecond XUV pulses are promising candidates for ultrafast imaging experiments, they suffer from low photon flux and it is difficult and demanding to extend the wavelength of the HHG radiation to the x-ray range. Since the photon energy depends on the kinetic energy of the returning electron, which scales as $E_{\mathrm{kin}} \propto I\lambda^2$, it is advantageous to use mid-infrared radiation for the creation of high-harmonics, which is the subject of current research [32].

Another class of imaging methods, so-called self-imaging methods, have emerged in the last 20 years [33]. One of the most appealing and promising method in this catergory is called laser-induced electron diffraction (LIED), first proposed in 1996 [34]. The principle underlying LIED is similar to HHG. After tunnel ionization, a fraction of the released electrons can be driven back by the laser field to their parent ion and they can either recombine and emit HHG or they can elastically or inelastically scatter. It was shown that high-energy elastically scattered electrons in photoelectron momentum distributions (PEMDs) contain structural information about the molecule they scatter off [34]. The LIED method exhibits several advantages compared to other electron diffraction methods. First of all, the electrons are released and return within a fraction of the laser cycle, typically a few fs, depending on the wavelength of the driving field. Their kinetic energy at the instant of rescattering is a function of the exact time of ionization. This means that in principle subcycle timing information is contained in the measured electron distributions. Another advantage is that LIED constitutes a complete pump-probe experiment using only a single pulse because the ionization process triggers nuclear motion in the molecules, which is probed within a few femtoseconds. Moreover, the electron current that scatters from the target is higher than in any other electron diffraction method. Another important advantage over conventional electron diffraction methods is that much lower electron kinetic energies are employed in LIED. The electron-atom elastic scattering cross sections at high scattering energies scale as Z^n, where Z is the nuclear charge of the atomic target that is imaged and $n \geq 1$ a positive number. Thus, the overall scattering signal from a molecule in UED is highly dominated by the most heavy atomic scatterers and scattering from light atoms, such as hydrogen, is difficult to be observed. With LIED it is possible to measure bond lengths involving hydrogen as one of the bond partners [35]. Since higher electron kinetic energies at the instant of rescattering result in higher spatial resolution, it is favourable to use mid-infrared ionizing fields in LIED. This is also one reason why more than 15 years passed from the first proposal until the first experimental realization with atomic resolution [36], owing to the required development of high-intensity laser sources in the mid-IR wavelength range. The LIED method was successfully tested in atoms [37, 38], diatomic molecules [36, 39, 40], and recently also in simple poylatomic molecules such as in acetylene [35], ethylene [41], or benzene [42]. First experiments revealing ultrafast bond breaking in acetylene have been reported [43]. Although there was quite some progress and success in using LIED over the last years, it is not clear if the method is suited for atomic-resolution imaging of the dynamics of large polyatomic molecules and how the experiments and theory have to be conceived to fulfill this aim. In addition, the potential of the inherent time resolution of the LIED method has not been routinely utilized so far.

1.2. Cold Controlled Molecules

So far we have only discussed the most promising methods for atomic and molecular imaging and the requirements that the electron and photon sources have to fulfill to enable high-resolution time-resolved structural retrieval in pump-probe experiments.

However, there are also strong requirements on the targets, the atoms and molecules, such that the aforementioned imaging experiments can provide clean measurements with a maximum of information content. Experiments in the gas phase are typically conducted on large ensembles of particles, which are needed to achieve good statistics with a high signal-to-noise ratio. It is therefore important to be able to prepare the particles in well defined initial states such that all individual measurements are conducted under the same conditions, otherwise information is lost. For molecules with many degrees of freedom this means that amongst other things the initial state distribution must be restricted to as little initial states as possible.

Isolated gas-phase molecules in molecular beams are ideally suited for imaging experiments since they are not significantly perturbed by their surrounding. Cold molecular beams can be formed through supersonic expansion [44, 45]. In a supersonic expansion large part of the internal energy of a molecule is transferred to its translational degree of freedom when the molecules are expanded from a high pressure region into vacuum. The rotational, vibrational and electronic degrees of freedom are thereby cooled, allowing to obtain molecules in their electronic and vibrational ground states with rotational temperatures below one Kelvin [1, 46]. Using pulsed nozzles, such as the Even-Lavie valve [44], allows to use higher pressures of the seed gas before the expansion compared to continuous flow nozzles, and to create pulsed molecular beams with sub-Kelvin rotational temperatures and higher peak densities [47, 48]. However, depending on the size of the molecule and the energy spacing between its rotational states, at a rotational temperature of 1 K typically still tens to several hundreds of states are significantly populated. Hence, other methods are needed to further confine the initial state distribution.

The manipulation of atomic and molecular beams, exploiting external electric and magnetic fields to achieve quantum-state selectivity and spatial control, is almost as old as the field of atomic and molecular beams itself. One of the most famous early experiments in this context is the Stern-Gerlach experiment, in which an inhomogeneous magnetic field was used to spatially separate neutral silver atoms in the $5s$ state into two distinct beams [49], a controversy at the time, which was later resolved through the existence of the electron spin. Otto Stern was awarded the Nobel Prize in Physics in 1943, amongst others for his contributions to the field of molecular beams. Another famous example is the electrostatic quadrupole focuser, which was used as a selective lens to focus only ammonia molecules with a population inversion into a microwave cavity, leading to the discovery of the MASER [7]. Such multipole focuser have been used in various experiments but they were limited to the manipulation of the transverse motion of molecules only [50]. The first successful demonstration in which also the longitudinal motion of neutral polar molecules was manipulated was achieved using the Stark decelerator [51]. A Stark decelerator consists of a periodic array of electrodes in which at a given time only the odd or even numbered stages are switched to high voltages, whereas the other stages are grounded. Molecules experience the inhomogeneous electric field as a potential hill and loose kinetic energy when climbing the hill. In order to prevent the molecules from gaining again the lost kinetic energy after the peak of the potential hill toward smaller field strengths, the fields are switched such that the molecules find themselves continuously in front of a potential hill and loose continuously kinetic energy.

Since the force exerted on a molecule depends on its effective dipole moment, which is a quantum-state-specific property, the Stark decelerator can be used as a quantum-state-selective filter [50]. The Stark decelerator method turned out to work only for molecules in low-field seeking quantum states, a limitation that was overcome with the alternating gradient focuser [52–54]. Using these methods to slow down molecules allows to control precisely the relative velocity in molecular collisions in crossed beam experiments [55], to increase the precision of spectroscopic measurements by increasing the interaction time of the molecules with the radiation field [56, 57] and to trap slow particles through additional multipole traps [58, 59], allowing to measure radiative lifetimes of excited states with high precision [60].

The electrostatic analogue to the inhomogeneous magnetic field, used in the Stern-Gerlach experiment, is the electrostatic Stark deflector [1], which was used in almost all experiments presented in this work. In the electrostatic deflector a strong, static inhomogeneous electric field is used to spatially deflect and, hence, separate neutral polar molecules in different quantum states with different effective dipole moments. Quantum-state and conformer selection can be achieved using this method as well as the separation of different clusters, i. e., separation of the monomer from the dimer, trimer etc. [1]. Furthermore, it was shown that an almost pure ground-state ensemble could be separated in small molecules [61, 62]. More complete overviews over this large field, describing in detail the different elaborate methods to control and manipulate atomic and molecular beams can be found in [1, 50, 63].

Employing the aforementioned methods involving electric and magnetic fields, allows to manipulate the transverse and longitudinal motion of molecules and to isolate quantum-state specifically molecules from the initially mixed molecular ensemble. However, this is still not sufficient, because many chemical and physical processes depend on the relative orientation of the interacting particles, amongst others steric effects in chemical reactions [64], molecular scattering [65], the ionization efficiency of molecules [66], x-ray diffraction [14, 67, 68], and electron diffraction [25, 69]. Molecules in the gas phase rotate freely and all observables are measured in the laboratory-fixed frame (LFF), i. e., the measured observables are averaged over all orientations of the molecules. In order to access the molecule-fixed frame (MFF) one has to fix the molecules with respect to the LFF, commonly referred to as alignment and orientation of molecules [70].

The first studies to orient molecules using electric fields employed the electrostatic hexapole, in which a single rotational quantum state was selected and oriented along the electric field axis [71, 72]. However, the degree of orientation was moderate due to the weak fields used and the method was only applicable to a single selected rotational state. In the 1990's another method using electrostatic fields, dubbed brute-force orientation, was proposed, in which strong dc fields were used to create oriented molecular samples through mixing of field-free rotational states [73–77]. Nevertheless, even with such strong dc fields the achievable degree of orientation was limited. Shortly thereafter the potential of using non-resonant non-ionizing ac laser fields to align molecules was recognized, which provided much higher field strengths compared to the static dc fields used hitherto [78, 79]. With this new approach the class of molecules that can be aligned was extended to a

wider range, where in principle all molecules with an anisotropic polarizability tensor can be aligned [70]. When linearly polarized laser fields are used, only the most polarizable axis of a molecule is aligned resulting in 1D alignment. Using elliptically polarized laser pulses or multiple linearly polarized pulses that are cross polarized one can achieve 3D alignment, where all 3 molecular axes are confined with respect to the LFF [80–83]. Two distinct regimes of alignment were recognized, categorized according to the pulse duration of the laser field compared to the rotational period of the molecule. When long pulses are used, the field-free rotor eigenstates evolve adiabatically into field-dressed pendular states, which are angularly confined eigenstates of the optical double-well potential, formed by the alignment laser field [84]. This regime is called adiabatic alignment and it turned out to be an efficient and elegant way to achieve a high degree of alignment (DOA) during the presence of the laser field [85–88]. In the other regime, the so called impulsive alignment, a short laser pulse creates a rotational wavepacket by coherently populating excited rotational states [89–91]. The DOA achieved in this regime depends critically on the laser pulse parameters where the breadth of the rotational wavepacket, i. e., the number of populated rotational states, and their phase relationship defines the DOA. The strength of impulsive alignment compared to adiabatic alignment is that molecules can be aligned under field-free conditions [92, 93] without the permanent presence of the alignment laser field, which may disturb the actual experiment and its outcome.

The dependence of the DOA on the laser pulse parameters when impulsive alignment is employed opens up the possibility to manipulate the laser fields and to search for optimal solutions yielding the highest DOA. Systematic studies have been carried out and several schemes proposed and tested to optimize the degree of alignment and orientation, including multiple alignment pulses [94–98], coherent control schemes [99], the combination of long and short pulses [100, 101], switched wavepackets [102] and shaped laser pulses [103–106]. Another critical parameter that strongly affects the final achievable DOA is the rotational temperature of the molecular beam, i. e., the initial state distribution. It was shown that the DOA could be improved to a large extent when quantum-state-selected molecular samples with a single or few initial rotational states were used compared to a thermal distribution [68, 107–109]. By using such state-selected molecular samples and choosing the pulse duration of the alignment laser pulses to be on the order of the rotational period of the molecule, wavepackets with only few or even only two rotational states were formed [110, 111]. Finally, utilizing both, ac laser fields to align molecules and dc fields to orient molecules, the mixed-field orientation approach was proposed [112–115], which proved to be a very efficient way to achieve high degrees of orientation [116, 117].

It should be mentioned that using detection schemes in which particles are measured in coincidence, such as reaction microscopes, for example Cold Target Recoil Ion Momentum Spectroscopy (COLTRIMS) [118, 119], the orientation of a molecule with respect to the LFF can be recovered from the measured data a posteriori [120, 121]. However, there are several reasons why field-free alignment is still an indispensable tool. The count rates in reaction microscpes are limited to at most one molecule per shot otherwise the one-to-one mapping between the detected fragments and their positions and momenta is lost. Experiments on isotropic molecular samples yield therefore very low count rates

for any chosen orientation within a differential solid angle. The experimental acquisition time that is required to get enough statistics for one specific orientation exceeds therefore by orders of magnitude the stability of the experimental setup [122]. Therefore, even for such experiments, pre-alignment and orientation is an important prerequisite.

Huge efforts were undertaken and big steps made toward the goal of real-time imaging of chemical reactions. The most important prerequisites for the recording of such a molecular movie are imaging methods that provide the required combined atomic spatio-temporal resolution with probe pulses of high-enough brightness. At the same time the atomic and molecular targets must be controlled with high precision such that clean and reproducible initial conditions are prepared that allow to draw definite conclusions from such imaging experiments. However, besides the requirements on the experimental side, substantial theoretical support is inevitable, in particular because our current understanding of far-off-equilibrium dynamics in molecules is very limited. A combination of the presented state-of-the-art imaging methods with strongly aligned or oriented, cold, controlled molecules is a promising route toward recording the molecular movie.
But this journey is just starting.

1.3. This Thesis

The main objective of this work is twofold. The first main goal concerns the extension and optimization of existing methods for laser-induced field-free molecular alignment, ranging from linear molecules to arbitrarily complex asymmetric top rotors without rotational symmetries and marker atoms. The second main goal concerns the imaging of molecules with atomic resolution by employing the laser-induced electron diffraction (LIED) method and the investigation of the effect of the MFF on such measurements.

The structure of this thesis is the following. In chapter 2, the fundamental theoretical, experimental and numerical concepts that were used throughout this thesis will be presented. The fundamental principles underlying quantum-state selection of neutral molecules, pulse shaping techniques, laser-induced alignment and orientation of molecules, the different numerical methods and programs used to simulate the rotational dynamics of molecules, ionization and rescattering of electrons from atoms and molecules, the LIED method and how to retrieve structural information from it, will be discussed. In chapter 3, the general experimental setup with an emphasis on the setup built at the Max-Born Institute (MBI) in Berlin will be presented.

The remaining chapters of the thesis can be divided roughly into two parts. In chapter 4, chapter 5 and chapter 6, field-free alignment of molecules, with successively increasing complexity will be presented. It will be shown how shaped laser pulses can be used to optimally align molecules in chapter 4, chapter 5 and chapter 6 via different shaping methods. In chapter 4, a Mach-Zehnder interferometer was used to create two time-delayed pulses and successively kick OCS molecules to achieve optimal field-free alignment. In chapter 5, 1D alignment of OCS and iodobenzene (IB) was achieved using a spectrally truncated chirped pulse (STCP). This pulse was shaped using a long-pass

transmission filter which cut out part of the spectrum and lead to an altered pulse shape in the time domain, characterized by a fast fall-off from its maximum value to almost zero intensity within a few ps. In chapter 6, a spatial light modulator (SLM) was used to 3D align indole molecules using linearly-chirped elliptically-polarized truncated alignment pulses. Using the SLM the turn-off time of the truncated pulse could be reduced from ∼8 ps in the transmission filter method to below 3 ps.

The second part, consisting of chapter 7 and chapter 8, concentrates on imaging using the LIED method. In chapter 7, LIED measurements of the rare gas atoms argon and krypton and of isotropic OCS at a wavelength of 2 µm are presented. For OCS the molecular structure could be retrieved with atomic resolution to better than ±5 pm by employing the quantitative rescattering theory (QRS), the independent-atom model (IAM) and atomic scattering amplitudes computed using a relativistic partial-wave scattering code. In chapter 8, molecular-frame angularly-resolved photoelectron spectra (MF-ARPES) are presented that were measured from strongly field-free aligned OCS molecules, probed at different wavelengths. The effect of different alignment distributions on the photoelectron momentum distributions (PEMDs) is discussed and the connection to the MFF, in particular to the highest occupied molecular orbital (HOMO) of OCS. Angle-dependent ionization yields and strong-field photoelectron holography (SFPH), observed at different orientations of the molecules with respect to the probe-laser polarization, are presented and their differences are discussed.

Finally, in chapter 9, a summary of what has been achieved and an outlook over ongoing work and projects that are planned for the near future and extend the work presented in this thesis is given. In the Appendix more detailed information about the calculation of expectation values, that were used for the characterization of molecular alignment and orientation, molecular data for the three investigated molecules OCS, IB and indole, and the detector calibration can be found.

2 Fundamental Concepts

This chapter serves as an overview over the theoretical, experimental and numerical methods and concepts used throughout this thesis.

2.1. Molecules in Electric Fields

The interaction of light with matter is at the heart of a plethora of physical phenomena and, in particular, forms the basis of almost all methods to investigate the structure of matter and chemical reactions. The most complete description of light-matter interactions is in terms of Quantum Electrodynamics, which constitutes the physical theory tested with the highest accuracy to date. Nevertheless, many effects can be described in a semi-classical manner, where the bound atomic or molecular system is described quantum mechanically and the light fields classically. We will follow this semi-classical approach throughout this work.

The interaction of molecules with external electric fields $\vec{\epsilon}(t)$ leads to the splitting of degenerate energy levels and energy shifts, which can be described through a series expansion about the field-free energy $E(t_0)$ at some time t_0 before the onset of the field [123]:

$$E(t) = E(t_0) + (\partial_i E)|_{t_0}\epsilon^i(t) + \frac{1}{2}(\partial_i\partial_j E)|_{t_0}\epsilon^i(t)\epsilon^j(t) + \frac{1}{6}(\partial_i\partial_j\partial_k E)|_{t_0}\epsilon^i(t)\epsilon^j(t)\epsilon^k(t) + \dots, \tag{2.1}$$

$$= -\mu_i\epsilon^i(t) - \frac{1}{2}\alpha_{ij}\epsilon^i(t)\epsilon^j(t) - \frac{1}{6}\beta_{ijk}\epsilon^i(t)\epsilon^j(t)\epsilon^k(t) + \dots, \tag{2.2}$$

where $i, j, k = x, y, z$ are cartesian coordinates, $\partial_i E = \frac{\partial E}{\partial \epsilon^i}$, and a sum over repeated co- and contravariant indices is implied (Einstein summation convention). The partial derivatives evaluated at time t_0 can be identified as

$$-(\partial_i E)|_{t_0} = \mu_i, \qquad -\frac{1}{2}(\partial_i\partial_j E)|_{t_0} = \alpha_{ij}, \qquad -\frac{1}{6}(\partial_i\partial_j\partial_k E)|_{t_0} = \beta_{ijk}, \tag{2.3}$$

being the permanent dipole moment, the static polarizability tensor of second order, and the hyperpolarizability tensor of third order, respectively. Usually only terms up to the polarizability tensor are included since on the one hand the series in (2.1) typically converges fast, with higher-order terms being negligibly small, and on the other hand there do not exist reliable data, neither measured nor computed, for the higher-order tensors.

Hereafter, we consider the coupling of molecules to static electric fields, as provided in a velocity map imaging spectrometer (VMIS) [124] or a Stark deflector [1], and to

alternating electric fields employed for laser-induced alignment [70]. The Hamiltonian for a polar molecule coupled to a static and alternating electric field can be written as [125]

$$\hat{H} = \hat{H}_{\mathrm{r}} + \hat{H}_{\mathrm{Stark}} + \hat{H}_{\mathrm{laser}} \,. \tag{2.4}$$

The first term in (2.4) describes the field-free rigid rotor Hamiltonian

$$\hat{H}_{\mathrm{r}} = B_x \hat{J}_x^2 + B_y \hat{J}_y^2 + B_z \hat{J}_z^2 \,, \tag{2.5}$$

with $B_i = \hbar/2I_{ii}$ being the rotational constants of the molecule, depending on the moments of inertia I_{ii} in the principal axis system of inertia, and $\hat{J}_i$ being the angular-momentum operators defined in the molecule-fixed frame (MFF) with $i = x, y, z$.
The second term in (2.4) describes the coupling of the molecule to a static electric field ϵ_s [126].

$$\hat{H}_{\mathrm{Stark}} = -\vec{\mu} \cdot \vec{\epsilon}_s = -\epsilon_s \sum_i \mu_i \Phi_{iZ} \,, \tag{2.6}$$

where $\vec{\mu}$ is the permanent dipole moment of the molecule and ϵ_s was chosen to point along the Z axis in the laboratory-fixed frame (LFF). The transformation from the MFF with $i = x, y, z$ to the LFF with $J = X, Y, Z$ is given by a rotation around the three Euler angles (ϕ, θ, χ), described through the direction cosines Φ_{iJ}, i. e., the entries of the rotation matrix [127]. The Stark effect will be discussed in more detail in subsection 2.1.1.
The last term $\hat{H}_{\mathrm{laser}}$ in (2.4) describes the coupling of the molecule to a non-resonant non-ionizing ac laser field $\vec{\epsilon}(t)$, given by [70]

$$\hat{H}_{\mathrm{laser}} = -\vec{\mu} \cdot \vec{\epsilon}(t) - \frac{1}{4} \sum_{J,K} \epsilon_J(t) \alpha_{JK} \epsilon_K(t) \,, \tag{2.7}$$

where the space-fixed components α_{JK} of the polarizability tensor with $J, K = X, Y, Z$ are related to the molecule-fixed components α_{mn} through [70]:

$$\alpha_{JK} = \sum_{m,n} \Phi_{Jm} \alpha_{mn} \Phi_{nK} \,. \tag{2.8}$$

The first term in (2.7) describes the coupling of the permanent dipole moment to the laser field and it is typically neglected, since for lasers in the visible or near infrared part of the spectrum the oscillations of the field are fast compared to the rotational dynamics of the molecules, i. e., the dipole moment contribution averages to zero over one optical cycle [78]. A more detailed discussion of the Hamiltonian in (2.7) will be presented in the context of molecular alignment in section 2.3.

2.1.1. Stark Effect

A polar molecule has a permanent dipole moment in the MFF, i. e., the centers of positive and negative charge distributions do not coincide. The interaction of such a molecule with a static electric field leads to energy shifts and hybridization of the wavefunction

according to the dc Stark effect [128]. The energy correction W can be calculated by perturbation theory [126], resulting in the first-order correction for a symmetric top rotor

$$W^{(1)} = \langle JKM| \hat{H}_{\text{Stark}} |JKM\rangle = -\mu\epsilon_s \langle JKM| \Phi_{zZ} |JKM\rangle = -\frac{\mu\epsilon_s KM}{J(J+1)}\,, \tag{2.9}$$

where $\hat{H}_{\text{Stark}}$ is defined in (2.6), J is the angular-momentum quantum number, M its projection onto a lab-fixed axis, K its projection onto a molecule-fixed axis and $|JKM\rangle$ are the symmetric rotor eigenstates. For linear molecules, as well as symmetric top molecules in states with $K = 0$, the first-order correction vanishes and there is no linear Stark effect. The second-order correction, or quadratic Stark effect, for a linear molecule is accordingly calculated as [126]

$$W^{(2)} = \sum_{J'} \frac{|\langle JM| \hat{H}_{\text{Stark}} |J'M\rangle|^2}{E_J - E_{J'}} = \frac{\mu^2\epsilon_s^2}{2hB} \frac{J(J+1) - 3M^2}{J(J+1)(2J-1)(2J+3)}\,. \tag{2.10}$$

In general, to second order perturbation theory, the total energy correction can be written as

$$W = W^{(1)} + W^{(2)} = -(\vec{\mu} + \vec{\mu}_{\text{ind}}) \cdot \vec{\epsilon}_s = -\mu_{\text{eff}}\epsilon_s\,, \tag{2.11}$$

where $\vec{\mu}_{\text{ind}} = \underline{\underline{\alpha}}\vec{\epsilon}_s$ is the induced dipole moment and μ_{eff} the space-fixed effective dipole moment along the electric field axis in the LFF. The effective dipole moment can be calculated as the first derivative of the energy correction according to

$$\mu_{\text{eff}}(\epsilon_s) = -\frac{\partial W}{\partial \epsilon_s}\,. \tag{2.12}$$

In Figure 2.1 a, the Stark effect energy correction as a function of the applied electric field strength is shown for the linear molecule OCS for its six lowest energy eigenstates and in Figure 2.1 b the corresponding effective dipole moments. One observes that for certain states the energy increases with increasing field strength whereas for most states it decreases. These states are called low-field seeking and high-field seeking states, respectively. Since molecules interacting with the external electric field tend to minimize their energy, molecules in low-field seeking states are repelled and high-field seeking states are attracted to regions of high field strengths.

The field-strength dependence of the energy shift and of the effective dipole moment in (2.12) can be used to manipulate the motion of molecules. In an inhomogeneous field a force

$$\vec{F} = -\vec{\nabla}W = \mu_{\text{eff}} \cdot \vec{\nabla}\epsilon_s \tag{2.13}$$

is exerted on the molecules. According to (2.13), molecules with different effective dipole moments will experience different forces and, hence, follow different trajectories. This is the basic idea underlying the concept of quantum-state selection using the electrostatic deflector [1]. Two electrodes at different potentials create a static electric field, homogeneous in one direction and strongly inhomogeneous in the perpendicular direction. Molecules in different quantum states are spatially dispersed according to (2.13), with the rotational ground state $|J = 0, M = 0\rangle$ experiencing the strongest shift (see Figure 2.1 a,b).

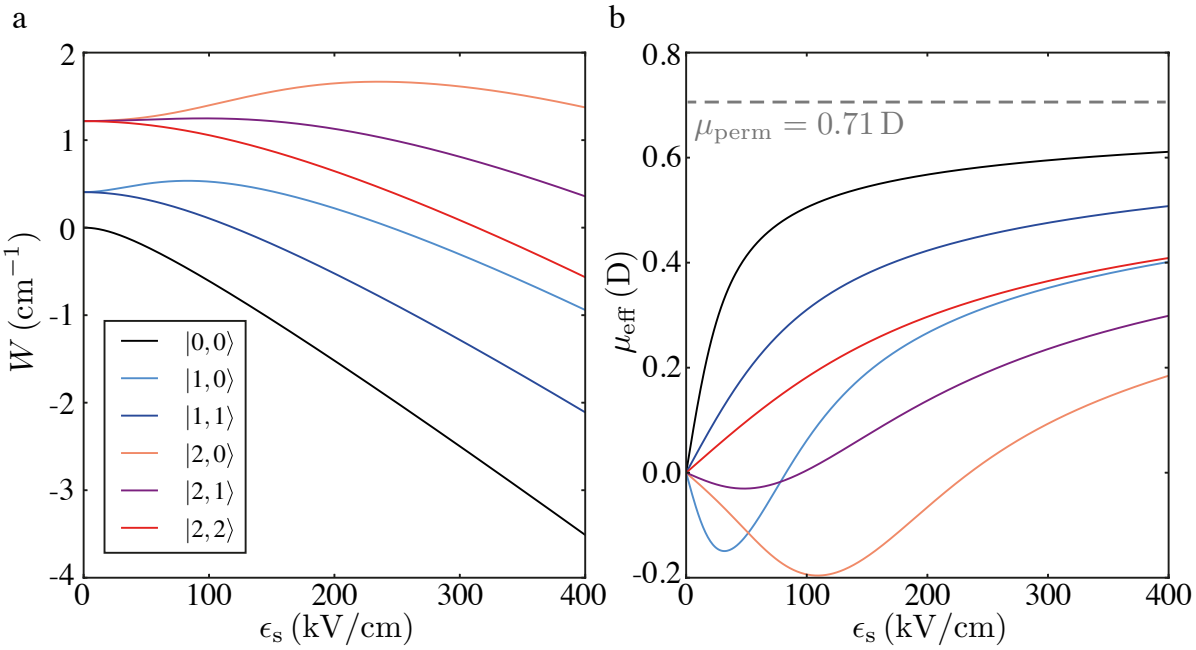

Figure 2.1.: Stark curves with energy shifts and effective dipole moments of the six lowest rotational states of OCS. **a** Energy shift calculated from dc Stark effect, **b** effective dipole moments calculated as first derivative of energy shift with respect to electric field strength. The curves were calculated using CMIstark [129], the image is taken from [61].

For molecules with large permanent dipole moments and very different magnitudes of the effective dipole moments for different quantum states, this allows to spatially separate a part of the molecular beam which contains an almost pure ground-state contribution [1, 62, 130, 131].

2.2. Pulse Shaping

In subsection 2.3.3, the dependence of the rotational dynamics of molecules on the pulse parameters of the alignment laser is discussed. Different pulse parameters generally lead to different dynamics, which defines the problem of finding optimal pulse forms to control the rotation of molecules. This can be achieved using optimally tailored laser pulses. The term pulse shaping in general refers to any modification of the electric field of a laser pulse. However, in particular for ultrashort laser pulses, it is difficult to modify the electric field by shaping it in the time domain, because the response time of materials is slower than the duration of the light fields. Therefore, shaping of femtosecond and picosecond long laser pulses is performed in the frequency domain.

A laser pulse is completely characterized either by its electric field $\epsilon(t)$ or its spectrum $\epsilon(\omega)$. The spectrum is related to the electric field via a Fourier transformation

$$\epsilon(\omega) = \int_{-\infty}^{\infty} \epsilon(t) e^{i\omega t} \mathrm{d}t \,. \tag{2.14}$$

A pulse shaper is a device that modifies the electric field or its spectrum and can be approximated to first order as a linear system which takes an input pulse and returns an output pulse. The effect of the linear system can be uniquely described by its impulse response function $h(t)$ in the time domain, or equivalently, by its transfer function $H(\omega)$ in the frequency domain. Input functions $f(t), F(\omega)$ and output functions $g(t), G(\omega)$ are related via

$$g(t) = (f * h)(t)\,, \tag{2.15}$$

$$G(\omega) = F(\omega)H(\omega)\,. \tag{2.16}$$

The effect of the pulse shaper on the input pulse is, therefore, uniquely characterized if one knows the impulse or transfer function of the pulse-shaping device.

Some of the simplest pulse-shaping devices are for example the Michelson or Mach-Zehnder interferometers, which split an input pulse into two pulses, delayed with respect to each other; dispersive media that delay pulses and introduce spatial and temporal chirps; and grating compressors, used to introduce or remove chirps in the electric field [132]. Pixelated liquid-crystal pulse shaper, called SLM, contain a large number of pixels that are used as waveplates and can be controlled individually through an applied voltage [133, 134]. The phase introduced through each pixel is

$$\phi(\omega, U) = \frac{\omega \Delta n(\omega, U) e_{\mathrm{CL}}}{c}\,, \tag{2.17}$$

where $\Delta n(\omega, U)$ is the difference between the refractive index of the fast and the slow axis of the nematic liquid crystals, U is the applied voltage, c is the speed of light and e_{CL} is the distance the light travels inside the liquid crystal pixel. Using a $4f$-setup, also called zero-dispersion line, one can separate and focus different wavelengths onto different pixels and, therefore, act individually on different components of the spectrum. Recombining them afterwards with a changed phase pattern leads to a new waveform [132]. More details on pulse shaping can be found in the review articles [132, 135] and references therein.

2.3. Alignment and Orientation of Molecules

Both terms, alignment and orientation, refer to the confinement of molecular axes with respect to the laboratory-fixed frame (LFF). One speaks of one-dimensional alignment, if only one molecular axis is confined and of three-dimensional alignment, if all three molecular axes are confined. Aligned molecules still possess a head-to-tail symmetry, corresponding to rotations of 180 ° around an axis perpendicular to the laser polarization axis. If this symmetry is broken, one speaks of orientation, in particular 1D/3D orientation for one axis being oriented or all three axes having preferred directions in space, respectively. Molecules in the gas phase rotate freely and are randomly aligned and oriented. Ensemble-averaged measurements do not allow to access the molecule-fixed frame (MFF) and yield isotropic angular distributions. Alignment and orientation is in

this sense equivalent to the creation of anisotropic angular distributions where the degree of anisotropy is a measure of how well-aligned and oriented the molecules are [136]. The concepts introduced above are illustrated in Figure 2.2 for the asymmetric top rotor iodobenzene (IB) for both, 1D and 3D.

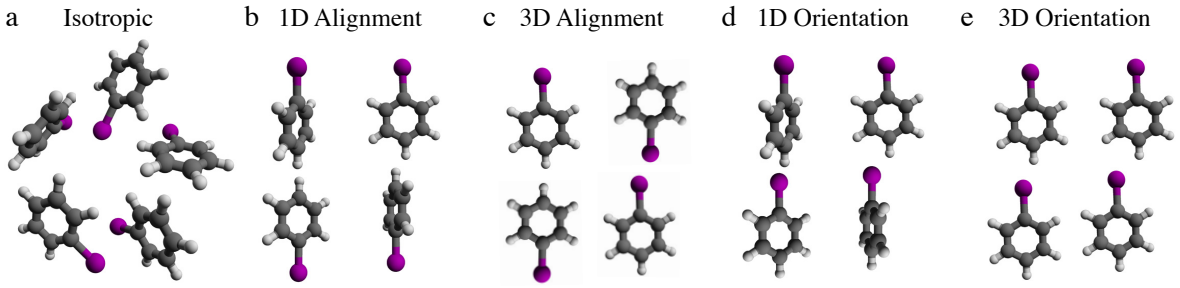

Figure 2.2.: Schematic visualization of alignment and orientation of the asymmetric top rotor iodobenzene. **a** Isotropic distribution of molecular axes without external field, **b** one-dimensional alignment as created using a linearly-polarized laser pulse, **c** three-dimensional alignment where all molecular axes are fixed in space as created by using two linearly cross-polarized or an elliptically-polarized laser pulse, **d** one-dimensional orientation as created by using a dc field, and **e** three-dimensional orientation as created by using mixed-field orientation, i. e., 3D alignment combined with a static electric field.

We will restrict our discussion to alignment of molecules using non-resonant non-ionizing laser pulses [70] and mixed-field orientation [112, 113], where in addition to alignment a static electric field is used to define a preferred direction in space. The Hamiltonian for this scenario was already introduced in (2.4). In most experiments, where laser-induced alignment is employed, lasers with wavelengths centered at 800 nm or 1064 nm are used, since they are well detuned from any resonances in most molecules. At these wavelengths the laser cycle is much faster than the rotational period of the molecules and the dipole moment term in (2.7) can be neglected [78]. Thus, molecular alignment can be simply described through the interaction of the laser with the polarizability tensor of the molecule, and, in particular, with the polarizability anisotropy as we will see in the following.

The interaction Hamiltonian in (2.7) can be re-expressed for linearly-polarized light interacting with a linear molecule as [84]

$$H_{\text{ind}} = -\frac{\epsilon_0^2}{2}(\Delta\alpha \cos^2\theta + \alpha_\perp)\,, \tag{2.18}$$

with the polarizability anisotropy $\Delta\alpha = \alpha_\parallel - \alpha_\perp$ and the components of the polarizability tensor parallel and perpendicular to the internuclear axis $\alpha_\parallel, \alpha_\perp$. The angle θ is the Euler angle between the laser polarization and the molecular axis. The degree of alignment (DOA) is usually characterized using the expectation value

$$\langle \cos^2\theta \rangle = \int_0^{2\pi}\int_0^{2\pi}\int_0^{\pi} P(\theta,\phi,\chi)\cos^2\theta\,\sin\theta\,\mathrm{d}\theta\,\mathrm{d}\phi\,\mathrm{d}\chi\,, \tag{2.19}$$

where $P(\theta,\phi,\chi) = |\Psi(\theta,\phi,\chi)|^2$ is the angular distribution describing the arrangement

of molecular orientations. This measure, however, is proportional to the lowest-order moment of an expansion of the total angular distribution in terms of Legendre polynomials, for example. For most experiments $\langle\cos^2\theta\rangle$ is already good enough to characterize the anisotropy in the angular distribution but, as we will see in chapter 4, higher-order terms might become important.

For three-dimensional alignment all three molecular axes have to be confined. As a measure of the DOA, either the three expectation values $\langle\cos^2\theta_{xX}\rangle$,$\langle\cos^2\theta_{yY}\rangle$ and $\langle\cos^2\theta_{zZ}\rangle$ between the principal axes of the polarizability tensor of the molecule and the LFF coordinate system or the expectation values of the three Euler angles $\langle\cos^2\theta\rangle$,$\langle\cos^2\phi\rangle$ and $\langle\cos^2\chi\rangle$ are typically utilized. There exist also other metrics to characterize the degree of 3D alignment, e. g., using only a single expectation value [137].

In this work molecular alignment is measured through Coulomb-explosion imaging (CEI), in which molecules are fragmented using short, strong laser pulses that multiply ionize the molecules. Ion-momentum distributions are recorded for different ionic fragments using a velocity map imaging spectrometer (VMIS) [124] combined with a 2D MCP/Phosphor screen detector, see chapter 3 for details. The measured 2D signal represents the projected 3D rotational probability density, weighted with the angle-dependent ionization efficiency and, depending on the fragmentation process, convoluted with a distribution originating from potential non-axial recoil. If the axial-recoil approximation holds, the orientation of the molecular axes prior to fragmentation can be reconstructed in principle, otherwise complete knowledge of the non-axial recoil distribution, i. e., the fragmentation process is required. In such experiments the observable that can be directly accessed is $\langle\cos^2\theta_{\mathrm{2D}}\rangle$, where the angle θ_{2D} is the polar angle in the plane of the detector with respect to the laser polarization axis. If cylindrical symmetry is preserved one can employ an inverse Abel transformation to reconstruct the 3D distribution [138], otherwise usually a complete tomography is required. For an isotropic distribution, the expectation value is given by $\langle\cos^2\theta_{\mathrm{ND}}\rangle = 1/N$, where N is the dimensionality, such that in three dimensions the value is $1/3$ and in two dimensions it is $1/2$. In both cases the upper bound of the DOA is 1, corresponding to perfect alignment. The relation $\langle\cos^2\theta_{\mathrm{2D}}\rangle \geq \langle\cos^2\theta\rangle$ always holds, where the equal sign applies for the case of perfect alignment.

2.3.1. Adiabatic Alignment

The interaction Hamiltonian in (2.18) induces an optical potential V_{ind}, which is illustrated in Figure 2.3 a for OCS. Depending on the timescale on which the laser field is switched on or switched off, compared to the rotational period of OCS, the resulting rotational dynamics behaves quite differently. A necessary but not sufficient condition for adiabacity is given by

$$\tau_{\mathrm{laser}} \gg \max\{T_{\mathrm{A}}, T_{\mathrm{B}}, T_{\mathrm{C}}\}\,, \tag{2.20}$$

with the pulse duration of the alignment laser τ_{laser} and the rotational period T_{X} for a rotation around the principal axis X = A,B,C. This relation ensures adiabacity, if there is no conical intersection or avoided crossing involved and the Born-Oppenheimer approximation is valid. When the adiabatic theorem of quantum mechanics holds [139], the

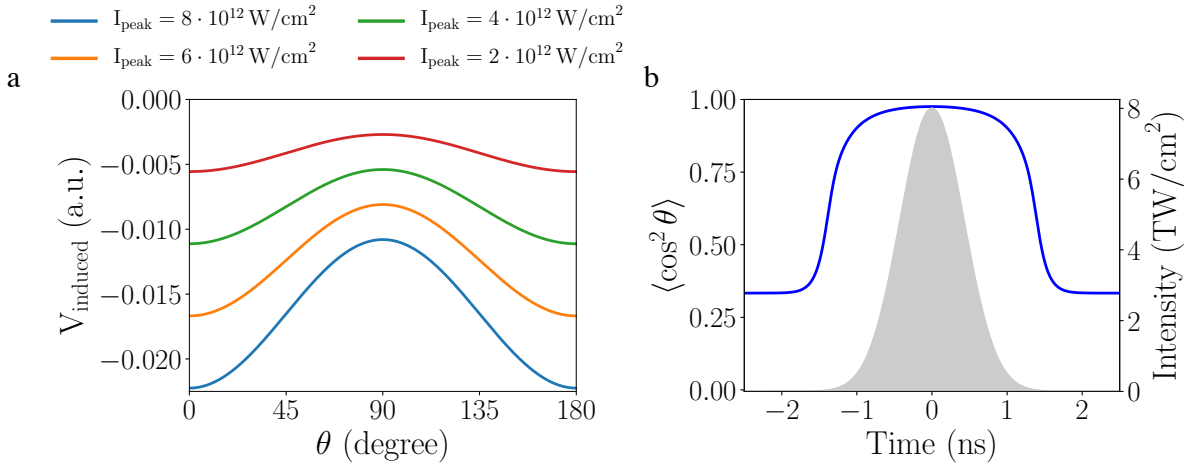

Figure 2.3.: Adiabatic laser-induced alignment of OCS with a Gaussian-shaped laser pulse with 1 ns pulse duration. **a** Optical double-well potential induced through the polarizability-laser interaction, plotted for different peak intensities **b** 3D alignment of OCS for a peak intensity of $8 \times 10^{12}\,W/cm^2$. After the pulse has passed, the alignment returns to its isotropic value of 1/3.

field-free eigenstates of the rotational Hamiltonian adiabatically evolve into field-dressed states, which in this case are also called field-induced pendular states [73, 84]. These pendular states are eigenstates of the optical double-well potential shown in Figure 2.3 a and are angularly confined. The degree of angular confinement depends amongst others on the depth of the potential well and rises with increasing intensity, limited by the onset of ionization. In Figure 2.3 b, the 3D degree of adiabatically aligned OCS is shown. Since in the adiabatic limit no population transfer takes place, molecules can only be aligned during the pulse.

2.3.2. Impulsive Alignment

Adiabatic alignment suffers from the disadvantage that alignment only exists as long as the alignment laser field is present. The presence of this field can result in severe perturbations of the dynamics under investigation and influence the outcome of the measurements. If the turn-on or turn-off of the laser field is much faster than the rotational period of the molecule

$$\tau_{laser} \ll \min\{T_A, T_B, T_C\}\,, \tag{2.21}$$

one speaks of impulsive alignment. In this case the interaction of the polarizability anisotropy with the laser field leads to the population of excited rotational states and a coherent rotational wavepacket is formed [89, 92, 140]. This is achieved via non-resonant two-photon Raman transitions which impose the selection rules $\Delta J = 0, \pm 1, \pm 2$ on rotational transitions, see Figure 2.4 a. The angular confinement is related to the fact that angular momentum J and alignment angle θ are canonically conjugate variables, such that the broader the wavepacket in J-space is, the higher the DOA becomes, if the rotational states are in phase.

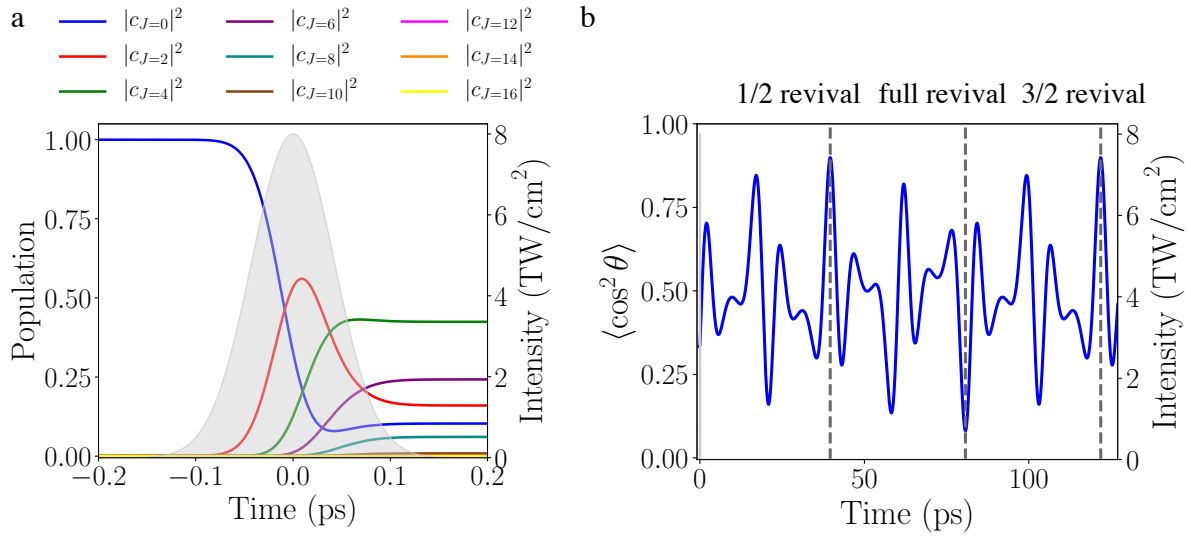

Figure 2.4.: Impulsive laser-induced alignment of OCS with a Gaussian-shaped laser pulse with 8 TW peak intensity and 100 fs pulse duration. **a** Population transfer with $\Delta J = 0, \pm 2$ during the laser pulse and creation of coherent rotational wavepacket, **b** 3D degree of alignment with its characteristic interference pattern of collapses and revivals. Dashed grey lines indicate the positions of the half revival, the first full revival and the 3/2 revival.

The resulting rotational wavepacket Ψ can be expressed as coherent superposition

$$\Psi(\theta, \phi, \chi, t) = \sum_{J,K,M} c_{JKM}(t) \langle \Omega | JKM \rangle \ , \tag{2.22}$$

where $\Omega = (\theta, \phi, \chi)$, $c_{JKM}(t)$ are the time-dependent complex coefficients, $|JKM\rangle$ are the symmetric rotor eigenstates and

$$\langle \Omega | JKM \rangle = (-1)^{M-K} \sqrt{\frac{2J+1}{8\pi^2}} D^J_{-M,-K}(\Omega) \tag{2.23}$$

are the symmetric rotor eigenfunctions with $D^J_{-M,-K}(\Omega)$ the Wigner D-functions. This expansion holds not only for symmetric top molecules, but also for linear molecules, where $K = 0$ and the eigenfunctions reduce to spherical harmonics. For asymmetric top rotors, whose eigenfunctions cannot be cast in an analytical form, an expansion in the symmetric top basis is usually carried out [126]. The DOA can then be expressed in the symmetric top basis as

$$\langle \cos^2\theta \rangle(t) = \sum_{J,K,M} \sum_{J',K',M'} c_{JKM}(t) c^*_{J'K'M'}(t) \langle J'K'M' | \cos^2\theta | JKM \rangle \ . \tag{2.24}$$

In the field-free region, after the alignment laser pulse has passed, the time dependence of each individual term in the DOA is $e^{i/\hbar(E_{JKM} - E_{J'K'M'})t}$, i. e., oscillating at frequency $\omega_{ij} = \hbar^{-1}(E_i - E_j)$, where E_i is the energy of the rotational eigenstate with quantum numbers $i = \{J, K, M\}$. The wavepacket coefficients are complex and the DOA shows a characteristic interference pattern with collapses and revivals, as shown in Figure 2.4 b

for OCS. At the half revival the strongest alignment is observed, i. e., the molecules are confined within a cone around the laser polarization direction, whereas at the full revival the molecules are anti-aligned, i. e., localized in a plane perpendicular to the laser polarization, and the lowest degree of alignment is observed. Since the energy-level structure of a linear molecule is $E_J = hBJ(J+1)$, its revival period is given by $T_{\text{rev}} = \frac{1}{2B}$, where B is its rotational constant in Hz. Fractional revivals such as the half revival at $T_{\text{rev}}/2$ and, depending on the spin statistics of the molecule [62, 141, 142], higher-order revivals $T_{\text{rev}}/4, T_{\text{rev}}/8, \ldots$, are observed, too. Symmetric and asymmetric top rotors also show revival structures which are more complex than for linear molecules due to their more complex energy-level structure. The most common revivals for a molecule with rotational constants A, B, C are J-type transients [143] which occur at $t = n/4(B+C)$ for nearly-perfect or perfectly symmetric top rotors with $B \simeq C$ and with n an integer number, A-type transients at $t = n/4A$, C-type transients at $t = n/4C$ where C is the rotational axis pointing perpendicular to the molecular plane for planar molecules, and K-type transients at $t = n/4(A-B)$ for prolate top and $t = n/4(|C-B|)$ for oblate top molecules. The rotational energies are in general non-commensurable in asymmetric top rotors and, hence, no true rephasing occurs and the revivals quickly dephase and are only observed for a short time [81, 82, 127, 144–147].

More complete treatment of alignment and orientation can be found in the literature, in particular in the review articles [70, 91, 148, 149] and references therein.

2.3.3. Alignment by Shaped Laser Pulses

In laser-induced impulsive alignment the highest degree of angular confinement that can be achieved depends critically on the structure of the rotational wavepacket that is created, i. e., populations and relative phases of rotational states, which in turn depend on the exact parameters of the alignment laser pulse, i. e., pulse shape, peak intensity, polarization, pulse duration, spatial and temporal chirps. This can be realized if one considers that the pulse duration of the alignment laser has on the one hand to be short enough to fulfill quation (2.21), but on the other hand the state with maximum angular momentum, populated during the pulse, is $J_{\text{max}} \sim \tau_{\text{laser}}/\Omega_R^{-1}$, where Ω_R is the two-photon Rabi frequency. Therefore, if $\tau_{\text{laser}} \gg \Omega_R^{-1}$, the pulse is sufficiently long to coherently excite high-lying J-states and create strong angular confinement [70, 91]. The two-photon Rabi frequency itself is proportional to the square of the field and, hence, depends critically on the field parameters.

This observation can be used, in combination with the pulse-shaping methods presented in section 2.2, to find pulse parameters that optimize the degree of alignment. This was the major objective of the first part of this thesis.

For linear molecules the structure of the rotational wavepackets is quite simple and it is possible to achieve very high degrees of alignment using relatively simple pulse-shaping methods, such as pulse trains [97, 98]. Nevertheless, laser pulses where the pulse shape itself is optimized can lead to the same optimal DOA with a narrower rotational state distribution due to stronger rephasing amongst the populated rotational states [150].

For asymmetric top rotors the rotational wavepackets are more complex and no true revivals occur anymore. For such molecules, a different strategy is required to achieve strong field-free alignment. Promising methods include the usage of truncated adiabatic laser pulses [151] or the combination of long and short laser pulses [101, 103]. The idea behind this approach is to first utilize adiabatic alignment leading to strong angular confinement during the pulse. When the pulse is abruptly turned off, the pendular states are projected onto the field-free eigenbasis and a coherent rotational wavepacket is formed. Using a short kick pulse before truncation can lead to an even broader wavepacket and stronger phasing. Due to their inertia the molecules stay aligned for a short time after turn-off, which, when the truncation is fast enough, leads to field-free alignment.

In real experiments the turn-off time of the laser fields is always finite and the resulting wavepacket depends critically on it. For turn-off times long enough, such that substantial population transfer occurs during the truncation, the resulting field-free wavepacket is considerably modified with respect to the superposition of states at the peak of the adiabatic alignment field.

2.3.4. Numerical Simulations

In this section we give an overview over the numerical methods and computer programs used to simulate the rotational dynamics of linear and asymmetric top molecules subject to external laser fields and static electric fields. These programs were used to calculate expectation values, simulate VMIS images and to analyze the experiments, presented in chapter 4, chapter 5 and chapter 6, where the alignment of linear and asymmetric top rotors was investigated.

First we present the program TDasyrot, which is used to solve the time-dependent Schrödinger equation (TDSE) for both, linear and asymmetric top rotors, when the polarizability tensor is diagonal in the principal axis system of inertia and the polarization of the laser fields remains constant during the pulse. It uses symmetry-adapted basis sets, depending on the symmetries of the Hamiltonian in the presence of the fields, to block diagonalize the Hamiltonian. For these cases TDasyrot provides an optimized package. For general, more complex molecules, with less symmetries and interacting with arbitrary fields that may change their polarization during the pulse, the code RichMol is used.

TDasyrot

The numerical results presented in chapter 4 and chapter 5 were obtained using the program TDasyrot, which stands for *time-dependent asymmetric rotor*, originally developed by the group of Rosario González-Férez [115, 152–155].

TDasyrot is used to solve the non-relativistic TDSE for linear and asymmetric top molecules, coupled to non-resonant ac laser fields and static electric fields for arbitrary angles β between the laser polarization and the static electric field direction. The code solves the rotational part of the TDSE for a rigid rotor, assuming the validity of the Born-Oppenheimer approximation and neglecting couplings to vibrationally and electronically excited states as well as fine and hyperfine interactions and nuclear spin-statistical effects.

For an elliptically-polarized laser field, the Hamiltonian (2.7), describing the interaction of a molecule with the laser field, is explicitly given within the rotating-wave approximation [82] as

$$\hat{H}_{\text{laser}} = -\frac{I_{ZZ}(t)}{2c\epsilon_0}(\alpha^{zx}\cos^2\theta_{zZ} + \alpha^{yx}\cos^2\theta_{yZ}) - \frac{I_{XX}(t)}{2c\epsilon_0}(\alpha^{zx}\cos^2\theta_{zX} + \alpha^{yx}\cos^2\theta_{yX})\,. \tag{2.25}$$

In (2.25), I_{ZZ} and I_{XX} are the laser intensities along the major and the minor axes of the polarization ellipse, $\alpha^{ij} = \alpha^{ii} - \alpha^{jj}$ is the polarizability anisotropy and the angles θ_{iJ} are the angles formed between axis i in the MFF and axis J in the LFF. For linear polarization, either $I_{ZZ} = 0$ or $I_{XX} = 0$, such that expression (2.25) simplifies and only one of the two terms remains. The TDSE is solved using an expansion of the rotational wavefunction in terms of symmetric rotor eigenfunctions as presented in (2.22). The time propagation of the Schrödinger equation is carried out using the short iterative Lanczos propagation method [156, 157].

Exploiting the symmetries of the Hamiltonian allows to block diagonalize the Hamiltonian matrix and save computational time, which is particularly important if many time steps need to be propagated. A unitary transformation, the so-called Wang transformation [126], yields a block diagonalization of the Hamiltonian into small sub-blocks H_k for each symmetry species k.

$$H_{\text{Wang}} = \tilde{X}HX = \sum_k H_k = \mathbf{E}^+ + \mathbf{O}^+ + \mathbf{E}^- + \mathbf{O}^-\,. \tag{2.26}$$

Applying the Wang transformation results in a new symmetry-adapted eigenbasis, consisting of superpositions of symmetric rotor eigenstates, called Wang states.

$$|JKMs\rangle = \frac{1}{\sqrt{2}}(|JKM\rangle + (-1)^s\,|J-KM\rangle) \qquad (K>0)\,, \tag{2.27}$$

$$|J0M0\rangle = |J0M\rangle\,, \qquad (K=0)\,, \tag{2.28}$$

with s taking the values $0, 1$, where the $+$ and $-$ in equation (2.26) correspond to $s = 0$ and $s = 1$, respectively. The symmetry operations under which the Hamiltonian remains invariant, depend on the relative orientation of the fields. For a more complete discussion of the symmetries and symmetry-adapted eigenfunctions of asymmetric top rotors in external electric fields see [126, 155], and for further details about molecular symmetries see [126, 141].

RichMol

For the calculations of the rotational dynamics of indole in chapter 6 the RichMol code [158] was used. The purpose of the program is to treat time-dependent rovibrational dynamics of polyatomic molecules in external electric fields based on a variational approach. It is to some extent an extension of the older program TROVE [159].

The coupling of the electric fields with the molecules is described within the Born-

Oppenheimer approximation in terms of multipole moments as shown in (2.1). The rovibrational energies and eigenfunctions can be calculated ab initio, using a variational code such as TROVE, taking as input the geometry of the molecule under consideration. Since for the calculations on indole the coupling to excited vibrational states was not considered, a different approach was followed instead in which the field-free Hamiltonian in (2.5), using experimentally determined rotational constants, was utilized to compute the rotational eigenenergies and eigenfunctions. For the time propagation in the external field, the eigenfunctions are expanded in the field-free eigenbasis of the molecule. The time-dependent wavepacket coefficients are obtained by numerically solving the TDSE using the split-operator method with the time evolution operator being computed using the iterative approximation, based on Krylov subspace methods, as implemented in the Expokit package [160].

The strength of RichMol is that it can handle arbitrary fields in time and space. The multipole moments, i. e., the dipole moment and the static polarizability tensor, have to be taken either from literature, if known, or to be calculated using quantum chemistry codes.

Evolutionary Algorithms

Throughout this thesis optimization algorithms were used, either to compare how well simulated data fit to experiments or to optimize the degree of alignment and to predict optimal experimental parameters.

Evolutionary Algorithms (EAs) are a special class of optimization algorithms, inspired from biological evolution and the idea of survival of the fittest as coined by Darwin, where the parameter space is randomly sampled [161]. Evolutionary Algorithms are in many aspects superior compared to derivative-based optimization methods, in particular when the dimensionality of the parameter space is large, if many local optima exist or if the hypersurface is shallow. Methods using derivatives probe the search space only locally and often one has to provide a good initial guess, close enough to the target solution, in order to achieve convergence. EAs circumvent this problem and enhance the probability to find the global optimum by randomly sampling the full parameter space. In Figure 2.5, the main flow of an EA is illustrated. First, the initial *population* $\vec{q}_{0,0}, \vec{q}_{1,0} \dots \vec{q}_{k,0}$ with a population size of k *individuals* is initialized. The first index indicates the name of the individual and the second index the *generation* number. Each individual carries n *genes*, i. e., the parameters which shall be optimized

$$\vec{q}_{i,j} = \begin{pmatrix} \text{parameter}_1 \\ \text{parameter}_2 \\ \vdots \\ \text{parameter}_n \end{pmatrix} . \tag{2.29}$$

The initial parameters are either randomly chosen within some bounds or given as initial guess. The objective is to find the fittest individual with its n optimal genes that optimizes some fitness function f. In the context of molecular alignment the genes can

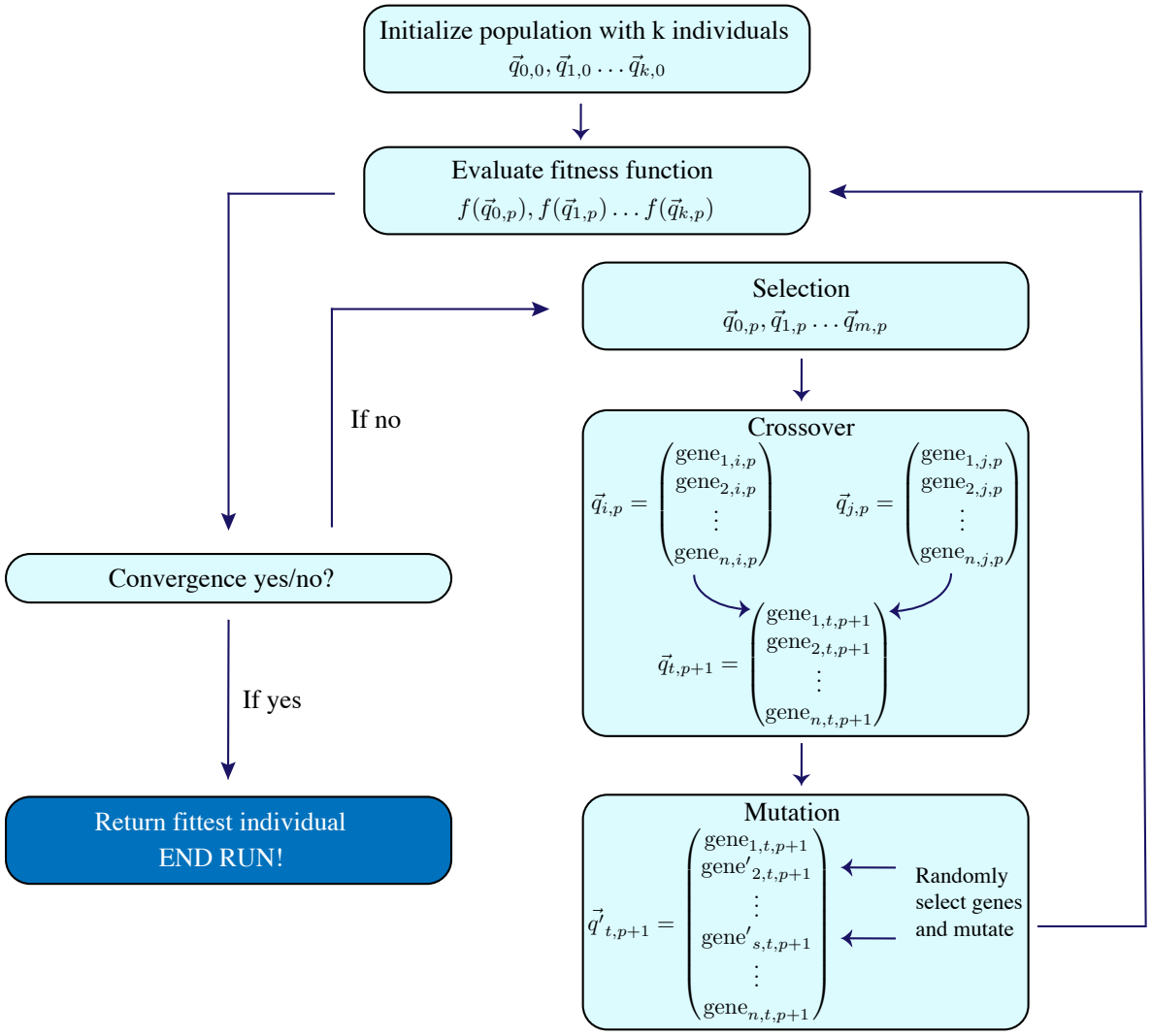

Figure 2.5.: Flow diagram illustrating the working principle of Evolutionary Algorithms.

be for example the alignment laser pulse duration and the peak intensity or the spectral components and their relative phases, and the fitness function the DOA. In the first step the fitness function is evaluated for all individuals $f(\vec{q}_{0,0}), f(\vec{q}_{1,0}) \dots f(\vec{q}_{k,0})$. In the *selection* step, out of the k individuals, the m fittest individuals are selected whereas the remaining $k - m$ individuals are dismissed. The selected m individuals are then subject to a *crossover* to create a set of l new individuals $\vec{q}_{0,1}, \vec{q}_{1,1} \dots \vec{q}_{l,1}$, where l can be equal to k, larger or smaller. In most problems $l = k$ is chosen, such that the total size of the population in each generation is kept constant and two individuals out of the m are randomly chosen and give birth to one descendant. In the next step *mutation* is introduced, i. e., genes of individuals in the new generation are randomly chosen and modified. The probability for mutation to happen is defined by the user. In general a large probability slows down convergence but leads to sampling of a larger part of the parameter space, whereas a small probability acts the opposite. The final step consists in calculating again the fitness function $f(\vec{q}_{0,1}), f(\vec{q}_{1,1}) \dots f(\vec{q}_{l,1})$ for these new individuals and to check whether the convergence criterion is met. If it is met, the algorithm ends

and returns the fittest individual, otherwise the procedure is repeated until convergence is reached.

In this thesis the Differential Evolution Algorithm [162] and the Distributed Evolutionary Algorithms in Python framework (DEAP) [163] were used. More information on EAs can be found for example in [161, 164].

2.4. Molecules in Ionizing Fields

One of the most prominent effects in the realm of light-matter interactions is ionization, in which one or more electrons are released from the system they were initially bound to. The freed electrons carry information about the physical system they originate from and their study can provide important insight into quantum mechanical structure and dynamics. Different ionization mechanisms exist and, depending on the field strength and the frequency of the external light field, one or the other may dominate. In the context of ionization one speaks of strong fields when the field strength of the external light field is comparable to the fields inside matter and typically cannot be treated as a small perturbation anymore.

2.4.1. Ionization Mechanisms

In this section we will briefly discuss the different ionization mechanisms. They can be roughly divided into two main categories, namely perturbative and strong-field ionization. In the first case, the electric fields are relatively weak compared to the field strengths inside atoms and molecules and the dominant ionization mechanism is photon ionization. If the energy of a single photon is enough to overcome the ionization potential (IP), one speaks of single-photon ionization, and if several photons are needed, of multi-photon ionization, which are schematically illustrated in Figure 2.6 a,b, respectively. The ionization probability in this case can be written as

$$w_{\mathrm{n}}(t) = \sigma_{\mathrm{n}}(\omega, \epsilon)\frac{I^n(t)}{\omega^n}\,, \tag{2.30}$$

with $\sigma_{\mathrm{n}}(\omega, \epsilon)$ being the generalized n-photon cross section, ω the frequency of the light field, $n \geq 1$ the number of absorbed photons and $I^n(t)$ the n-th power of the light intensity. The generalized cross section does not depend on the light intensity and is completely characterized through the quantum mechanical structure of the bound system, the polarization of the light field ϵ and its frequency ω. It can be calculated through perturbation theory [165], which implies that the more photons are absorbed, the higher the order of the interaction and the less probable it is, the latter being a necessary condition for the perturbative power series to converge. A characteristic feature of electrons, released through photon absorption, is that they emerge with finite kinetic energy in the continuum, according to

$$\mathrm{E}_{\mathrm{kin}} = n\hbar\omega - (\mathrm{I}_{\mathrm{p}} + \mathrm{U}_{\mathrm{p}})\,, \tag{2.31}$$

with the ionization potential I_p and the ponderomotive potential $U_p = \frac{I}{4\omega^2}$, i. e., the cycle-averaged quiver energy an electron gains when it is accelerated in the ionizing field. For $n \geq N$, where N is the minimum number of photons required for ionization, one speaks of above-threshold ionization (ATI) [166], which is schematically illustrated in Figure 2.6 c. In the energy domain, ATI is interpreted as the absorption of an excess number of photons by the electron. One can consider ATI also in the time domain and interpret it alternatively as the result of interfering electron wavepackets, emitted at successive times that differ by one optical cycle of the field. ATI spectra appear in 2D photoelectron momentum distributions (PEMDs) as concentric rings, spaced by the energy of one photon, with a characteristic nodal structure in the angular distribution reflecting the number of absorbed photons, i. e., angular momentum conservation [167, 168].

If the intensity is increased more and more or the frequency of the ionizing field ϵ is lowered, one enters a regime where the ionization rate increases exponentially with field strength [169], as shown in (2.32)

$$w(t) \propto e^{-(2I_p)^{3/2}/3\epsilon}\,, \tag{2.32}$$

in contrast to the power law in (2.30). Ionization in this regime is called adiabatic ionization or tunnel ionization. A qualitative understanding can be obtained by considering that when the field strength of the external light field is comparable to the fields inside matter, it cannot be treated as a perturbation anymore, but instead it heavily distorts the binding potential. If the frequency of the external field is low, compared to typical response frequencies in the bound system, the distortion is quasi-static from the point of view of a bound electron. Assuming a static, pure Coulomb field and the light-matter interaction within the dipole approximation, the Hamiltonian of the combined bound system and light field can be written as

$$H_{\text{atom - field}} = -\frac{Z}{r} - q\epsilon r\,. \tag{2.33}$$

The resulting potential is schematically illustrated in Figure 2.6 d. It is distorted and bent on one side and the barrier height is significantly lowered, such that tunneling becomes probable, with the tunneling probability increasing exponentially with decreasing barrier height, i. e., higher field strength.
At even higher field strengths, one finally reaches a regime, where the distortion of the binding potential is so strong, that the formerly bound state is now connected to the continuum, which is called over-the-barrier ionization, Figure 2.6 e.

The most prominent models developed to understand and describe tunnel ionization, are the ADK model named after Ammosov, Delone and Krainov [170] and the KFR theory named after Keldysh, Faisal and Reiss [171–173], also known as strong-field approximation (SFA). These methods were first developed to describe ionization of atoms, but they were later extended to ionization of molecules and to include effects of the Coulomb potential, which was initially neglected in the SFA. An overview over these models and their applicability can be found in [174, 175].

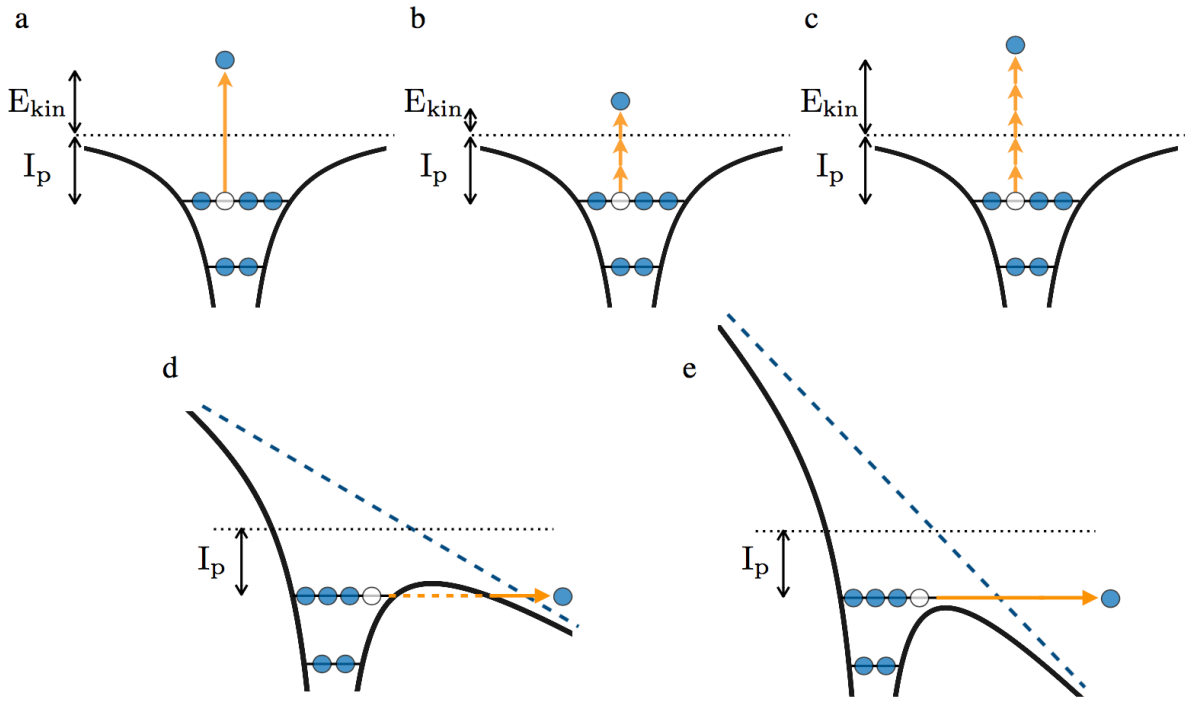

Figure 2.6.: Schematic representation of different ionization mechanisms. **a** Single-photon ionization, **b** multi-photon ionization, **c** above-threshold ionization (ATI), **d** tunnel ionization and **e** over-the-barrier ionization.The dashed black line represents the ionization potential of the unperturbed binding potential, the dashed blue line indicates the electric field responsible for the deformation of the binding potential.

The adiabacity parameter $\gamma = \sqrt{\frac{I_p}{2\,U_p}}$, also called Keldysh parameter, is often a good measure to characterize the regime of ionization. It can be interpreted either as the ratio of the momentum of the bound electron to the field-induced momentum, or equivalently, as the classical tunneling time compared to the laser-field frequency. The parameter γ decreases for smaller field frequencies ω or higher field intensities I. For $\gamma \ll 1$ the tunneling picture applies and, if $\gamma \gg 1$, the multi-photon picture holds and ionization can be described through perturbation theory. It is important to note that most experiments to date are in a regime with $\gamma \sim 1$, where neither a pure tunneling nor a pure multi-photon picture holds. In this intermediate regime the ionization mechanism is a mixture of both, multi-photon and tunnel ionization and is referred to as non-adiabatic ionization [175].

2.4.2. Simple-Man's- and Classical Recollision Model

A simple semi-classical model to interpret strong-field phenomena such as HHG and non-sequential double ionization (NSDI) was developed in the early 1990's by Kulander [176] and Corkum [177], called the simple man's or three-step model. Shortly later, G. Paulus [178] extended the model to include rescattering and to explain the high-energy cutoff in high-energy above-threshold ionization (HATI). In these models, the aforementioned phenomena are explained through the following succesive steps. First, an electron is emitted into the continuum through tunnel ionization. In the next step, the quantum

nature of the electron wavepacket and its residual Coulomb interaction with the cation is neglected and the electron is treated as a classical particle, subject to a force due to the external light field. The electron is accelerated in this field and either directly travels to the detector, commonly referred to as direct electron, or it is driven back to the cation when the field reverses its direction. One possible scenario for the returning electron is to recombine with its parent ion and release its kinetic energy, accumulated during its propagation in the laser field, as a high-energy photon, dubbed high harmonic generation (HHG). Alternatively, it may inelastically rescatter and strip-off a second electron from the cation, called non-sequential double ionization (NSDI). Yet, another possibility is to scatter off the parent ion and to be further accelerated in the laser field after rescattering. Electrons undergoing the latter process can emerge as high-energy electrons in photoelectron momentum distributions (PEMDs), called HATI, and are observed in the recollision plateau above $2\,U_p$. The fraction of elastically scattered electrons is utilized in the LIED method to determine the molecular structure consisting of bond lengths and bond angles, as discussed in detail in subsection 2.4.3. Inelastically scattered electrons typically contribute only a few percent to the total number of scattered electrons [36] and are neglected henceforth.

The ionization step, which is the first step in the simple-man's model, can be treated for instance by the strong-field approximation (SFA). The second step is treated classically solving Newton's equation of motion

$$m_e \ddot{z} = e\epsilon_0 \sin \omega t \,, \tag{2.34}$$

for a free electron in an ac electric field $\epsilon(t) = \epsilon_0 \sin \omega t$. In the following we employ atomic units with $m_e = e = \hbar = 1$. Assuming the electric field to be linearly polarized along the z direction, the liberation time of the electron, also referred to as 'time of birth' in the following, to be at $t = t_0$ and the initial conditions chosen as $z_0 = 0$, $\dot{z}_0 = 0$, the solution to Newton's equation reads

$$\dot{z}(t) = \frac{\epsilon_0}{\omega}(\cos \omega t_0 - \cos \omega t) \,, \tag{2.35}$$

$$z(t) = \frac{\epsilon_0}{\omega^2}(\sin \omega t_0 - \sin \omega t) + \frac{\epsilon_0}{\omega}(t - t_0) \cos \omega t_0 \,. \tag{2.36}$$

The approximation $\dot{z}_0 = 0$ is well justified since an electron released through tunnel ionization enters into the continuum with a narrow momentum distribution peaked around $\vec{p} = 0$ [175]. The condition for an electron to return back to its parent ion at the origin at some time $t_r > t_0$ is a solution of the equation

$$\sin \omega t_r - \sin \omega t_0 = \omega(t_r - t_0) \cos \omega t_0 \,. \tag{2.37}$$

The classical equations of motion considered so far can describe already quite well some qualitative features observed in experimental photoelectron spectra (PES). For phases $0\,^\circ < \omega t < 90\,^\circ$, the electron never returns to its parent ion and it is observed as direct, low-energy electron. As the phase of birth evolves from $0\,^\circ$ to the peak of the electric field at $90\,^\circ$, the ionization probability increases and, simultaneously according to (2.35),

the kinetic energy decreases from its maximum value of $2\,U_p$ to 0. This coincides with the observation that the highest yield in PES is at low energies and gradually decreases until $2\,U_p$. For phases $90\,° < \omega t < 180\,°$, the electron returns to the parent ion with the possibility to rescatter or recombine. Its return energy can be calculated from (2.35) for $t = t_r$ and is shown in Figure 2.7 a in blue as a function of the phase of birth. The

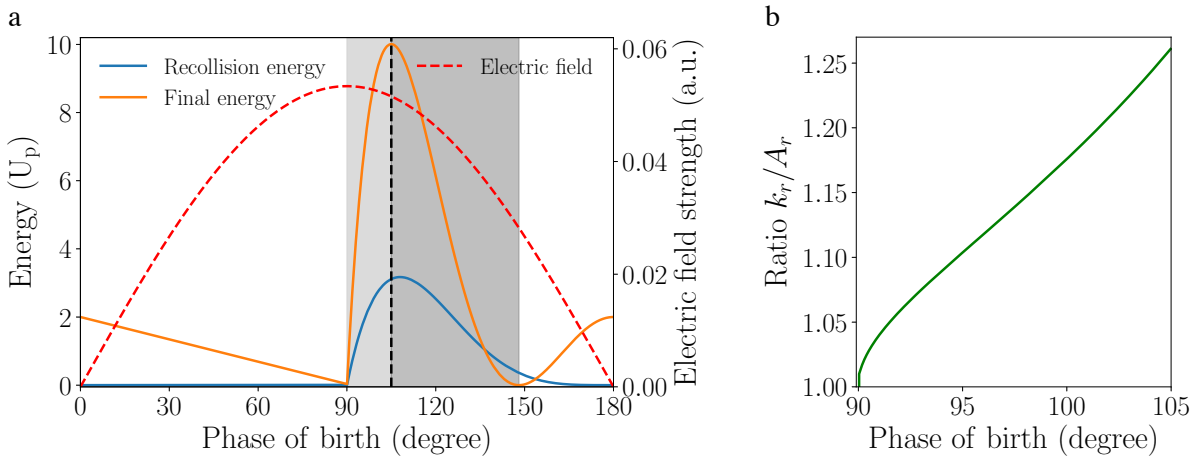

Figure 2.7.: Classical rescattering model. **a** Kinetic energies of electrons at time of their return to the parent ion (blue) and of backscattered electrons ($\theta_r = 180\,°$) measured at the detector (orange) as a function of the phase of birth. The electric field with $\lambda = 2\,\mu m$, $I_{peak} = 10^{14}\,W/cm^2$, responsible for ionization, is indicated as dashed red line. Electrons released at phases in the light grey area follow long trajectories and those in the dark grey area follow short trajectories. **b** Ratio of electron momentum to vector potential at time of recollision (green).

maximum kinetic energy at the first return is $3.17\,U_p$ and occurs for a phase of birth of $\omega t = 107\,°$, i. e., $17\,°$ after the peak of the field.

Consider now that the returning electron elastically scatters from its parent ion at a scattering angle θ_r with respect to its incident direction. Its velocity components parallel and perpendicular to the polarization axis of the laser field are given by

$$\dot{z}(t) = -\frac{\epsilon_0}{\omega}\left[\cos\omega t - \cos\omega t_r + \cos\theta_r(\cos\omega t_r - \cos\omega t_0)\right], \tag{2.38}$$

$$\dot{y}(t) = -\frac{\epsilon_0}{\omega}\sin\theta_r(\cos\omega t_r - \cos\omega t_0)\,. \tag{2.39}$$

The final kinetic energy measured at the detector is then

$$E_k = 2\,U_p\left[\cos^2\omega t_0 + 2(1-\cos\theta_r)\cos\omega t_r(\cos\omega t_r - \cos\omega t_0)\right], \tag{2.40}$$

corresponding to the time averaged kinetic energy in the electric field after subtraction of the ponderomotive energy. The maximum kinetic energy reaches up to $10.007\,U_p$ and it is observed for a phase of birth of $\omega t = 104\,°$ and backscattering with $\theta_r = 180\,°$. Electrons scattered in the forward direction emerge as low-energy electrons. Two trajectories contribute to each final kinetic energy, called long and short trajectories, indicated by the light and dark grey shadowed areas in Figure 2.7 a, respectively. Electrons being released at phases $90\,° < \omega t < 104\,°$ follow long trajectories and return

at $\omega t > 265\,^\circ$, whereas electrons born at phases larger than $104\,^\circ$ return at phases $\omega t < 265\,^\circ$. Electrons following long trajectories have higher ionization probabilities compared to short trajectories since they are released closer to the peak of the field. Hence electrons from long trajectories contribute most to experimentally measured PEMDs. Note that the rescattering probability decreases very fast with increasing ellipticity of the laser polarization because elliptically polarized fields induce an initial transverse velocity component and the electrons miss the parent ion upon their return. The highest rescattering probability is thus obtained for pure linear polarization in this model.

Using the classical model described above, many observed effects can be described and be, at least, qualitatively understood. Nevertheless, the model is severely limited and leaves out all quantum aspects in the propagation of the electron in the laser field, in the interaction with the residual Coulomb field of the cation and in the rescattering process, which may be important for a deeper or complete understanding. Unfortunately, a strict quantum approach to describe these processes is intractable in most cases, in particular for long-wavelength driving fields, because the excursion of the electron before it returns to its parent ion is on the order of several tens to hundreds of atomic units. Numerically one would need computational boxes in three dimensions of several hundred atomic units in each dimension, which is not feasible. For wavelengths up to 1300 nm and 1500 nm a full quantum mechanical calculation in terms of time-dependent density-functional theory is still possible [179].

2.4.3. Laser-Induced Electron Diffraction

The concept of laser-induced electron diffraction (LIED) was first introduced in 1996 in the seminal publication of Zuo, Bandrauk and Corkum [34], where simulated nonlinear multiphoton PEMDs of H_2^+ revealed interference patterns containing structural information about the molecule. The fundamental idea of LIED is that after tunnel ionization, the fraction of returning electrons that elastically rescatters from its parent ion, diffracts off it in a similar way as an ordinary external electron beam from a molecular target in ultrafast electron diffraction (UED). The first revisit of an electron at its parent ion occurs within a fraction of a single laser cycle, therefore opening the possiblity to probe dynamics on ultrafast, femtosecond time-scales. Furthermore, since most of the electrons are released within a short time interval around the peak of the laser field and return with different kinetic energies, depending on their exact time of birth and the number of revisits, the measured PEMDs comprise doubly-differential elastic scattering cross sections from which energy- and angle-resolved differential cross sections (DCSs) can be extracted. It took more than 15 years after the proposal of LIED until the first experimental realization with sub-100 pm resolution was reported [36]. The reason for this delay is mostly related to the fact that it took time to develop efficient, tunable, high-power table-top laser sources providing mid-infrared wavelengths.

In the following we will present the quantitative rescattering theory (QRS), developed to extract experimental DCSs from PEMDs, the independent-atom model (IAM), and some general considerations about the range of validity of these approaches.

Quantitative Rescattering Theory

In order to extract structural information, such as the scattering potential or bond lengths and bond angles of molecular targets through electron diffraction, one needs a scattering theory that is simple enough to be inverted from momentum space to real space. The quantitative rescattering theory (QRS) [180–182] was developed to provide such a simple scattering theory, from which field-free, elastic, electron-ion scattering cross sections from measured PEMDs can be extracted. The main proposition of QRS is to express the measured PEMDs $S(k,\theta)$ as the product of the returning electron wavepacket $W(k_r)$ and a field-free electron-ion scattering DCS $\overline{\sigma}(k_r,\theta_r)$. This is expressed as

$$S(k,\theta) = W(k_r)\overline{\sigma}(k_r,\theta_r)\,, \tag{2.41}$$

where $\vec{k} = (k,\theta)$ is the momentum of the measured photoelectron and $\vec{k}_r = (k_r,\theta_r)$ is the momentum of the electron at the time of recollision. In contrast to UED, where external electron sources are used, in LIED the atoms and molecules are imaged by their own electrons. Therefore, the DCS depends also on the ionization rate, which is a function of the angles between the ionizing laser and the molecular axes. For molecules, the averaged DCS $\overline{\sigma}(k_r,\theta_r)$ is thus related to the bare DCS $\sigma(k_r,\theta_r,\Omega_{\text{mol}})$ through

$$\overline{\sigma}(k_r,\theta_r) = \int N(\Omega_{\text{mol}})\rho(\Omega_{\text{mol}})\sigma(k_r,\theta_r,\Omega_{\text{mol}})\mathrm{d}\Omega_{\text{mol}}\,, \tag{2.42}$$

with Ω_{mol} describing the orientation of the molecule with respect to the returning electron wavepacket, the angle-dependent ionization rate $N(\Omega_{\text{mol}})$ and the angular distribution $\rho(\Omega_{\text{mol}})$ describing the alignment or orientation of the molecules.

The rescattering process occurs within the laser field, leading to an additional drift momentum $\vec{A}_r$ due to the vector potential, such that the total momentum gain along the laser polarization is given by $\vec{k} = \vec{k}_r - \vec{A}_r$. If the detector lies in the (y,z) plane and the electric field is polarized along z, the momentum right after recollision and the detected momentum are then related through

$$\begin{aligned} k_y &= k\sin\theta = k_r\sin\theta_r\,,\\ k_z &= k\cos\theta = \pm A_r \mp k_r\cos\theta_r\,. \end{aligned} \tag{2.43}$$

The vector potential A_r is taken at the instant of recollision and if only long trajectories are considered, there exists a one-to-one relation $A_r = A(t_r)$. The highest detected kinetic energy is about $10\,U_p$ [178], which corresponds to electrons scattered in the backward direction with $\theta_r = 180\,^\circ$. If only long trajectories are considered, the ratio k_r/A_r ranges from 1.01 for electrons released at the peak of the field to 1.26 for electrons released at a phase of $14\,^\circ$ after the peak of the field, see Figure 2.7 b.

According to (2.43), the DCS as a function of the scattering angle θ_r and for a fixed scattering momentum k_r is then obtained from the PEMDs on a circle with its center at $(0,\pm A_r)$ and radius k_r. Doing this for all $k_r < k_{r,\text{max}}$, the doubly-differential cross section $\frac{\mathrm{d}\sigma}{\mathrm{d}E\mathrm{d}\Omega}$ is obtained.

Independent-Atom Model

A prominent model to extract bond lengths and bond angles of molecules in UED is the independent-atom model (IAM) [183]. In the IAM a molecule is modelled as a collection of atoms which form the scattering centers just like the slits in double-slit diffraction. The model completely neglects intra-molecular interactions such as chemical bonding and the impact of molecular orbitals. The total scattering amplitude for elastic scattering from a molecule is given as the sum [184, 185]

$$F(\vec{k}, \Omega_{\text{mol}}) = \sum_i f_i e^{i\vec{q}\cdot\vec{R}_i} \,, \tag{2.44}$$

where $f_i(k, \theta)$ are the individual complex atomic scattering amplitudes, $\vec{k} = (k, \theta, \phi)$ is the momentum of the scattered electron, $\vec{q} = \vec{k} - \vec{k_0}$ is the momentum transfer with magnitude $q = 2k\sin(\theta/2)$, $\vec{k_0}$ is the momentum of the incoming electron, Ω_{mol} describes the orientation of the molecule with respect to the incoming electron flux and $\vec{R}_i$ is the position of the $i-$th atom in the molecule. The sum extends over all atoms in the molecule. The molecular DCS is then calculated in the far-field as the sum of the scattered waves from all atoms. This yields the expression for the bare DCS [184, 185]

$$\sigma(k, \theta, \Omega_{\text{mol}}) = \sum_{i,j} f_i f_j^* e^{i\vec{q}\cdot\vec{R}_{ij}} = \sum_i |f_i|^2 + \sum_{i\neq j} f_i f_j^* e^{i\vec{q}\cdot\vec{R}_{ij}} \,, \tag{2.45}$$

where $\vec{R}_{ij} = \vec{R}_i - \vec{R}_j$, $|f_i|^2$ is the incoherent DCS for scattering from atom i, and the last sum containing terms of the form $f_i f_j^* e^{i\vec{q}\cdot\vec{R}_{ij}}$ is the molecular interference term. The bond lengths and the bond angles appear in the phase of the molecular interference term. The final DCS $\overline{\sigma}(k, \theta)$, as described in the QRS, is then expressed as

$$\overline{\sigma}(k, \theta) = \sum_i |f_i|^2 \int N(\Omega_{\text{mol}})\rho(\Omega_{\text{mol}})\mathrm{d}\Omega_{\text{mol}} + \sum_{i\neq j} f_i f_j^* \int N(\Omega_{\text{mol}})\rho(\Omega_{\text{mol}}) e^{i\vec{q}\cdot\vec{R}_{ij}}\mathrm{d}\Omega_{\text{mol}} \,. \tag{2.46}$$

The cross section is dominated by the large incoherent atomic contribution, superimposed with small oscillatory modulations due to the molecular interference term. It is advantageous to calculate the so-called molecular contrast factor (MCF) [184]

$$\gamma_{\text{MCF}} = \frac{I - I_{\text{atom}}}{I_{\text{atom}}} = \frac{\sum_{i\neq j} f_i f_j^* \int N(\Omega_{\text{mol}})\rho(\Omega_{\text{mol}}) e^{i\vec{q}\cdot\vec{R}_{ij}}\mathrm{d}\Omega_{\text{mol}}}{\sum_i |f_i|^2 \int N(\Omega_{\text{mol}})\rho(\Omega_{\text{mol}})\mathrm{d}\Omega_{\text{mol}}} \,, \tag{2.47}$$

in which these modulations are more pronounced and which is more sensitive to small changes in the bond lengths and bond angles compared to the DCS. The bond lengths and bond angles can then be determined, e. g., through comparison of the experimentally obtained MCF with the calculated MCF through least-squares minimization.

General Considerations

As shown in subsection 2.4.2, the returning electrons have a velocity distribution with a maximum return energy of $3.17\,U_p$, depending on the phase of the field at the time of ionization. Assuming a wavelength of the driving field of 2 µm, a peak intensity of $1 \times 10^{14}\,W/cm^2$ and taking OCS with an IP of 11.18 eV as an example, the Keldysh parameter is $\gamma = 0.39 < 1$, the ponderomotive energy amounts to $U_p = 37.3\,eV$ and, hence, the maximum return energy is $3.17\,U_p = 118.3\,eV$. This corresponds to a de Broglie wavelength of 112.7 pm which defines the spatial resolution. The 2 µm wavelength of the field corresponds to a laser cycle period of T = 6.67 fs.

In order to increase the spatial resolution one can either increase the peak intensity of the field or the wavelength, because $U_p \propto I\lambda^2$. Increasing the intensity is severly limited by the fact that the probability for ionization from several orbitals and for multiple ionization increases. The difference in energy between the HOMO and HOMO-1 is typically on the order of 1 eV. Electrons from different molecular orbitals smear out the structure in PEMDs and structure retrieval becomes difficult or impossible. Therefore, the peak intensity should be chosen such that, at the given wavelength, ionization is far from saturation [122]. The other option is to increase the wavelength, which is more demanding in terms of laser technology and has the unwanted effect that the number of rescattered electrons decreases rapidly. The flux of returning electrons scales very unfavourably with $\sim\lambda^{-4}$ to $\sim\lambda^{-6}$ [186]. One possibility to circumvent this scaling problem is to increase the repetition rate of the laser system from the standard 1 kHz for Ti:Sapphire systems to several kHz or the MHz range. In addition to the aforementioned points, one should also keep in mind that for longer wavelengths the breakdown of the dipole approximation occurs at lower peak intensities [122]. The validity of the dipole approximation is an important requirement because it guarantees that the magnetic field is negligible compared to the electric field and consequently the electrons do not acquire a significant additional transverse momentum in the field.

Compared to UED experiments with high-energy electron beams of tens or hundreds of keV, the scattering energy in LIED is very low. Naturally the question arises whether this method is capable to deliver DCS containing structural information of the targets with atomic resolution. The key to LIED is that one can obtain large momentum transfer $q = 2k\sin(\theta/2)$ either for high scattering momenta k and small angles θ, as is the case in UED where forward small-angle scattering is observed, or for small k but large scattering angles θ, meaning near backward scattering. The latter one is employed in the LIED method. For large enough momentum transfer close collisions occur, the IAM is valid and bond lengths and bond angles can be determined with atomic resolution from PEMDs using the methods presented before.

3 Experimental Setup

Due to our close collaboration with Arnaud Rouzée at the MBI in Berlin and Henrik Stapelfeldt's group in Aarhus, the experiments presented in this thesis were conducted in different laboratories and experimental setups. Although the setups differ in their details, mostly the laser systems, their general structure is similar, in particular the molecular beam apparatus. The experiments presented in chapter 4, chapter 7 and chapter 8 were collaboratively set up and conducted at the MBI, the experiments presented in chapter 5 in Aarhus and the experiments presented in chapter 6 in Hamburg at CFEL.

In this chapter, first the general aspects of all setups will be discussed. Since my work included setting up the molecular beam machine and most of the optical setup at the MBI, except for the laser system that was already installed and functional, I will focus on this setup and discuss it in more detail. Additionally, measurements that were conducted for the characterization of the molecular beam and electrostatic deflection profiles of OCS are shown. More specific details on the individual setups are presented in the corresponding chapters.

3.1. General Experimental Setup

The experimental setup consists of two major parts, the molecular beam machine, which is schematically illustrated in Figure 3.1, and the optical laser setup, which is schematically illustrated in Figure 3.5.

First, a molecular beam is expanded into the source chamber through supersonic expansion using a pulsed Even-Lavie valve [44]. The molecular beam passes two skimmers and enters the electrostatic deflector [1, 61]. After the deflector, the beam passes a third, movable skimmer that is used to filter out the coldest part of the molecular beam and to separate it from the undeflected seed gas. In the detection chamber the beam enters the interaction region in the velocity map imaging spectrometer (VMIS) [124], between the repeller and extractor electrodes, where the laser beams cross the molecular beam at right angles. One or more laser pulses are utilized to align the molecules and another pulse is used to probe them. In order to characterize the degree of alignment, Coulomb-explosion imaging (CEI) is employed, in which the molecules dissociate rapidly upon multiple ionization and the velocity components and angular distributions of the emerging ionic fragments are recorded. In the LIED experiments, the molecules are strong-field ionized and angularly-resolved electron-momentum distributions are recorded. Depending on the sign of the voltage applied to the VMIS electrodes, electrons or ions are accelerated through a short field-free flight tube toward a combined 77 mm dual multi-channel plate (MCP) and phosphor-screen detector. The image created on the phosphor screen is read out on a computer using a charge-coupled device (CCD) camera.

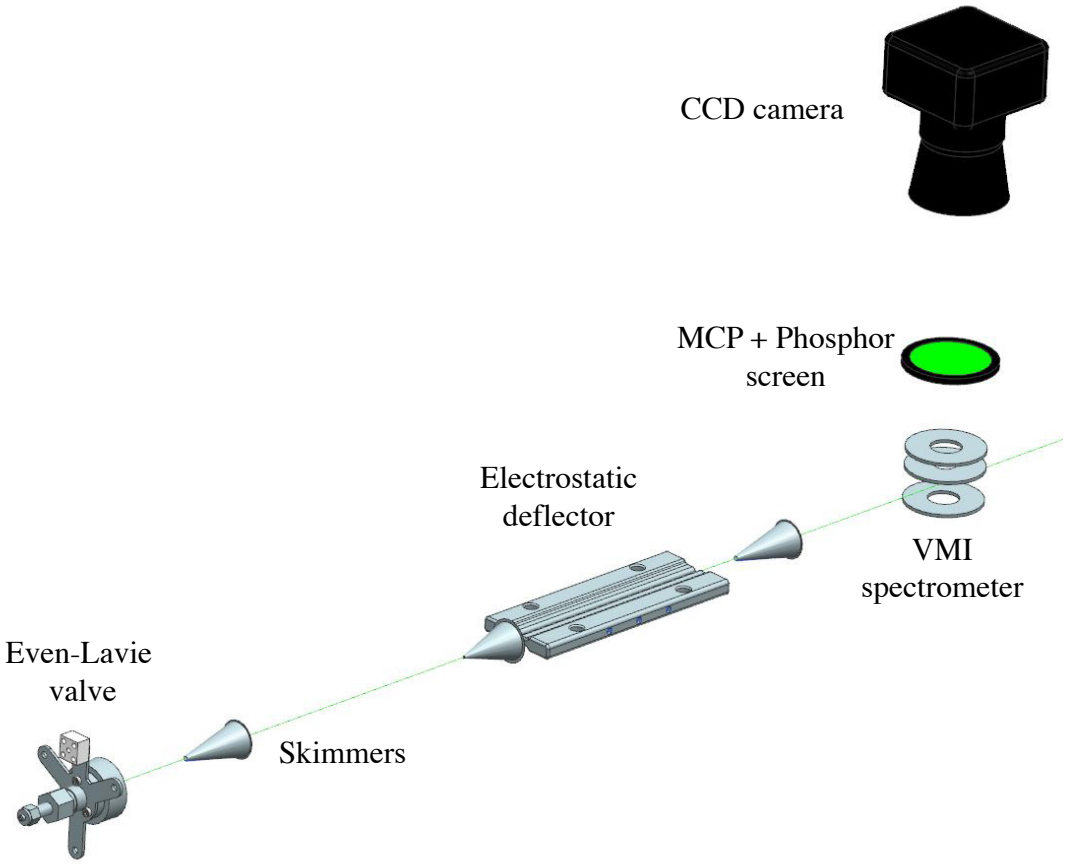

Figure 3.1.: Sketch of general experimental setup with emphasis on the parts of the molecular beam machine.

The VMIS was used in both, spatial imaging and velocity map imaging mode, where spatial imaging was used to characterize the molecular beam and record time-of-flight spectra, and the velocity-map imaging mode was used to measure angular distributions of aligned molecules and photoelectron momentum distributions. The MCP can be gated to filter out different ionic fragments according to their arrival time, i. e., their mass to charge ratio. The gating is realized using a fast switch (e. g., Behlke HTS 31-03-GSM), which applies a rectangular gate of 1 kV within a short temporal window, with a time duration of typically 10 ns to 100 ns. A permanent voltage is applied on the MCP, chosen such that its sensitivity is low and no counts are recorded without the external gate. When the gate is applied, the sensitivity is increased and only ions and electrons arriving within the gating time window are recorded.

3.2. Molecular Beam

In a supersonic expansion [187, 188] using a pulsed Even-Lavie valve [44, 46, 47], a high-pressure gas mixture is expanded through a small orifice into vacuum. The major part of the gas mixture consists of an inert atomic gas such as helium, neon or argon. Throughout this thesis helium was used. These valves are specified to be operated at repetition rates up to 1 kHz, but often leakage occurs due to magnetization of the plunger and the beam suffers from time-dependent density and beam-profile modifications. We thus operated the valve typically at 250 Hz, or at most at 500 Hz. In Figure 3.2, the

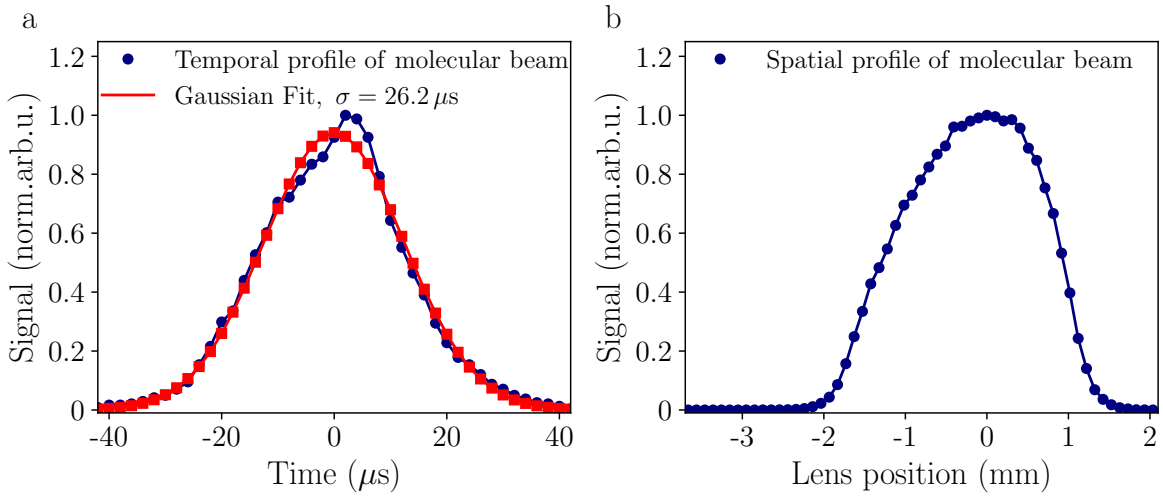

Figure 3.2.: Measured temporal and spatial profile of molecular beam with 500 ppm OCS seeded in helium, operated at a repetition rate of 250 Hz. **a** Temporal profile of the molecular beam with FWHM = 26.2 µs and **b** spatial profile of the molecular beam.

temporal and spatial profile of the molecular beam is shown, as measured with 500 ppm of OCS seeded in helium at a stagnation pressure of 90 bar. The valve was operated at repetition rate of 250 Hz and had an opening diameter of 100 µm, defined by the aperture of the front gasket in the valve. The spatial and temporal beam profiles, shown in Figure 3.2, were recorded with the experimental setup at the MBI. The gas pressure and opening time of the valve were chosen such that no cluster formation was observed, which would result in a higher beam temperature.

3.3. Electrostatic Deflector

Except for the experiment performed in Aarhus (see chapter 5), an electrostatic deflector was used to spatially disperse quantum states in the molecular beam according to their effective dipole moment and to separate the molecules from the helium seed gas. Both, the a-type deflector [1] and later its successor, the b-type deflector [61], were used. The electrostatic fields of both are shown in Figure 3.3. The deflection profile shown in Figure 3.4 was recorded in the MBI setup with the b-type deflector at voltages of

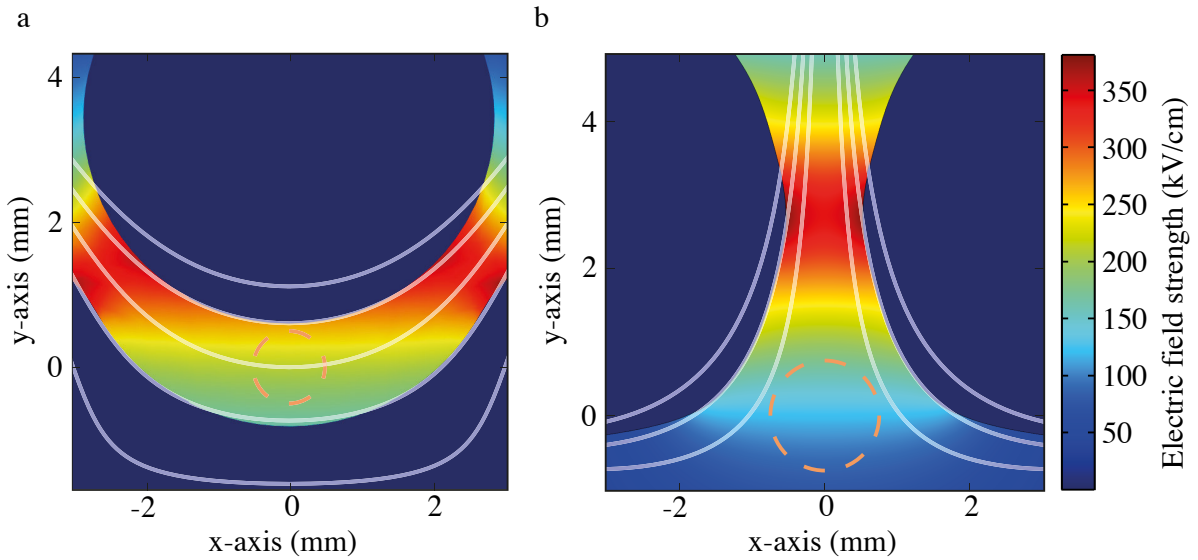

Figure 3.3.: Inhomogeneous electric fields in a-type and b-type electrostatic deflectors. **a** electric field inside a-type deflector, **b** electric field inside b-type deflector. The figures are taken from [61].

±15 kV applied to the two electrodes. These measurements were performed on the same molecular beam as shown in Figure 3.2. The beam exhibits strong deflection and

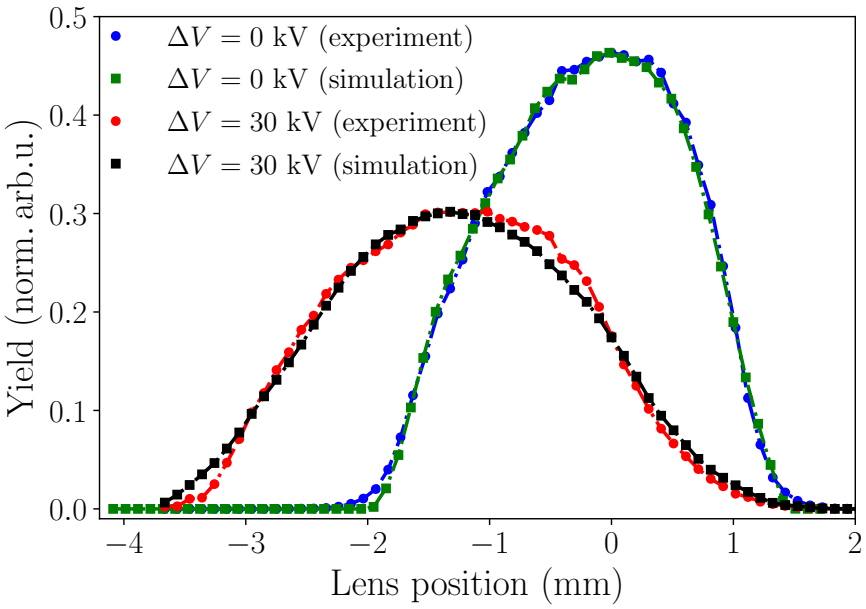

Figure 3.4.: Spatial molecular beam profiles for 500 ppm of OCS seeded in helium. The undeflected (0 kV) and deflected (±15 kV) spatial molecular beam profiles, measured after they have passed the b-type deflector, are shown together with corresponding simulations. The best fit of the undeflected beam profile was obtained for a rotational temperature of $T_{\mathrm{rot}} = 0.6\,\mathrm{K}$.

experiments were performed in the deflected part at a lens position around −3 mm. The best fit from the simulated beam profiles yielded a rotational temperature in the undeflected beam of $T_{\mathrm{rot}} = 0.6\,\mathrm{K}$. The choice of the spatial position in the molecular

beam that is probed represents a compromise between the most deflected and, hence, coldest part of the beam and still having high enough signal to perform the experiments with high signal-to-noise ratio.

3.4. Laser System

The laser system used at the MBI consists of a commercial Ti:Sapphire laser system (KMLabs, Wyvern30), delivering laser pulses with a duration of 38 fs (FWHM), a repetition rate of 1 kHz, a central wavelength of 800 nm and pulse energies of 30 mJ. The beam was compressed in a grating compressor to account for chirps, acquired during its propagation through the optics and crystals. The beam was then further divided into two parts, whose time delay was controlled using a motorized delay stage. The weaker beam (3 mJ) was used as pump (alignment) laser for the molecules and the high-energy beam (20 mJ) was sent into a tunable optical parametric amplification system (HE-TOPAS, Light Conversion). A simplified sketch showing the most important components of the

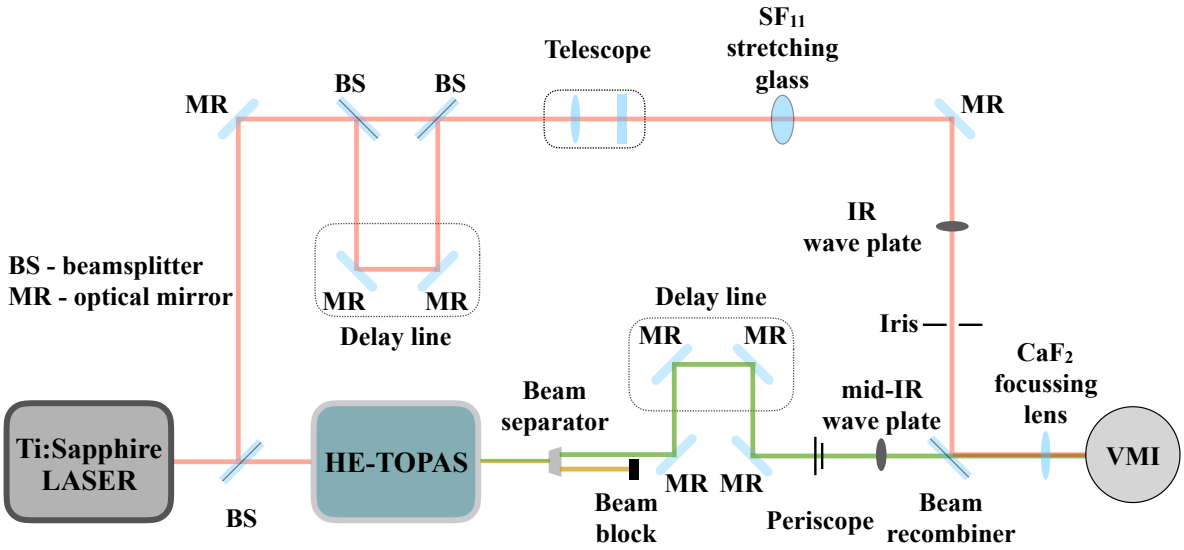

Figure 3.5.: Sketch of optical laser setup. The optical setup with the two-pulse alignment beamline is shown. This setup was used in chapter 4, chapter 7 and chapter 8.

optical setup is shown in Figure 3.5. Through successive optical parametric amplification, output pulses with a total energy of 6.5 mJ (signal+idler) and a pulse duration of 60 fs were achieved. The central wavelength of the signal could be tuned in the range from 1.2 µm to 1.6 µm yielding wavelengths in the range from 1.6 µm to 2.4 µm for the idler, respectively. The IR pump pulse(s), used for alignment, and the mid-IR probe pulse were finally collinearly combined using a beam recombiner, with the IR in reflection and the mid-IR in transmission. Both beams were then focussed into the VMIS using a 25 cm focal length CaF_2 lens.

4 Molecular movie of ultrafast coherent rotational dynamics of OCS[1]

4.1. Introduction

The filming of nuclear motion during molecular dynamics at relevant timescales, dubbed the "molecular movie", has been a longstanding dream in the molecular sciences [9, 189]. Recent experimental advances with x-ray-free-electron lasers and ultrashort-pulse electron guns have provided first glimpses of intrinsic molecular structures [14, 190, 191] and dynamics [26, 189, 192]. However, despite the spectacular progress, the fidelity of the recorded movies, in comparison to the investigated dynamics, was limited so far. Especially for high-precision studies of small molecules, typically only distances between a few atoms were determined [14, 26, 191].

Rotational quantum dynamics of isolated molecules provides an interesting and important testbed that provides and requires direct access to angular coordinates. Furthermore, different from most molecular processes, it can be practically exactly described by current numerical methods, even for complex molecules. Rotational wavepackets were produced through the interaction of the molecule with short laser pulses [70, 92, 193], which couple different rotational states through stimulated Raman transitions. The resulting dynamics were observed, for instance, by time-delayed Coulomb-explosion ion imaging [92, 142, 194], photoelectron imaging [195], or ultrafast electron diffraction [196]. The rotational wavepackets were exploited to connect the molecular and laboratory frames through strong-field alignment [70, 92] and mixed-field orientation [106, 111], as well as for the determination of molecular-structure information in rotational-coherence spectroscopy [197, 198]. Coherent rotational wavepacket manipulation using multiple pulses [199] or appropriate turn-on and -off timing [110] allowed enhanced or diminished rephasing, and it was suggested as a realisation of quantum computing [199]. Furthermore, methods for rotational-wavepacket reconstruction of linear molecules [200] and for benzene [201] were reported.

Here, we demonstrate the direct experimental high-resolution imaging of the time-dependent angular probability-density distribution of a rotational wavepacket and its reconstruction in terms of the populations and phases of field-free rotor states. Utilizing a state-selected molecular sample and an optimized two-laser-pulse sequence, a broad

[1] This chapter is based on the publication: *Molecular movie of ultrafast coherent rotational dynamics of OCS*, Evangelos T. Karamatskos, Sebastian Raabe, Terry Mullins, Andrea Trabattoni, Philipp Stammer, Gildas Goldsztejn, Rasmus R. Johansen, Karol Długołęcki, Henrik Stapelfeldt, Marc J. J. Vrakking, Sebastian Trippel, Arnaud Rouzée and Jochen Küpper, *Nature Communications* **10**, 3364 (2019), *arXiv*:1807.01034. I contributed to setting up the experiment and recording the data. I analyzed the data, performed the simulations and I contributed to writing the manuscript.

phase-locked rotational wavepacket was created. Using mid-infrared-laser strong-field ionization and Coulomb-explosion ion imaging, an unprecedented degree of field-free alignment of $\langle\cos^2\theta_{2D}\rangle = 0.96$, or $\langle\cos^2\theta\rangle = 0.94$, was obtained at the full revivals, whereas in between a rich angular dynamics was observed with very high resolution, from which the complete wavepacket could be uniquely reconstructed. While the dynamics has low dimensionality, The resulting — purely experimentally obtained — movie provides a most direct realisation of the envisioned "molecular movie". We point out that the data also is a measurement of a complete quantum carpet [202].

In order to achieve such a high degree of alignment, better than the theoretical maximum of $\langle\cos^2\theta\rangle = 0.92$ for single-pulse alignment [96, 203], we performed a pump-probe experiment with ground-state-selected OCS molecules [1], with $> 80\,\%$ purity, as a showcase. Two off-resonant near-IR pump pulses of 800 nm central wavelength, separated by 38.1 (1) ps and with a pulse duration of 250 fs, i. e., much shorter than the rotational period of OCS of 82.2 ps, were used to create the rotational wavepacket. These pulses were linearly polarized parallel to the detector plane. The probe pulse with a central wavelength of 1.75 µm was polarized perpendicularly to the detector plane to minimize the effects of geometric alignment and ensures that the observed degree of alignment was a lower boundary of the real value. The probe pulse multiply ionized the molecules, resulting in Coulomb explosion into ionic fragments. 2D ion-momentum distributions of O^+ fragments, which reflect the orientation of the molecules in space at the instance of ionization, were recorded by a velocity map imaging (VMI) spectrometer [124] for different time delays between the alignment pulse sequence and the probe pulse. Further details of the experimental setup are presented in *Methods*.

4.2. Results and Discussion

In Figure 4.1, snapshots of the experimentally recorded molecular movie, i. e., 2D ion-momentum distributions, are shown for several probe times covering a whole rotational period. The phase of 0 and 2π correspond to t =38.57 ps and 120.78 ps after the peak of the first alignment laser pulse at $t = 0$, respectively. The simplest snapshot-images, reflecting an unprecedented degree of field-free alignment $\langle\cos^2\theta_{2D}\rangle = 0.96$, were obtained for the alignment revivals at phases of 0 and 2π, which correspond to the prompt alignment and its revival regarding the second laser pulse. Here, the molecular axes are preferentially aligned along the alignment-laser polarization. For the anti-alignment at a phase of π the molecules are preferentially aligned in a plane perpendicular to the alignment laser polarization direction. Simple quadrupolar structures are observed at $\pi/2$ and $3\pi/2$. At intermediate times, e. g., at $\pi/3$ or $7\pi/12$, the images display rich angular structures, which could be observed due to the high angular experimental resolution of the recorded movie, which is 4° as derived in the Supplementary Information. This rich structure directly reflects the strongly quantum-state selected initial sample exploited in these measurements, whereas the structure would be largely lost in the summation of wavepackets from even a few initially populated states.

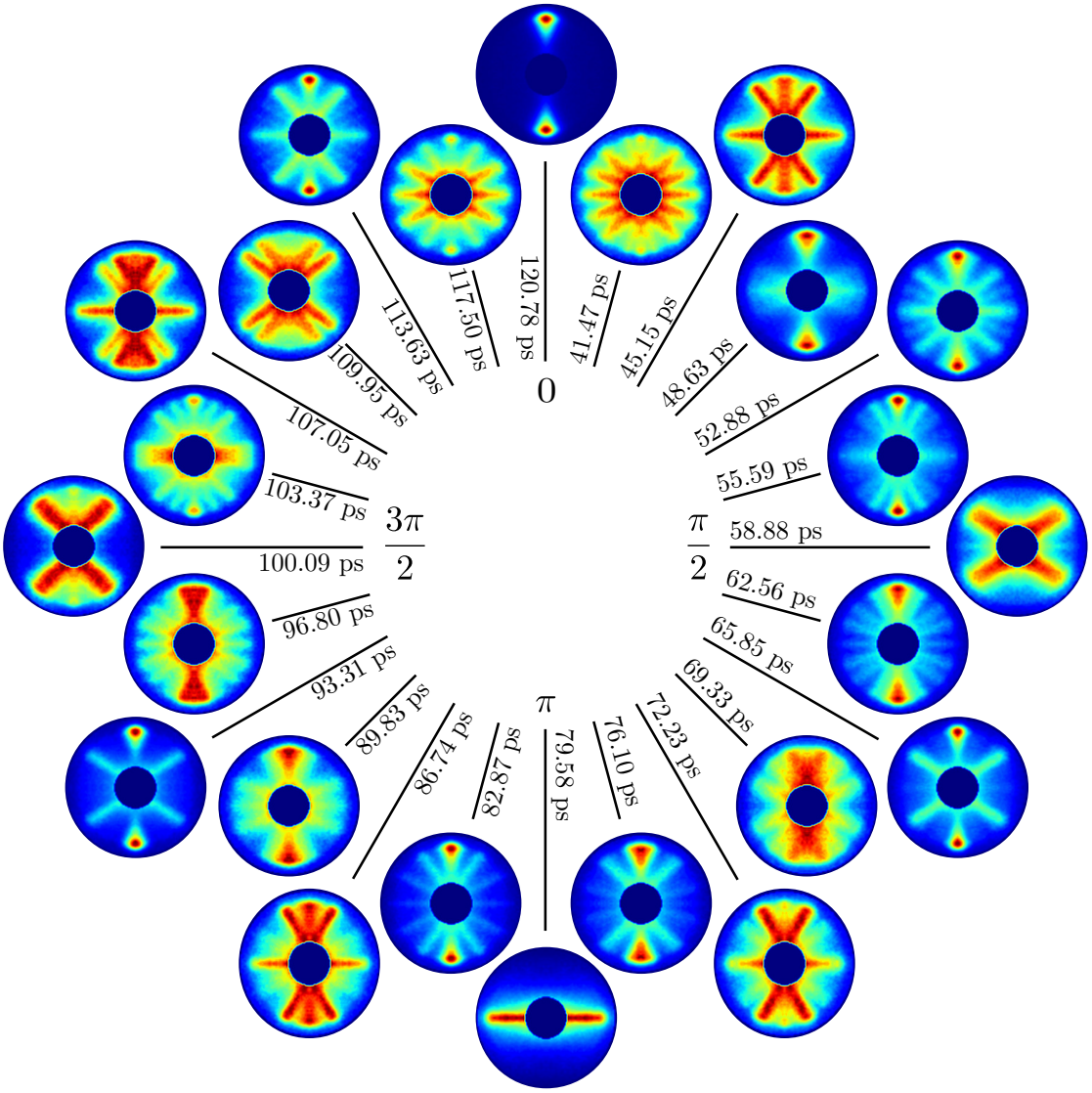

Figure 4.1.: Rotational clock depicting the molecular movie of the observed quantum dynamics. Individual experimental VMI images of O^+ ion-momentum distributions depicting snapshots of the rotational wavepacket over one full period. The displayed data was recorded from the first (prompt) revival at 38.57 ps (0) to the first full revival at 120.78 ps (2π); the phase-evolution of $\pi/12$ between images corresponds to 3.43 ps and the exact delay times of the individual images are specified.

The dynamics was analyzed as follows: Through the interaction of the molecular ensemble with the alignment laser pulses, a coherent wavepacket was created from each of the initially populated rotational states. These wavepackets were expressed as a coherent superposition of eigenfunctions of the field-free rotational Hamiltonian, i. e.,

$$\Psi(\theta, \phi, t) = \sum_J a_J(t) Y_J^M(\theta, \phi), \tag{4.1}$$

with the time-dependent complex amplitudes $a_J(t)$, the spherical harmonics $Y_J^M(\theta, \phi)$, the quantum number of angular momentum J, and its projection M onto the laboratory-fixed

axis defined by the laser polarization. We note that M was conserved and thus no ϕ dependence existed. The angular distribution is defined as the sum of the squared moduli of all $\Psi(\theta, \phi, t)$ weighted by the initial-state populations. The degree of alignment

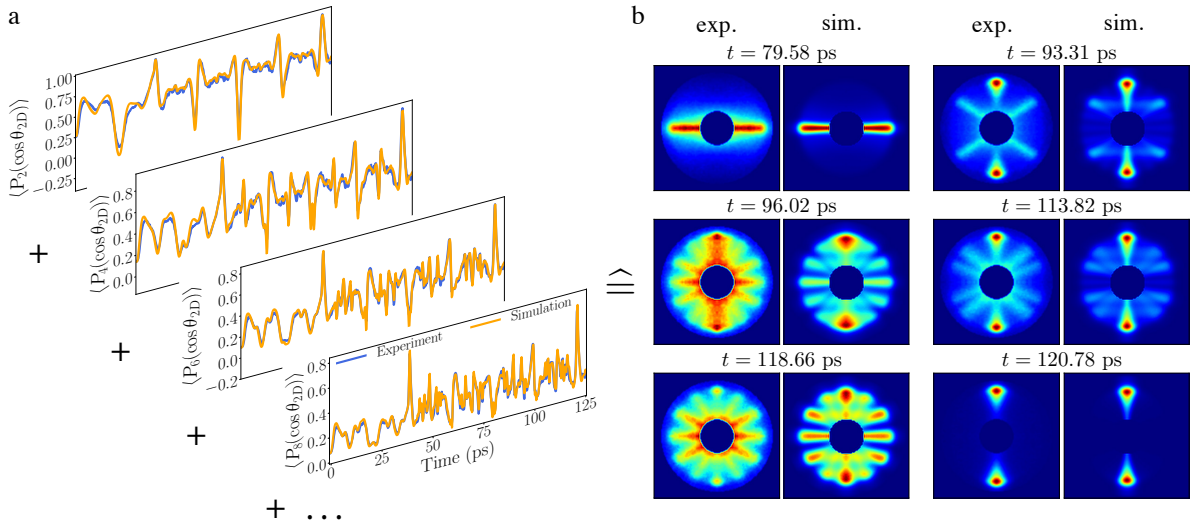

Figure 4.2.: Decomposition of angular distributions into their moments. **a** Comparison of the decomposition of the experimental and theoretical angular distributions in terms of Legendre polynomials. **b** Simulated and experimental angular-distribution VMI images for selected times; the radial distributions in the simulations are extracted from the experimental distribution at 120.78 ps, see text for details.

was extracted from the VMI images using the commonly utilized expectation value $\langle\cos^2\theta_{2D}\rangle$. The maximum value observed at the alignment revival reached 0.96, which, to the best of our knowledge, is the highest degree of field-free alignment achieved to date. Comparing the angular distributions at different delay times with the degree of alignment $\langle\cos^2\theta_{2D}\rangle$, see Figure 4.7 in the Supplementary Information, we observed the same degree of alignment for angular distributions that are in fact very different from each other. This highlights that much more information is contained in the angular distributions than in the commonly utilized expectation value [70]. Indeed, $\langle\cos^2\theta_{2D}\rangle$ merely describes the leading term in an expansion of the angular distribution, for instance, in terms of Legendre polynomials, see (4.2) in the Supplementary Information. In order to fully characterize the angular distribution a description in terms of a polynomial series is necessary that involves the same maximum order as the maximum angular momentum J_{max} of the populated rotational eigenstates, which corresponds to, at most, $2J_{max}$ lobes in the momentum maps.

As the probe laser is polarized perpendicularly to the detector plane, the cylindrical symmetry as generated by the alignment-laser polarization was broken and an Abel inversion to retrieve the 3D angular distribution directly from the experimental VMI images was not possible. In order to retrieve the complete 3D wavepacket, the time-dependent Schrödinger equation (TDSE) was solved for a rigid rotor coupled to a non-resonant ac electric field representing the two laser pulses as well as the dc electric field of the VMI spectrometer. For a direct comparison with the experimental data the

rotational wavepacket and thus the 3D angular distribution was constructed and, using a Monte-Carlo approach, projected onto a 2D screen using the radial distribution extracted from the experiment at the alignment revival at 120.78 ps. The relation between the 3D rotational wavepacket and the 2D projected density is graphically illustrated in Figure 4.5 of the Supplementary Information. The anisotropic angle-dependent ionization efficiency for double ionization, resulting in a two-body breakup into O^+ and CS^+ fragments, was taken into account by approximating it by the square of the measured single-electron ionization rate. Non-axial recoil during the fragmentation process is expected to be negligible and was not included in the simulations.

The initial state distribution in the quantum-state selected OCS sample as well as the interaction volume with the alignment and probe lasers were not known *a priori* and used as fitting parameters. For each set of parameters the TDSE was solved and the 2D projection of the rotational density, averaged over the initial state distribution and the interaction volume of the pump and probe lasers, was carried out. The aforementioned expansion in terms of Legendre polynomials was realised for the experimental and simulated angular distributions and the best fit was determined through least squares minimization, see Supplementary Information. Taking into account the eight lowest even moments of the angular distribution allowed to precisely reproduce the experimental angular distribution. The results for the first four moments are shown in Figure 4.2 a; the full set is given in Figure 4.6 in the Supplementary Information as well as the optimal fitting parameters. The overall agreement between experiment and theory is excellent for all moments. Before the onset of the second pulse, centred around t =38.1 ps, the oscillatory structure in all moments is fairly slow compared to later times, which reflects the correspondingly small number of interfering states in the wavepacket before the second pulse, and the large number thereafter.

Theoretical images, computed for the best fit parameters, are shown in Figure 4.2 b. The theoretical results are in excellent agreement with the measured ion-momentum angular distributions at all times, see Supplementary Information, and prove that we were able to fully reconstruct the 3D rotational wavepacket with the amplitudes and phases of all rotational states included. In Figure 4.3 a, the extracted rotational-state populations are shown for the wavepacket created from the rotational ground state after the first and the second alignment laser pulse. It clearly shows that the rotational-state distribution is broader after the second pulse, reaching up to $J \geq 16$. This also matches the convergence of the Legendre-polynomial series, with eight even terms, derived from the fit to the data above. In Figure 4.3 b, the corresponding phase differences for all populated states relative to the initial state with the largest population in the wavepacket are shown, where $\phi(J)$ is the phase of the complex coefficient a_J in (4.1). Combining these populations and phases it became clear that the very high degree of alignment after the second alignment pulse arises from the combination of the broad distribution of rotational states, reaching large angular momenta, and the very strong and flat rephasing of all significantly populated states at the revival at 120.78 ps, Figure 4.3 b (red). Similarly, the anti-alignment at 79.58 ps occurs due to alternating phase differences of π between adjacent populated rotational states, Figure 4.3 b(black).

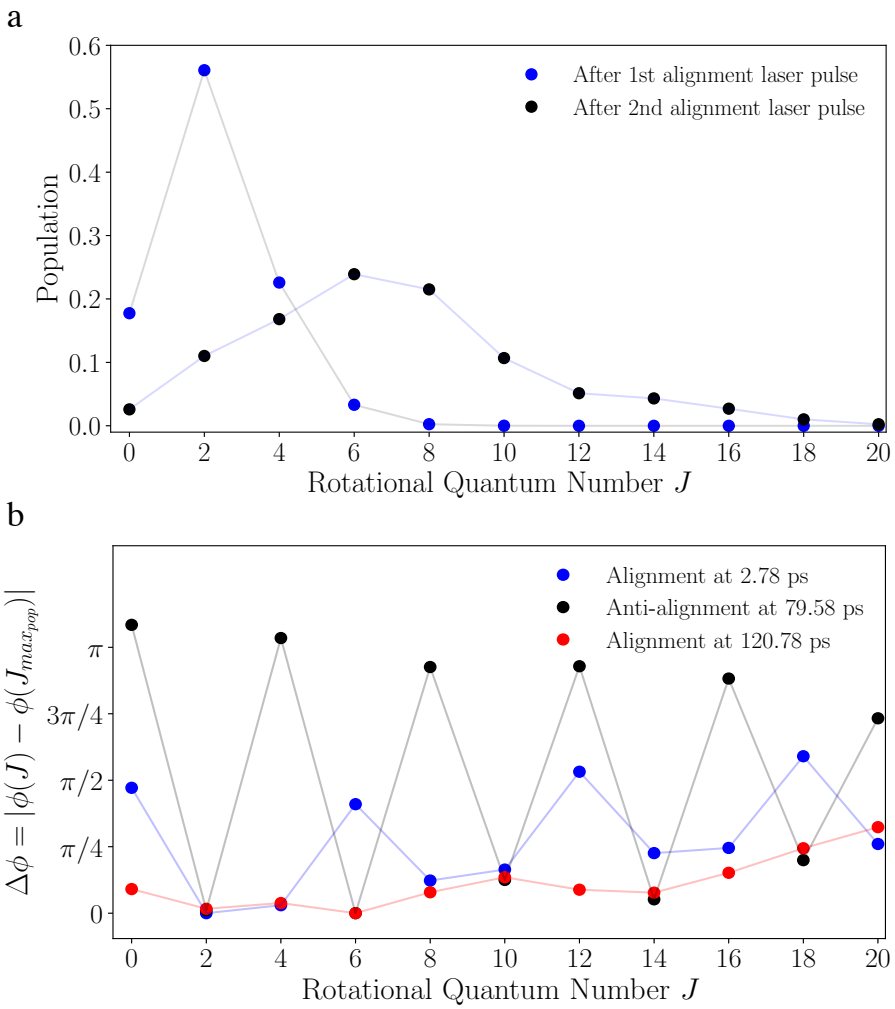

Figure 4.3.: Populations and phase differences in the rotational wavepacket at alignment and anti-alignment times. **a** Rotational-state populations and **b** phase-differences to the phase of the state with largest population, $J = 2, J = 6$, respectively, at the alignment revival following a single-pulse excitation, 2.78 ps (blue dots), and the two-pulse excitation, 120.78 ps (red dots) as well as for the antialignment at 79.58 ps (black dots, populations coincide with the red dots). Only states with even angular momentum are populated due to the Raman-transition selection rules $\Delta J = \pm 2$.

4.3. Conclusions

In conclusion, we were able to record a high-resolution molecular movie of the ultrafast coherent rotational motion of impulsively aligned OCS molecules. State-selection and an optimized two-pulse sequence yielded an unprecedented degree of field-free alignment of $\langle\cos^2\theta_{2D}\rangle = 0.96$, with a very narrow angular confinement of 13.4 ° FWHM. Limiting the analysis to a determination of $\langle\cos^2\theta_{2D}\rangle$, as it is common in experiments on time-dependent alignment, did not allow to capture the rich rotational dynamics, while the use of a polynomial expansion up to an appropriate order did. We reconstructed the rotational wavepacket, from which the complex coefficients and, hence, the full information about the rotational wavepacket under study was extracted. The 2D projection of the

reconstructed rotational wavepacket allowed a direct comparison with the experimentally measured data.

Regarding the extension toward the investigation of chemical dynamics, we point out that strong-field-ionization-induced Coulomb-explosion imaging can be used, for instance, to image the configuration of chiral molecules [204] or internal torsional dynamics [205]. Following the dynamics of such processes with the detail and quality presented here would directly yield a molecular movie of the chemical and, possibly, chirality dynamics [206]. Furthermore, the very high degree of field-free alignment achieved here would be extremely useful for stereochemistry studies [64, 207] as well as for molecular-frame imaging experiments [12, 14, 35, 68, 191, 196, 208–210].

4.4. Methods

A cold molecular beam was formed by supersonic expansion of a mixture of OCS (500 ppm) in helium, maintained at a backing pressure of 90 bar from a pulsed Even-Lavie valve [46] operated at 250 Hz. After passing two skimmers, the collimated molecular beam entered the Stark deflector. The beam was dispersed according to quantum state by a strong inhomogeneous electric field [1] with a nominal strength of ∼200 kV/cm. Through a movable third skimmer, the molecular beam entered the spectrometer. Here, it was crossed at right angle by laser beams, where the height of the laser beams allowed to probe state-selected molecular ensembles, i. e., a practically pure rovibronic-ground-state sample of OCS [62, 110, 111].

The laser setup consisted of a commercial Ti:Sapphire laser system (KM labs) delivering pulses with 30 mJ pulse energy, 35 fs (FWHM) pulse duration, and a central wavelength of 800 nm at a 1 kHz repetition rate. One part (20 mJ) of the laser output was used to pump a high-energy tunable optical parametric amplifier (HE-TOPAS, Light Conversion) to generate pulses with a central wavelengths of 1.75 µm, a pulse duration of 60 fs, and a pulse energy of ∼1.5 mJ. 900 µJ of the remaining 800 nm laser output was used for the laser-induced alignment, i. e., the generation of the investigated rotational wavepackets. This beam was split into two parts with a 4:1 energy ratio using a Mach-Zehnder interferometer. A motorised delay stage in one beam path allowed for controlling the delay between the two pulses. This delay was optimized experimentally and maximum alignment was observed for $\tau_{exp} = 38.1 \pm 0.1$ ps, in perfect agreement with the theoretically predicted τ_{sim} =38.2 ps. The pulses were combined collinearly and passed through a 2 cm long SF_{11} optical glass to stretch them to 250 fs pulse duration (FWHM). Then the alignment pulses were collinearly overlapped with the 1.75 µm mid-infrared pulses using a dichroic mirror. All pulses were focused into the velocity map imaging spectrometer (VMI) using a 25 cm focal-distance calcium fluoride lens.

At the center of the VMI the state-selected molecular beam and the laser beams crossed at right angle. Following strong-field multiple ionization of the molecules, the generated charged fragments were projected by the VMI onto a combined multichannel-plate (MCP) phosphor-screen detector and read out by a CCD camera. The angular resolution of the imaging system is 4 °, limited by the 1 megapixel camera, see Supplementary Information.

2D ion-momentum distributions of O^+ fragments were recorded as a function of the delay between the 800 nm pulses and the ionizing 1.75 µm pulses in order to characterize the angular distribution of the molecules through Coulomb-explosion imaging. The polarization of the 800 nm alignment pulses was parallel to the detector screen whereas that of the 1.75 µm ionizing laser was perpendicular in order to avoid geometric-alignment effects in the angular distributions. For this geometry, unfortunately, it was not possible to retrieve 3D distributions from an inverse Abel transform. 651 images were recorded in steps of 193.4 fs, covering the time interval from −0.7 ps up to 125 ps, which is more than one and a half times the rotational period of OCS of 82.2 ps.

4.5. Supplementary Information

4.5.1. Optimization of Two-Pulse Field-Free Alignment

Optimization calculations were performed in order to predict the optimal pulse parameter for single and two-pulse field-free alignment. In the simulations, the rotational part of the Schrödinger equation for a linear rigid rotor within the Born-Oppenheimer approximation coupled to non-resonant ac alignment laser pulses and a static electric field, as provided by the VMI in the interaction region, was used. The Hamiltonian of the system is described in detail in reference [152]. The global differential-evolution optimization algorithm [162] was used to calculate the optimal alignment characterized through the expectation value $\langle\cos^2\theta\rangle$ in a closed-feedback-loop approach. The optimization parameters used were the intensities and one common duration of Fourier-limited Gaussian pulses and the delay between the pulses in the case of two-pulse alignment. In the calculations a pure rotational ground state ensemble was assumed and no integration over the interaction volume was carried out. The former is justified as we know that the ground state contribution to alignment is dominant and the exact experimental conditions were not known a priori. Furthermore, exploiting the electrostatic deflector, as in our experiment, almost pure ground state ensembles can be prepared [1, 62]. Including also thermally excited rotational states lead to an additional incoherent sum over all states present in the initial distribution of rotational states and in general to a decrease of the degree of alignment. The same holds for the interaction volume of the laser since only molecules at the center of the beam experience the optimal alignment intensity while molecules at some distance from the center interact with a lower field. In this sense the calculated values constitute an upper limit for the alignment under optimal conditions. Time-evolution curves of the optimal two-dimensional (2D) and three-dimensional (3D) alignment are shown in Figure 4.4. The results for the single pulse optimization yielded a pulse duration of 114.5 fs and a maximum intensity of 5.6 TW/cm^2. The corresponding maximum degree of field-free 3D alignment was found to be $\langle\cos^2\theta\rangle = 0.92$, which is in agreement with an upper bound of 0.92 derived previously [203]; this corresponds to a 2D degree of alignment of $\langle\cos^2\theta_{2D}\rangle = 0.95$.

The optimal parameters for the case of two alignment pulses were found to be a pulse duration of 273.4 fs, a pulse separation between the two pulses of 38.2 ps, and

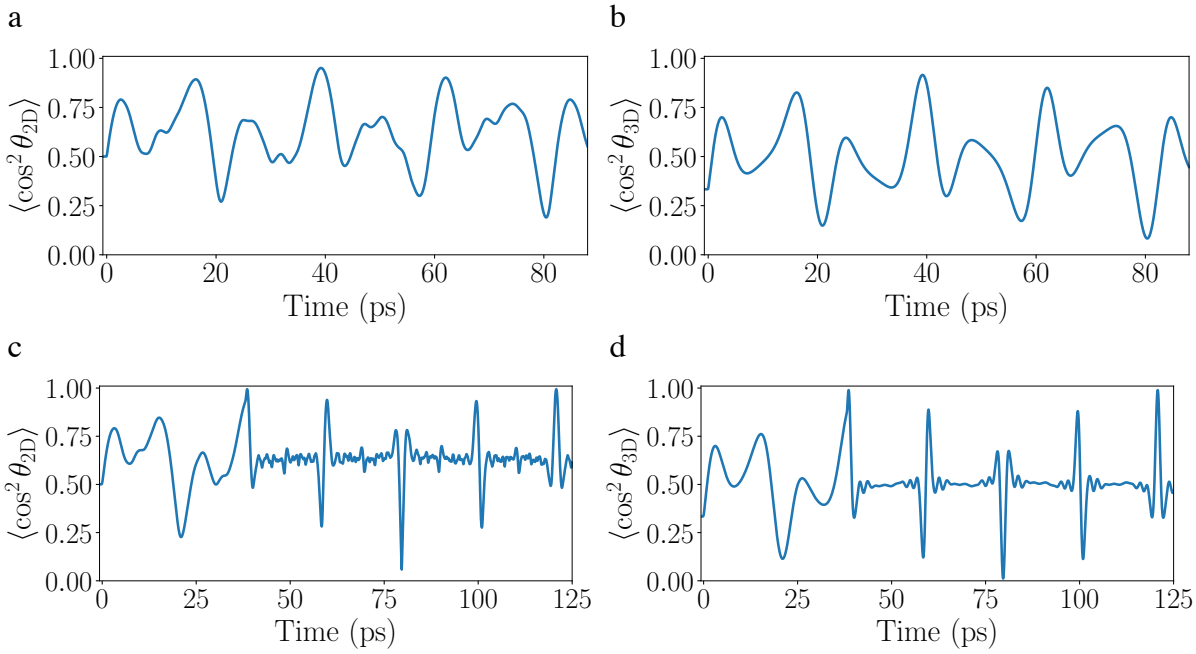

Figure 4.4.: Optimized **a, c** 2D and **b, d** 3D field-free alignment with **a, b** one and **c, d** two alignment pulses.

an intensity-ratio of $\sim 1:5$ with the first pulse being weaker than the second one, in agreement with previous results [95, 96]. The maximum intensity of the first pulse was determined to be $1.93\,\mathrm{TW/cm^2}$ and that of the second pulse $10\,\mathrm{TW/cm^2}$, which was the upper bound of intensities included in the calculations since for higher values at a wavelength of 800 nm a non-negligible amount of ionization of OCS sets in. The maximum degree of 3D field-free alignment calculated with these parameters were $\langle\cos^2\theta\rangle = 0.99$ and $\langle\cos^2\theta_{2D}\rangle = 0.99$, substantially higher than in the single pulse case. The experiment presented in the main paper was performed under experimental conditions approximating these optimized parameter. We note that the optimal pulse separation was calculated to be 38.2 ps, which was confirmed in the experiment, for which a scan of the pulse separation yielded the best alignment revival for 38.1 ± 0.1 ps.

4.5.2. Moments of Angular Distribution

There are several ways to expand the angular distribution of the wavepacket in a power series[2], but a natural basis consists of the Legendre polynomials, as for $\Delta M = 0$ the eigenstates are independent of ϕ and the spherical harmonics simplify to Legendre polynomials. Only even order polynomials appear in the expansion since for a ground-state-selected ensemble the odd order moments describe orientation of the molecular axes,

[2]We had indeed originally performed the analysis in terms of squared Chebyshev polynomials $\langle\cos^2 n\theta_{2D}\rangle$ for numerical convenience and the results of both approaches are identical.

which was not present. The expansion takes on the form

$$P(\theta_{2D}, t) = \sum_{k=0, k\,\text{even}}^{J_{\max}} a_k(t) \mathcal{P}_k(\cos\theta_{2D}) \tag{4.2}$$

where the full time-dependent angular distribution is denoted as $P(\theta_{2D}, t)$ and a_k ($k = 0, 2 \ldots J_{\max}$) are the expansion coefficients corresponding to the k-th Legendre polynomial $\mathcal{P}_k$; $J_{\max}$ is the angular momentum quantum number of the highest populated rotational state in the wavepacket.

In order to characterize the initial state distribution of rotational states in the molecular beam, the eight lowest even-order moments of the experimental angular distributions were fitted simultaneously using least squares minimization. For each moment, squared differences were summed according to

$$\chi_n^2 = \sum_t \left(\langle \mathcal{P}_{2n}(\cos\theta_{2D})_{\text{exp}} \rangle(t) - \langle \mathcal{P}_{2n}(\cos\theta_{2D})_{\text{sim,vol}} \rangle(t) \right)^2 , \tag{4.3}$$

where the sum runs over all measured delay times t and $n = 1 \ldots 8$. In order to compute $\langle \mathcal{P}_n(\cos\theta_{2D})_{\text{sim,vol}} \rangle(t)$, several steps were followed. First, the coherent wavepackets, created through the interaction with the alignment laser pulses, were for every initial state described in the basis of field-free eigenstates as

$$\Psi_{J_\text{i},M_\text{i}}(\theta, \phi, t) = \sum_J a_J(t) Y_J^{M_\text{i}}(\theta, \phi), \qquad a_J(t=0) = \delta_{JJ_\text{i}}, \tag{4.4}$$

where $a_J(t) = |a_J(t)| e^{i\phi_J(t)}$ are time-dependent complex coefficients with amplitude $|a_J(t)|$, phase $\phi_J(t)$, and initial condition $a_J(t=0) = \delta_{JJ_\text{i}}$, δ_{JJ_i} is the Kronecker delta, obtained from the solution of the time-dependent Schrödinger equation; $Y_J^M(\theta, \phi)$ are the spherical-harmonic functions and J_i, M_i are the quantum numbers of the initial state from which the wavepacket is formed. The sum runs only over J, since M was a good quantum number due to cylindrical symmetry, as imposed by the linear polarization of the alignment laser, and, hence, $\Delta M = 0$ and $M = M_\text{i}$ was conserved. Furthermore, the selection rules for transitions between different rotational states were $\Delta J = \pm 2$, since the population transfer is achieved via non-resonant two-photon Raman transitions. Moreover, the static VMI field was perpendicular to the alignment laser polarization and does not mix different M states. Since more than one rotational state were initially populated, the 3D rotational density was obtained through the incoherent average with statistical weights $w_{J_\text{i},M_\text{i}}$

$$P_{\text{sim,3D}}(\theta, \phi, t) = \sum_{J_\text{i},M_\text{i}} w_{J_\text{i},M_\text{i}}\, p(\theta)\, |\Psi_{J_\text{i},M_\text{i}}(\theta, \phi, t)|^2 , \tag{4.5}$$

which were not known *a priori* and used as fitting parameters. The function $p(\theta)$ describes the angle-dependent ionization probability, which was approximated through the square of the measured angular-dependent single-electron ionization rate. Finally, a focal average over the interaction region with the alignment and probe laser beam profiles, assumed to

be Gaussian, was performed. The average over intensities in the laser focus was calculated through integration

$$\langle P_{\mathrm{sim,3D}}(\theta,\phi,t)\rangle_{\mathrm{vol}}(t) = \frac{1}{N}\int_0^{r_{\mathrm{max}}} \langle P_{\mathrm{sim,3D}}(\theta,\phi,I_{\mathrm{align}}(r),t)\rangle\, e^{-2r^2/w^2_{\mathrm{probe}}}\, r\mathrm{d}r \tag{4.6}$$

with radius r_{max} at I_{align} =$1\times10^9\,\mathrm{W/cm^2}$ and N a normalisation factor. The dependence of the rotational wavepackets on the alignment laser intensities is explicitly stated in (4.6). The widths of the laser beams were also not known *a priori* and were included as

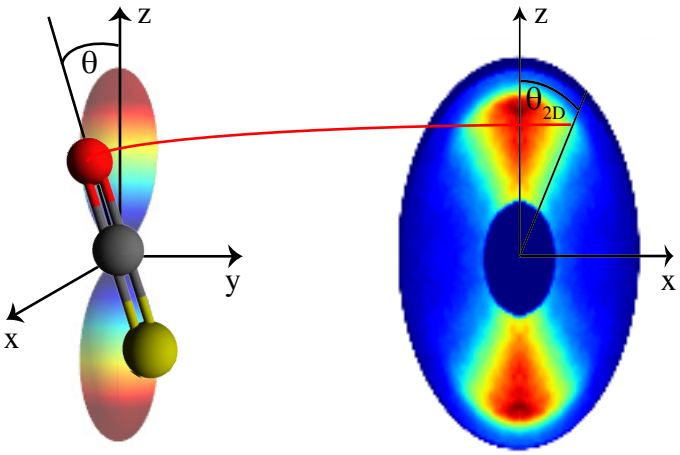

Figure 4.5.: Relation between the Euler angle θ, defining the alignment of the molecular axis with respect to the pump laser polarization axis, and θ_{2D}, corresponding to the angle between the pump laser polarization and the detected ion-momentum distribution on the 2D detector.

further fitting parameters. The resulting focal- and initial-state-averaged 3D rotational densities were projected onto a 2D plane using a Monte-Carlo sampling routine, which included the experimental radial distribution extracted at the full revival at a delay time of 120.78 ps, yielding the simulated VMI images in Figure 4.2 in the main part. The relation between the 3D rotational density and the 2D projected density is graphically illustrated in Figure 4.5. The Legendre moments of the angular distribution were then extracted from the 2D projected images and compared to experiment through χ^2_n, as described in (4.3). The statistical weights $w_{J_\mathrm{i}M_\mathrm{i}}$ of the initial state distribution and the laser focal sizes were varied until $\sum_n \chi^2_n$ converged to its minimum. The individual populations determined through the fitting procedure are $w_{00} = 8.2\cdot10^{-1}$, $w_{10} = 3.7\cdot10^{-2}$, $w_{11} = 7.5\cdot10^{-2}$, $w_{20} = 1.5\cdot10^{-2}$, $w_{21} = 2.1\cdot10^{-2}$ and $w_{22} = 3.2\cdot10^{-2}$ and the optimal focal parameter were determined to be w_{align} =130 µm for the alignment laser and w_{probe} =60 µm for the probe laser. The results are consistent with the fact that the probe laser was tighter focused than the alignment laser such that only molecules exhibiting strong alignment, close to the beam center, are probed.

The final results of the fitting procedure are shown in Figure 4.2 in the main part and in Figure 4.6. The simulated angular distributions and the moments of the angular distribution are in excellent agreement with the experiment, in particular all oscillations are correctly captured, even for the highest-order moments. The experimental parame-

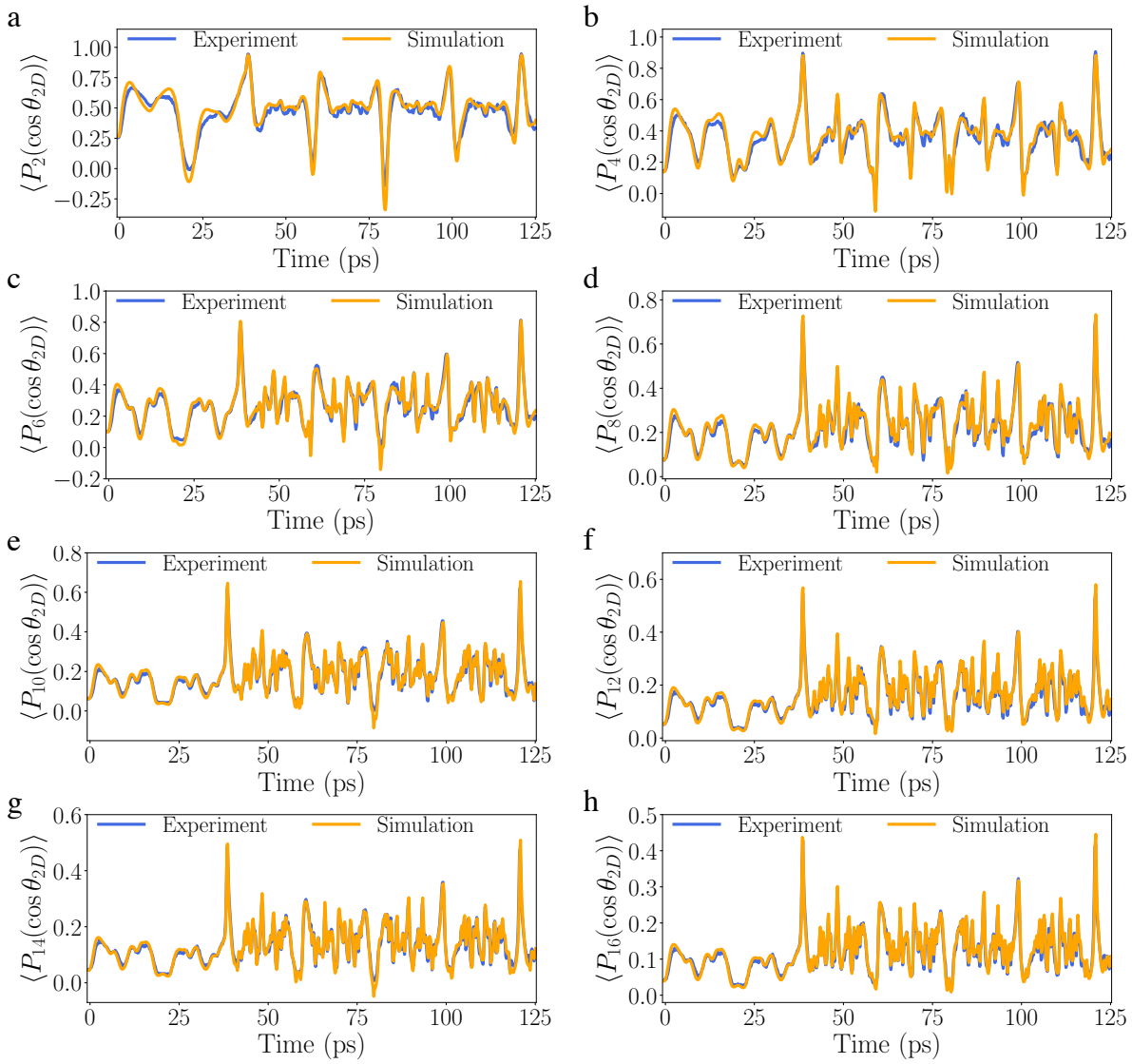

Figure 4.6.: Even order moments 1 to 8 of the angular distribution **a** $\langle P_2(\cos\theta_{2D})\rangle$, **b** $\langle P_4(\cos\theta_{2D})\rangle$, **c** $\langle P_6(\cos\theta_{2D})\rangle$, **d** $\langle P_8(\cos\theta_{2D})\rangle$ **e** $\langle P_{10}(\cos\theta_{2D})\rangle$, **f** $\langle P_{12}(\cos\theta_{2D})\rangle$, **g** $\langle P_{14}(\cos\theta_{2D})\rangle$, **h** $\langle P_{16}(\cos\theta_{2D})\rangle$.

ters used for the simulations were the peak intensities for the two alignment pulses of $I_{\text{align},1}$ =1.92 TW/cm^2 and $I_{\text{align},2}$=5.5 TW/cm^2, the pulse duration of the alignment laser pulses τ_{align} =255 fs, the time delay between the two alignment laser pulses τ_{delay} =38.1 ps, and the pulse duration of the probe laser τ_{probe} =60 fs. Calculations with 21 initial states, i. e., $J = 0 \ldots 5, M = 0 \ldots 5$, included in the initial rotational state distribution were originally performed, but convergence was already reached for the 6 lowest-energy states and the fitting procedure was restricted to using these 6 lowest rotational states, i. e., $J = 0 \ldots 2, M = 0 \ldots 2$, and the focal volume was averaged over 100 intensities in $I_{\text{align}} = 1 \cdot 10^9 \ldots 5.5 \cdot 10^{12}$ W/cm^2. In all calculations the basis for each coherent wavepacket included all rotational states up to $J = 50$.

4.5.3. Angular Distributions

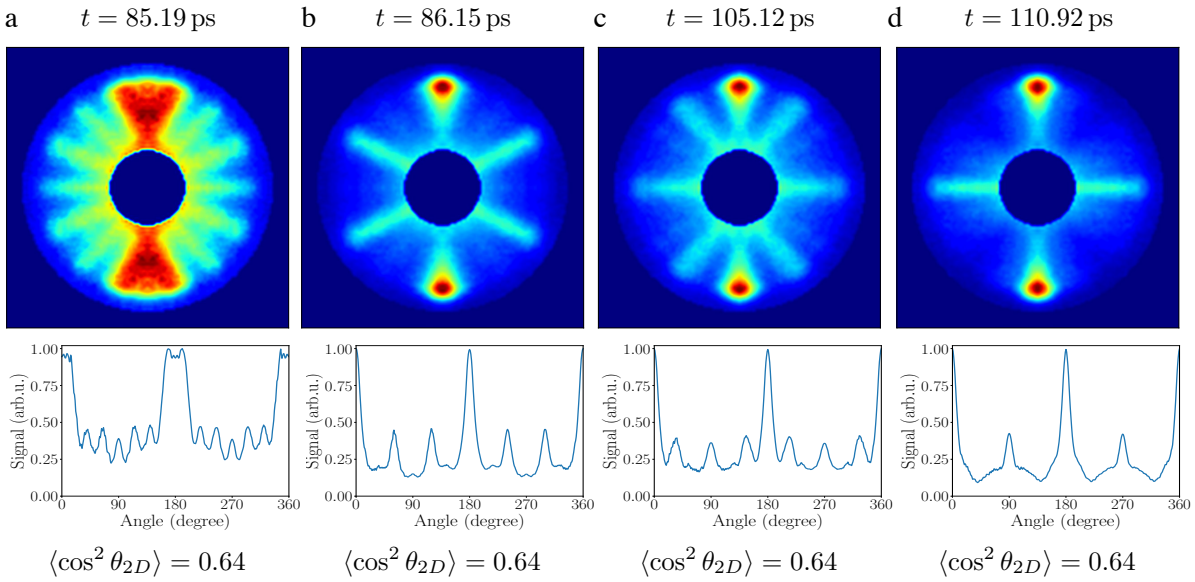

Figure 4.7.: Four O^+ ion-momentum probability distributions recorded at different time delays, displaying very different angular distributions, but having all the same degree of alignment of $\langle \cos^2 \theta_{2D} \rangle = 0.64$. These distributions were recorded for delay times of **a** 85.19 pss, **b** 86.15 ps, **c** 105.12 ps, and **d** 110.92 ps.

As pointed out in the main text, we observed angular probability distributions showing the very rich time evolution of the rotational wavepacket created by the two alignment laser pulses. When characterizing the degree of alignment using the commonly used $\langle \cos^2 \theta_{2D} \rangle$ we observed that completely different angular distributions possess the same degree of alignment, which pointed out the need for higher order terms in the expansion of the total angular distribution, e. g., in the basis of Legendre polynomials, to be able to reconstruct the complete rotational wavepacket. In Figure 4.7, we present O^+ ion-momentum distributions measured at four different delay times together with their corresponding angular distributions corroborating this observation. The delay times were chosen such that all distributions have the same $\langle \cos^2 \theta_{2D} \rangle = 0.64$, corresponding to the permanent alignment level. Although the degree of alignment is quite low compared to the maximum degree of alignment achieved, one clearly sees in particular in Figure 4.7 b–d that nevertheless there is a substantial amount of molecules being strongly aligned. Thus it is clearly not sufficient to just use the degree of alignment in terms of $\langle \cos^2 \theta_{2D} \rangle$ to characterize the molecular alignment distribution, but the knowledge of the whole angular distribution is needed.

Comparison of Angular Distributions from Experiment and Simulations

We show a comparison of angular distributions extracted from experiment and from the simulated, 2D projected rotational densities for selected times, starting after the arrival of the second alignment laser pulse in Figure 4.8. The angular distributions display rich features, the simplest one being the alignment revival at a delay time of 120.78 ps. For

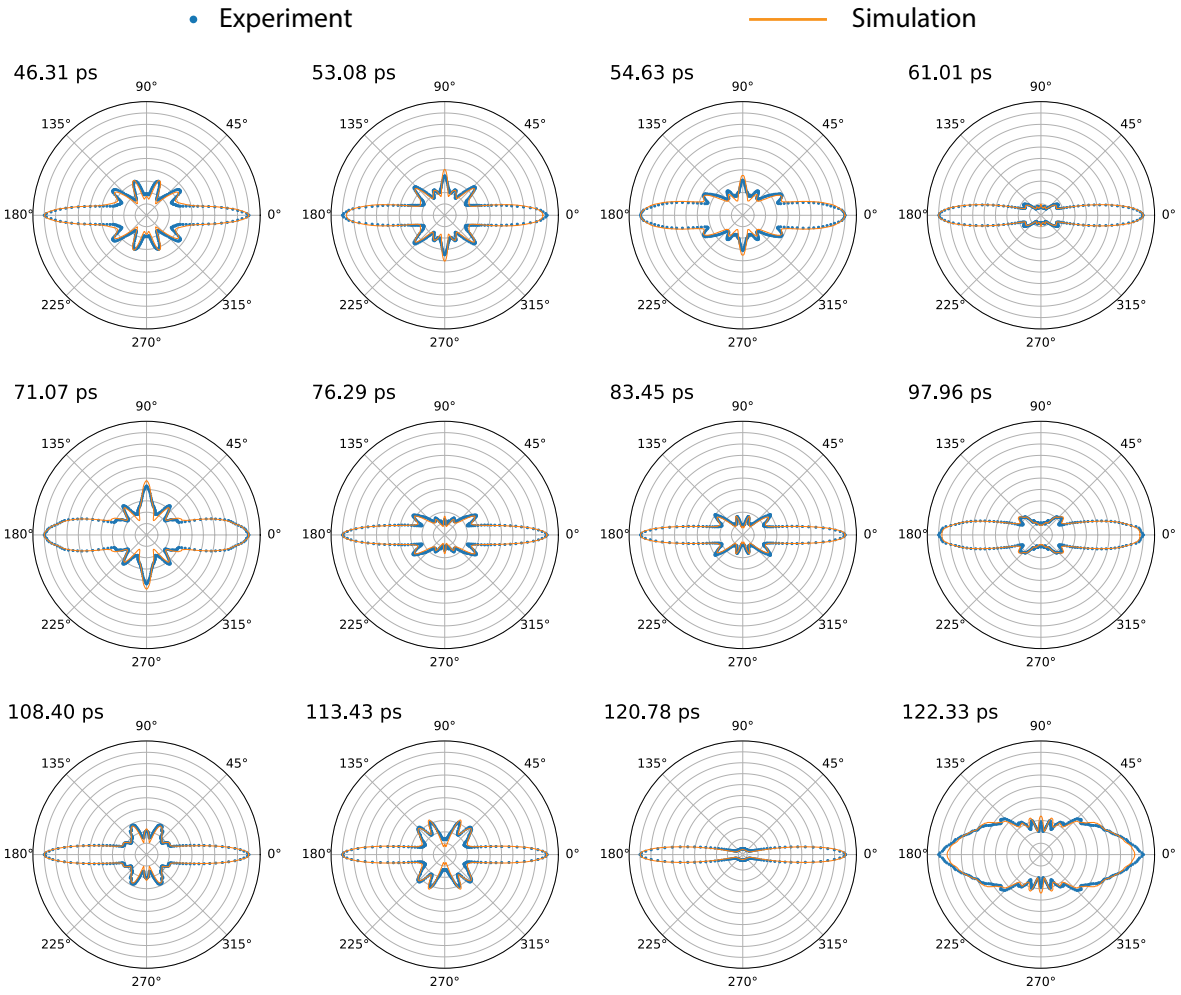

Figure 4.8.: Comparison of experimental and simulated angular distributions for some selected delay times after the second alignment laser pulse has arrived.

better visibility the angular distributions have all been scaled up individually to maximise visibility, except for the alignment revival at 120.78 ps.

4.5.4. Angular Resolution

The angular resolution was defined by the radius of the Coulomb channel in the VMI image, at which the angular distribution was extracted, and the number of pixels needed to distinguish two successive maxima or minima. The center of the radial Coulomb channel was at a radius of 46 pixel, which yielded an angle of 1.26 ° per pixel, corresponding to a limit for the resolution to separate two maxima or minima of 4 °. In Figure 4.9 a, a O^+ ion momentum distribution recorded at a delay time of 98.5 ps is shown with lines indicating the angles at which maxima in the angular distribution appear. In Figure 4.9 b, the corresponding angular distribution is shown, where the maxima are clearly visible and distinguishable.

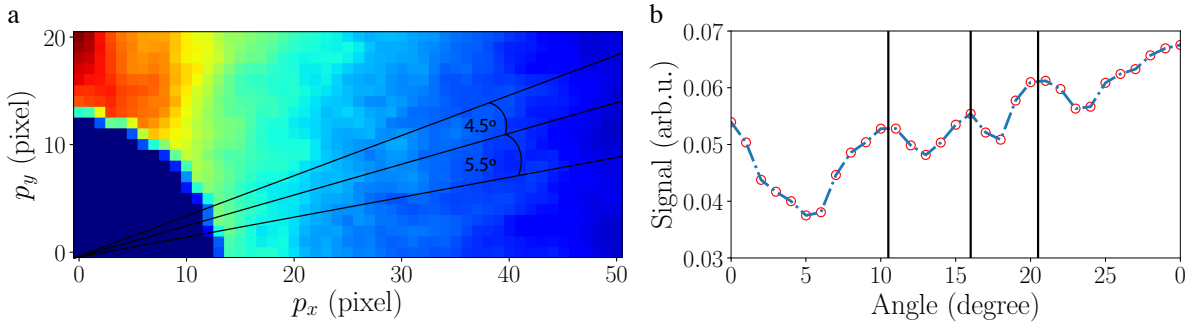

Figure 4.9.: Determination of angular resolution. **a** Part of the recorded VMI image at a delay time of 98.5 ps is shown with lines indicating the angles at which maxima in the angular distribution were observed. **b** Angular distribution for the same cutout of the VMI image, shown with the position of the maxima indicated by vertical lines. The smallest measured angle between maxima in the angular distribution is 4.5 °, close to the angular resolution of 4 °.

4.5.5. Highest Observed Degree of Alignment

In Figure 4.10 a, the O^+ ion-momentum distribution of the strongest observed field-free alignment is shown. The image was recorded at a delay time of 120.78 ps, which is the alignment revival, one rotational period after the arrival of the second alignment pulse. The degree of alignment was $\langle \cos^2\theta_{2D} \rangle = 0.96$ as stated in the main text. The value was obtained through integration in the shell between $r_{min} = 40$ and $r_{max} = 64$. In Figure 4.10 b, the corresponding angular distribution is shown, which yielded an opening angle of FWHM = 13.4 °.

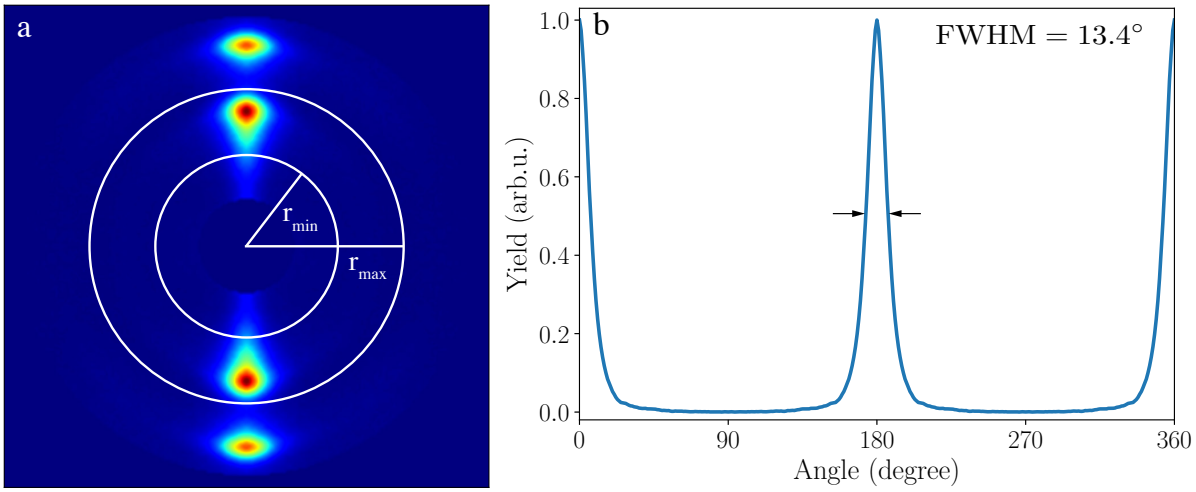

Figure 4.10.: Highest observed degree of alignment of $\langle \cos^2\theta_{2D} \rangle = 0.955$. **a** O^+ ion-momentum distribution recorded at the alignment revival at a delay time of 120.78 ps. The integration for the calculation of $\langle \cos^2\theta_{2D} \rangle$ was carried out in the shell between $r_{min} = 40$ and $r_{max} = 64$ pixel. **b** Corresponding angular distribution with a full opening angle of FWHM = 13.4 °.

5 Switched Wave Packets with Spectrally Truncated Chirped Pulses[3]

5.1. Introduction

Quantum control of molecular dynamics is one of the ultimate goals of chemical physics. Essentially, the aim is to create a custom wave packet with precisely controlled population and phases of each eigenstate. To date, the most successful approach for creating controlled wave packets is to use shaped ultrafast laser pulses. [211–213]. The construction of wave packets composed of states ranging from rotational [95, 214–217] to electronic [218–220], has been demonstrated.

A special case of shaped laser pulses are truncated pulses which are switched off much faster than they are switched on. The slow turn-on of the laser pulse adiabatically transforms the field-free states of the molecule into the eigenstates of the molecule in a dressed potential. The rapid truncation nonadiabatically projects the field-dressed states onto their field-free counterparts with well-defined phases. The archetypal example of this scheme, termed switched wave packets, is in molecular alignment dynamics where the wave packet is composed of rotational states populated by a non-resonant laser pulse. They were theoretically introduced by Seideman [89, 221], and realized experimentally by Stolow and coworkers [102, 222]. Switched rotational wave packets are especially interesting as (for symmetric tops) the peak alignment acquired during the long pulse should reconstruct exactly during the phase revivals, giving a route to extremely confined field-free alignment. In effect, switched wave packets offer a best-of-both-worlds compromise between adiabatic alignment, which enables a high degree of alignment at the cost of a field present, and impulsive alignment, which enables field-free alignment, but often with a lower degree of alignment [70, 91].

The generation of the necessary pulses with a very long turn-on and a very rapid turn-off was, traditionally, quite difficult. The slow turn-on precluded the use of standard pulse shaping technology, and instead a complex plasma shutter methodology was used [223], involving nonlinear effects to truncate a long pulse with a synchronized femtosecond pulse. Nevertheless, despite the interest in switched wave packet alignment dynamics and the promises it offers, very few experimental demonstrations were performed [102, 222, 224–226]. Recently, using chirped alignment pulses [227], switched wave packet

[3]This chapter is based on the publication: *Communication: Switched wave packets with spectrally truncated chirped pulses*, Adam S. Chatterley, Evangelos T. Karamatskos, Constant Schouder, Lars Christiansen, Anders V. Jørgensen, Terry Mullins, Jochen Küpper, and Henrik Stapelfeldt, *The Journal of Chemical Physics*, **148**, 221105 (2018). My contributions were the simulations of the alignment of iodobenzene, the comparison of simulations with experiment and I assisted in writing the manuscript.

dynamics have been demonstrated using non-Gaussian picosecond pulses with short [110] or long [111, 228] turn-offs, but not with the combination of a slow turn-on and a fast turn-off.

Here, we show a new, simple method for forming high-contrast truncated pulses with only a single passive optic. We demonstrate switched wave packets in the alignment dynamics of both linear molecules and asymmetric tops. The experimental dynamics match very well with numerical solutions to the time-dependent Schrödinger equation, demonstrating that the pulse is well characterized and the dynamics can be completely explained by the interference of rotational eigenstates.

5.2. Methods

5.2.1. Experiment

The experimental setup is identical to our previous chirped pulse adiabatic alignment experiments [228, 229], with the exception of the addition of a longpass interference filter into the alignment beampath. Carbonylsulfide (OCS) or IB is seeded in 80 bar helium and expanded through an Even-Lavie pulsed valve, giving an estimated rotational temperature of 1 K [47, 62, 228]. The uncompressed output of a Ti:sapphire chirped pulse amplifier (160 ps FWHM, GDD = $+1.3\,\mathrm{ps}^2$) is truncated using a longpass filter to form the STCP, which aligns molecules and prepares a switched wave packet. The compressed portion of the beam (35 fs FWHM) is focused to an intensity of $4 \times 10^{14}\,\mathrm{W/cm}^2$ and probes the molecules by Coulomb explosion, sampling at least every 3.5 ps. The degree of alignment of the molecules is measured by recording the expectation value $\langle\cos^2\theta_{2D}\rangle$ of the projection of the emission angle of S^+ or I^+ ions relative to the alignment polarization using velocity map imaging. The degree of alignment is quantified by computing the expectation value $\langle\cos^2\theta_{2D}\rangle$. The STCP was linearly polarized parallel to the detector plane, and the femtosecond probe pulse was polarized along the detector normal. The probe focal spot size was significantly smaller ($\omega_0 = 20\,\mu\mathrm{m}$) than the STCP focal spot size ($\omega_0 = 38\,\mu\mathrm{m}$) to minimize focal volume effects.

5.2.2. Theory

To characterize the experimental results, the degree of alignment was numerically simulated by solving the time-dependent Schrödinger equation (TDSE) using the experimental alignment-pulse profiles. Two separate codes were used to calculate the rotational dynamics for the linear-top molecule OCS [230] and the asymmetric-top molecule iodobenzene (IB) [155, 231], respectively. In brief, the rotational part of the Schrödinger equation was solved for the rigid-rotor coupled to a non-resonant laser field, where relativistic, fine- and hyperfine interactions as well as nuclear spin effects were neglected. For IB, the asymmetric top wave functions were expanded in a symmetry-adapted basis built of symmetric rotor states [231]. In both cases, the simulations assumed a rotational temperature of 1 K and included focal volume averaging determined by the experimental

spot sizes of the laser beams. The 2D projection of the degree of alignment, $\langle\cos^2\theta_{2D}\rangle$, was computed to provide a direct comparison with the experimental results.

5.3. Results and Discussion

5.3.1. Spectrally Truncated Chirped Pulses

Key to switched wave packet methodologies are laser pulses with a slow turn-on and a rapid turn-off, in comparison to the characteristic timescale of the wave packet in question. For plasma shutters, the turn-on time is defined by the pulse duration of the long pulse, and the turn-off time is defined by the duration of the short pulse, allowing nanosecond turn-ons, with tens of femtosecond turn-offs. However, plasma shutters are not without limitations. The required optical setup is fairly elaborate and sensitive, as it depends on highly nonlinear interactions. Additionally, without great care there is a residual field after truncation, which in most demonstrated applications has had an intensity of several percent of the peak before truncation [102, 224]. This significant residual field means that the truncation does not project wave packets onto true field-free eigenstates, but rather modestly coupled ones.

By working with highly chirped pulses in the spectral domain, truncated pulses in the time-domain can be produced that overcome the limitations of plasma shutters, while also allowing for a much simpler optical setup. Highly chirped broadband pulses have previously been used for adiabatic and intermediate regime alignment [88, 110, 111, 227, 232, 233], and our truncation technique is a natural extension. Its essence comes in the observation that for broadband laser pulses with large amounts of chirp (second order dispersion), the time-domain pulse shape has a 1:1 correspondence with the spectrum. This implies that the temporal profile of the chirped pulses can be directly shaped by modifying the spectrum with a device as simple as an interference transmission filter. Truncation of a positively (negatively) chirped pulse can be achieved through simple application of a long- (short-) pass filter.

Figure 5.1 (a) shows the spectrum of the uncompressed (positively chirped) output of a Ti:sapphire chirped pulse amplifier, after transmission through an 800 nm longpass spectral filter (Thorlabs FELH0800). The spectrum is abruptly cut at 800 nm. The influence of spectrum on temporal profile is shown in Figure 5.1 (b), which shows the frequency-resolved sum frequency generation cross correlation between the truncated chirped pulse and a transform limited 35 fs, 800 nm short pulse. The arrival time of each wavelength increases linearly with frequency, until the 800 nm component is reached, when the pulse is abruptly truncated. The temporal profile, found by integrating Figure 5.1 (b) over the wavelength, is shown in Figure 5.1 (c). The turn-on time for this pulse is around 100 ps (10–90 %), while the turn-off time (90–10 %) is approximately 8 ps. The residual intensity is 2–3 orders of magnitude lower than the pulse peak immediately after truncation, and undetectable after 30 ps (see supplementary material). Spectrally truncated chirped pulses (STCPs) offer high post-truncation contrast and a simple generation method. The drawback is that the truncation time is limited by the sharpness

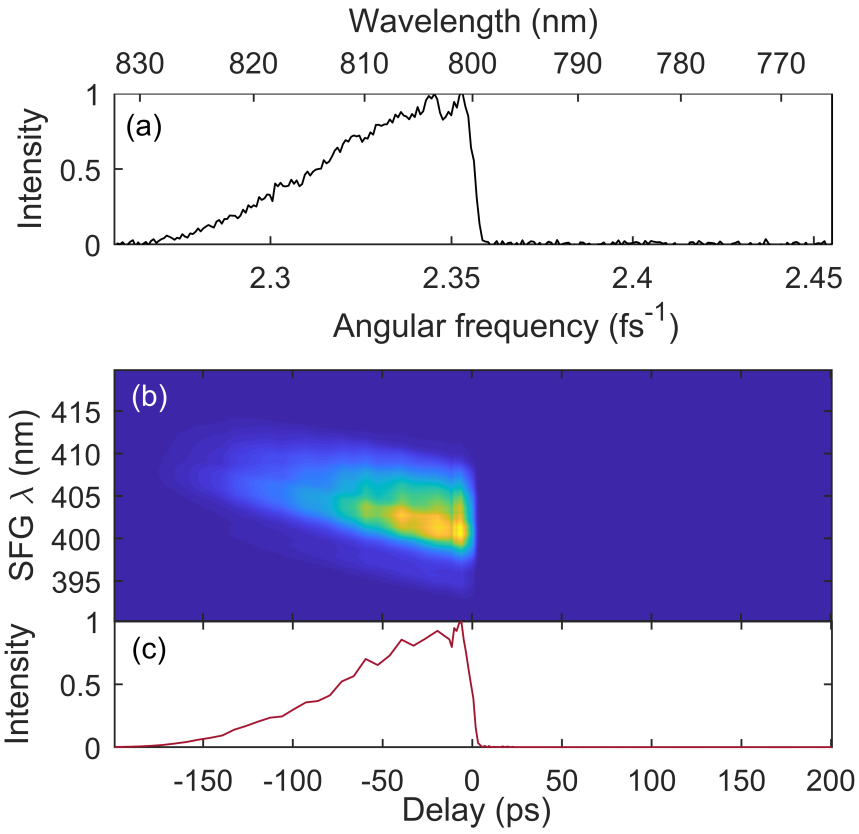

Figure 5.1.: (a) Spectrum of the uncompressed output of a Ti:sapphire chirped pulse amplifier after transmission through an 800 nm long-pass filter. (b) Spectrally resolved sum-frequency cross correlation of the truncated chirped pulse with a short 800 nm pulse. (c) Temporal profile of the intensity of the spectrally truncated chirped pulse. Time zero has been defined as half of maximum intensity on the falling edge.

of the spectral filter, which in this case limits us to an 8 ps turn-off time. As we show below, this turn-off time is still sufficiently fast to produce switched wave packet dynamics, even in light rotors such as OCS. If sharper edges are required, they could be obtained by replacing the transmission filter with a pulse shaper based on diffractive optics and spatial filtering, i.e., diffraction gratings and a razor blade [135]. Such a setup would be more complex than the simple transmission filter, but could likely reduce the turn-off time to a few ps or less.

5.3.2. Alignment of Linear Molecules

Our first demonstration of alignment using STCPs is with the linear OCS molecule. Alignment (and orientation) dynamics of OCS have previously been well studied, with both impulsive alignment [62, 117, 234, 235], switched wave packet methodologies [224], and intermediate regimes with moderately long alignment pulses [110, 111], so a direct comparison is possible. Figure 5.2 shows as red curves the value of $\langle\cos^2\theta_{2D}\rangle$ as a function of delay relative to the STCP (shaded area), for peak alignment intensities ranging from $5 \times 10^{10}\,\mathrm{W/cm^2}$ to $8 \times 10^{11}\,\mathrm{W/cm^2}$. The value of $\langle\cos^2\theta_{2D}\rangle$ is determined by observing

the recoil direction of S^+ fragments following Coulomb explosion with the probe pulse. As expected, the degree of alignment increases smoothly during the pulse turn-on, reaching a maximum of $\langle\cos^2\theta_{2D}\rangle = 0.85$ for the $8 \times 10^{11}\,\mathrm{W/cm^2}$ pulse (Figure 5.2 (e)). The peak of alignment is similar to that observed previously with 50 ps and 500 ps duration pulses and a similar intensity [110, 111]. Following truncation, a clear oscillating revival structure is observed, with a full period of 82.2 ps. As the alignment intensity is increased, the revivals become sharper, and the average alignment post-truncation increases.

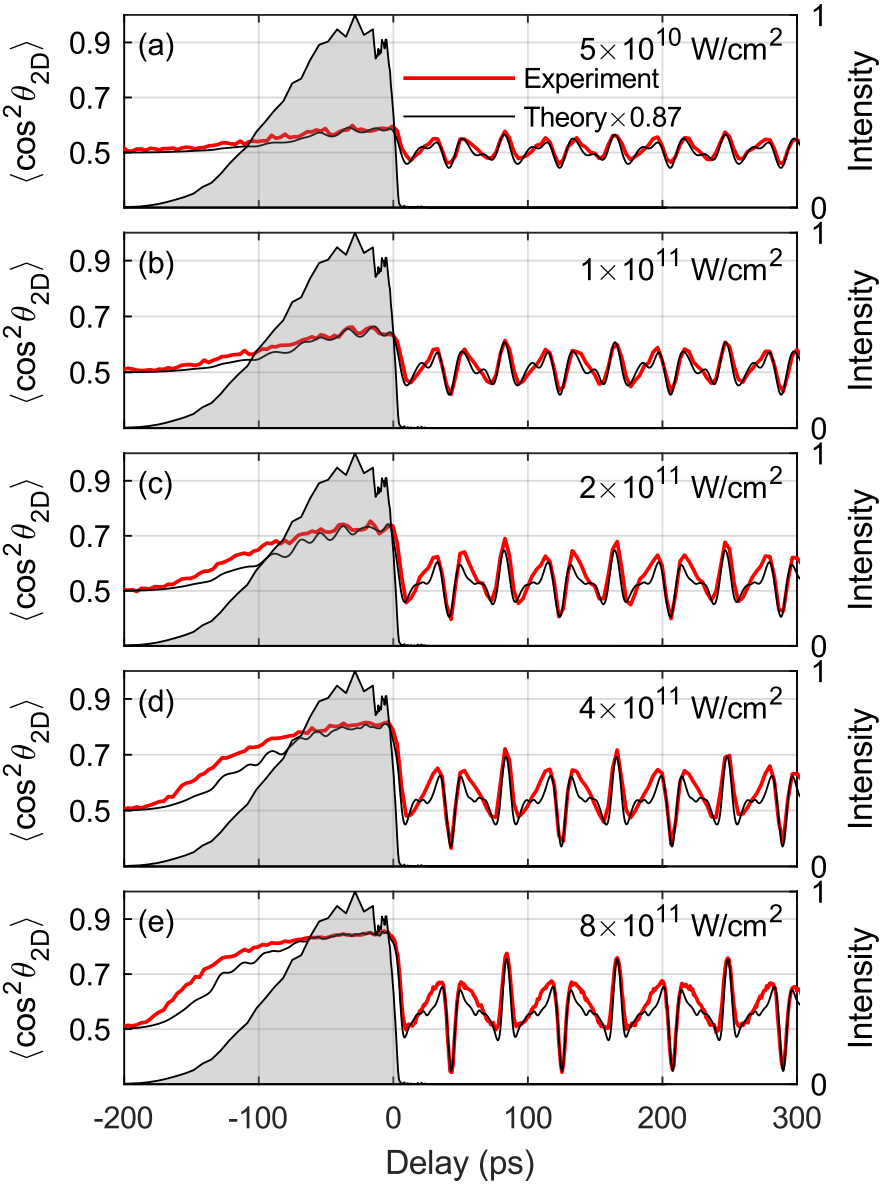

Figure 5.2.: Alignment dynamics of OCS with a spectrally truncated chirped pulse (shaded area) with increasing peak intensity, found experimentally (thick red) and numerically (thin black). The experimental $\langle\cos^2\theta_{2D}\rangle$ is determined using the angular distribution of S^+ fragments following Coulomb explosion. The peak alignment intensity is given in the top right of each plot. To account for non-axial recoil in the experimental $\langle\cos^2\theta_{2D}\rangle$, the numerical results have been scaled around 0.5 by an arbitrary value of 0.87.

To explain the observed alignment dynamics, we turn to numerical simulations (black curves in Figure 5.2). In Figure 5.2, the displayed values of $\langle\cos^2\theta_{2D}\rangle$ of the simulated data have been scaled by an arbitrary factor of 0.87, symmetrically centered around 0.5, as a simple means to account for non-axial recoil and probe selectivity in the Coulomb explosion process depressing the experimental values [205]. Except for a slight discrepancy on the rising edge of the pulse, the numerical simulations capture the experimental dynamics remarkably well. The shape of the revivals are well reproduced, and there is even a capturing of the slight oscillatory structure visible on the rising edges of the lower intensity curves. The quality of agreement between theory and experiment gives us a high degree of confidence both of the accuracy of the alignment pulse measurement, and of our ability to simulate alignment dynamics with these complex pulses.

The change of the shape of the alignment revivals as intensity increases is a direct reflection of the number of rotational J states populated during the pulse turn-on. The lowest intensity trace (Figure 5.2 (a)) has an almost sinusoidal pattern, suggesting a few-state wave packet similar to that previously observed when exciting with a low intensity, 50 ps long pulse [110]. On the other hand, the most intense trace, in Figure 5.2 (e), has a much more complex structure, suggesting rather more frequency components. The calculated J populations (shown in the supplementary material) provide further insight: after truncation the lowest intensity trace reaches a maximum angular momentum of only $J_{max} = 2$, while the highest has $J_{max} = 6$. Note, however, that these values of J_{max} are very low compared to typical impulsive alignment experiments. A simulation (using the same code) with a 150 fs kick pulse with equal fluence to that in Figure 5.2 (a) gives $J_{max} > 30$ (see supplementary material). Although many more J states are populated with impulsive alignment, adiabatic turn-on produces a significantly flatter phase between the few states that are populated. This highlights the power of switched wave packets to reach a previously unexplored regime of field-free alignment dynamics, where very high degrees of alignment are obtained with the help of a much stronger phase relationship than is found in impulsive alignment, where many more rotational states are populated [70, 150].

In the limit of instantaneous pulse truncation, we would expect that at each full revival the wave packet should reconstruct exactly, and $\langle\cos^2\theta_{2D}\rangle$ should be identical to the peak of alignment prior to truncation [89, 102, 221]. In our case the peak of alignment during the full revivals reaches $\sim 90\%$ of the peak alignment, for the highest intensity, and $\sim 95\%$ for the lowest intensity, indicating that the pulse truncation is not a completely impulsive process, and that some reduction in angular momentum must occur during the truncation. This result is unsurprising, as the 8 ps truncation time is not negligible when compared to the 82.2 ps rotational period of OCS [110]. The calculations (see supplementary material) demonstrate this emphatically: during truncation of the high intensity pulse the $J = 6$ level is almost completely depopulated, while the $J = 2$ level is mostly unaffected. We note, however, that switched wave packet experiments using rapid truncation with plasma shutters also have not achieved complete wave packet reconstructions at the peak of revivals; this is likely an effect of the residual field following truncation with that method [102, 224].

5.3.3. Alignment of Asymmetric Tops

Although alignment of linear molecules provides a simple test case for STCP dynamics, in reality most molecules are asymmetric tops with much more complex rotational dynamics. Asymmetric tops have three rotational constants which contribute to alignment dynamics, and their revival structures are much richer than linear or symmetric top molecules. To benchmark the behaviour of asymmetric tops when aligned with STCPs, we have measured and calculated the alignment dynamics of iodobenzene (IB). IB has been extensively studied using both impulsive [95, 144, 145, 236, 237] and adiabatic alignment [227, 238], and was recently explored using a plasma shutter truncated pulse by Sakai and co-workers, who observed a very surprising persistent alignment for many picoseconds following truncation [225]. Figure 5.3 shows (as thick red lines) the alignment dynamics

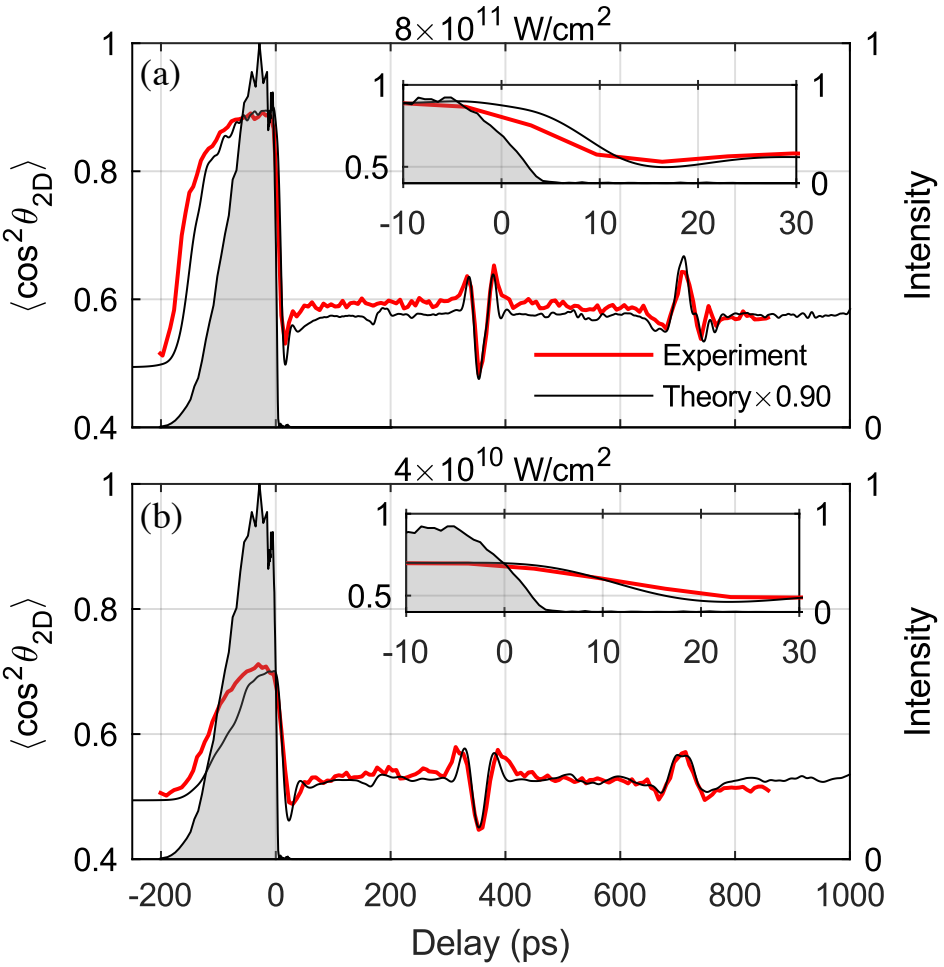

Figure 5.3.: Alignment dynamics of iodobenzene with truncated pulses. The pulse intensity profile is given by the shaded area. Experimental values of $\langle\cos^2\theta_{2D}\rangle$ are shown as thick red lines, while the calculated dynamics are given by the thin black lines, for (a) $8 \times 10^{11}\,\mathrm{W/cm^2}$ and (b) $4 \times 10^{10}\,\mathrm{W/cm^2}$ peak alignment intensities. To account for non-axial recoil in the experiment, calculated curves have been scaled by 0.90, symmetrically around 0.5.

of IB, when subjected to STCPs of either $8 \times 10^{11}\,\mathrm{W/cm^2}$ (a) or $4 \times 10^{10}\,\mathrm{W/cm^2}$ (b) peak intensities. The inset expands the region around the truncation point. Simulations, using

the experimental pulse, are overlaid as thin black lines. Similar to the OCS simulations, these have been scaled symmetrically around 0.5 to account for non-axial recoil in the experimental data, in this case by a factor of 0.9. Following truncation, the degree of alignment abruptly decreases, then returns to a permanent alignment of $\langle\cos^2\theta_{2D}\rangle \sim 0.59$ and 0.53 for the high and low intensity STCP, respectively. Prominent, broad revival features are observed, centered at 359 ps and 712 ps. The agreement between the experiment and theory is very good, all major features in the experimental trace are accurately reproduced by the theory.

We first consider the behaviour of the revivals in the field-free regime. Compared to IB dynamics following impulsive alignment [145], several striking aspects are immediately observable. Firstly, only J-type revivals are observed, which correspond to symmetric-top like motion. With high intensity impulsive alignment, C-type revivals, which correspond to motion around the axis perpendicular to both the molecular plane and the C-I bond are visible at 380 and 757 ps, however we see no evidence for these with either high or low alignment intensity STCPs. C-type revivals are associated with high lying rotational states [93], so it is reasonable that they are not observed with our adiabatically prepared alignment. Intriguingly, our simulations show that only rotational states with $K = 0$ are accessed, which may further explain the symmetric-top like behavior (see supplementary material). Secondly, the directions of the revivals are inverted: with impulsive alignment the half-revival is a positive feature, and the full revival negative, the exact inverse of the dynamics we observe. This inversion must reflect reflect the different preparation methods of the wave packets, and in particular the relative phases of their components. A similar inversion of revivals is observed in alignment produced by one-photon excitation, which selectively excites aligned molecules [239]. This suggests that this is an effect of having the molecules physically spatially aligned when the wave packet is formed, as opposed to impulsive alignment where the wave packet is formed in momentum space on an isotropically aligned sample. Investigations of the phases of the simulated wave packets bear this out: switched wave packets have a relatively flat phase, while impulsive alignment leads to highly varied phases (see supplementary material). Finally, the STCP revivals are exceedingly broad, compared to impulsive revivals. The main peaks of both the full- and half-revivals are around 50 ps wide, compared to around 20 ps when excited with a 200 fs, 16 TW/cm^2 kick [145]. The breadth of these revivals is a further consequence of the few rotational states that are populated when truncated pulses are used for alignment - there simply are not enough Fourier components to construct a sharp feature.

We now turn to the behavior of the alignment at the moment of pulse truncation (inset Figure 5.3). As soon as the pulse truncation is complete, ($t = 5$ ps), the degree of alignment drops appreciably, reaching a minimum at $t = 18$ ps with a high intensity STCP, and at $t = 28$ ps with a low intensity STCP. The theory captures the general trend, although somewhat overestimates the speed of the drop for the high intensity, and underestimates it for the low intensity. This discrepancy is likely due to either temperature or focal volume effects differing slightly between simulation and experiment. The slower drop in alignment with low intensity can again be explained by the lower number of populated rotational states giving insufficiently high frequency Fourier components for a

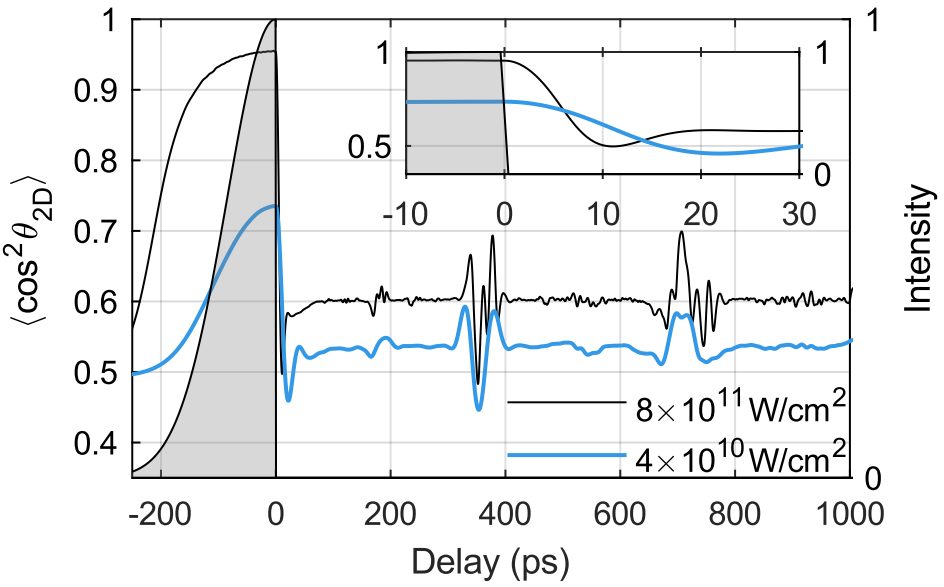

Figure 5.4.: Calculated values of $\langle\cos^2\theta_{2D}\rangle$ with a <200 fs rapidly truncated alignment pulse with peak intensity of 8×10^{11} W/cm^2 (thin black line), 4×10^{10} W/cm^2 (thick blue line).

fast drop. This behavior, however, stands in stark contrast to the dynamics observed by Sakai and coworkers, using a pulse shaped by a plasma shutter [225]. They reported a high degree of alignment that appeared to persist for ∼10 ps after the pulse was very abruptly (< 200 fs) truncated. Could it be the case that very abrupt pulse truncation leads to significant field-free alignment, which is not present if the pulse turns off too slowly? To investigate this possibility we have also performed simulations, with identical conditions and alignment intensities to our experiment, but with the turn-off time of the pulse reduced to 150 fs, shown in Figure 5.4. The excellent experimental agreement of our simulations with a slow turn-off time, Figure 5.3, give us confidence that our calculations accurately and comprehensively model the alignment dynamics of asymmetric top systems, and so we fully trust our simulations with rapidly truncated pulses. On the whole, the alignment dynamics are similar to those with the longer turn-off time, however the revivals are more structured and show evidence of C-type behavior, particularly with high alignment intensity. This demonstrates that the populated rotational states are better preserved during rapid truncation, in agreement with our findings from OCS and the predictions of Seideman [89].

Compared to the experimental STCP, the falling edge of the alignment is faster, in agreement with the intuitive expectation that the quicker the field is removed, the sooner molecules should no longer be aligned by it. The alignment begins to drop appreciably within 2 ps of the field truncation, regardless of whether a high or a low intensity alignment field is used. The slope is less severe with a weak alignment intensity, but as this necessitates a weak degree of alignment, this effect cannot be exploited for high quality field-free alignment. These findings lead us to suspect that further experimental aspects, such as possibly the residual post-truncation field, may have led to the reported findings by Sakai and co-workers [225]. That group also reported an absence of revivals in their IB alignment dynamics [240], which are observed very clearly by us in both theory

and experiment. It is feasible that whatever experimental complication led to a lack of observable revivals also led to apparent long-lived field-free alignment after truncation.

5.4. Conclusions

We have developed a new scheme for creating truncated laser pulses for preparation of switched wave packets, by spectrally filtering chirped laser pulses. Compared to the previous standard methodology for producing truncated pulses, our method has a trivial optical setup, high repetition rates, very good contrast after the pulse is truncated, and uses technologies already proven for free-electron laser experiments [232]. The primary drawback is a slower truncation time, which could be significantly enhanced if a more complex spectral filter was employed.

Using the newly developed STCPs to align the linear OCS molecule, we have observed high degrees of alignment while the alignment pulse is present, and rich rotational dynamics after the pulse is truncated. Compared to traditional impulsive alignment, very few rotational states are populated, leading to simple alignment dynamics. Numerical simulations, using the experimentally determined pulse shape, accurately reproduce the alignment dynamics. The degree of alignment at the revival is close to that during the maximum of adiabatic alignment, and it could be enhanced further by, for example, a scheme to 'kick' the molecule at the peak of a revival [203].

In iodobenzene, an asymmetric top system, we again observe excellent alignment during the pulse, and after truncation we see very broad symmetric top-like J-type revivals, composed of few rotational levels. Computations accurately predicts these, even with the complex pulse shape involved. The alignment begins to decay as soon as the pulse is truncated, in contrast to previously reported experiments with IB and truncated pulses where field-free alignment was observed [225]. By comparison with simulation, we suspect that those findings may have been due to an experimental artefact.

Our results pave the way for new investigations on switched wave packets. Since the invention of the methodology over a decade ago, switched wave packets have been of great interest to the community, but rather few experiments have been performed. With the development of the trivial STCP methodology, many laboratories will be able to investigate switched wave packets. Additionally, STCPs are extremely useful for molecular alignment, even without exploiting switched wave packets. If a superfluid helium solvent is present, then alignment persists for a brief time after the pulse is truncated, giving a simple route to field-free molecular alignment for several picoseconds [233]. We have very recently employed helium droplets and STCPs to perform field-free 3D alignment on a range of complex molecules.

5.5. Supporting Information

In the supplementary information we show the STCP intensity plotted on a log scale, and the calculated J and K state populations and phases from the alignment simulations.

Logarithmic plot of the spectrally truncated chirped pulse intensity

In Figure 5.5 the STCP intensity plotted on a log scale is presented.

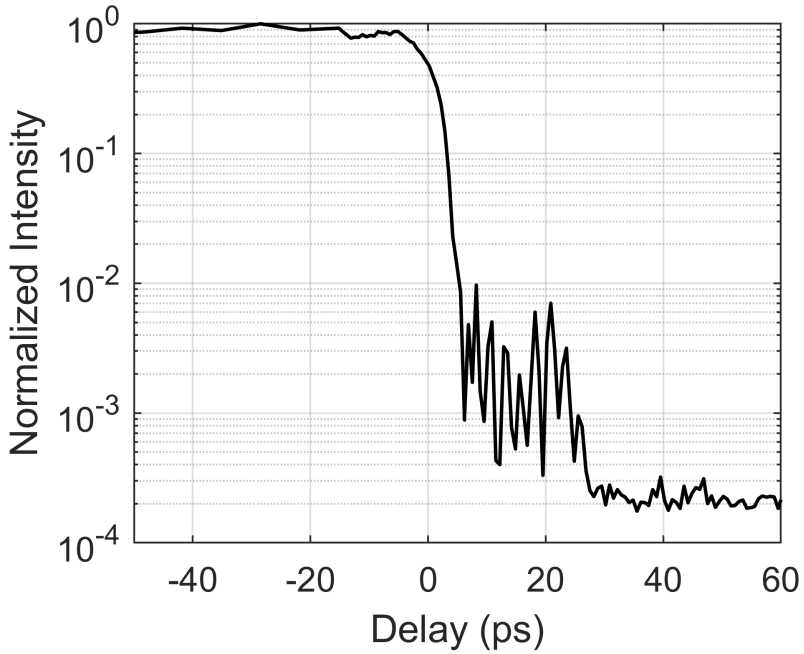

Figure 5.5.: Log-plot of the intensity of the spectrally truncated chirped pulse, derived by sum-frequency mixing with a 35 fs 800 nm pulse. The data in this plot are identical to those in Figure 5.1 (c) of the main text. The intensity at 40 ps represents the noise floor of these measurements. The structure visible around 5 ps to 20 ps is likely introduced by the interference coating of the long-pass filter optic.

Simulated J populations and phases for OCS

To further describe the alignment of OCS, we have extracted the J state populations and revival phases from our simulations, starting at J = 0 and without focal volume averaging, for both STCPs with the highest and lowest intensities studied (Figure 5.6), and for an impulsive kick (Figure 5.7). The STCP calculations show that very few J states are populated, but with a very flat phase. On the other hand, aligning with a kick results in many J states being populated, but there is only a handful that are in phase with each other at the revivals, and this phase is not as flat as in the truncated pulse case.

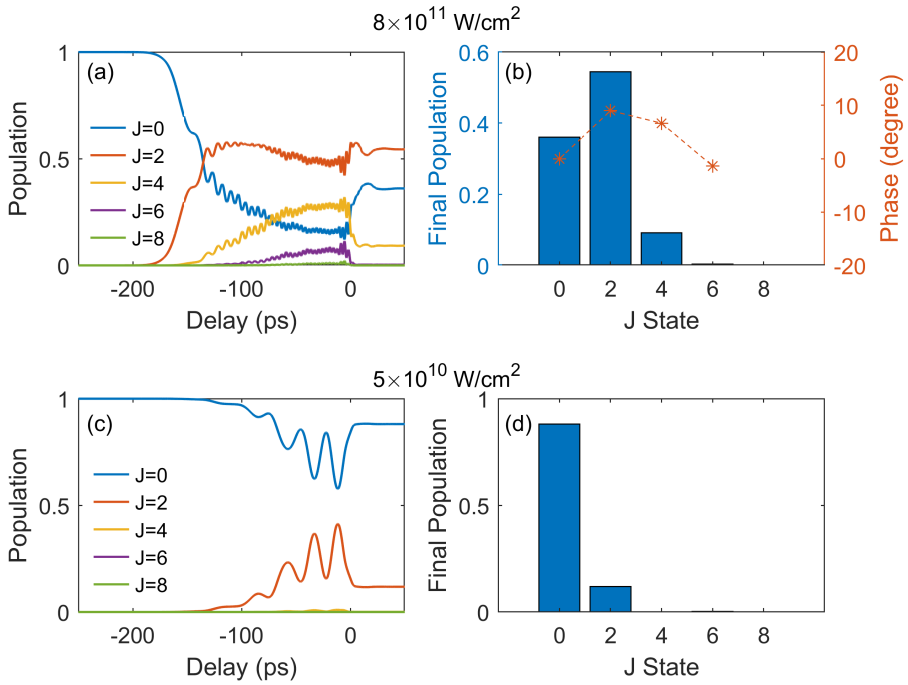

Figure 5.6.: **(a)** & **(c)**: The calculated J state population in OCS as a function of time for the highest and lowest alignment intensities employed (Figure 5.2 (e) & (a)), starting in the absolute ground state and using the experimental alignment pulse profile. During the truncation, significant depopulation of the higher J states is observed. **(b)** & **(d)**: The final (field free) J state population, along with the phases of the populated states at the peak of the first revival in the high power case. Very few J states are populated, and their phases vary by less than 10 ° at the revival.

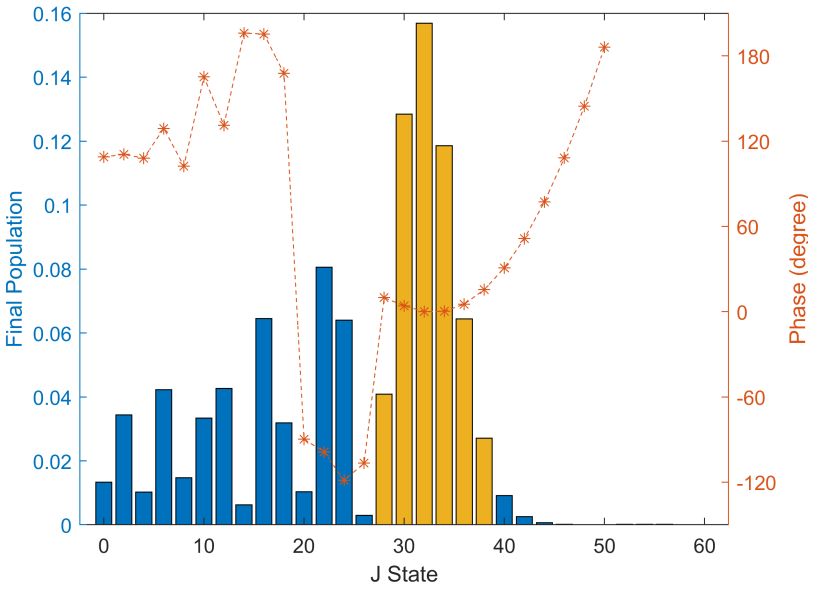

Figure 5.7.: The calculated J state distribution and phases at the peak of the first half revival of OCS, impulsively aligned using a 150 fs Gaussian kick with equal total kick energy to that of the lowest energy STCP used (Figure 5.2 (a)). The simulated pulse energy is 90 mJ and the fluence is 4 J/cm^2. High lying J states are populated, with significant variation in phases. The states from J = 28 to J = 38, highlighted in yellow, possess a quadratic phase with a spread of ∼15 °. Only these high lying states contribute to the alignment at the revival, the lower lying states are out of phase and so in fact detract from the maximum attainable alignment.

Simulated J and K populations and phases for IB

Similar to OCS, we have also extracted the population and revival phases of the rotational states in IB, in a symmetric top basis. As IB is an asymmetric top, the state space is now two dimensional because K may take non-zero values. To best visualize the breadth of wave functions in this large state space, we chose therefore to show the summed total population per J state, summed over all K states. To examine the K state population and wave function phases, we have also plotted the populations and revival phases of the 20 most populated states, $|\mathrm{J},\mathrm{K}\rangle$. Figure 5.8 and Figure 5.9 show these plots using the experimental STCP with peak intensities of $8 \times 10^{11}\,\mathrm{W/cm^2}$ and $4 \times 10^{10}\,\mathrm{W/cm^2}$, respectively. For comparison, Figure 5.10 shows the simulated populations using a 150 fs,

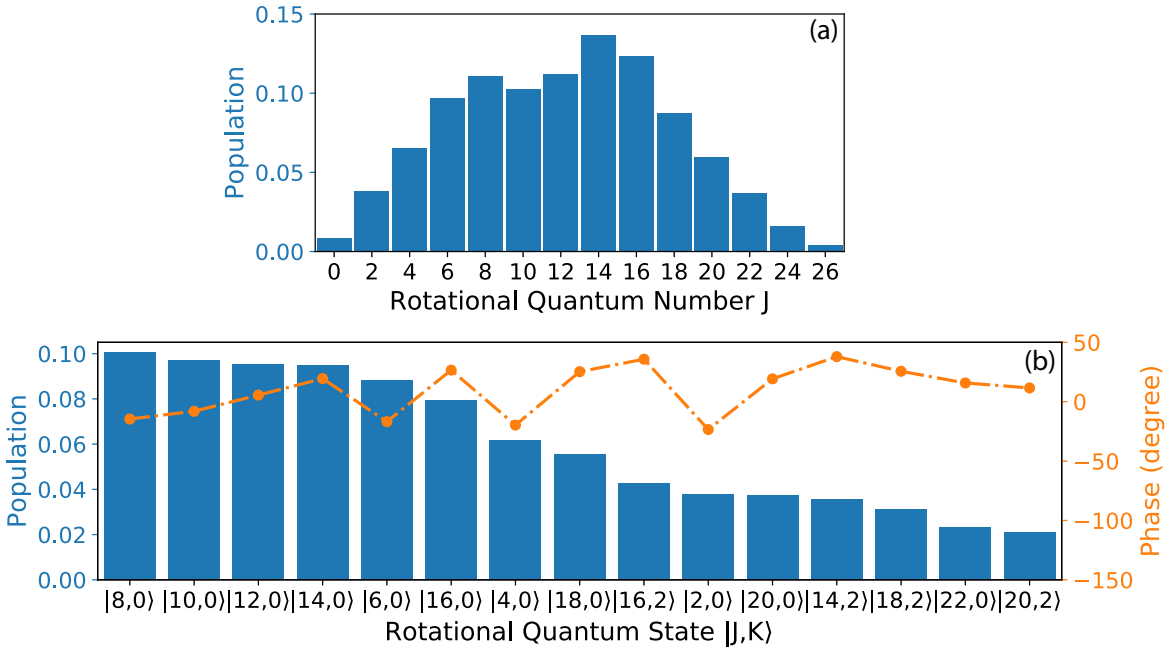

Figure 5.8.: **(a)** The calculated summed J state distribution at the peak of the first half revival of IB, aligned using the experimental truncated pulse with peak intensity of $8 \times 10^{11}\,\mathrm{W/cm^2}$, and starting in the ground $|0,0\rangle$ state. J states ≤ 26 are accessed. **(b)** The population and phases of the 15 most populated rotational states. For almost all of the population, $\mathrm{K} = 0$ and the phase is relatively flat.

$4\,\mathrm{J/cm^2}$ kick pulse, which has previously been shown to produce J type revivals, but inverted from those seen with truncated pulses [145]. Comparing the truncated pulse populations with the impulsively kicked populations, there are several striking effects. Firstly, as in OCS, truncation leads to much less broad wave packets than kicking, however these narrower wave packets have a much flatter phase than in the kicked case. Secondly, for almost all population in switched wave packets, the quantum number K (which represents the projection of angular momentum onto the principle molecular axis) takes the value of 0, while kicked wave packets have much higher values of K. The fact that switched wave packets of IB behave very much like symmetric tops seems to be in agreement with all $\mathrm{K} = 0$.

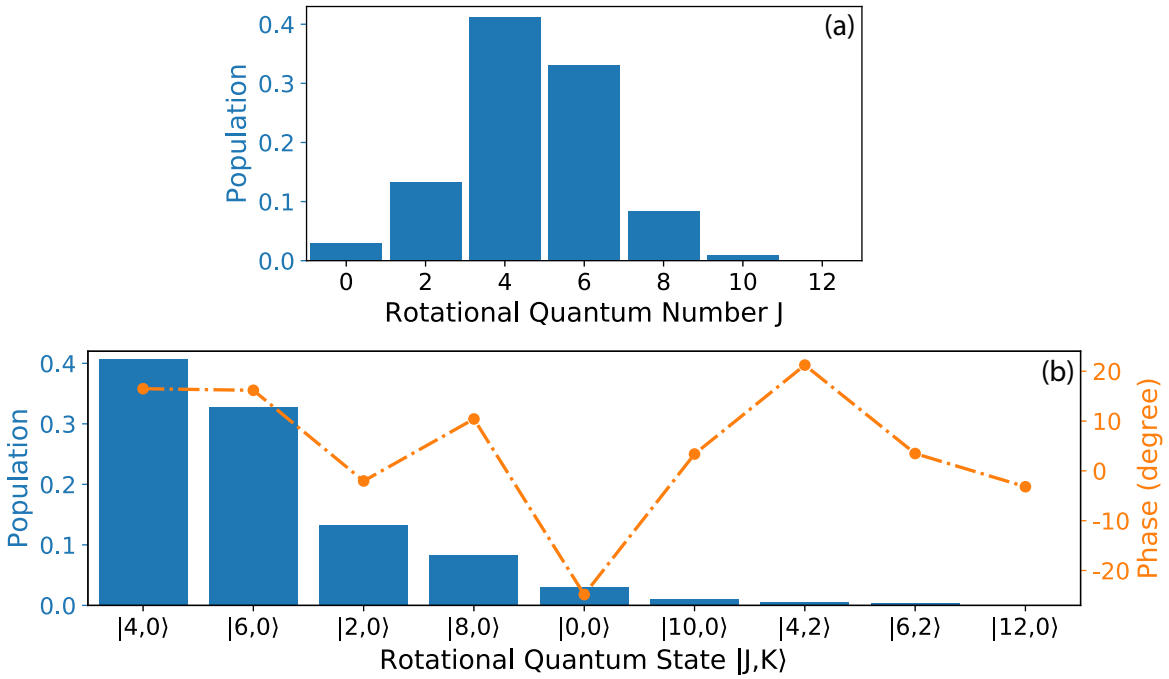

Figure 5.9.: **(a)** The calculated summed J state distribution at the peak of the first half revival of IB, aligned using the experimental truncated pulse with peak intensity of $4 \times 10^{10}\,\mathrm{W/cm^2}$, and starting in the ground $|0,0\rangle$ state. Only J states ≤ 10 are accessed. **(b)** The population and phases of the 9 most populated rotational states. Almost all of the population has K = 0, and the phase varies by less than $20\,^\circ$ for $\sim$95% of the population.

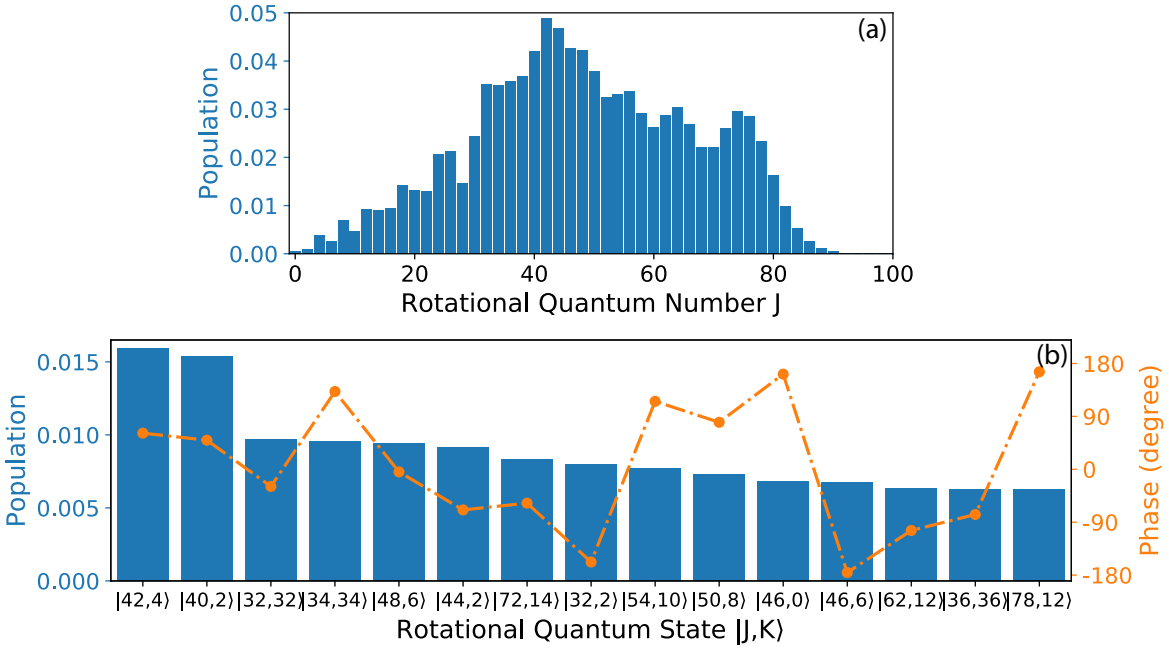

Figure 5.10.: **(a)** The calculated summed J state distribution at the peak of the first half revival of IB, impulsively aligned using a 150 fs, $4\,\mathrm{J/cm^2}$ kick pulse, and starting in the ground $|0,0\rangle$ state. Very high J states are accessed. **(b)** The population and phases of the 15 most populated rotational states. High values of K are accessed, and very little phase relation is visible between these states.

6 Creating and Characterizing Strong Three-Dimensional Field-Free Alignment of Complex Molecules[4]

6.1. Introduction

Laser-induced alignment of gas-phase molecules has proven to be an efficient and elegant way to access the molecular frame [70, 78]. It has been extensively used in high harmonic generation [210, 241], electron diffraction [35, 40, 69, 196, 242], x-ray diffraction [14], and strong-field-ionization [66, 243] experiments, enabling the imaging of molecular structure and dynamics in the molecule-fixed frame or to retrieve the shape of molecular orbitals [208, 209, 244].

Although long laser pulses are well suited to adiabatically align molecules [86, 125, 227], alignment is only present during the laser field. Furthermore, experiments may suffer from the presence of the additional alignment laser field and their outcome might be affected. Therefore, the interest in impulsive alignment has grown, in which a coherent rotational wavepacket is formed and alignment under field-free conditions is achieved [90, 245]. For diatomic and small linear molecules, high degrees of field-free alignment have been demonstrated with the use of multiple short kicking pulses [97, 246], which works well due to the regular rotational energy level structure in these molecules.

The impulsive method is somewhat more difficult for asymmetric top molecules, due to their irregular energy level structure [81, 82, 144–147]. A promising method for aligning asymmetric top molecules consists of using a truncated adiabatic laser field [151], or an adiabatic laser field with a kick at the end [103], which combines both of the above methods: The adiabatic alignment gives good angular confinement of the molecules. When the laser pulse is suddenly truncated, i. e., "turned-off", the dressed pendular state, which was produced by the adiabatic pulse, is projected onto the field-free eigenstates as a coherent superposition. At short times after the laser pulse truncation, the angular confinement remains, due to the inertia of the molecules. Such truncated-pulse alignment experiments have been performed successfully for 1D [151, 224, 225, 247] and 3D alignment [226], although some of the observed alignment dynamics [225, 226] were shown to be controversial [247]. Furthermore, so far alignment experiments with asymmetric-top molecules utilized heavy marker atoms, such as iodine or fluorine [144, 226], as good

[4] This chapter is based on a draft of the manuscript: *Creating and characterizing strong three-dimensional field-free alignment of complex molecules*, Terry Mullins, Evangelos T. Karamatskos, Joss Wiese, Jolijn Onvlee, Andrey Yachmenev, Arnaud Rouzée, Sebastian Trippel and Jochen Küpper. My contributions were the simulation of the alignment of indole, the comparison of simulations with experiment and I assisted in writing the manuscript.

indicators for the detection of the molecules' alignment through axial recoil of the leaving fragments following strong-field ionization. Thus, the set of asymmetric top molecules for which alignment has been demonstrated is very limited.

Alignment is achieved via the interaction of the laser field with the molecular polarizability anisotropy. As the polarizability generally is strongly related to a molecules shape [248, 249] one should be able to align, in principle, every molecule with an asymmetric shape. The major challenge, besides aligning the molecules in the first place, consists therefore in the ability to characterize the degree of alignment of complex molecules without good leaving groups and symmetry.

Here, we demonstrated the field-free 3D alignment of indole (C_8H_7N, Figure 6.1 a) by a truncated elliptically-polarized laser field, using velocity-map imaging (VMI) of H^+, C^+, and $HCNH^+$ fragments after Coulomb explosion. Indole is a characteristic representative of organic molecules without rotational symmetries and marker atoms. Thus, the demonstration of 3D alignment for indole provides the testbed for further studies on large (bio)molecules.

6.2. Experimental Setup

The general experimental setup has been described elsewhere [227]. Briefly, molecules were cooled in a supersonic expansion from a pulsed Even-Lavie valve [47], operated at a temperature of 80 °C and at a repetition rate of 100 Hz, limited by pumping speed and the final rotational temperature of the deflected indole molecules. Around 1.4 mbar of indole was seeded in 95 bar of He, which was expanded into vacuum and state-selected by an electrostatic deflector [1]. Inside a velocity map imaging spectrometer (VMIS), the more strongly deflected and, therefore, rotationally colder molecules [109] were aligned using a shaped 250 ps long laser pulse with a peak intensity of $6 \cdot 10^{11}$ W/cm^2. The laser pulses were produced by a commercial laser system with a 1 kHz repetition rate and a spectrum similar to a rounded saw tooth, then strongly negative chirped to a duration of ∼600 ps using a grating based compressor [227]. The alignment laser pulses were elliptically polarized with the major axis vertical and a 3 : 1 ratio between major and minor axes, had an energy of 2.5 mJ after exiting the vacuum chamber, and a peak intensity of 1.25×10^{12} W/cm^2 in the focus.

A second, time-delayed, laser pulse was used to multiply ionize indole, resulting in Coulomb explosion. These pulses were circularly polarized in order to avoid any secondary dynamics induced by electron rescattering [250]. Velocity-mapped fragments were detected on a multi-channel plate (MCP) detector equipped with a phosphor screen. The voltage on the MCP could be switched between 2050 V (MCP "on") and 1150 V (MCP "off") using a fast switch (Behlke HTS 31-03-GSM) with 100 ns rise and fall-times to select the different ion fragments based on their time-of-flight (TOF). A camera (Optronis CL600) recorded single-shot images of the phosphor screen at 200 Hz. Images without pulses from the molecular beam were subtracted from those with the molecular beam to account for any signal from background molecules in the interaction region. After selection of a suitable 2D radial range, the 2D angular degree of alignment $\langle \cos^2\theta_{2D} \rangle$

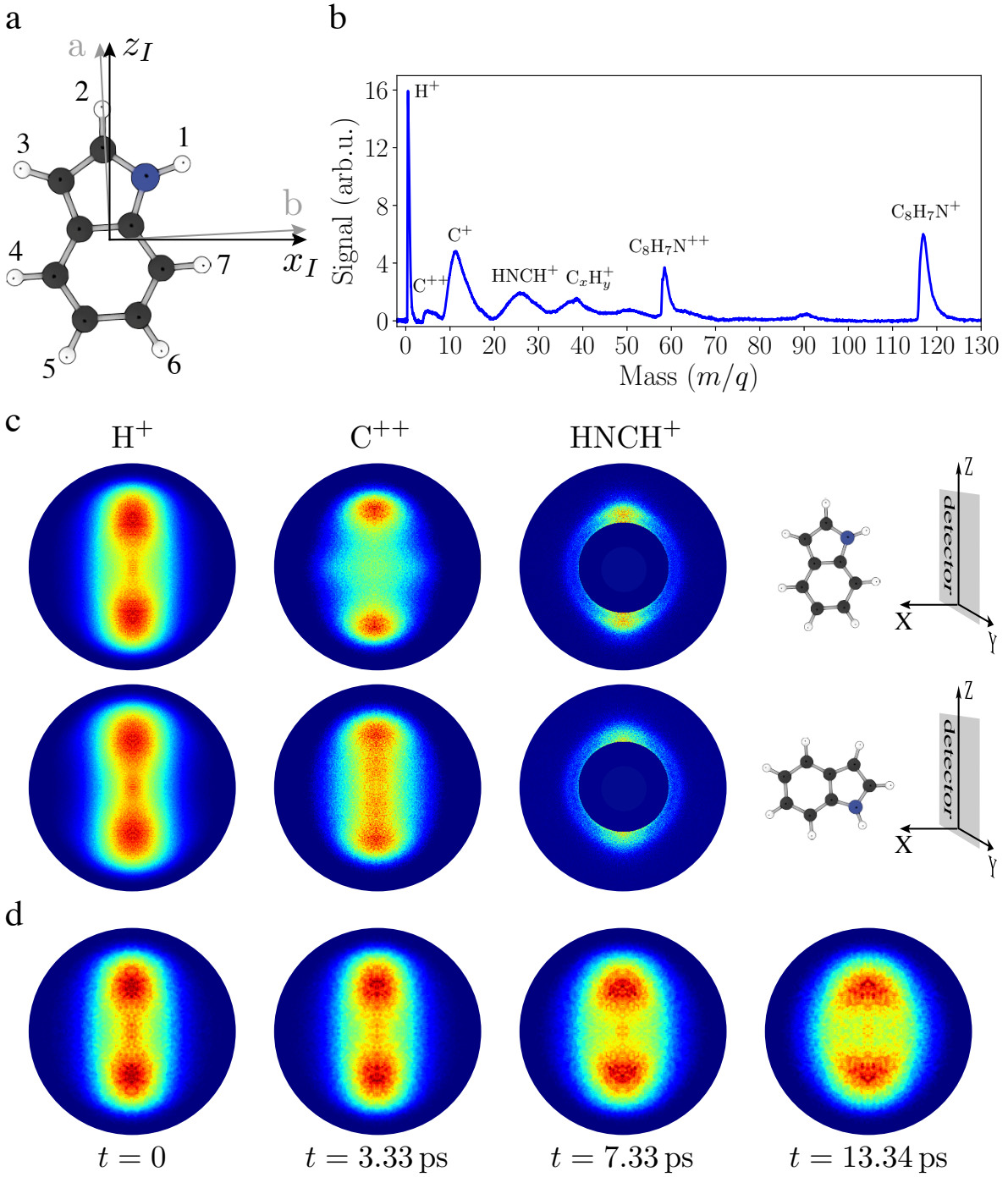

Figure 6.1.: a The structure of indole, along with the principle axes of inertia, labeled $z = a$ and $x = b$, $y = c$ is out of the plane. The principle axes of the polarizability tensor are labelled x_I and z_I, y_I is out of the plane. The numbering of the H atoms is also shown. **b** A typical time-of-flight (TOF) spectrum of indole showing the most prominent observed fragments. **c** In the first row, measured 2D VMI images are shown for the three fragments H^+, C^{++} and $HNCH^+$ at the time of peak alignment at $t = 3.3$ ps, with the major axis of the alignment laser polarization being parallel to the detector plane. In the second row the same fragments are shown for the major axis of the alignment laser pointing perpendicular to the detector plane. **d** In the last row, snapshots of H^+ fragments at different delay times are shown.

was calculated.

For truncation the strongly chirped 9 mJ pulses were sent through a zero dispersion $4f$ shaping setup [251] with a spatial light modulator (SLM, Jenoptik S640d) situated at the Fourier plane. The SLM was used to alter the spectral phase of the negatively chirped pulses to remove the chirp, i. e., the phase curvature, for wavelength components on the long-wavelength side of the peak intensity of the spectrum at 815 nm. Wavelengths longer than ∼816 nm were blocked by a razor blade, situated just before the SLM. This was necessary due to Nyquist sampling limits encountered when shaping such highly chirped pulses. Phase shaping improved the temporal fall-off time by a factor of 2.5 compared with simply cutting the spectrum. The most relevant part of the temporal profile, around the cutoff, is shown in Figure 6.2. The pulse consists of a slow rise beginning at −250 ps (not shown), followed by some amplitude modulation, a short kick, and, finally, a fast truncation. The pulse intensity falls rapidly within 2 ps (90 % to 10 %) to below 1 %, i. e., to within the noise level of the measurement. The post-pulse at 13 ps is unwanted, and probably originates from imperfect phase compensation from the SLM or space-time coupling in the pulse shaping setup. However, the post pulse is irrelevant to the degree of alignment within the first 10 ps after the temporal truncation, which is the important temporal region of these experiments.

6.3. Results and Discussion

The in-plane principal axes of inertia and polarizability are shown in the ball-and-stick representation of indole in Figure 6.1 a. For both, two axes lie in the plane of the molecule with an angle of 2.75 ° between them. Upon Coulomb explosion, several fragmentation channels were detected using a velocity map imaging spectrometer (VMI). The resulting time-of-flight mass spectrum is depicted in Figure 6.1 b. Despite the low symmetry, several fragments showed anisotropic momentum distributions. To retrieve the degree of alignment we analysed the H^+, C^{++}, and $HNCH^+$ VMIs. The ion-momentum distributions for a delay time of $t = 3.3$ ps, corresponding to the highest observed degree of 3D alignment, are shown for two configurations of the alignment laser polarization , ie, with the major polarization axis parallel, 0 °, and perpendicular, 90 °, to the detector plane, shown in the upper and lower row of Figure 6.1 c, respectively. A full tomographic 3D distribution was obtained from VMIs that were recorded by rotating the alignment laser polarization ellipse around the laboratory-fixed Y-axis from 0 ° to 180 ° in steps of 2 °. Furthermore, ion-momentum distributions of H^+ as a function of the delay time between the alignment laser and the probe laser, with some typical snapshots, are shown in Figure 6.1 d. $t = 0$ corresponds to the peak intensity of the alignment laser field, $t = 3.3$ ps to the strongest observed field-free alignment, and $t = 7.33, 13.34$ ps correspond to later times where the alignment has already decreased due to dephasing of the field-free rotational wavepacket. Due to the larger count rates the H^+ data was of a higher quality than for the other fragments. VMIs of other fragments displaying alignment are shown in the Supplementary Information.

The delay-dependent measured 2D degree of alignment is shown for a variety of ion fragments in Figure 6.2. Assuming axial recoil, H^+ fragments would have measurable momentum components only within the *ab* plane of indole [252]. Hence, the H^+ fragments are a measure of the planar alignment of indole in the laboratory frame. The slow rise of the alignment pulse aligned the plane of the indole molecules in a quasi-adiabatic fashion [110, 227] to a maximum 2D degree of alignment of $\langle\cos^2\theta_{2D}\rangle^{exp}_{H^+} = 0.74$.

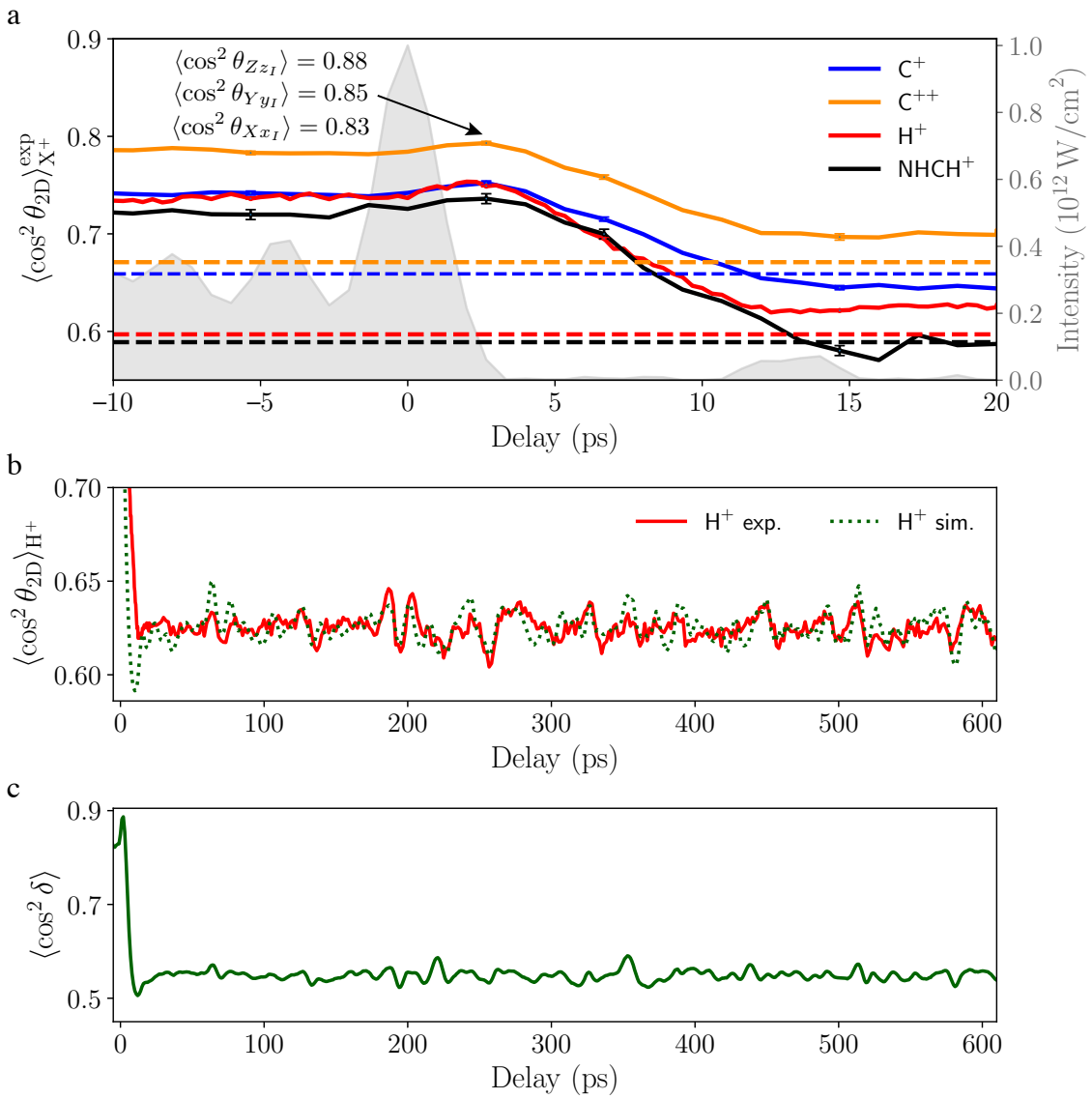

Figure 6.2.: **a** Temporal evolution of the alignment of indole. The solid lines show the measured 2D degree of alignment $\langle\cos^2\theta_{2D}\rangle^{exp}_{X^+}$ for different fragments X^+ and the dashed lines indicate values of the 2D degree of alignment obtained without alignment laser. Statistical error bars, representing the standard error, are shown for selected delays. The grey area shows the intensity profile of the alignment laser pulse. **b** The alignment revival structure of H^+ fragments for longer times is shown in red. The dotted green line shows the fitted simulation for the H^+ fragment. **c** Simulated 3D degree of alignment, characterized through the single-scalar metric $\langle\cos^2\delta\rangle$, see text/SI for details. Note the peak after truncation reaching $\langle\cos^2\delta\rangle = 0.89$ at $t = 3.3$ ps.

Following the kick at the end of the alignment pulse, the degree of alignment increased slightly to $\langle\cos^2\theta_{2D}\rangle^{exp}_{H^+} = 0.75$ before monotonically decreasing over ∼10 ps towards $\langle\cos^2\theta_{2D}\rangle^{exp}_{H^+} = 0.62$, slightly higher than the value $\langle\cos^2\theta_{2D}\rangle^{exp}_{H^+} = 0.6$ observed without alignment laser, i. e., due to the geometric alignment from an isotropic distribution. At a delay of 3.3 ps the intensity of the alignment pulse decreased to the noise level, below 1 % of its maximum, and the "field-free" region begins. At this delay the degree of alignment was $\langle\cos^2\theta_{2D}\rangle^{exp}_{H^+} = 0.75$, which is even larger than the alignment measured just before the kick, confirming that the planar alignment in the field-free region is even better than for an adiabatic alignment pulse [103].

All other fragments showed similar dynamics to the H^+ fragment, with the measured degrees of alignment larger for the C^{++} fragment and lower for the $HNCH^+$ fragment. The difference in the measured alignment between the fragments was attributed to non-axial recoil or to the geometry of Coulomb explosion fragmentation, i. e., the velocity vectors of the fragments in the molecular frame.

The angular distribution of the ionic fragments within the indole plane enabled full determination of the 3D alignment. By rotating the polarization ellipse of the alignment laser around the laser propagation axis, at a fixed delay, the laboratory axes to which the a and b axes of indole align, are commensurately rotated. In the laboratory frame, the transverse momenta of ionic fragments recoiling within the plane of indole will depend on the rotation angle. By counting only those fragments impinging at the centre of the detector, within a small radius r, the distribution of fragments within the plane can be determined [151]. In the 3D reconstruction of the tomography of H^+ fragments at $t = 3.3$ ps, shown in Figure 6.5 in the Supplementary Information, no fragments are observed at low momenta. Thus, the measured ion signal at the centre of the VMI can be related to the in-plane fragments recoiling along the detector normal. Angular scans of this "masked VMI" measurements are shown in Figure 6.3 for H^+ and C^{++} fragments, integrated over $r = 20$ pixel, as a function of the angle α between the Z laboratory axis and the laser's major polarization axis. For both fragments, there is a clear angle-dependent structure on top of a significant isotropic background. C^{++} ions show two smaller peaks at $\alpha \approx \pm 30\,^\circ$ and a much stronger peak at $\alpha \approx 88\,^\circ$. The H^+ signal shows a peak at $\alpha \approx 88\,^\circ$, similar to C^{++}, and a smaller peak at $\alpha \approx 0\,^\circ$. At $90\,^\circ$ the alignment laser's major polarization axis pointed towards the detector. Since the radius of $r = 20$ pixel on the detector was chosen to be significantly smaller than any measured feature in the angular distribution, the width of the peaks at $88\,^\circ$ are related to the non-axial in-plane recoil of the fragments. Considering only the major peaks, centered around $88\,^\circ$ in Figure 6.3, we observed in-plane degrees of alignment of $\langle\cos^2\alpha\rangle^{exp}_{H^+} = 0.82$ and $\langle\cos^2\alpha\rangle^{exp}_{C^{++}} = 0.88$.

Experimentally, all ions with a given mass to charge ratio potentially contributed to the measured 2D momentum distributions, regardless of their origin and velocity vectors within the neutral indole molecule as it is multiply ionized and undergoes Coulomb explosion. There are seven sites from which the H^+ fragments originate and eight sites from which the C^{++} fragments originate. The positions and the labelling of the hydrogen atoms in indole is shown in Figure 6.1 a. Each site will result in a different momentum

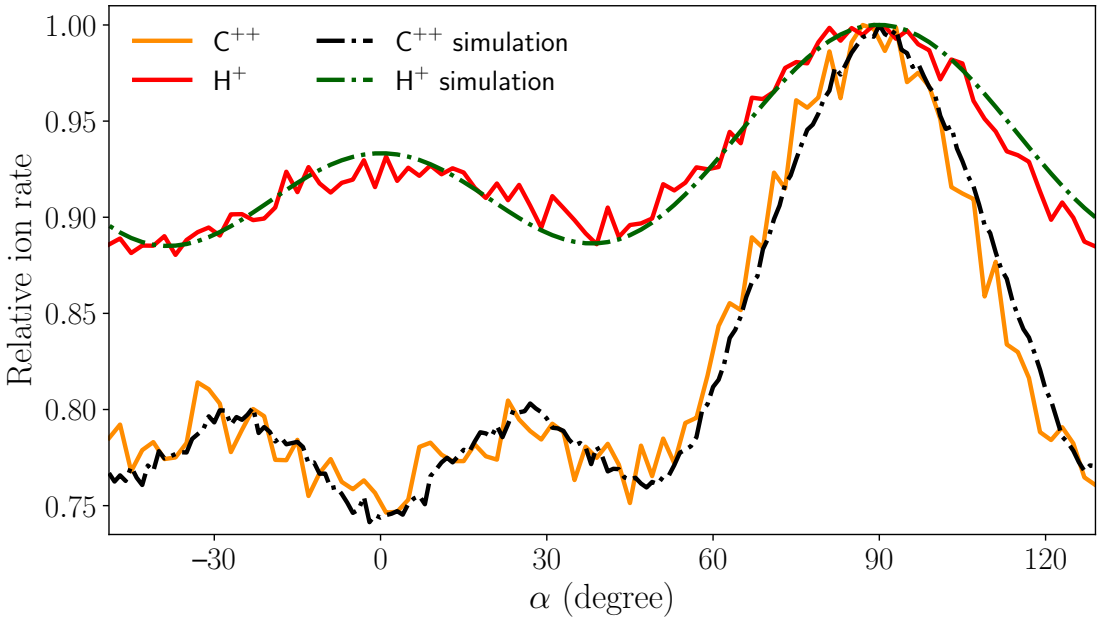

Figure 6.3.: Measured masked-VMI ion count rates of H^+ and C^{++} fragments as the major axis of the alignment laser's polarization ellipse is rotated; see text for details. Solid lines indicate measured values, the dashed lines are simulations based on fitted atomic-ion contributions, see text for details.

and recoil axis of the ionic fragment with the total measured experimental distribution being the sum of all of these.

In order to quantify the 3D degree of alignment, the rotational dynamics of indole was simulated using RichMol [158], yielding time-dependent laboratory-frame 3D angular probability distributions of the molecule for all delay times. Rotational-probability-density distributions were computed for all seven hydrogen atoms and the eight carbon atoms of indole individually. Coulomb explosion of indole was modelled by assuming axial recoil of the hydrogen ions along the C-H and N-H bond vectors, whereas for carbon the vectors connecting the center of mass with each carbon atom were chosen as recoil axes. For direct comparison between experiments and simulations, 2D projections of the rotational probability densities onto the labory YZ plane were carried out using a Monte-Carlo sampling routine. From these computed 2D momentum distributions, the time-evolution of $\langle\cos^2\theta_{2D}\rangle^{sim}_{H^+}$ was retrieved for all hydrogen atoms, choosing the same radial cuts that were used to retrieve the experimental $\langle\cos^2\theta_{2D}\rangle^{exp}_{H^+}$. For the comparison with the angle-dependent masked VMI measurements for H^+ and C^{++}, the rotational probability density at $t = 3.3$ ps was rotated in steps of 1° around the laboratory Y-axis. At each angle, 2D projected momentum distributions were computed for all hydrogen and carbon atoms, and the signal within $r = 20$ pixel of the centre was integrated.

Finally, for comparison with the measurements, a least-squares fitting procedure was employed. The contribution of individual hydrogen ions were determined by simultaneously fitting the alignment revival trace and the angle-dependent masked VMI measurements. An eighth fit parameter was included to take account of non-axial recoil

within the indole plane. The parameter was the width of a single Gaussian with which the angular distributions were convoluted. Without this additional parameter, the fitted masked VMI yields did not satisfactorily reproduce the data. Non-axial recoil might arise from many body fragmentation and also a time-dependent charge distribution on the remains of the parent ion during the Coulomb explosion process, driven by the circularly polarized Coulomb explosion pulse [253, 254]. Both of these processes result in spatially extended and time-dependent charge distributions within the indole plane from which the fragments are repelled. Intensity-dependent measurements of ionic fragments, when varying the energy of the Coulomb explosion laser (not shown), suggest H^+ ions were only produced when 4 electrons were removed from indole. On the contrary, for the fit of the C^{++} angular distributions, the axial recoil approximation yielded excellent agreement between the experiment and the simulation, and no convolution to model non-axial recoil was required. The resulting fit of the alignment revival trace of H^+ is shown in Figure 6.2 and the resulting fits of the angular distributions of H^+ and C^{++} are shown in Figure 6.3. The computed weights for the hydrogen and carbon atoms and more details about the simulations are given in the Supplementary Information.

The excellent agreement between the experiment and our simulations provides the required confidence to extract the 'real' 3D degree of alignment of the polarizability frame of indole with $\alpha_{z_I} > \alpha_{y_I} > \alpha_{x_I}$ with respect to the laboratory-fixed frame XYZ from our simulations. The planar alignment was quantified to be ∼0.84 at $t = 3.3$ ps, described by the two expectation values $\langle\cos^2\theta_{Y y_I}\rangle = 0.85$ and $\langle\cos^2\theta_{X x_I}\rangle = 0.83$. These values are higher than the measured degree of alignment, which is due to non-axial recoil of the H^+ fragments and different recoil axes that contribute to the measured ion-momentum distributions. A computed in-plane alignment of $\langle\cos^2\theta_{Z z_I}\rangle = 0.88$ was obtained, in agreement with the experimentally determined $\langle\cos^2\alpha\rangle^{\mathrm{exp}}_{C^{++}} = 0.88$ from the angular distribution of C^{++} in Figure 6.3. The simulated time-dependent alignment revivals, characterizing the 3D degree of alignment, can be found in the Supplementary Information. A single scalar metric [137], describing the overall degree of 3D alignment and defined by $\cos^2\delta = \frac{1}{4}(1 + \cos^2\theta_{Z z_I} + \cos^2\theta_{Y y_I} + \cos^2\theta_{X x_I})$, is shown in Figure 6.2 c. A maximum field-free alignment of $\langle\cos^2\delta\rangle = 0.89$ was achieved.

The degree of field-free alignment demonstrated in our experiment is comparable to or even larger than the degree of alignment achieved in typical experiments employing adiabatic alignment for asymmetric top molecules [68, 88]. The achieved degree of alignment is, however, limited by the number of initially populated states in the molecular beam [62, 68] and the finite truncation time of ∼3 ps of the alignment laser field [247]. Improving the fall-off time of the field and the creation of colder molecular beams with a narrower initial state distribution could lead to an even higher degree of field-free alignment.

6.4. Conclusions

We demonstrated strong laser field-free 3D alignment of the asymmetric top molecule indole induced by a shaped truncated quasi-adiabatic laser pulse. The strongly-chirped broad-band alignment laser pulse was amplitude and phase controlled by an SLM, resulting in a truncation time far superior to truncation by amplitude shaping alone. The combination of quasi-adiabatic alignment with a kick at the end of the pulse, followed by a sudden truncation, yielded a higher degree of field-free alignment compared to the alignment in the field. The full 3D alignment of indole was determined through measurements of the planar alignment, given by the time-dependent alignment revival trace of the H^+ fragment, and the in-plane alignment, characterized through the angular distributions of H^+ and C^{++} fragments, obtained by rotating the molecular plane with respect to the detector and integrating the signal at the center of the detector. Our model of the Coulomb explosion of indole allowed to reproduce the experimental measurements, where in the case of hydrogen non-axial recoil had to be taken into account. The excellent agreement between the experiment and the simulations shows that the real degree of alignment is much higher compared to the experimentally measured value. The real degree of field-free alignment was characterized to be $\langle\cos^2\theta_{Zz_I}\rangle = 0.88$, describing the confinement within the indole plane, and $\langle\cos^2\theta_{Yy_I}\rangle = 0.85$ and $\langle\cos^2\theta_{Xx_I}\rangle = 0.83$, describing the angular confinement of the indole plane with respect to the polarization plane of the alignment laser.

The demonstration of strong field-free alignment for an asymmetric top rotor without rotational symmetries and heavy leaving groups pave the way for strong field-free alignment of general (bio)molecules. This opens up new prospects for probing native (bio)molecules without chemically attaching heavy marker atoms, e. g., halogen atoms, which also significantly influence their properties and function.

6.5. Supplementary Information

6.5.1. Fragments of Indole Showing Alignment

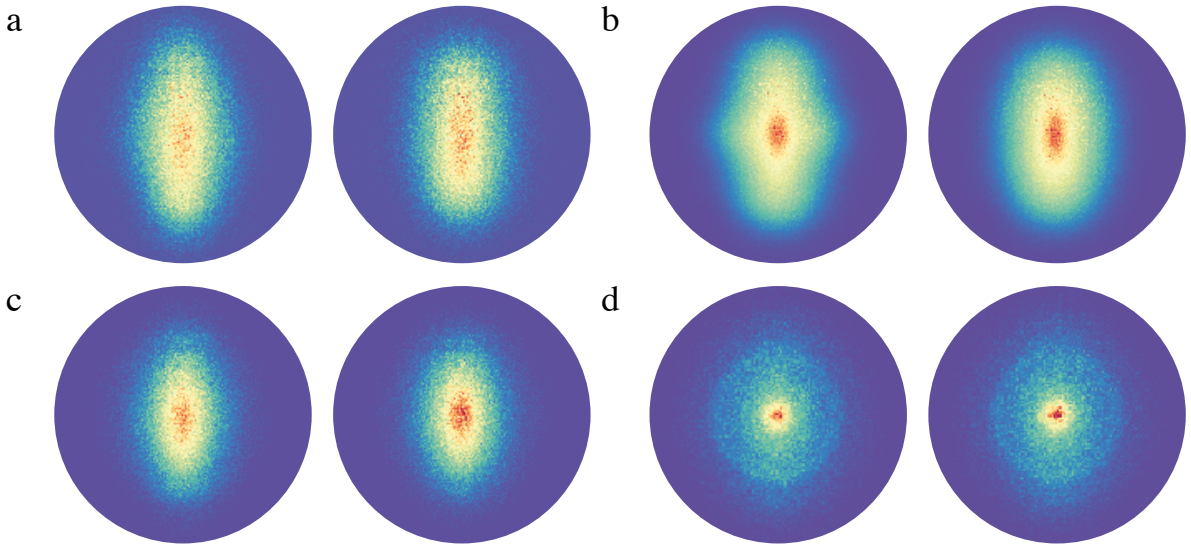

Figure 6.4.: VMI images of different fragments showing alignment. Left side are with major axis of alignment laser polarization parallel to detector surface and vertical, right side are with minor axis of alignment laser polarization parallel to detector surface and vertical. **a** C_2^+, **b** C^+, **c** $C_3H_x^+$, **d** $C_4H_x^+$.

In Figure 6.1 in the main text, ion-momentum distributions for the H^+, C^{++} and $HNCH^+$ fragments were shown at a delay time of $t = 3.3\,\text{ps}$, corresponding to the highest observed field-free alignment. In Figure 6.4, as in Figure 6.1, ion-momentum distributions are shown at peak aligment at a delay time of $t = 3.3\,\text{ps}$ for the fragments C_2^+, C^+, $C_3H_x^+$ and $C_4H_x^+$, which were not shown in the main text. In analogy with Figure 6.1, the images in the left column show the ion-momentum distributions with the major polarization axis of the alignment laser being parallel and the minor polarization axis being perpendicular to the detector plane, whereas in the right column the major polarization axis is perpendicular and the minor polarization axis is parallel to the detector plane.

6.5.2. 3D Tomographic Reconstruction of H^+ Momentum Distribution

In Figure 6.5, isosurfaces of the 3D momentum distribution of H^+, obtained from a tomographic reconstruction of the individual 2D projections, which were used for Figure 6.3 in the main text, are shown for three different orientations of indole. In Figure 6.5 a, the plane spanned by the a and b axes is shown, in Figure 6.5 b, the plane spanned by the a and c axes is shown, and in Figure 6.5 c, the plane spanned by the b and c axes is shown. Due to the presence of the 2 kV dc field in the VMIS, minor orientation effects were observed. For the $HNCH^+$ fragment, a degree of orientation $\langle\cos\theta_{2D}\rangle$ ranging from

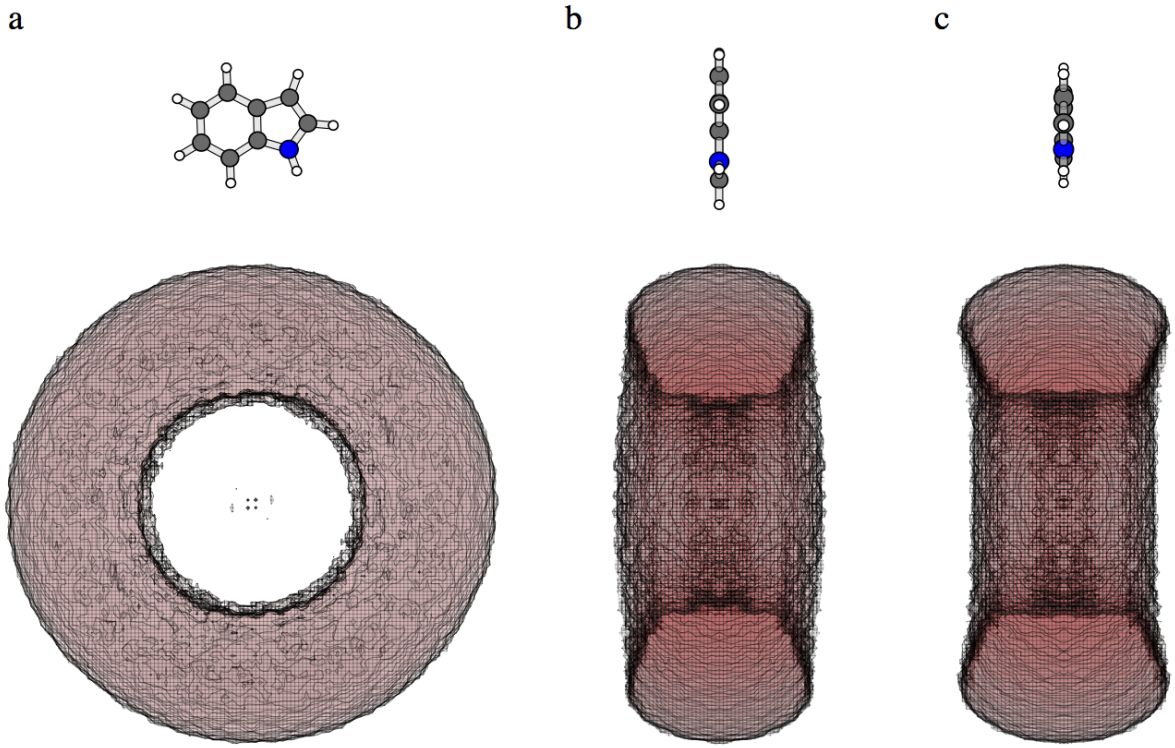

Figure 6.5.: Reconstructed isosurfaces from H^+ ion-tomography shown for three different orientations of the molecule with **a** a-b axes in plane **b** c-a axes in plane **c** c-b axes in plane. The orientation of indole is indicated by the ball-and-stick model of the indole molecule.

-0.05 to 0.05 was measured when the laser polarization was rotated by 90 °. The 2D ion-momentum distributions of H^+ were thus symmetrized prior to the 3D reconstruction, such that the 3D momentum distributions in Figure 6.5 represent the average over the four degenerate orientations of indole, which are related via rotations of 180 ° around the a and b axes.

6.5.3. Simulations

The field-free rotational motion of indole was modelled using the rigid-rotor Hamiltonian with rotational constants (in MHz) $A = 3877.9$, $B = 1636.1$, and $C = 1150.9$ [255]. The electric polarizability tensor for the equilibrium molecular geometry was computed *ab initio* at the CCSD/aug-cc-pVTZ [256, 257] level of theory in the frozen core approximation. Electronic structure calculations employed the quantum chemistry package Dalton [258].

Time-dependent quantum dynamics simulations used the computer program Rich-Mol [158], which is a general purpose code designed for quantum mechanical modelling of molecule-field interactions. In the simulations, the time-dependent wavefunction was built from a superposition of field-free eigenstates and the time-dependent coefficients were obtained by numerically solving the time-dependent Schrödinger equation (TDSE). The latter was solved using the iterative approximation based on Krylov subspace methods, as implemented in the Expokit computational library [160]. The elliptically polarized

alignment laser field was modelled by the function

$$E(t) = E_0(t)\{\mathbf{e}_x \cos(\omega t)/\sqrt{3}, \mathbf{e}_z \sin(\omega t)\}, \tag{6.1}$$

where $E_0(t)$ is the electric field amplitude, computed from the measured experimental peak intensity, and the carrier frequency was fixed to $\omega = c/(2\pi \cdot 800\ \text{nm})$. The time-dependent wavefunction was expressed in the basis of field-free rotational eigenstates of indole, where all rotational states with $J \leq 30$ were included. The time step used for wavefunction propagation was fixed and set to 10 fs. Convergence with respect to the size of the rotational basis set and the time step size have been carefully verified. Since alignment depends nonlinearly on the laser intensity, which is not constant within the focused volume, we have integrated all simulated observables over the interaction volume. This has been approximated by repeating the calculations for five individual laser amplitudes, obtained by scaling the originally measured peak intensity $I(t)$ with factors 0.2, 0.4, 0.6, 0.8, and 1.0. The focal volume averaging was carried out using the measured Gaussian beam profiles with widths (FWHM) of $\sigma_{\text{align}} = 60\,\mu\text{m}$ and $\sigma_{\text{probe}} = 24\,\mu\text{m}$.

In order to characterize the degree of alignment, measured in the experiment, we computed the rotational probability-density distributions for all hydrogen and carbon atoms in the molecule. The evaluations of the rotational-density functions required calculation of the Wigner rotation matrices, which were carried out using the Fourier-series based algorithm developed in [259]. For different time delays, two-dimensional projections of the rotational probability density onto the YZ laboratory plane were computed for each atom individually, assuming the recoil along the molecular bond axis. Other recoil axes, such as along the atomic position vector from the center of mass or the center of charge, have been experimented with, which all gave essentially similar results. The 2D projections yielded simulated momentum distributions for all hydrogen atoms, from which the $\langle\cos^2\theta_{\text{2D}}\rangle$ was extracted just the same as from the experimental momentum distributions. Furthermore, by rotating the simulated rotational probability-density around the laboratory Y-axis in steps of 1 ° and carrying out the 2D projection for each rotation angle, the tomography measurements were mimicked. The signal within a radius of 20 pixel was integrated for each angle and for every hydrogen and carbon atom. Finally, in the case of hydrogen the weighted simulated alignment traces and the angle-dependent integrated probability density from the center of the detector were simultaneously fitted to experiment employing least squares fitting. The resulting time-dependent alignment revival fit is shown in Figure 6.2 b in the main text and the angle-dependent masked VMI fit is shown in Figure 6.3 in the main text. For carbon only the angle-dependent masked VMI simulation was fitted to the experimental data, shown in Figure 6.3 in the main text.

The fitting procedures yielded weights representing the contribution of all individual hydrogen and carbon atoms to the measured ion-momentum distributions. Due to the structure of indole, Hydrogen atoms that have near similar angles (e. g., H_4 and H_7, see Figure 6.1 a) with respect to the z_I axis of indole, result in revivals and angle-dependent masked VMI distributions that are indistinguishable from each other in this experiment.

The total probabilities for near similar Hydrogens were thus summed and calculated to be H_1+H_3 $\sim$ 0.07, H_2 $\sim$ 0.21, H_4+H_7 $\sim$ 0.42, H_5+H_6 $\sim$ 0.30 with $\chi^2_{\text{min}} \sim 0.06$. For carbon the same procedure yielded C_2 $\sim$ 0.07, C_3 $\sim$ 0.34, C_{3a}+C_{7a} $\sim$ 0.41, C_4+C_7 $\sim$ 0.06 and C_5+C_6 $\sim$ 0.12 with $\chi^2_{\text{min}} \sim 0.017$. The nomenclature for the carbon atoms in indole is the same as for hydrogen, where C_i is the carbon atom bound to hydrogen H_i. The two carbon atoms connecting the five- and the six-membered rings are labelled C_{3a} and C_{7a}. An error estimation from the χ^2 least-squares fitting procedure, employing the variance-covariance matrix, yielded error estimates on the order of approximately ± 0.02 for the summed weights.

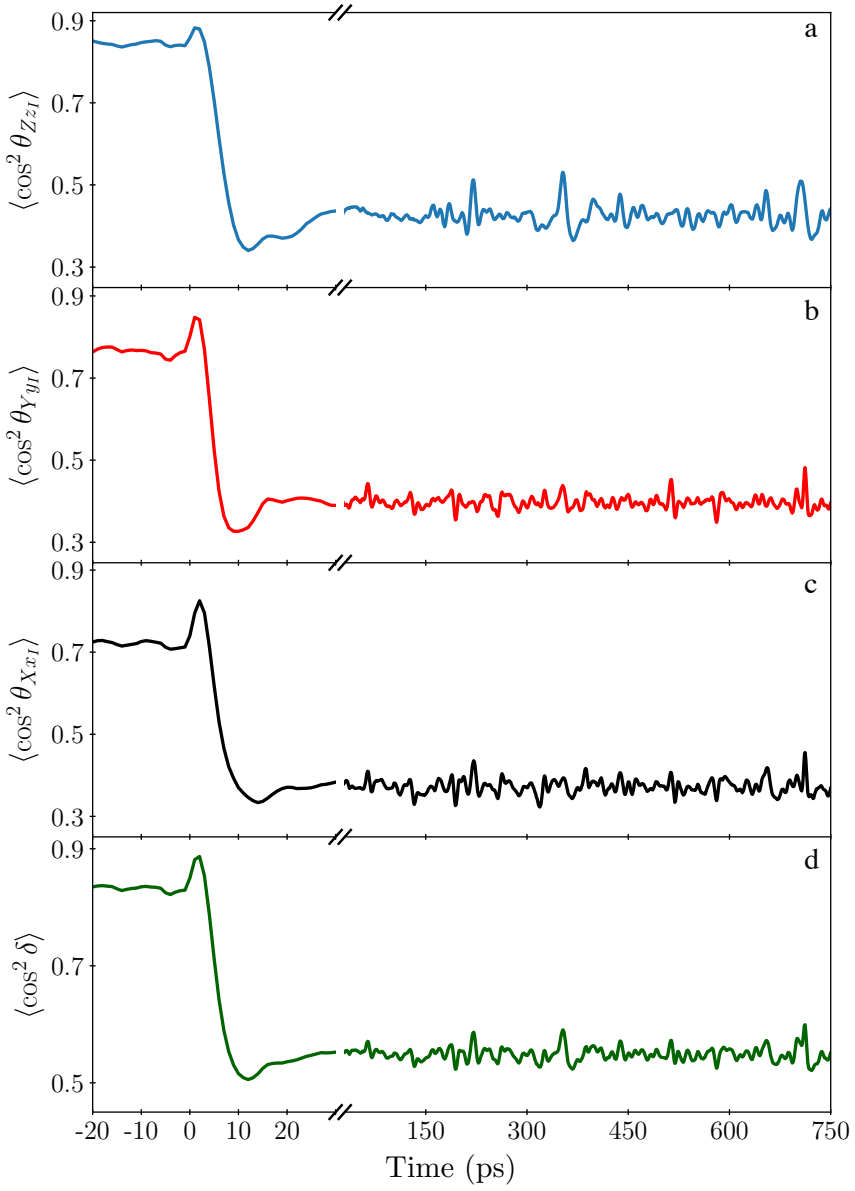

Figure 6.6.: Simulated 3D degree of alignment characterised through the expectation values **a** $\langle\cos^2\theta_{Zz_I}\rangle$, **b** $\langle\cos^2\theta_{Yy_I}\rangle$, **c** $\langle\cos^2\theta_{Xx_I}\rangle$ and **d** $\langle\cos^2\delta\rangle$ with the cartesian principal axes of the polarisability tensor frame z_I, y_I, x_I, the cartesian axes of the laboratory-fixed frame X, Y, Z and $\cos^2\delta = \frac{1}{4}(1 + \cos^2\theta_{Zz_I} + \cos^2\theta_{Yy_I} + \cos^2\theta_{Xx_I})$ a single scalar metric to characterise 3D alignment [137].

The expectation values of the alignment cosines were computed for the three main polarizability axes in the principle-axis polarizability frame with respect to the laboratory-fixed frame by employing Monte-Carlo integration, converged to better than 10^{-3} using $\sim 10^5$ sampling points. The simulated degree of alignment for the main polarizability axes of the molecule $\alpha_{z_I} > \alpha_{y_I} > \alpha_{x_I}$ with respect to the laboratory axes XYZ is shown in Figure 6.6. The highest achieved 3D degree of alignment is thus characterized to be $\langle\cos^2\theta_{Zz_I}\rangle = 0.88$, $\langle\cos^2\theta_{Yy_I}\rangle = 0.85$, $\langle\cos^2\theta_{Xx_I}\rangle = 0.83$ and $\langle\cos^2\delta\rangle = 0.89$, where $\cos^2\delta = \frac{1}{4}(1 + \cos^2\theta_{Zz_I} + \cos^2\theta_{Yy_I} + \cos^2\theta_{Xx_I})$.

Finally we note that rigid rotor calculations for indole (not shown) indicate that a fall-off time of at maximum $\leq$2 ps is required to obtain essentially identical dynamics to having an instantaneous fall-off. For this reason, the phase shaping using the SLM based shaper was necessary, instead of the more simple frequency filter used in [247], which would result in a 8 ps fall-off in the best case.

Calculations of the theoretically expected alignment pulse shape, taking into account SLM pixellation, SLM pixel gaps, the laser beam diameter, and the spectral spread at the Fourier plane, resulted in an expected laser intensity at times between $t = 4$ ps and $t = 10$ ps to be a factor of 70 lower than at the peak of the alignment pulse at $t = 0$ ps.

7 Atomic-Resolution Imaging of Carbonyl Sulfide by Laser-Induced Electron Diffraction[5]

7.1. Introduction

Probing the structure of small to medium-size molecules in the gas phase is a formidable challenge. Femtosecond x-ray diffractive-imaging experiments have been recently demonstrated at free-electron lasers (FELs) [14, 260] and first electron-diffraction experiments using relativistic electron beams have been performed [26, 27]. Alternatively, new laser-based approaches are being developed that make use of strong-field ionization with intense and ultrashort laser pulses. In a strong laser field, an electron can tunnel ionize near the peak of the oscillatory laser field and is then accelerated in the field. Depending on the ionization time within the laser period, the electron can be driven back by the laser field and elastically scatter from its parent ion [177]. The scattered electron is accelerated again in the laser field, reaching a very high kinetic energy. This process is responsible for the appearance of a recollision plateau in the photoelectron momentum distribution. Extracting the differential cross section (DCS) of the molecule from the angular distribution of these high-energy electrons allows to derive the molecular structure [36, 261].

Laser-induced electron diffraction (LIED) has been first applied in atoms [37, 38], in diatomic molecules [36, 39] and more recently in polyatomic molecular systems, such as acetylene [35], ethylene [41], and benzene [42]. To extract structural information from a LIED experiment, the returning electron wavepacket should have a de Broglie wavelength comparable to the bond lengths that occur in the molecule. This is typically achieved using a mid-infrared laser field, as the ponderomotive energy $U_p/\mathrm{eV} = 9.33\, I/(10^{14}\ \mathrm{W/cm^2})\, \lambda^2/\mu\mathrm{m}^2$ scales quadratically with the laser wavelength.

While coupled rotational-electronic wavepacket dynamics in NO [242] and ultrafast bond breaking in acetylene dications in the presence of the strong ionizing laser field [43] have been recently characterized by LIED, the suitability of this technique for retrieving transient molecular structures following photoexcitation has yet to be demonstrated. In this context, carbonyl sulfide (OCS) is a particularly interesting system. Photoexcitation of ground-state OCS ($X^1\Sigma$) in the (220–250 nm) UV wavelength range has been intensively

[5] This chapter is based on the publication: *Atomic-resolution imaging of carbonyl sulfide by laser-induced electron diffraction*, Evangelos T. Karamatskos, Gildas Goldsztejn, Sebastian Raabe, Philipp Stammer, Terry Mullins, Andrea Trabattoni, Rasmus R. Johansen, Henrik Stapelfeldt, Sebastian Trippel, Marc J.J. Vrakking, Jochen Küpper and Arnaud Rouzée, *The Journal of Chemical Physics* **150**, 244301 (2019), *arXiv*:1905.03541. I contributed to setting up the experiment and recording the data. I analyzed the data, performed the simulations and I contributed to writing the manuscript.

investigated [262–264] and is known to be dominated by a transition to the A' state, leading to fragmentation of the molecules predominantly into $CO(X\,^1\Sigma^+) + S(^1D_2)$ [262]. Non-adiabatic coupling along the bending coordinate is responsible for the formation of low-speed $S(^1D_2)$ fragments [263] and the production of rotationally excited CO fragments [264]. Therefore, OCS can serve as a benchmark to test the suitability of the LIED method for recording molecular movies of molecular dynamics, in this case imaging of molecular dissociation involving bending motion.

Interestingly, strong-field ionization of OCS, performed with 800 nm radiation and intensities above $10^{15}\,W/cm^2$, showed evidence for a bending deformation of the molecule during Coulomb explosion [265]. This suggests that the molecular geometry can substantially change both during and after ionization, with a large impact on the retrieval of the molecular structure in a LIED experiment. Therefore, it is important to test the ability of the LIED technique to image the structure of the OCS molecule in its equilibrium geometry before performing any dynamical investigation.

Here, we present a LIED measurement on OCS molecules, photoionized by strong 2 µm wavelength laser pulses. Different from previous investigations [35, 36, 43], the experiment was performed using a velocity map imaging spectrometer (VMIS) [124] that allowed the detection of all electrons with kinetic energies up to 500 eV. Our new experimental apparatus was benchmarked by strong-field ionization experiments on argon and krypton. DCSs extracted from measured photoelectron angular distributions for a recolliding electron energy of 100 eV were compared to results from partial-wave calculations for scattering of electrons by atoms performed using the Elsepa package [266], and agree very well. The same procedure was applied to the experimental data for OCS. Fitting the calculated DCS to the experimental one with the O-C and C-S bond lengths and the ∠(O-C-S) bending angle as adjustable parameters, we were able to confirm the linear structure and were able to extract the internuclear distances of the molecule to a precision better than 4 pm. Our experimentally determined values agree very well with reported bond lengths of the OCS molecule [267] and suggest that accurate structures can be retrieved for OCS using the LIED technique.

7.2. Experimental Setup

The experiments were performed using 2 µm radiation pulses, obtained from an optical parametric amplifier pumped by 800 nm laser pulses from a commercial amplifier system, delivering 30 mJ, 38 fs(full width at half maximum, FWHM) pulses at a repetition rate of 1 kHz. The linearly polarized 2 µm laser pulses were focused into a beam of nearly pure ground-state OCS molecules at the center of a high-energy velocity map imaging spectrometer (VMIS) using a CaF_2 lens with a 25 cm focal length, see Figure 7.1. The laser polarization axis was aligned in the plane of the detector, corresponding to the vertical axis in all images presented, *vide infra*.

The molecular beam was formed by supersonic expansion of a mixture of OCS in helium with a mixing ratio 1/2000 and a constant pressure of 90 bar, using an Even-Lavie valve running at a repetition rate of 250 Hz. In the experiments performed on atoms, a

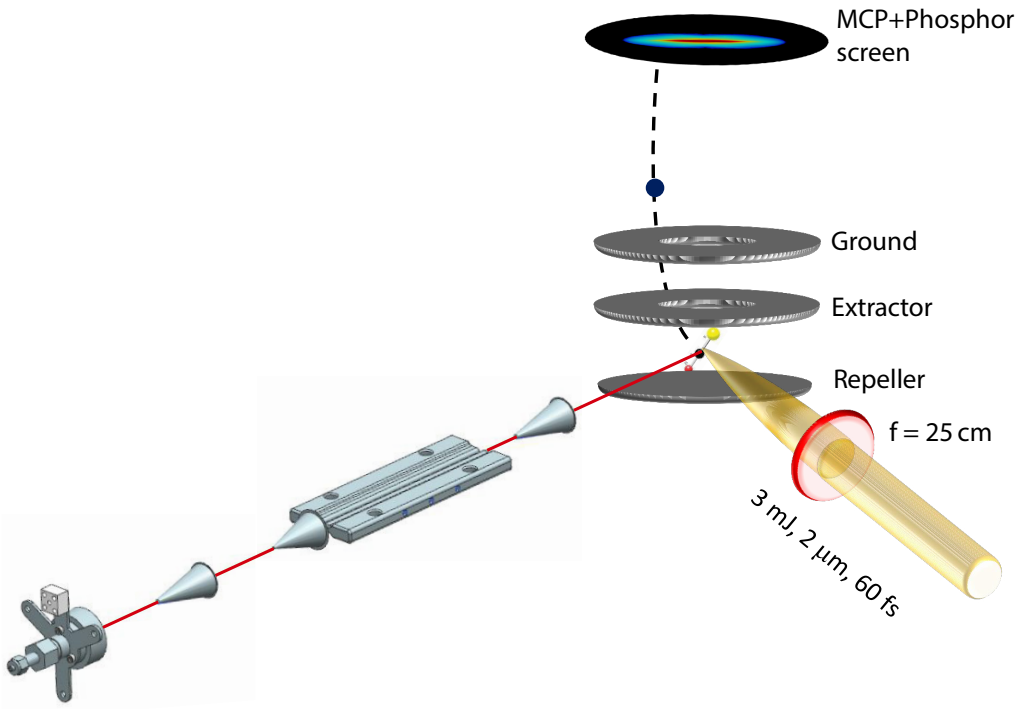

Figure 7.1.: Sketch of the experimental setup. 2 µm laser pulses are focused into a beam of state-selected OCS molecules at the center of a velocity map imaging spectrometer (VMIS). The molecular beam is formed by supersonic expansion of a dilute mixture of OCS in helium. A deflector and a skimmer are used to spatially separate the OCS molecules from the helium carrier gas. The photoelectrons are projected onto a multichannel-plate/phosphor-screen assembly and the resulting 2D electron momentum distribution is recorded with a CCD camera.

pure sample of either argon or krypton was expanded into vacuum, where the stagnation pressure was limited to 1 bar to avoid cluster formation. An electrostatic deflector [61] was operated at ±13.5 kV to spatially separate OCS molecules from the helium carrier gas [1]. We note that this device is ideally suited for quantum-state selection and the preparation of structurally pure samples, even of complex molecules [1, 130, 268]. Here, the deflection provided the sample of OCS molecules in their rotational ground-state [62, 246].

Photoelectrons from strong-field ionization (SFI) by the 2 µm laser pulses were accelerated into a 10 cm long field-free flight tube before being detected on a 77 mm diameter dual microchannel-plate/phosphor-screen assembly. The projected 2D electron momentum distributions were recorded using a CCD camera and inverted using an Abel-inversion procedure based on the BASEX algorithm [138] in order to yield 3D electron momentum distributions.

7.3. Results and Discussion

In order to validate our experimental methodology, experiments were first performed for pure samples of rare-gas atoms. Projected 2D electron momentum distributions recorded in argon and krypton and corresponding slices through their 3D momentum distributions

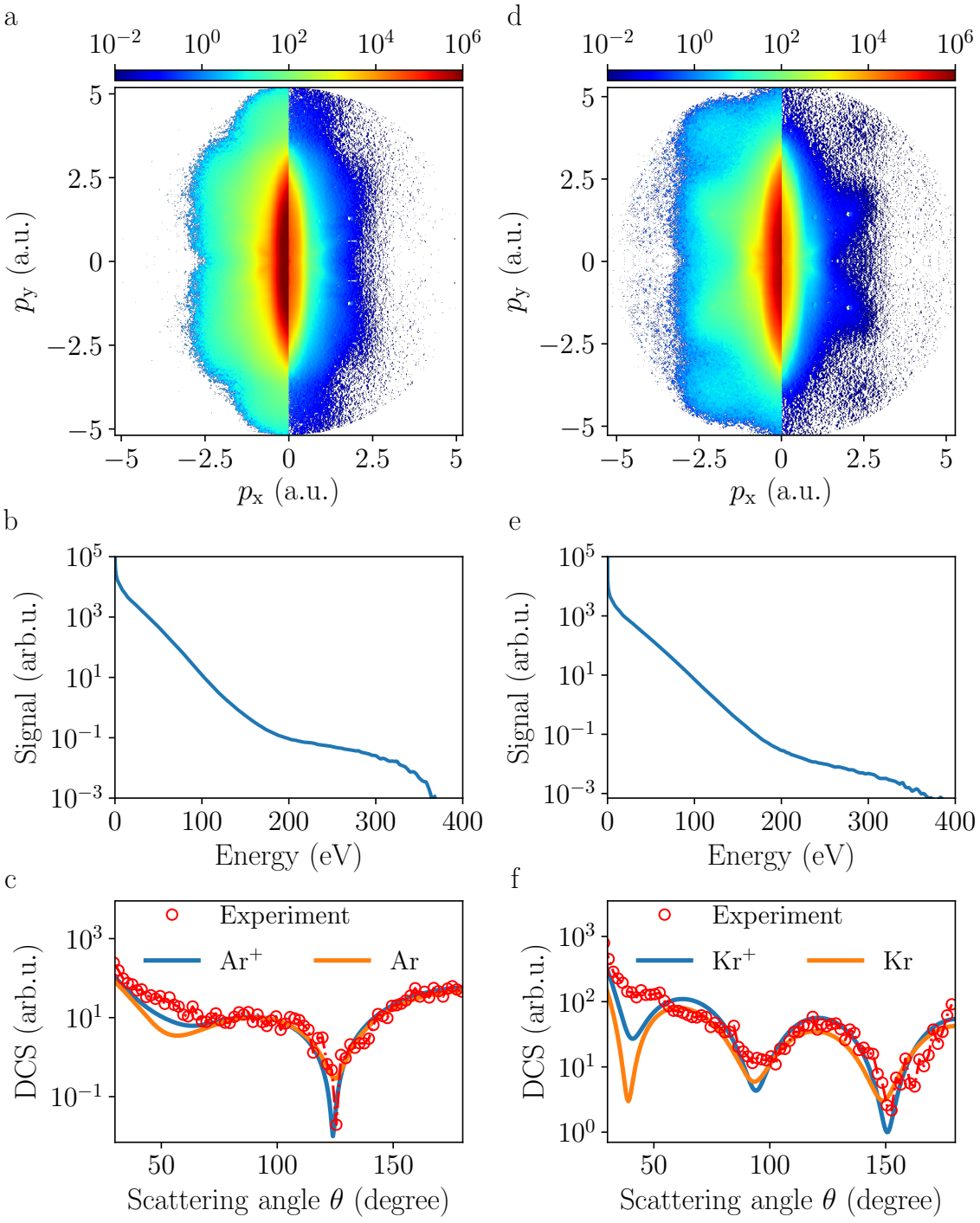

Figure 7.2.: Projected 2D electron momentum distribution (left) and slice through the 3D electron momentum distribution obtained after Abel inversion (right) recorded for (a) argon and (d) krypton, ionized by intense 2 µm laser pulses. (b, e) Corresponding photoelectron kinetic energy spectra. (c, f) Field-free differential cross sections extracted from the angle-resolved photoelectron kinetic energy spectra (red dots) for electrons with a return energy of ∼100 eV. The DCS calculated using the Elsepa package is shown, for comparison, for a neutral atom (orange line) and a singly charged ion (blue line); see text for details.

are presented in Figure 7.2 a, d. The laser intensity was $\sim 1 \times 10^{14}\,\mathrm{W/cm^2}$, which corresponds to a Keldysh parameter of $\gamma = \sqrt{I_\mathrm{p}/2\,\mathrm{U_p}} \approx 0.38$, with the ponderomotive energy $\mathrm{U_p} = 37.3\,\mathrm{eV}$, and I_p =11.2 eV the ionization potential, indicating that the experiment was performed deep into the tunneling regime. The angle-resolved photoelectron spectra were averaged over 10^6 laser shots. To account for rest gas, an image obtained without atomic beam was subtracted from the 2D electron momentum distributions prior to Abel inversion.

In a classical picture of the strong-field ionization [177], electrons that have experienced a single recollision with the parent ion can reach a maximum kinetic energy of $10\,\mathrm{U_p}$, whereas electrons that do not further interact with the parent ion – commonly called "direct electrons" – can have a maximum kinetic energy of $2\,\mathrm{U_p}$. In our measurement, the direct electron yield is five to six orders of magnitude larger than the contribution from rescattered electrons, see Figure 7.2. For argon and krypton, the photoelectron spectra observed experimentally extend to a kinetic energy close to 400 eV.

Field-free DCSs of argon and krypton were extracted from our measurements following a procedure given by the quantitative rescattering theory [180, 269]. The high-energy rescattered photoelectron momentum distribution $D(k, \theta)$ is expressed as the product of the momentum distribution $W(k_r)$ of the returning electron (with k_r the momentum at the instant of recollision) and the DCS $\sigma(k_r, \theta_r)$, with θ_r the scattering angle. The relationship between the measured electron momentum k and k_r is obtained by considering that the scattered electrons gain an additional momentum after the recollision, which is given by the vector potential $-A(t_r)$ at the time of recollision t_r:

$$k_y = k\cos\theta = -A(t_r) + k_r\cos\theta_r \tag{7.1}$$

$$k_x = k\sin\theta = k_r\sin\theta_r \tag{7.2}$$

with y defined as the laser polarization axis. According to the classical equations of motion and neglecting the effect of the Coulomb potential on the electron trajectories, the maximum recollision electron momentum satisfies $k_r = 1.26A_0$, with A_0 the magnitude of the vector potential, corresponding to a maximum kinetic energy of $\sim 3.17\,\mathrm{U_p}$ which is equal to $\sim$118 eV for a wavelength of 2 µm and an intensity of $\sim 1 \times 10^{14}\,\mathrm{W/cm^2}$. The DCS $\sigma(k_r, \theta_r)$ for the highest recollision energy can, therefore, be extracted from the photoelectron angular distribution (PAD) by measuring the photoelectron yield on a circle with radius $k_r = 1.26A_0$ [37] and centered at $(k_x, k_y) = (0, \pm A(t_r))$. We note that this procedure yields the DCS weighted by the ionization yield.

Figure 7.2 c, f shows the field-free DCS extracted for argon and krypton using this method. The results were obtained using an integration range of $\Delta k_r \approx 0.05 k_r$ and an angular integration width of $\Delta\theta = 1°$. For krypton two pronounced minima at scattering angles of 94 ° and 151 ° are clearly observed. For argon, the DCS presents a strong dip near 124 ° and a broad minimum near 60 °. These results are in very good agreement with previous LIED experiments [38] as well as with conventional electron-scattering experiments using an external electron source [270, 271]. The DCS for both atoms compare also very well with theoretical calculations for field-free electron–atom collisions obtained using the Elsepa package [266] (shown as orange and blue curves

in Figure 7.2 c, f). In these calculations, the nuclear charge distribution was approximated by a point charge and the electron charge density of the atomic cation was evaluated from self-consistent Dirac-Fock calculations. Exchange and correlation-polarization potentials were neglected. The simulations were performed considering both a neutral and an ionic atomic target. We note that to achieve the best agreement with the experimental DCS, the magnitude of the vector potential and, therefore, the laser intensity used to extract the DCS from the PAD was fitted. Best agreement was found for intensities of $9.1 \times 10^{13}\,\mathrm{W/cm^2}$ and $8.3 \times 10^{13}\,\mathrm{W/cm^2}$, with corresponding return electron kinetic energies of 98 eV and 107 eV, for argon and krypton, respectively. These values are in close agreement with the estimated intensity based on the laser-pulse parameters used in these experiments. We attribute the difference observed between the two atomic targets to a small variation of the pulse energy between the two measurements. The comparison between the experimentally retrieved DCS and the simulated DCS, obtained for a neutral and an ionic atomic target shown in Figure 7.2 c, f, reveals that a better agreement is found when considering that the returning electron interacts with a singly charged atomic ion. Subsequently, we recorded the PAD resulting from SFI of OCS.

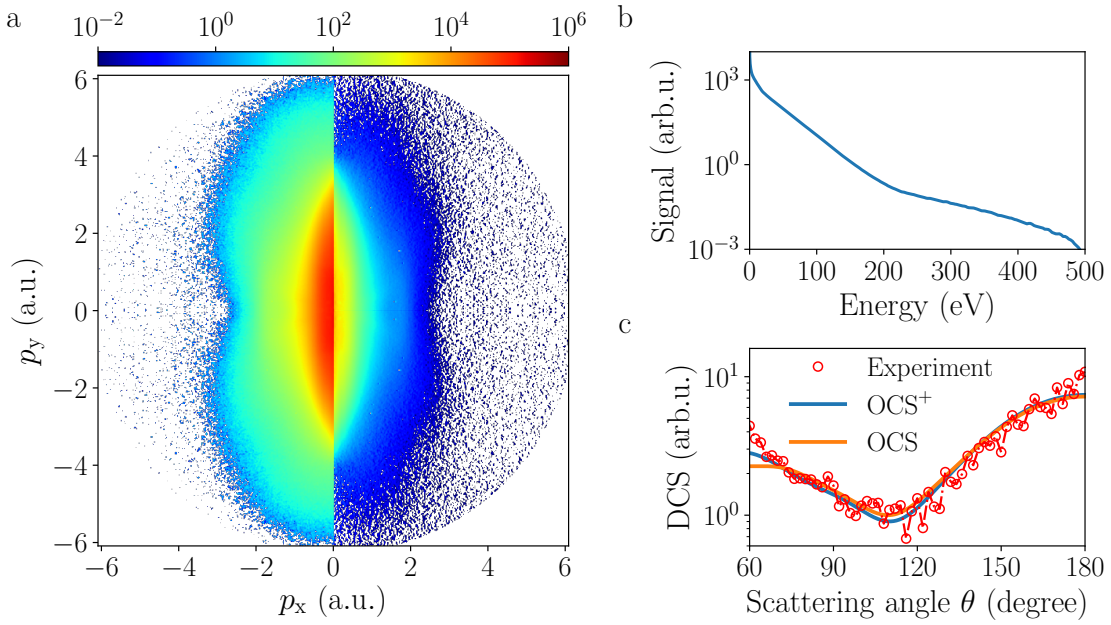

Figure 7.3.: a Projected 2D electron momentum distribution (left) and slice through the 3D electron momentum distribution obtained after Abel inversion (right) recorded in OCS ionized by an intense 2 µm laser pulse with a laser intensity of $\sim 1.3 \times 10^{14}\,\mathrm{W/cm^2}$. **b** Corresponding photoelectron kinetic energy spectra. **c** Field-free differential cross section extracted from the angle-resolved photoelectron kinetic energy spectra (dotted red line) for electrons with a return energy of ∼100 eV. The DCS calculated using the molecular Elsepa package that best fits the measurement is shown as well for neutral OCS (orange line) and for singly charged OCS^+, where the scattering amplitude of neutral sulfur was replaced by the corresponding ionic scattering amplitude (blue line).

Note that no laser alignment was used in the experiment, and hence the OCS molecules were randomly oriented prior to their interaction with the laser. The laser intensity was

adjusted to observe only the parent molecular ion in an ion time-of-flight measurement (fragmentation $< 1\%$) in order to minimize the influence of multiple ionization channels. The 2D momentum distribution recorded for OCS and its corresponding photoelectron kinetic-energy spectrum are shown in Figure 7.3 a, b. The kinetic energy spectrum extends to 480 eV, suggesting an intensity $\sim 1.3 \times 10^{14}\,\mathrm{W/cm^2}$, i. e., slightly higher than in the measurements for argon and krypton.

Similarly to the atomic case, the field-free DCS was retrieved from the PAD for a return electron energy of 100 eV and is shown in Figure 7.3 c. A broad minimum near 110 ° is observed, similar to previously reported electron-scattering experiments with 100 eV kinetic energy projectiles [272, 273]. The minimum observed at 110 ° is known to be dominated by the atomic form factor of the sulfur atom, smeared out by the molecular structure [272]. To extract the internuclear distances of OCS from our measurement, we applied a procedure that was first introduced in reference [36] to retrieve the internuclear distance of diatomic molecules from LIED measurements. For a fixed-in-space molecule, oriented at Euler angles Ω_L with respect to the laser polarization axis y, the PAD is written as:

$$D(k, \theta, \Omega_L) = W(k_r) N(\Omega_L) \sigma(k_r, \theta_r, \Omega_L), \tag{7.3}$$

with $N(\Omega_L)$ the angle-dependent ionization probability. For an isotropic molecular sample the measured signal is then given by:

$$I(k, \theta) = W(k_r) \int d\Omega_L N(\Omega_L) \sigma(k_r, \theta_r, \Omega_L). \tag{7.4}$$

Recent studies [274] have shown that the shape of molecular orbitals can leave its imprint on the recollision probability. Moreover, in molecular ionization, multiple orbitals can contribute to ionization [179, 275]. For OCS, the HOMO (IP=11.2 eV) and HOMO-1 (15.1 eV) orbitals are separated by $\sim$4 eV and the contribution of the HOMO-1 orbital to the ionization dynamics is expected to be negligible. Since randomly oriented molecules were used in the experiment, we assume that the influence of the shape of the molecular orbital from which the electron is emitted is washed out during the propagation of the electron wavepacket in the laser field. Using this assumption, the field-free DCS in (7.4) can be approximated by an independent-atom model (IAM) and expressed as:

$$\sigma(k_r, \theta_r, \Omega_L) = \sum_{i,j} f_i(\theta_r) f_j^*(\theta_r) e^{i\vec{q}\cdot\vec{R}_{ij}}, \tag{7.5}$$

with the momentum transfer $q = 2k_r \sin(\theta_r/2)$, the internuclear distances R_{ij} and the scattering amplitude $f_i(\theta_r)$ for atom i. The returning electron interacts with the molecular ion, which we modeled by a singly charged sulfur atom and neutral carbon and oxygen atoms. This is well justified as the removal of an electron from the HOMO of OCS is expected to lead to a molecular ion with a final charge mainly localized on the sulfur atom [209], see supplementary information for further details.

Combining the IAM with the QRS yields the following expression that was used for the analysis of our measurements:

$$I(k,\theta) = W(k_r)\left(\sum_i |f_i|^2 \int N(\Omega_L)d\Omega_L + \sum_{i\neq j} f_i f_j^* \int N(\Omega_L) e^{i\vec{q}\cdot\vec{R}_{ij}} d\Omega_L\right). \tag{7.6}$$

The first term corresponds to an incoherent sum over the scattering amplitudes I_{atom} of the individual atoms whereas the second term corresponds to a molecular interference term. Following the standard approach [36], we define the molecular contrast factor (MCF) γ_{MCF} as:

$$\gamma_{\text{MCF}} = \frac{I - I_{\text{atom}}}{I_{\text{atom}}} = \frac{\sum_{i\neq j} f_i f_j^* \int N(\Omega_L) e^{i\vec{q}\cdot\vec{R}_{ij}} d\Omega_L}{\sum_i |f_i|^2 \int N(\Omega_L) d\Omega_L}. \tag{7.7}$$

In order to extract bond lengths from our measurement, we have compared the MCF

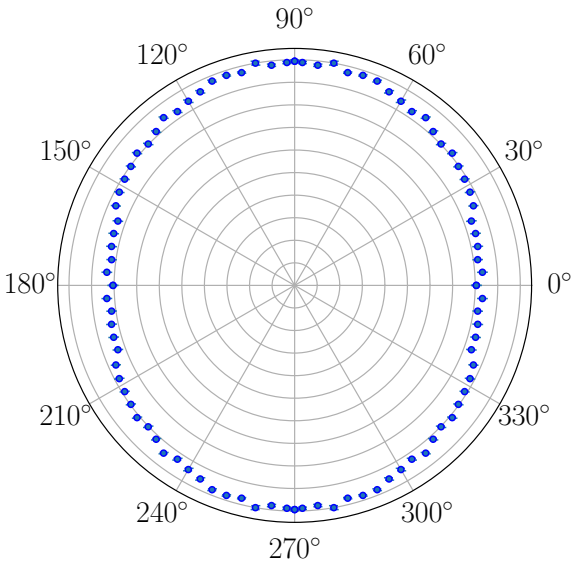

Figure 7.4.: Measured ionization rate from strong-field ionization of OCS by a linearly polarized 2 µm laser pulse with a laser intensity of $\sim 1.3 \times 10^{14}\,\text{W/cm}^2$ as a function of the angle between the internuclear axis and the laser polarization axis.

extracted experimentally with simulations using expression (7.7). The neutral atomic scattering factors were obtained using the Elsepa package [266]. To estimate the angle-dependent ionization probability $N(\Omega_L)$ necessary to calculate the MCF, the following experiment was performed. A sequence of two laser pulses, at a wavelength centered at 800 nm and with 255 fs pulse duration, were used to strongly align the molecule prior to the 2 µm laser pulse, see reference [246] for details. The angle-dependent ionization probability was then obtained experimentally by monitoring the ionization yield as a function of the angle between the molecular axis and the ionizing laser polarization, see Figure 7.4, and then used to calculate the MCF. Finally, the $R_{\text{O–C}}$ and $R_{\text{C–S}}$ bond distances were fitted in order to minimize the variance between experiment and theory

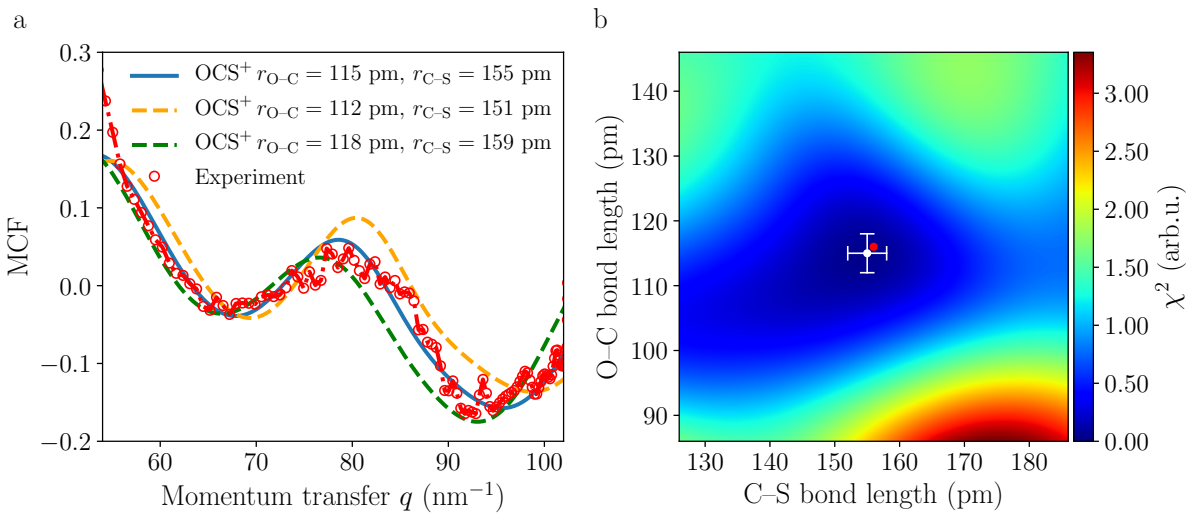

Figure 7.5.: a Comparison between the MCF extracted from the experiment (red open circles) and the calculated molecular contrast factor obtained for the best fit of the bond lengths (blue line). Dashed lines depict the expected behavior for bond lengths changed by $\pm\sigma$ (green and orange). **b** χ^2 map as a function of the bond lengths considering a linear configuration of the molecule. The minimum (white dot) corresponds to the best fit and the crossed bars depict the 1σ error; this result agrees very well with reference values for the internuclear distances of OCS (red dot).

using the following expression for the error:

$$\chi^2(\beta, R_{ij}) = (\gamma^{exp}_{\mathrm{MCF}} - \gamma^{th}_{\mathrm{MCF}})^2 = \left(\frac{\beta I_{\mathrm{exp}} - I_{\mathrm{th}}}{I_{\mathrm{atom}}}\right)^2, \tag{7.8}$$

with β a normalization constant, I_{exp} the DCS extracted from the measured photoelectron spectrum and I_{th} the DCS calculated using (7.6). The result from this procedure is shown in Figure 7.5. The best agreement is obtained for $R_{\mathrm{O\text{–}C}} = 115 \pm 3$ pm and $R_{\mathrm{C\text{–}S}} = 155 \pm 4$ pm. Even for the relatively low return electron energy of 100 eV, a precision of ± 4 pm is reached. These values are in very close agreement with the known values $R_{\mathrm{O\text{–}C}} = 116 \pm 2$ pm and $R_{\mathrm{C\text{–}S}} = 156 \pm 3$ pm obtained by microwave absorption spectroscopy [267], which are marked by the red dot in Figure 7.5 b.

As previously mentioned, we cannot *a priori* exclude a possible deformation of the molecule following its ionization by the intense laser field. If this deformation takes place on a timescale shorter than the duration between ionization and recollision, it would be observed in our experiment as a deformed, bent or stretched OCS geometry upon recollision. However, we did not observe any indication of stretching of the bond distances of the molecule, even when we performed an extended analysis of our measurement using the overall O–S distance as an additional fitting parameter. Best agreement was found for $R_{\mathrm{O\text{–}S}} = 270$ pm, with $R_{\mathrm{O\text{–}C}} = 114 \pm 4$ pm and $R_{\mathrm{C\text{–}S}} = 155 \pm 5$ pm, i. e., for the linear configuration of the molecule. This suggests that in our experiment, with intensity $\sim 1 \times 10^{14}$ W/cm^2 and wavelength 2 µm, corresponding to a laser period of 6.67 fs, the molecular structure remains essentially unchanged during the time interval between ionization to recollision. In this context we note that recent ab-initio calculations [276]

for laser pulses centered at 790 nm and an intensity of 1×10^{15} W/cm^2 have shown that the atomic distances and bending angle ∠(O-C-S) are changing on a timescale longer than 10 fs, i. e., longer than the optical period in our experiment.

7.4. Conclusions

We have recorded angle-resolved photoelectron spectra of argon, krypton and OCS, ionized by short laser pulses at 2 µm, with a high-energy VMIS. We extracted field-free differential electron rescattering cross sections at 100 eV, which are in excellent agreement with calculated DCSs for electron-atom and electron-molecule scattering. The geometry and bond distances of the OCS molecule were extracted from our measurement with a precision better than ±5 pm and in full agreement with the known structure of ground-state OCS.

It remains an open question to what extent the LIED technique can be used to retrieve multiple bond lengths and angles during molecular transformations, for instance following the photoexcitation of a molecule. Further investigations combining pump-probe schemes and LIED are ongoing to explore the possibility to use this technique to directly record a so-called "molecular movie" of these motions, in which the evolving structure is measured with femtosecond and picometer precision while the molecule is "in action".

7.5. Supplementary Information: Charge Distribution in the Independent-Atom Model

Structure retrieval in LIED experiments is typically achieved by employing the quantitative rescattering theory (QRS) [180, 269] combined with the independent-atom model (IAM) [2, 182]. Generally, the IAM is not well suited to incorporate scattering from singly charged cations, as in this model a molecule is described as a collection of independent atoms as the scattering centers for the incoming electron flux. However, the hole charge density is generally delocalized within the molecule, which cannot be described within the independent-atom model, where the substitution of neutral scattering amplitudes by the corresponding ones for singly charged ions leads to a strong localization of the hole charge density on one atomic site.

For OCS, it was shown that ionization from the HOMO of OCS leads to a molecular cation with ∼85 % of the hole charge density localized at the S atom [209]. Therefore, in the main text, the IAM model was applied by replacing the scattering amplitude of neutral sulfur by the corresponding ionic one. Here, for comparison, we provide the results obtained for a model in which OCS is either neutral or a singly charged ion with a final charge localized on the carbon or the oxygen sites. Except for neutral OCS, the other cases did not allow to retrieve the correct equilibrium geometry of OCS, confirming that the hole charge density of singly charged OCS is mostly localized at the sulfur site.

7.5.1. Neutral OCS

Figure 7.6 shows the results of the fitting procedure for neutral OCS, including only atomic scattering amplitudes of neutral oxygen, carbon, and sulfur. The experimental MCF fits the simulations only in the range $q = 60 \ldots 90$ nm^{-1} and a deviation for smaller and larger momentum transfer is observed. The fits were thus carried out only in this range of momentum transfer. Then, the best fit yielded values for the bond lengths of

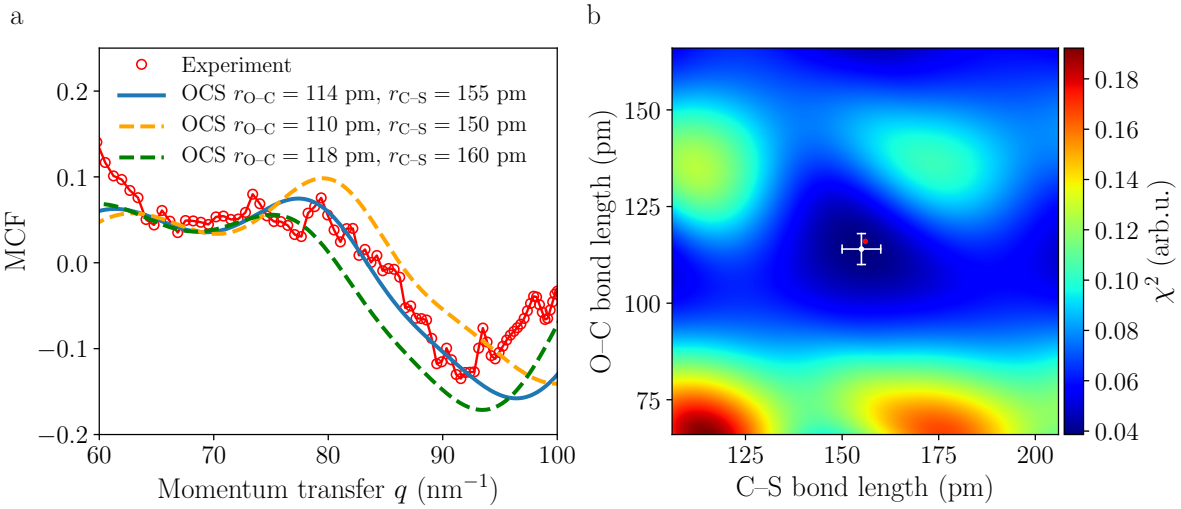

Figure 7.6.: Same as Figure 7.5 for the IAM model with neutral-atom scattering amplitudes for all atoms.

O–C $= 114 \pm 4$ pm and C–S $= 155 \pm 5$ pm with $\chi^2 = 0.0386$. While this provided bond lengths close to the known values [267], with this model the MCF is not well reproduced for low and large momentum transfers, whereas the cation model presented in the main text provides a robust overall description of the experimental data.

7.5.2. OCS^+ with the Charge Localized on O or C

The same procedure was applied for a molecular cation with the charge localized on the oxygen atom, see Figure 7.7 a, b, or on the carbon atom, see Figure 7.7 c, d. The best fits yielded values for the bond lengths of O–C $= 130 \pm 5$ pm and C–S $= 158 \pm 5$ pm for a charge localized on the oxygen atom with $\chi^2 = 0.1161$; and O–C $= 43 \pm 5$ pm and C–S $= 124 \pm 5$ pm for a charge localized on the carbon atom with $\chi^2 = 0.0595$. In these two cases, a large deviation from the known bond distances of OCS is retrieved from the fit, highlighting the relevance of an appropriate hole charge distribution in the analysis of LIED data. The best fit was obtained considering electron scattering from a molecular cation with a final charge localized on the sulfur atom, see Figure 7.5, yielding bond lengths of O–C $= 115 \pm 3$ pm and C–S $= 155 \pm 4$ pm with $\chi^2 = 0.0418$.

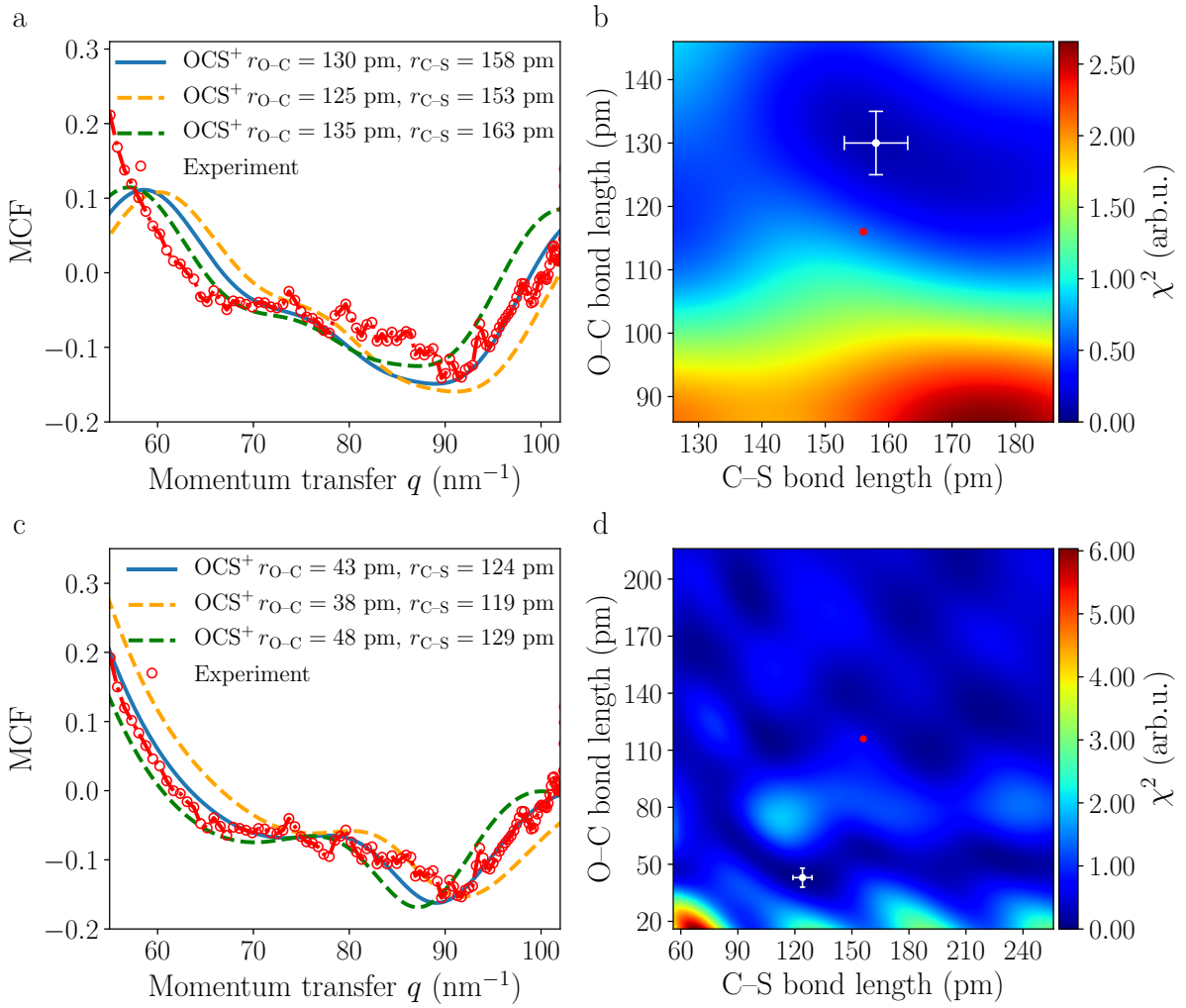

Figure 7.7.: a, b Same as Figure 7.5, considering electron scattering from a molecular cation with the charge localized on the oxygen atom. **c, d** Same as Figure 7.5, considering electron scattering from a molecular cation with the charge localized on the carbon atom.

8 Molecular-Frame Angularly-Resolved Photoelectron Spectroscopy of Strongly Field-Free Aligned OCS Molecules

8.1. Introduction

The possibility to fix molecules in space, described in the first chapters of this thesis, and to access the molecule-fixed frame (MFF) opens new prospects to image molecular structures and to investigate ultrafast photoinduced chemical processes. High-harmonic generation experiments performed on aligned molecules have shown a strong dependence of the emitted radiation on the alignment distribution [210, 241], opening up the possibility to image the shape of the underlying molecular orbital involved in the process [208, 244]. Similarly, photoelectron angular distributions (PADs), recorded on aligned molecules, showed a clear manifestation of the molecular orbital structure [209, 277]. The angular dependence of strong-field ionization yields has been measured for small diatomics [66] and complex asymmetric top rotors [278]. Amongst all published work, the contribution of several electronic ionization channels [278–280], the molecular orbital imprint in laser-driven electron recollisions [274], and channel- and angle-resolved ATI measurements [281], have been observed. Recently, the focus in strong-field ionization of molecules has shifted toward self-imaging methods such as laser-induced electron diffraction (LIED) and strong-field photoelectron holography (SFPH). While the former has already been introduced in chapter 7, SFPH corresponds to the interference between direct and rescattered electrons. Studies have shown that such holographic structures carry information about the electron motion on ultrafast timescales, reaching the sub-fs time domain [242, 243, 282].

While LIED and SFPH have been very successful in the past to retrieve the molecular structure for a number of relatively small molecules [35, 36, 39, 41] and sub-cycle electron dynamics [282–284], important questions remain with respect to the applicability of these techniques to retrieve the 3D structure and dynamics of complex molecules with atomic resolution. Structure retrieval in the LIED method relies on the quantitative rescattering theory (QRS) [180–182], see subsection 2.4.3, in which the shape of the electron wavepacket is washed out during its propagation and treated as a plane wave. Such a strong assumption breaks down when alignment is employed and the MFF is accessed. Also, the initial shape of the electron wavepacket is generally not well captured with the current theory based on the strong-field approximation (SFA) or the Ammosov-Delone-Krainov model (ADK) [66, 243]. In addition to these challenges, the

use of these techniques for structural determination may be further complicated by the number of ionization channels and, hence, molecular orbitals that contribute to the final MFPADs [275].

In this chapter, we investigated strong-field ionization of strongly field-free aligned OCS molecules for different alignment distributions, ionized at various mid-IR wavelengths, which allowed us to observe the main features characterizing the molecular-frame photoelectron angular distributions (MFPAD). After introducing the experimental setup, we show and discuss how the ionization yield, SFPH structures and the signal in the rescattering plateau depend on the molecular alignment distribution. Our experiments and analysis demonstrate that a new model is required to retrieve the 3D structure from such measurements.

8.2. Methods

Most of the experimental setup has already been described in chapter 3, section 4.4 and section 7.2. Briefly, a cold molecular beam was formed by supersonic expansion of a mixture of OCS in helium, utilizing an Even-Lavie valve. Using an electrostatic Stark deflector, ground-state-selected OCS molecules with $> 80\,\%$ purity were formed at the edge of the deflected molecular beam. Strong field-free alignment of OCS was achieved using two off-resonant near-IR pulses with a central wavelength of 800 nm, a pulse duration (FWHM) of 250 fs and a separation of 38.1 ps. The degree of alignment (DOA) in all measurements, presented in the following, was characterized to be $\langle\cos^2\theta_{2D}\rangle \geq 0.95$. Strong-field ionization was achieved by using the output of a high-energy tunable optical parametric amplifier (HE-TOPAS, Light Conversion), delivering ∼60 fs-short probe pulses with pulse energies up to ∼3 mJ. Angularly-resolved photoelectron momentum distributions (PEMDs) at driving wavelengths of the mid-infrared probe laser of 1.7 µm, 1.8 µm and 2 µm were recorded with a velocity map imaging spectrometer (VMIS), combined with a MCP and phosphor-screen detector and read out by a CCD camera. Photolectron momentum distributions were recorded for different alignment distributions; in particular for the full alignment revival at ∼120.78 ps and the anti-alignment at ∼79.58 ps after the peak of the first alignment laser pulse, and for isotropically distributed molecules. The PEMDs for a given alignment configuration were recorded for different orientations of the alignment laser polarization with respect to the polarization of the ionizing laser field. Both, the pump and the probe pulses were linearly polarized, with the mid-IR probe laser polarization being always kept parallel to the detector, along the y-axis in all figures shown in the following, and the alignment laser polarization being rotated using a waveplate. In contrast to chapter 7, where measurements on isotropically distributed molecules were performed and cylindrical symmetry in the imaging geometry was conserved, allowing to retrieve the 3D PEMDs by employing an Abel inversion, this is not possible for the measurements presented in this chapter except for few alignment distributions. Hence, no Abel inversion was utilized in this chapter. The imaging geometry for parallel and perpendicular alignment is schematically illustrated in Figure 8.1, indicating also the shape of the HOMO of OCS. Finally, we

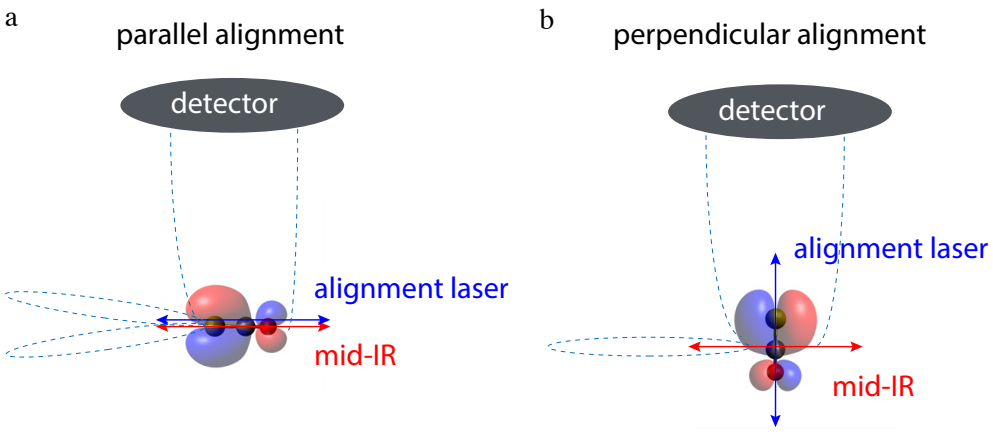

Figure 8.1.: Sketch of imaging geometry for parallel and perpendicular alignment with OCS HOMO indicated. **a** parallel alignment and **b** perpendicular alignment.

note that in all measurements ionization from multiple orbitals was tried to be minimized. To this end, time-of-flight (TOF) measurements were carried out and the laser power reduced until only the parent ion OCS^+ was observed. This point will be discussed in more detail in subsection 8.3.1 in the context of angle-dependent ionization yields.

8.3. Results and Discussion

8.3.1. Angle-dependent MF-ARPES of OCS at 1.8 µm

Photoelectron momentum distributions were first recorded for a series of angles between the molecular axis and the ionizing laser polarization. The molecular axis was rotated from 0° (molecular axis parallel to the ionizing laser polarization) to 90° (molecular axis perpendicular to the ionizing laser polarization) in steps of 4° by rotating the waveplate of the alignment laser. For each angle 50 measurements were conducted with each individual measurement being averaged over ∼5000 laser shots. Moreover, PEMDs for isotropically distributed molecules, averaged over ∼15000 laser shots each, were recorded before and after each set of measurements to compensate for fluctuations in the laser power and the molecular beam density. These measurements were used to normalize the yield of individual datasets, such that the ionization yields at different angles could be compared to each other. Figure 8.2 displays PEMDs for three alignment distributions, namely isotropic (Figure 8.2 a), parallel alignment (Figure 8.2 b) and perpendicular alignment (Figure 8.2 c). The visual inspection of these PEMDs does not allow to easily grasp substantial changes. Ionization yields for all measured angles between the alignment and the ionizing laser polarization were therefore extracted for different kinetic energy regions: the direct electrons with kinetic energies $<2\,U_p$ and the rescattered electrons with energies between $4\,U_p$ and $10\,U_p$, shown in Figure 8.3. The ionization yields were obtained by calculating the angle-integrated photoelectron kinetic energy spectra, subsequently determining the position of the $2\,U_p$, $4\,U_p$ and $10\,U_p$ cutoffs and integrating the PES over the signal in the relevant region. The total yield $\leq 10\,U_p$

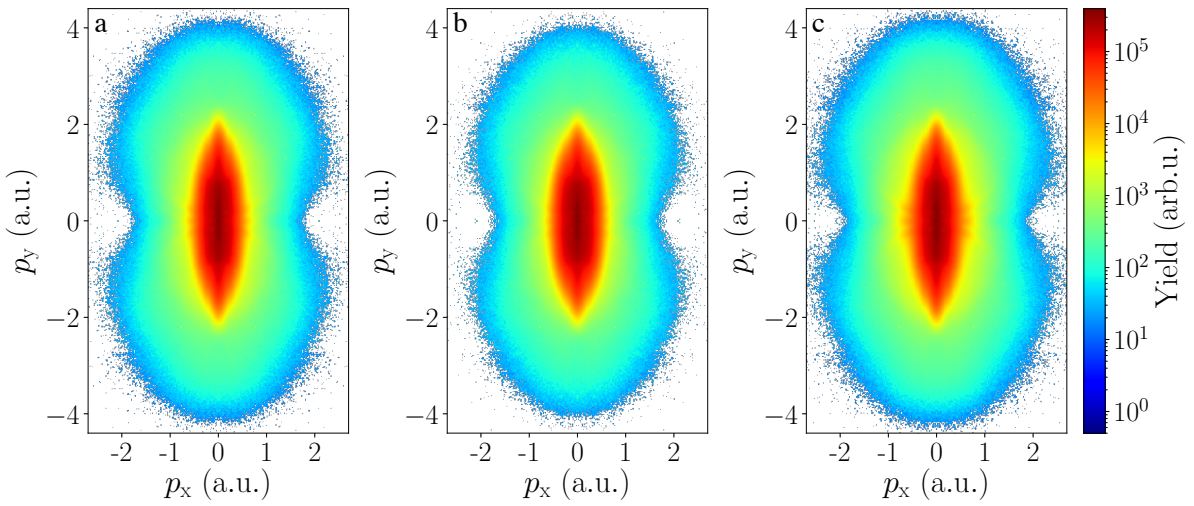

Figure 8.2.: Photoelectron momentum distributions of OCS for isotropically distributed molecules, parallel alignment and perpendicular alignment, ionized by a linearly polarized 1.8 µm wavelength mid-IR laser pulse. **a** isotropic distribution, **b** parallel alignment, **c** perpendicular alignment

in the corresponding isotropic measurements was extracted for all measurements and their ratio used as correction factor for the angle-dependent ionization yields. Due to the symmetry in the imaging geometry, the measurements in the range from 0 ° - 90 ° suffice to cover the whole range from 0 ° - 360 °. This is presented in Figure 8.3 b in a polar plot. In both momentum regions maximum electron emission is observed for

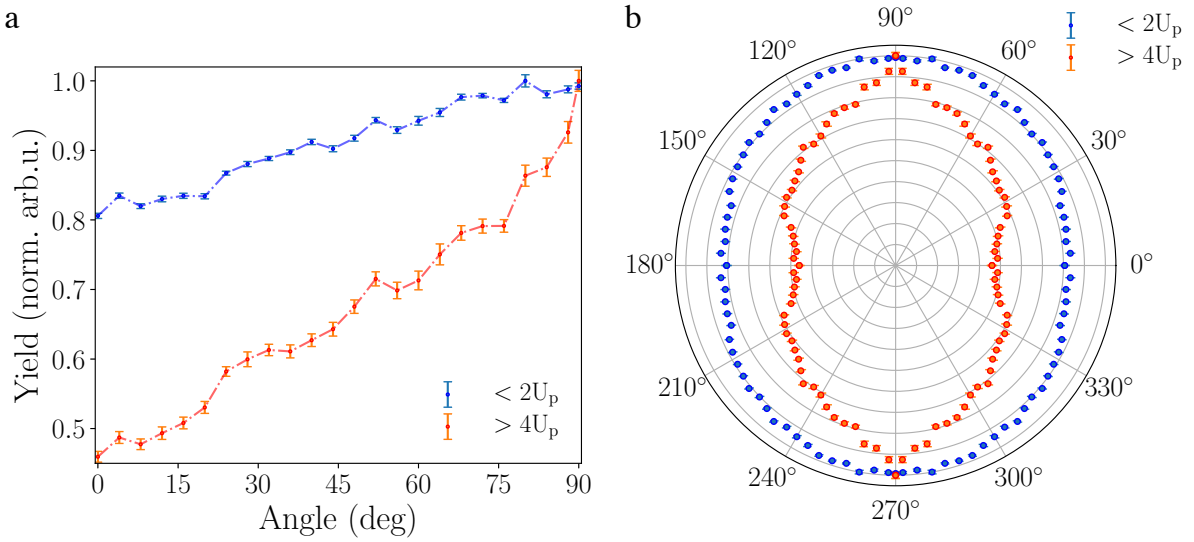

Figure 8.3.: Angle-dependent, normalized ionization yields for electrons <2 U_p and >4 U_p. **a** Angle-dependent, normalized ionization yields in the measured range from 0 ° to 90 °, **b** Polar plot covering the range from 0 ° to 360 °.

molecules aligned perpendicularly to the ionizing laser field. A higher contrast between the maximum yield at perpendicular alignment and the minimum yield at parallel alignment is observed in the rescattered electrons, showing a difference of more than 50% compared

to 20% in the direct electrons. The error bars represent the statistical standard error over 50 measurements. Our results are in qualitative agreement with earlier work on angle-dependent photoelectron yields of OCS [278, 279]. Interestingly, they observed a discrepancy to simulated ionization yields using the MO-ADK theory that predicts a maximum yield at an angle of ∼45 ° and a minimum at 90 °. The simulated maximum ionization yield at ∼45 ° can thereby be attributed to the nodal planes of the HOMO of OCS, leading to a decreased ionization efficiency when the molecules are aligned parallel or perpendicular to the ionizing field. Similar discrepancies have also been observed in the strong-field ionization of CO_2 [66]. Several effects have been proposed to explain the observed differences, including the contribution of several orbitals [280], the population of excited states during ionization [285, 286] and the possible deformation of orbitals by the strong ionizing field [287]. Additionally, ionization saturation effects can play an important role, which was shown for OCS to explain the discrepancy between the experiment and the MO-ADK results [279]. As a matter of fact, by decreasing the intensity by a factor of ∼2, the maximum at 90 ° turned into a minimum [279]. Therefore, we attribute the observed maximum of the ionization yield at 90 ° to ionization saturation.

As shown in Figure 8.3, the ionization yield observed in the rescattered electrons quickly increases with the molecular axis angle. The difference observed in the slopes for direct and rescattered electrons indicates that the alignment of the molecules does not only affect the ionization efficiency but also the return probability and the scattering cross section, since the probability to measure a rescattered electron is given by the product of the ionization efficiency, the return probability and the scattering cross section.

In the next section we will discuss how the electron trajectories are affected by the initial alignment of the molecules.

8.3.2. MF-ARPES of OCS at 2 µm

In Figure 8.4, photoelectron momentum distributions (PEMDs) of strongly field-free aligned OCS molecules are shown, ionized by 2 µm mid-IR laser pulses. Figure 8.4 a shows the photoelectron momentum distribution (PEMD), measured at the full alignment revival at a delay time of 120.78 ps after the peak of the first alignment pulse for parallel alignment. Figure 8.4 b was measured for the same alignment as in Figure 8.4 a, but with the alignment laser polarization perpendicular to the mid-IR polarization. Measurements at the anti-alignment, at a delay time of 79.58 ps, are shown in Figure 8.4 c for parallel polarization and in Figure 8.4 d for perpendicular polarization, respectively. Finally, in Figure 8.4 e, the PEMD for isotropically distributed molecules is shown. One observes that the PEMDs are clearly different, both, for large longitudinal momenta $p_y > 5$ a.u. and for small transverse momenta $p_x \sim 0$ a.u.. In Figure 8.5 a, a direct comparison between parallel alignment (left side) and perpendicular alignment (right side) is shown. One observes that for perpendicular alignment the high-energy cutoff extends to higher longitudinal momenta, whereas the low-energy cutoff $\sim 2\,U_p$ is similar.

In order to quantify the differences in the high-energy cutoffs, the angularly-integrated photoelectron spectra (PES), for all distributions presented in Figure 8.4, are shown

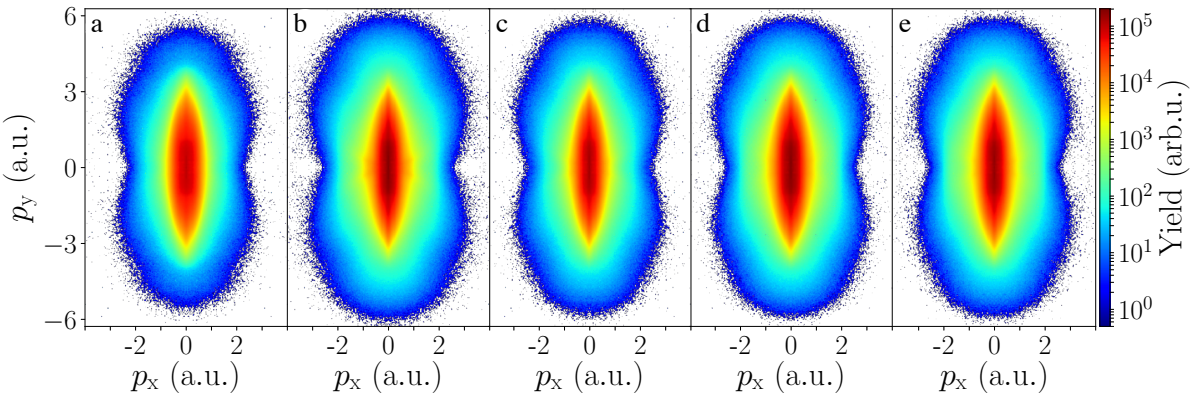

Figure 8.4.: Photoelectron momentum distributions of OCS at 2 µm for aligned, anti-aligned and isotropic distributions **a** alignment revival at 120.78 ps, parallel to detector, **b** alignment revival at 120.78 ps, perpendicular to detector, **c** anti-alignment at 79.58 ps, parallel to detector, **d** anti-alignment at 79.58 ps, perpendicular to detector, **e** isotropic distribution.

in Figure 8.5 b. The angular integration was carried out within a cone around the laser polarization with an opening angle of ±20 °, indicated in Figure 8.5 a. As already seen in the 2D momentum distributions in Figure 8.4, a large modification of the high-energy cutoff is observed for different alignment distributions. The cutoffs for anti-alignment parallel, anti-alignment perpendicular and the isotropic distribution are approximately at 9.5 U_p, 9.6 U_p and 9.8 U_p, respectively, whereas it reaches only 8.6 U_p for parallel alignment. Only for perpendicular alignment a high-energy cutoff of 10 U_p, in agreement with the

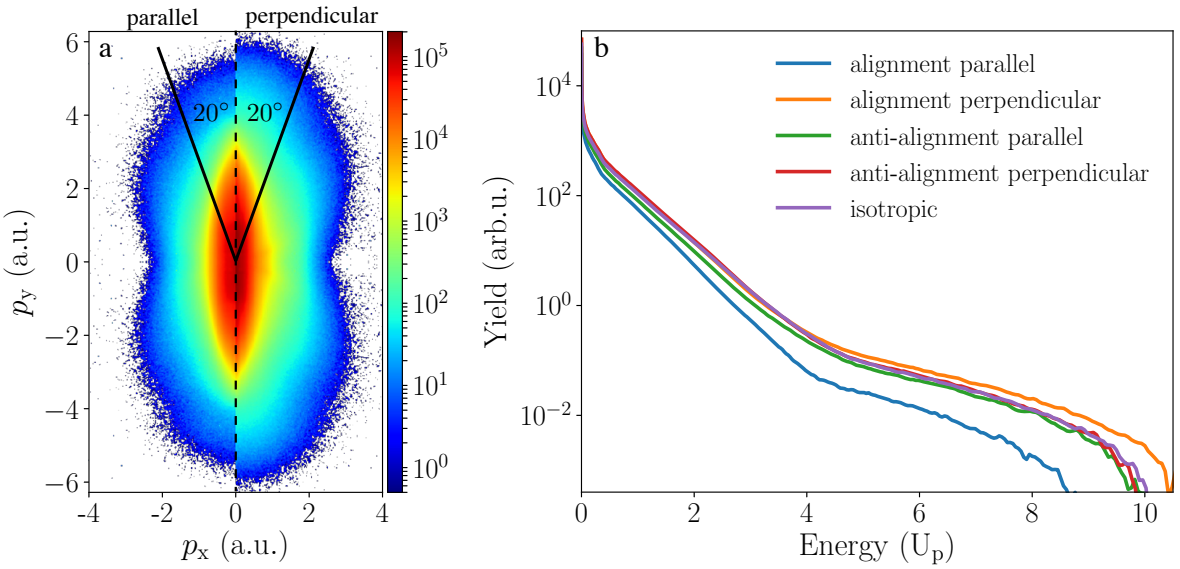

Figure 8.5.: Comparison of MF-ARPES of OCS **a** left side shows parallel alignment and right side shows perpendicular alignment **b** angularly-integrated PES measured in units of U_p, for same MF-ARPES as in Figure 8.4.

theoretical maximum high-energy cutoff, is observed. We note that the determined locations of the high-energy cutoffs were extracted from the 2D PEMDs and do not coincide with high-energy cutoffs, expected from the 3D PEMDs. In addition, the

exact positions of the high-energy cutoffs are smeared out due to focal volume intensity averaging. Nevertheless, our observation conforms with recent experiments, where OCS molecules were adiabatically aligned, parallel and perpendicular, and ionized using 1.3 µm and 1.5 µm mid-IR pulses [179].

The change of the cutoff with the molecular alignment distribution can be rationalized if we consider that the HOMO of OCS is a Π-orbital, infinitely degenerate around the internuclear axis, as is schematically illustrated in Figure 8.1. Electron ejection along the internuclear axis is expected to be strongly suppressed when to the nodal plane of the HOMO orbital is aligned with the ionizing laser polarization [209, 288]. In contrast, the second node, perpendicular to the internuclear axis, is not a symmetry element and electrons can be ejected in the perpendicular direction. We expect therefore that for parallel alignment electrons will be emitted with a substantial initial transverse momentum, and naively one would expect that the electron will gain less energy in the field and return with lower scattering energies to its parent ion.

In order to get a better understanding of the process leading to the observed reduced cutoff, we use the classical model, introduced in subsection 2.4.2, to calculate the kinetic energy of the electron when it returns to its parent ion and when it is detected. In this model, the kinetic energy can be expressed as a function of the travel time $\tau = \omega(t_r - t_0)$, with the time of ionization t_0 and the time of rescattering t_r, and the scattering angle θ_r as [289, 290].

$$E_{\text{kin}}(\tau, \theta_r) = E_r \left[g(\tau) \cos\theta_r \pm \sqrt{1 - g^2(\tau) \sin^2\theta_r} \right]^2 , \tag{8.1}$$

with the return energy at recollision

$$E_r = 2\,\mathrm{U_p}(2 - 2\cos\tau - \tau\sin\tau)^2(2 + \tau^2 - 2\cos\tau - 2\tau\sin\tau)^{-1} \tag{8.2}$$

and

$$g(\tau) = (1 - \cos\tau - \tau\sin\tau)(2 - 2\cos\tau - \tau\sin\tau)^{-1} . \tag{8.3}$$

These expressions were used to compute the final kinetic energy of an electron, in units of $\mathrm{U_p}$, shown in Figure 8.6 for backscattering ($\theta_r = 180\,^\circ$) and forward scattering ($\theta_r = 0\,^\circ$) as a function of the travel time τ, without initial transverse momentum. The return energy E_r at the instant of recollision is shown in orange.

The model predicts two families of cutoff energies that converge toward $8\,\mathrm{U_p}$ for backscattering electrons. For electron trajectories with an odd number of revisits at the parent ion the cutoff energy is above $8\,\mathrm{U_p}$ and reaches a maximum of $10\,\mathrm{U_p}$ at the first return. On the contrary, for an even number of revisits, the cutoff energy is always below $8\,\mathrm{U_p}$. Forward scattering leads to final kinetic energies $< 2\,\mathrm{U_p}$. We note here that these electrons are responsible for SFPH and will be discussed in subsection 8.3.4. At the third revisit the classical model predicts a high-energy cutoff for backscattering of $\sim$8.7 $\mathrm{U_p}$, close to the observed cutoff for parallel alignment. This suggests that due to the alignment of the molecules and the initial transverse momentum that results from this alignment, rescattering at the first return is suppressed. This has been confirmed

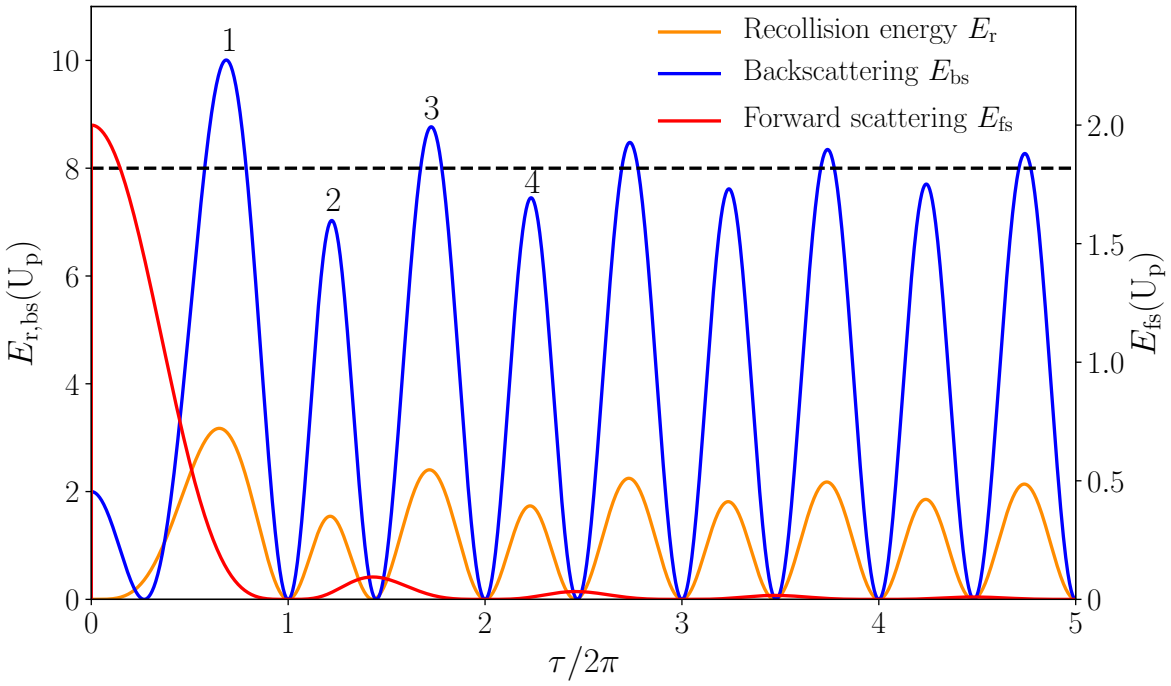

Figure 8.6.: Final kinetic energies of backscattered and forward scattered electrons as a function of their travel time. Shown are the return energy at the instant of recollision in orange, the final kinetic energy for backscattered electrons in blue and for forward scattered electrons in red. Note the different scales with maximum kinetic energies of $\sim 10\,U_p$ for backscattering at the first revisit and $2\,U_p$ for forward scattering. The maxima for backscattering at the first four revisits are marked by the corresponding number of revisits.The black dashed line depicts the limiting energy of $8\,U_p$, separating the two families with maxima $>8\,U_p$ and $<8\,U_p$.

in recent semi-classical simulations on OCS at 800 nm, in which ionization was treated using the Ammosov-Delone-Krainov model (ADK) and the propagation of the electron in the laser field and the recollision process were treated classically [291]. In this model the nodal plane and the initial transverse momentum are imprinted in the continuum electron wavepacket. For an OCS molecule aligned along the laser polarization this leads to a maximum electron emission at an angle of 45 °, as discussed in subsection 8.3.1. This model reveals that the return probability at the third revisit is enhanced with respect to the first revisit. This can be undestood as follows. Due to the initial emission angle, the electrons miss the parent ion at the first revisit and, hence, high-energy backscattered electron trajectories, leading to the $10\,U_p$ cutoff, are suppressed. One would expect a complete suppression of backscattered electron signal. However, the effect of the Coulomb field of the cation on the electron trajectories leads to an enhancement of the probability for an electron to return at the third revisit. This combined effect is responsible for the observed cutoff close to $\sim 8.7\,U_p$. This analysis implies that the QRS, which is traditionally used to extract molecular structures in LIED experiments, cannot be applied for a molecule with a Π orbital, once the molecule is aligned along the laser field, because the relationship between the return kinetic energy and the final kinetic energy (see subsection 2.4.2), is not valid anymore. The development to adapt the QRS

model to include the initial shape of the electron wavepacket is ongoing but beyond the scope of this thesis.

Instead of a classical model, a quantum description of the strong-field process, including the scattering process, can be employed by using the time-dependent density functional theory (TDDFT), which has been successfully applied already to describe the effect of the molecular alignment distributions on the PEMDs for lower driving wavelengths in CF_3I [275] and OCS [179]. However, such a description is prohibitive for the 2 µm wavelength used in our experiment due to the large computational grid needed to describe the propagation of the electron in the continuum. We note that the same reduced high-energy cutoff was observed in adiabatically aligned molecules, ionized at 1.3 µm, and reproduced using the TDDFT model [179].

8.3.3. Normalized Difference Momentum Maps

So far, mainly the effect of the alignment distributions on the high-energy cutoff and rescattered electrons has been discussed. In Figure 8.7, normalized differences of PEMDs, measured at 1.8 µm and taken between different alignment distributions, are shown. The normalized differences were computed according to

$$I_{\text{norm.diff.}} = \frac{I_a - I_b}{I_a + I_b}\,, \tag{8.4}$$

where I_a, I_b are the measured 2D PEMDs with $a, b \in$ {parallel alignment, perpendicular alignment, anti-alignment parallel, anti-alignment perpendicular}. In Figure 8.7 a, the normalized difference formed between parallel alignment and perpendicular alignment is shown. In the low-momentum region, i. e., $p_x \in [-1, 1]$ and $p_y \in [-2.5, 2.5]$, one observes a strong depletion in the difference signal along the laser polarization for $p_x \sim 0$, and a strong enhancement for $p_x \sim 0.5$ a.u. and for angles close to 45 °. The depletion along the probe laser polarization direction can be attributed, as eludicated in subsection 8.3.1 and subsection 8.3.2, to the alignment of the nodal plane of the HOMO of OCS with the laser polarization in the case of parallel alignment, leading to a suppresion of electron emission along it. The enhanced signal at angles close to 45 ° agrees with the expected maximum emission angle according to the MO-ADK model. At large longitudinal momenta $|p_y| > 2.5$ a.u., a strong depletion of the signal is observed. This effect can be well understood when considering again the results presented in subsection 8.3.1 and subsection 8.3.2, where it was demonstrated that the alignment of the nodal plane with the laser polarization axis leads to a decrease of the return and scattering probability due to the initial transverse momentum of the electron wavepacket. Hence, the strong depletion is a direct consequence of the large difference in the rescattered electron yield, presented in Figure 8.3, due to the effect of the nodal plane.

In addition, two more effects are clearly observed in Figure 8.7 a, holographic interference patterns and the fork structure. Strong-field photoelectron holography (SFPH) is observed along the laser polarization axis y, with two distinct structures being visible. One identifies the so-called outer spider structure, reaching up to momenta of

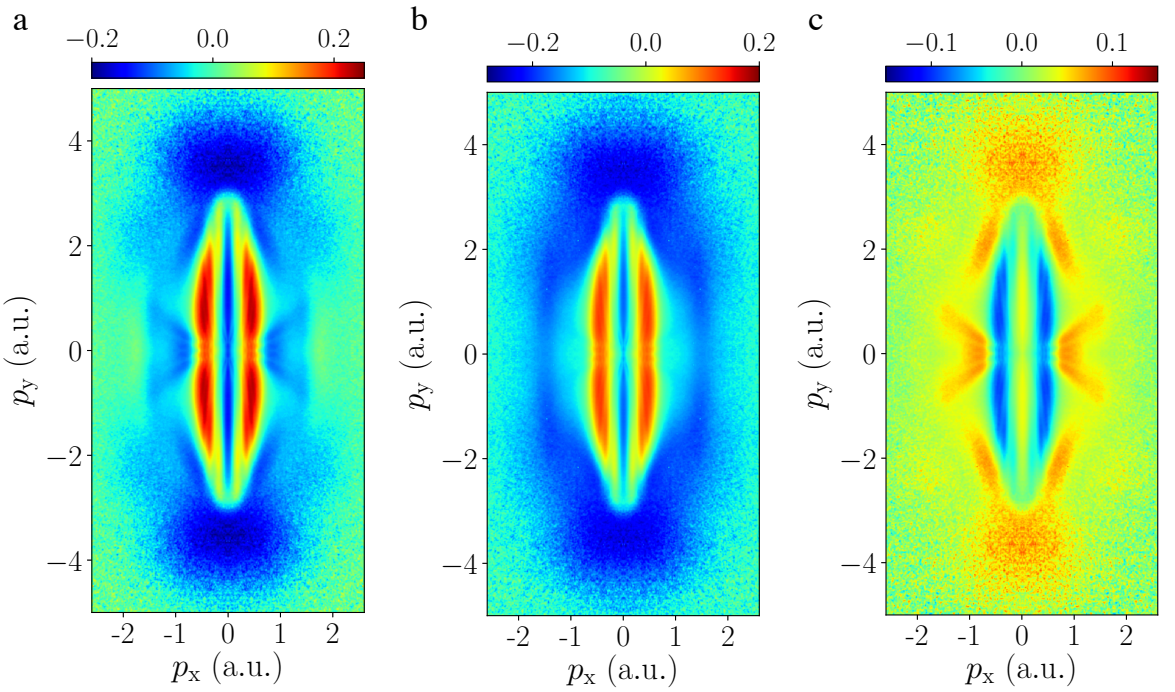

Figure 8.7.: Normalized difference PEMDs at 1.8 µm. **a** Alignment parallel minus alignment perpendicular, **b** alignment parallel minus anti-alignment parallel and **c** alignment perpendicular minus anti-alignment perpendicular.

$|p_y|$∼2.5 a.u., and the inner spider structure at small momenta p_x, p_y∼0. In contrast, the fork structure with 4 prongs is observed symmetrically around p_y∼0 at finite transverse momenta $|p_x|$∼1.5 a.u.. Both of these effects will be discussed in detail in subsection 8.3.4. We only note at this point that the fork structure as well as the inner holographic features dominate for perpendicular alignment.

Similarly, in Figure 8.7 b and Figure 8.7 c, normalized differences, formed between parallelly aligned and anti-aligned and perpendicularly aligned and anti-aligned molecules, are shown, respectively. The overall picture in Figure 8.7 b is similar to Figure 8.7 a, which can be undestood by considering that parallely anti-aligned molecules are aligned within a disk, perpendicular to the laser polarization of the probe laser. In Figure 8.7 c, the fork structure is strongly pronounced, originating from perpendicular alignment, as well as the enhancement in the high-energy electron yield $|p_y| > 2.5$a.u. .

In conclusion, by employing normalized difference momentum maps, large differences in the PEMDs were observed for different alignment distributions, confirming the observations in subsection 8.3.1 and subsection 8.3.2. For alignment distributions with the internuclear axis being aligned along the probe laser polarization axis, electron ejection along the the internuclear axis and in turn, high-energy backscattered electron trajectories from the first encounter with the parent ion, are strongly suppressed. Strong-field ionization and strong-field rescattering from aligned OCS molecules shows clear signatures of a dependence on the alignment distribution and, hence, a strong dependence on the MFF and the structure of the underlying molecular orbital.

8.3.4. Strong-Field Photoelectron Holography

In subsection 8.3.3, normalized difference momentum maps were presented, showing clear differences for different alignment distributions. In particular, different structures were observed in the low-momentum region $<2\,U_p$, the fork structure and holographic interferences. A visual inspection of the PEMDs in Figure 8.2 did not allow to directly observe these structures, mainly due to the smooth direct electron yield which is orders of magnitude higher and covers most of these structures.

In the following, we will concentrate on the low-energy region $<2\,U_p$ and discuss the structures therein. We apply a Laplace filter, typically used for edge detection and pattern recognition, in order to increase the contrast and to filter out the most important features. An edge is detected, if the condition

$$\Delta f = \frac{\partial^2 f}{\partial^2 x} + \frac{\partial^2 f}{\partial^2 y} = 0 \tag{8.5}$$

is fulfilled, i. e., the Laplacian of the two-dimensional signal function f is zero. The

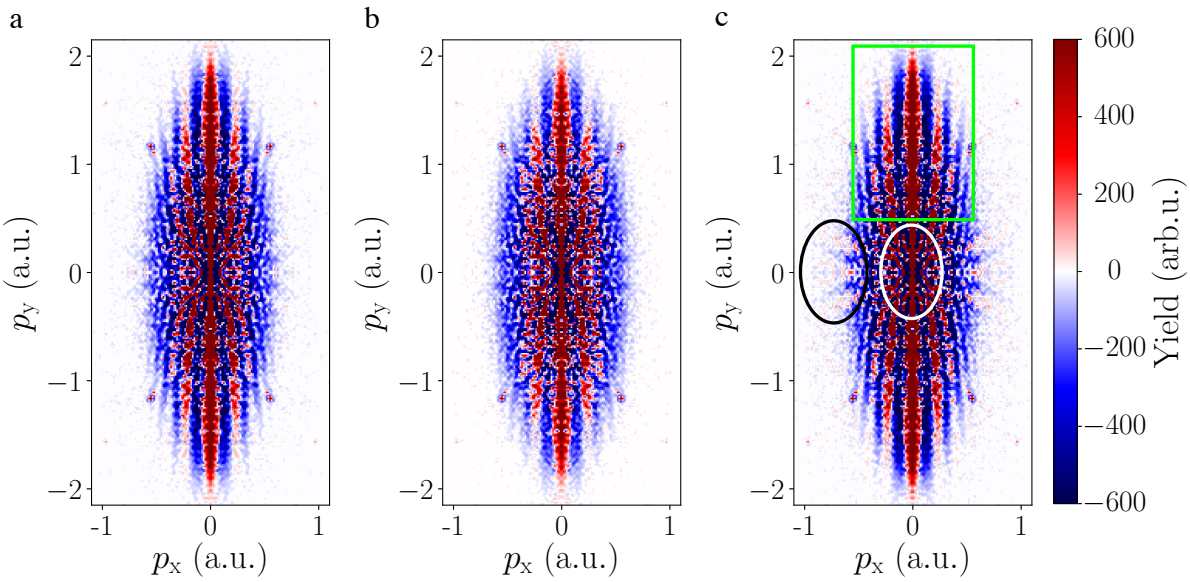

Figure 8.8.: Photoelectron momentum distributions of OCS for isotropically distributed molecules, parallel alignment and perpendicular alignment, ionized by a linearly polarized 1.8 µm wavelength mid-IR laser pulse, after application of a Laplace edge detection filter. **a** isotropic distribution, **b** parallel alignment, **c** perpendicular alignment. In **c**, three regions are emphasized. In the green box, the primary spider structure is visible, inside the white ellipse the inner spider structure and inside the black ellipse, the so called V or fork structure can be distinguished.

results, after applying the Laplace filter on the data shown in Figure 8.2, are presented in Figure 8.8. The Laplace filtered images are noisy but the most important features can be distinguished. In Figure 8.8 c, which shows the Laplace filtered PEMD for perpendicular alignment, three regions are emphasized. The holographic interference pattern inside the green box is known as the primary spider structure. Inside the white ellipse in the center of the image and for the lowest momenta, the inner spider structure is visible. The origin

of both spider structures is the same and due to interference of electrons scattered in the forward or near-forward direction with direct electrons, originating from the same quarter-cycle of the field [282, 284]. The primary spider structure is formed from the interference between electrons scattered in the forward direction at their first encounter with their parent ion and direct electrons. Upon successive revisits of the electron to its parent ion, its scattering momentum as well as its final momentum decreases [284]. Therefore, a series of spider structures at successively lower final momenta is observed, with the spider structures at lower final momenta being attributed to multiple revisits, i. e., the second revisit, the third revisit and so forth. The third region, marked with a black ellipse, is the so called V or fork structure, appearing symmetrically around zero transverse momentum, which is discussed in more detail in the following. Note, that the fork structure is most clearly visible for perpendicular alignment (Figure 8.8 c), slightly visible for the isotropic distribution (Figure 8.8 a) and not noticeable for parallel alignment (Figure 8.8 b). This leads to the conclusion that the observed fork structures in Figure 8.7 originate from the PEMDs for perpendicular alignment.

Fork Structure

The fork structure has first been introduced in the case of strong-field ionization of Xenon atoms [282, 289] and it consists of 4 prongs, two inner and two outer ones. In order to understand the origin of the fork structure, we employ the classical model [178], describing the propagation and scattering of an electron in an external field, introduced in subsection 2.4.2. The final momentum of an electron, as measured on the detector in an experiment, can be expressed as

$$p_x = \sqrt{2E_{\mathrm{kin}}(\tau, \theta_r)}\cos\theta_r \tag{8.6}$$

$$p_y = \sqrt{2E_{\mathrm{kin}}(\tau, \theta_r)}\sin\theta_r\,, \tag{8.7}$$

where $E_{\mathrm{kin}}(\tau, \theta_r)$ is the final kinetic energy, defined in (8.1). The final momentum depends on the travel time $\tau = \omega(t_r - t_0)$ of the electron in the laser field and the scattering angle θ_r. Selected final momentum distributions are depicted in the (p_x, p_y) plane in Figure 8.9, corresponding to the calculated cutoff energies, i. e., the maxima of $E_{\mathrm{kin}}(\tau, \theta_r)$ for different angles θ_r, which were already shown in Figure 8.6 for the limiting cases of $\theta_r = 0\,^\circ$ and $\theta_r = 180\,^\circ$. The two families of trajectories with cutoff energies at backscattering of $>8\,U_p$ (odd number of revisits) and $<8\,U_p$ (even number of revisits), discussed in subsection 8.3.2, are shown in red and blue, respectively, and the limiting curve with a cutoff energy of $8\,U_p$ in green. Figure 8.9 reveals that the fork structure originates from these different trajectories, specifically, it can be attributed to near-forward scattered electron trajectories with the inner prongs being due to an even number of revisits and the outer prongs due to an odd number of revisits. We note that from Figure 8.9 it is clear that forward scattering at the first revisit does not contribute to the fork structure. The fork structure is sensitive to the pulse duration of the ionizing laser field, since the trajectories in Figure 8.9 originate from scattering at multiple revisits [289]. Finally we note that the large DCS for forward and near-forward

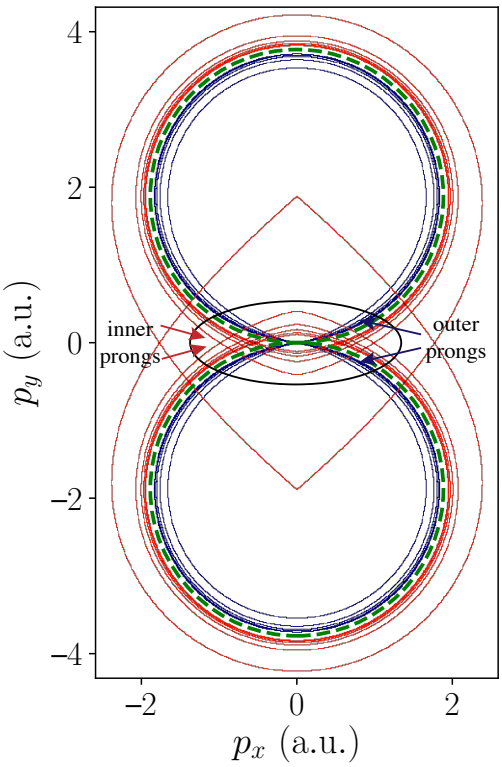

Figure 8.9.: 2D histogram showing maxima of $E_{\mathrm{kin}}(\tau, \theta_r)$, plotted in the (p_x, p_y) plane, for 1.8 µm wavelength and $I_{\mathrm{peak}} = 1 \times 10^{14}\,\mathrm{W/cm^2}$. The curves in blue and red belong to the two families of curves with high-energy cutoffs $<8\,\mathrm{U_p}$ and $>8\,\mathrm{U_p}$ for backscattered electrons, respectively. The fork structure is indicated by arrows with the outer prongs being the continuation towards forward scattering from the family $>8\,\mathrm{U_p}$ and the inner prongs from the family $<8\,\mathrm{U_p}$. The green dashed circles indicate the limiting curves with $8\,\mathrm{U_p}$ energy separating the two families of curves.

scattering allows the structure to compete with the smooth direct-electron signal [289].

Considering again the difference momentum maps in subsection 8.3.3, we conclude that the observed dominance of the fork structure originating from molecules at perpendicular alignment can be attributed to a higher yield of electrons scattered in the near-forward direction compared to parallel alignment.

Scaling Laws in SFPH

As already mentioned, the interference pattern observed in Figure 8.8 along the probe laser polarization in the low-energy region for momenta below $2\,\mathrm{U_p}$, dubbed the spider structure, is due to the interference of direct electrons with near-forward scattered electrons. The electron wavefunction in the ionizing laser field is composed of two parts

$$\psi = \psi_{\mathrm{s}} + \psi_{\mathrm{r}}\,, \tag{8.8}$$

where the reference wave ψ_{r} corresponds to direct electrons, travelling straight to the detector after ionization, and the signal wave ψ_{s} corresponds to electrons that rescatter

from the parent ion and end up with momenta $<2\,U_p$. The measured signal is then expressed as

$$|\psi|^2 = |\psi_s|^2 + |\psi_r|^2 + \psi_s^*\psi_r + \psi_s\psi_r^* = |\psi_s|^2 + |\psi_r|^2 + 2|\psi_s||\psi_r|\cos\Delta\phi\,, \tag{8.9}$$

showing an interference term $\propto \cos\Delta\phi$, where $\psi_{r,s} = |\psi_{r,s}|e^{i\phi_{r,s}}$ was used and the phase difference $\Delta\phi = \phi_r - \phi_s$ was introduced. An analytic expression, describing the phase difference between these direct and near-forward scattered electrons, has already been discussed in [282]. Based on the SFA, the observed fringe spacing can be relatively well described by

$$\Delta\phi \approx \frac{p_r^2(t_r - t_0)}{2}\,, \tag{8.10}$$

where p_r is the final momentum orthogonal to the laser polarization, t_r the time of rescattering and t_0 the time of ionization. This expression provides the dependence of the interfrence fringes on the laser parameter such as wavelength, pulse duration and peak intensity [292]. According to (8.10) one would expect a strong dependence of the fringe spacing on the wavelength because the period of the laser cycle defines the travelling time of the electron in the continuum and the time of rescattering. The transverse momentum contrariwise depends on the laser polarization and only weakly on the laser intensity as long as the dipole approximation is valid.

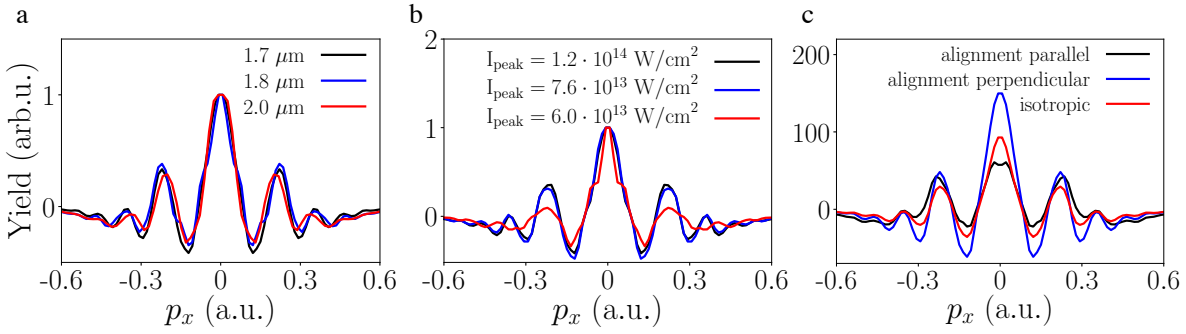

Figure 8.10.: Comparison of interference patterns in the primary spider structure, extracted at $p_y = 1$ a.u.. **a** Comparison of interference fringes for the three wavelengths 1.7 µm, 1.8 µm and 2 µm. **b** Comparison of interference fringes at 1.8 µm for the three different peak intensities $1.2 \times 10^{14}\,\mathrm{W/cm^2}$, $7.6 \times 10^{13}\,\mathrm{W/cm^2}$ and $6 \times 10^{13}\,\mathrm{W/cm^2}$. **c** Comparison of interference fringes at 1.8 µm for parallel alignment, perpendicular alignment and isotropic distribution.

The interference fringe spacing in the primary spider structure at a momentum of $p_y = 1$ a.u. was compared for the three wavelengths 1.7 µm, 1.8 µm and 2 µm, for the three different peak intensities $1.2 \times 10^{14}\,\mathrm{W/cm^2}$, $7.6 \times 10^{13}\,\mathrm{W/cm^2}$, $6 \times 10^{13}\,\mathrm{W/cm^2}$ at a wavelength of 1.8 µm and for three orientations of the molecules, i. e., parallel alignment, perpendicular alignment and isotropically distributed molecules. The results are shown in Figure 8.10. A clear shift of the fringe pattern at 2 µm with respect to the other wavelengths was observed in Figure 8.10 a, with the higher order peaks being shifted toward smaller momenta. This is expected from (8.10), where a longer wavelength results in a longer travel time $\Delta t = t_r - t_0$ and thus in a faster oscillation at higher frequency or

equivalently in a smaller spacing between the fringes [292]. Unfortunately, the resolution of our experiment is not sufficient to observe a difference in the fringe spacing measured at 1.7 µm and 1.8 µm. In Figure 8.10 b, the interference fringes for the two highest peak intensities coincide whereas for the lowest intensity a deviation in the higher order fringes and a decrease of the contrast is observed. These observations can be explained as follows. The tunneling exit of an electron upon strong-field ionization occurs at a position $\vec{r}_0 = \vec{\epsilon}_0 \mathrm{I_p}/\epsilon_0^2$, where $\mathrm{I_p}$ is the ionization potential and ϵ_0 is the peak electric field strength. In the high-intensity regime, $|\vec{r}_0| \sim 0$ and it does not change significantly with intensity compared to the excursion time $\alpha = \epsilon_0/\omega^2$ of the electron in the continuum. The travel time $\Delta t = t_r - t_0$ is thus dominated by the wavelength of the ionizing laser field in this regime, since the return time t_{ret} and the time of recollision t_r almost coincide. On the contrary, for low intensities, the initial displacement $|\vec{r}_0| \neq 0$ leads to an extra travel time $|\vec{r}_0|/v(t_{\mathrm{ret}}) = t_{\mathrm{ret}} - t_r$. This extra travel time scales as γ^2 for $\gamma \ll 1$, but only as γ for $\gamma \gtrsim 1$, where γ is the Keldysh parameter [292]. Hence, its contribution is non-negligible as the intensity is lowered and the Keldysh parameter approximates or exceeds 1, and the fringe spacing is affected by the peak intensity. At the same time, when the intensity is lowered, $\mathrm{U_p}$ decreases and, hence, also the kinetic energy of the electron and its spatial excursion in the continuum. In this case the influence of the core potential of the parent ion on the electron becomes significant and the holographic fringe pattern gets diminished, explaining the change in the contrast of the interference fringes [293, 294]. In Figure 8.10 c, a comparison for parallel alignment, perpendicular alignment and isotropically distributed molecules is presented. The oscillations coincide, but the contrast of the fringes is different and lowest for parallel alignment. The amplitude of the fringes is proportional to $2|\psi_{\mathrm{s}}||\psi_{\mathrm{r}}|$. As we have already concluded from the observations in subsection 8.3.3, the electron yield $|\psi_{\mathrm{s}}|$ for forward scattered electrons is lowest for parallel alignment, explaining the lowest contrast in the interference pattern.

We conclude that the interference fringe spacing strongly depends on the wavelength and only weakly on the intensity, confirming the results observed in Xenon [292]. Although for different orientations of the molecules the electron continuum wavepacket structure and, hence, also the rescattering process are expected to be different, no difference in the fringe spacing of the individual interference structures could be observed, possibly due to the lack of resolution. This result, however, is in agreement with earlier work, where it was shown that the structures in the low-energy region for atoms and small molecules with similar $\mathrm{I_p}$ were indistinguishable [295–297].

8.4. Conclusions

In this chapter we investigated the dependence of strong-field ionization and field-driven recollisions in OCS on the molecular alignment distribution. By employing almost perfect field-free alignment, the MFF could be accessed and the orientation of the internuclear axis of OCS with respect to the ionizing laser polarization could be controlled. The two most striking effects that were observed were the dependence of the high-energy electron yield in the rescattering plateau and the position of the high-energy cutoff for

backscattered electrons on the orientation of the internuclear axis with respect to the ionizing laser polarization axis. For parallel alignment of the internuclear axis with the probe laser polarization, a strong suppression in the rescattered electron signal was observed, which could be attributed to the nodal plane in the Π-shaped HOMO of OCS and a modified initial electron continuum wavepacket, having a substantial initial transverse momentum component. Due to this modified wavepacket structure, backscattering at the first encounter with the parent ion becomes highly unprobable and only at the third revisit significant scattering occurs, thus explaining the observed position of the high-energy cutoff. Direct comparison of PEMDs in terms of normalized difference momentum maps, formed between parallel and pependicular alignment, revealed a strong depletion of the electron yield along the internuclear axis and in the rescattering plateau, confirming the effect of the nodal plane on the PEMDs. Furthermore, SFPH was observed in the low-momentum region below $2\,U_p$, originating from the interference of direct and near-forward scattered electrons, as well as the fork structure, originating from near-forward scattered electrons. The lower contrast in the interference fringes in the primary spider structure and the absence of the fork structure for parallel alignment showed once more the effect of the nodal plane in the HOMO of OCS, leading to a lower electron yield of forward scattered electrons compared to perpendicular alignment.

Our measurements revealed a strong dependence of the measured photoelectron momentum distribution on the alignment of the HOMO of OCS and, hence, its nodal plane along the internuclear axis with the polarization axis of the ionizing laser. The different initial electron wavepackets for different alignment distributions lead to modifications in the return probability and the rescattering process, thus rendering it necessary to consider the initial wavepacket structure for the determination of the molecular structure. So far the QRS theory has been used for molecular structure retrieval in LIED experiments, completely neglecting the structure of the initial electron wavepacket. Our experiments suggest that this approach must be reconsidered and extended when employing aligned molecules with orbitals structures possessing nodal planes.

8.5. Supporting Information

8.5.1. Above-Threshold Ionization at 1.7 µm

In Figure 8.11 a, the PEMD of OCS, measured at 1.7 µm for perpendicular alignment, is shown after application of the Laplace filter. Figure 8.11 b shows a zoomed in view of the region inside the black box in Figure 8.11 a. One can clearly observe concentric ring-like

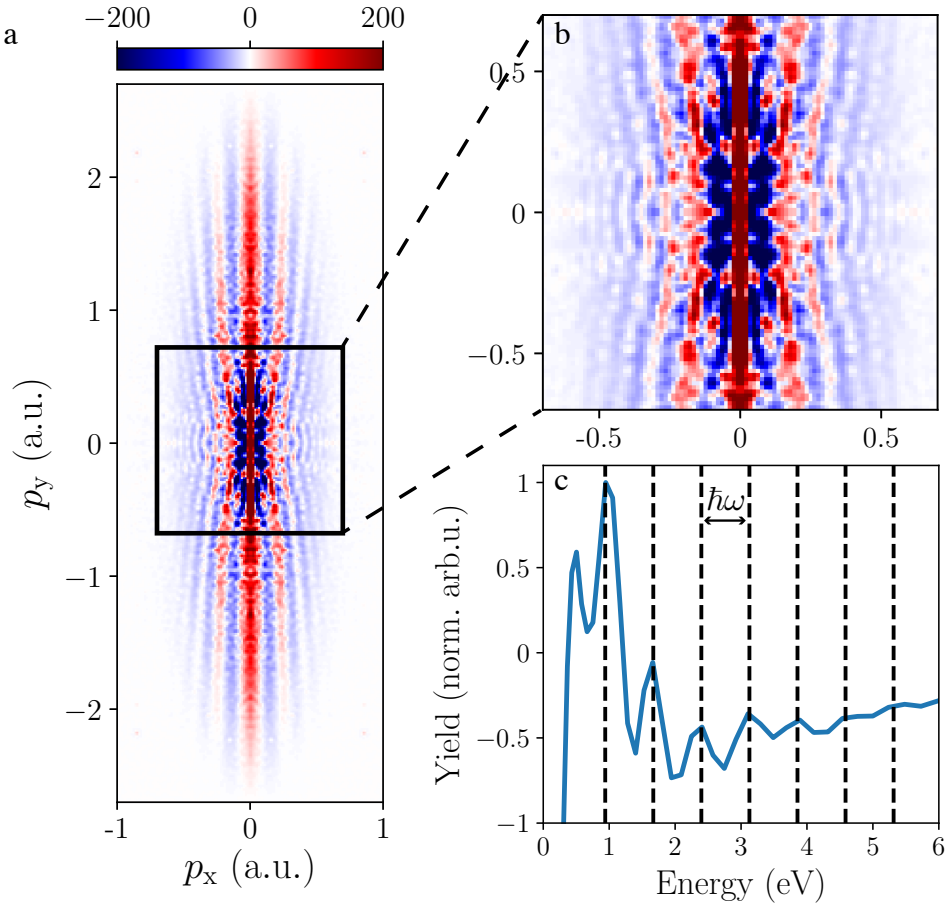

Figure 8.11.: ATI rings become visible for perpendicular alignment at 1.7 µm after application of Laplace filter. **a** PEMD for perpendicular alignment at 1.7 µm with Laplace filter applied, **b** zoom into low-energy region, indicated by black box in **a** and **c** angularly-integrated radial distribution showing ATI peaks. The black dashed lines are equally spaced by one photon energy of $\hbar\omega = 0.73\,\text{eV}$.

interference patterns at small transverse momenta, centered at zero momentum. These interference fringes are reminiscent of ATI which is indeed confirmed in Figure 8.11 c, where the angularly-integrated radial distribution is shown. Several peaks can be identified, where a spacing of one photon energy of 0.73 eV is indicated by black dashed lines. The ATI rings are otherwise completely covered by the direct electrons in the PEMDs and only visible after the application of the Laplace filter.

9 Conclusions and Outlook

The observation of chemical reactions in real time is a formidable task that poses strong requirements on the targets under study and on the imaging methods that are employed. Recording the molecular movie in gas-phase molecular samples requires, on the one hand, the ability to prepare and manipulate molecules with high precision, allowing to obtain clean and reproducible measurements with a high signal-to-noise ratio; and, on the other hand, the capability to observe structural changes with atomic spatial and temporal resolution. In the last decades methods to create high-density pulsed cold molecular beams, their manipulation with electric and magnetic fields, laser-induced alignment and mixed-field orientation, have been either developed or optimized, allowing to exert an unprecendented degree of control on molecules in the gas phase. At the same time, with the fast progress in the development of light sources, several sophisticated imaging methods, in particular self-imaging methods such as laser-induced electron diffraction (LIED), have emerged.

Two main objectives have been pursued in this thesis. The first objective was to achieve and optimize strong laser-induced field-free alignment of cold controlled molecules through tailored light fields, presented in chapter 4, chapter 5 and chapter 6. We have investigated field-free alignment of three molecules with increasing complexity, carbonyl sulfide (OCS), iodobenzene (IB) and indole, requiring also methods of increasing complexity, respectively. The second objective was to employ the LIED method and to apply it on the example of OCS. This included the structure retrieval of isotropically distributed OCS molecules with atomic spatial resolution, presented in chapter 7, and the investigation of the effect of molecular alignment on strong-field ionization and field-driven recollisions, presented in chapter 8.

In the following, a summary and discussion of the results achieved throughout this work, as well as an outlook of possible extensions of this work in the future are presented.

9.1. Toward Optimized Field-Free Alignment of Complex Molecules

In chapter 4, optimized field-free alignment of OCS, the smallest molecule investigated in this work, was presented. Ground-state-selected OCS molecules with $> 80\,\%$ purity in the probed deflected part of the molecular beam and an optimized two-pulse sequence yielded an unprecedented degree of field-free alignment of $\langle\cos^2\theta_{2D}\rangle = 0.96$, with a very narrow angular confinement of $13.4\,^\circ$ FWHM. Ion-momentum distributions of O^+ were recorded through Coulomb-explosion imaging (CEI) over more than one and a half rotational period of OCS, yielding a movie of the rotational wavepacket dynamics, initiated by the alignment

laser pulses. Optimal pulse parameters for the two alignment laser pulses, i. e., their peak intensities, their common pulse duration and the relative time separation between the two pulses, were determined through optimization calculations in which the TDSE was solved in a closed-feedback loop approach by employing evolutionary algorithms (EAs) with the degree of alignment (DOA) as fitness function. The experimental parameters were chosen as closely as possible to the calculated optimal pulse parameters. The hypersurface in the 4-dimensional parameter space turned out to be quite insensitive to changes in the peak intensities, within some bounds and under the constraint of the first pulse being weaker than the second one, showing many local maxima close to the global optimum. On the contrary, a strong dependence of the DOA on the exact time delay between the two pulses was found, which can be rationalized when considering that it defines the phase relationship between rotational states in the rotational wavepackets that are formed. This was experimentally confirmed with the optimal experimentally determined DOA being achieved for a time delay of $\tau_{exp} = 38.1 \pm 0.1$ ps, in perfect agreement with the theoretically predicted τ_{sim} =38.2 ps. The deviation from perfect alignment is attributed to the initial state distribution with more than one rotational state being populated, the finite focal volume with an intensity distribution in the interaction region of the alignment and probe lasers and a possible small contribution from non-axial recoil, rendering the measured $\langle\cos^2\theta_{2D}\rangle$ a lower bound of the actual degree of alignment. The observed time-dependent angular distributions directly reflected the time evolution of the rotational wavepacket, showing rich interference structures. An analysis of the angular distributions and the DOA in terms of the commonly used $\langle\cos^2\theta_{2D}\rangle$ did not allow to capture this rich rotational dynamics. Therefore, an expansion of the angular distributions in a series of Legendre polynomials was carried out that finally allowed to reconstruct the complete rotational wavepacket with its complex coefficients at all times, thus providing the maximum information available about the rotational wavepacket. This proved that the high DOA resulted from a broad strongly phase-locked rotational wavepacket.

In chapter 5, strong field-free 1D alignment of OCS and IB was presented. In order to achieve field-free alignment of IB, which is an asymmetric top rotor, more sophisticated methods are required compared to the multi-pulse alignment scheme presented in chapter 4. We followed a promising method of combining adiabatic alignment with a sudden truncation of the pulse, leading to the creation of a field-free rotational wavepacket upon fast switch-off of the alignment laser. The switch-off in the time domain was achieved by using a long-pass transmission filter that cut out the long-wavelength part of the spectrum. Using this method, a fall-off time of ∼8 ps was achieved. The temporal evolution of the DOA could be reproduced by solving the TDSE for the experimentally measured pulse profile and pulse parameters. Our simulations revealed that the finite fall-off time of ∼8 ps was rather long compared to the rotational period of IB, leading to a modified field-free rotational wavepacket compared to the superposition of states at the peak of the alignment laser pulse. In particular, population transfer during the fall-off led to a narrower final-state distribution. Furthermore, the shape and the linear polarization of the alignment laser pulse led only to significant population of states with $K = 0$ and, hence, to a linear-rotor like behaviour of the alignment revival structure.

Finally, in chapter 6, we addressed the problem to achieve strong field-free 3D alignment of organic asymmetric top molecules without rotational symmetries and marker atoms, which poses a challenge to properly characterize the DOA. Due to this difficulty, in most studies so far the alignment of complex asymmetric top rotors was investigated for molecules containing heavy leaving groups, which define one of the inertia and polarizability axes, such as iodine in IB. This allows to easily characterize the DOA by gating onto the mass of such a characteristic fragment, which can be unambigiously allocated within the molecule. At the same time, these choices severly limit the class of molecules investigated so far and for which alignment has been demonstrated. We investigated the field-free alignment of indole (C_8H_7N), whose polarizability tensor is not diagonal in the principal axis system of inertia. Indole does not contain any specific leaving group upon Coulomb explosion, which would allow to easily conclude the orientation of the molecule at the time it dissociates. In principle, every molecule with a sufficiently large polarizability anisotropy can be strongly aligned through laser-induced alignment. Therefore, besides the goal of achieving strong 3D field-free alignment in the first place, the major task consisted of finding a way to characterize the DOA of the major polarizability axes of indole. The solution to this second problem is particularly important because it allows to extend these methods for achieving alignment to practically all organic molecules.

3D field-free alignment of indole was achieved using a truncated quasi-adiabatic off-resonant laser pulse with a sharp intensity peak before truncation. The pulse was produced through phase and amplitude shaping of an extremely linearly-chirped broadband laser pulse using a liquid crystal spatial light modulator (SLM). In contrast to chapter 5, a SLM was used, which allowed to switch off the alignment laser pulse within less than 3 ps compared to 8 ps in the long-pass transmission-filter method. Many fragments showing alignment were observed upon Coulomb explosion, which was initiated by a circularly polarized femtosecond-short probe pulse. In order to characterize the 3D DOA, delay-time revival scans and tomographies for H^+, C^{++} and $HNCH^+$ were carried out. For different fragments, different peak alignment values were observed, which can be attributed to different angles between their recoil axes and the principle polarizability axes, as well as non-axial recoil of these fragments which possibly result from 3 or 4-body break-ups. Because hydrogen and carbon can come from anywhere in the molecule, simulations were carried out, in which the degree of alignment of all hydrogen and carbon atoms were computed individually. The rotational density for each of these atoms was computed by solving the TDSE and was then projected onto a 2D plane, mimicking the detector plane, by using a Monte-Carlo sampling method based on a metropolis algorithm. The weights for the individual hydrogen and carbon atoms were determined by fitting the time-dependent alignment revivals and the tomographies. The overall agreement between experiment and simulations gave us confidence that we were able to determine the 3D degree of alignment of the three principle polarizability axes. The simulated 3D DOA for the main polarizability axes of the molecule $\alpha_p > \alpha_q > \alpha_r$ with respect to the laboratory axes XYZ were characterized to be $\langle\cos^2\theta_{pZ}\rangle = 0.88$, $\langle\cos^2\theta_{rY}\rangle = 0.85$, $\langle\cos^2\theta_{qX}\rangle = 0.83$ and $\langle\cos^2\delta\rangle = 0.89$, where $\cos^2\delta = \frac{1}{4}(1 + \cos^2\theta_{pZ} + \cos^2\theta_{rY} + \cos^2\theta_{qX})$ constitutes a scalar metric for the DOA.

Our results suggest that we are able to strongly field-free align molecules and to characterize the DOA, ranging from linear rotors to asymmetric top rotors. We succeeded in demonstrating field-free alignment not only for asymmetric top rotors, which contain heavy marker atoms and exhibit coinciding polarizability and inertia frames, but also for organic asymmetric top rotors without rotational symmetries and marker atoms, such as indole. Depending on the complexity of the molecule, i. e., its structure and its rotational spectrum, different methods have been employed that allowed to achieve the pursued results. However, in particular in the last method, where tailored light fields were applied to align the molecules using a SLM, the full potential of the approach has not been fully employed yet. The pulse form of the alignment laser was chosen on the basis of earlier theoretical and experimental work that showed the potential of truncated adiabatic pulses. Nevertheless, this does not constitute a rigorous proof that it is also the optimal pulse form to achieve the highest field-free alignment. A possible extension of this work would be to exploit the full potential of combining pulse shaping techniques in the laboratory with closed-feedback optimization algorithms. This would enable to determine the optimally tailored light field, optimizing the DOA individually for each molecule under study, in the course of the experiment. A further extension of the work presented in this thesis would be the optimization of mixed-field orientation, such that the head-to-tails symmetry of aligned molecules is broken.

Another important question that arises is to determine to what extent these approaches can be applied to large biologically relevant macromolecules and proteins, where the number of fragments upon Coulomb explosion and the dissociation process are even more complex. Furthermore, it would be interesting to repeat our experiment with improved acquisition tools, such as the TimePix camera which allows to measure ionic fragments in coincidence. This would provide further information about the dissociation process during Coulomb explosion and possibly constrain the possible weights of individual hydrogen and carbon atoms. Finally, we mention that we observed a strong effect on the ionization efficiency of the probe laser when the alignment laser field was present. It is still not clear what the effect of the alignment laser is but we assume that during the quasi-adiabatic alignment, close to the peak, some molecules are already promoted to excited states, which leads to different dissociation pathways compared to the field-free region. This suggest even more that field-free alignment is an indispensable tool compared to adiabatic alignment, in particular for complex biomolecules, since the alignment laser may heavily perturb the resulting dynamics and, hence, the outcome of the experiment.

9.2. Imaging of Controlled Molecules

To date, all experiments on laser-induced electron diffraction (LIED) were carried out by employing either time-of-flight (TOF) measurements or reaction microscopes (COLTRIMS) [35, 36, 39]. Both methods provide a high dynamic range but require long acquisition times. In chapter 7, in contrast to earlier work, we measured photoelectron momentum distributions (PEMDs) of argon, krypton and isotropic OCS using a velocity map imaging spectrometer (VMIS). Employing the quantitative rescattering the-

ory (QRS) and the independent-atom model (IAM) with scattering amplitudes provided by the relativistic scattering code ELSEPA [266], we showed that the DCS of argon and krypton agree very well with the simulated DCS. We compared the experimental DCS, extracted at 100 eV, to simulated DCS of neutral atoms and singly charged ions and found the latter to agree much better with experiment and over a wider range of scattering angles. From the PEMDs, measured for isotropically distributed OCS molecules, we could extract the molecular structure, consisting of the bond lengths and the bond angle, with atomic resolution to better than ±5 pm. We showed that within the laser cycle of 6.67 fs, the structure of OCS remains essentially linear and identical to its equilibrium structure. In the IAM, molecules are modelled as a collection of non-interacting atoms acting as scattering centers for the incoming electron flux. Since in the LIED method the molecule's own electrons scatter off their parent ion, the description used so far and involving only neutral atomic scattering amplitudes is, in principle, wrong. We showed that by replacing the scattering amplitude of neutral sulfur with that of the singly charged ion, the agreement between theory and experiment could be greatly improved and the structure of OCS could be retrieved with a higher resolution compared to the neutral case. Although, strictly speaking our approach is still not correct, because the charge density is not localized on one atom alone in the OCS ion, this approach proved to work very well because ∼85% of the electron density of the HOMO is localized at the sulfur site. The same approach did not work at all when the scattering amplitudes of oxygen and carbon where replaced by the corresponding scattering amplitudes of singly charged ions. This showed that indeed ionization from the HOMO of OCS is most likely to happen at the sulfur site and that the hole charge density is mostly localized at the sulfur, too.

Finally, in chapter 8, we investigated the effect of strong field-free alignment of OCS on strong-field ionization (SFI) and field-driven recollisions. We observed striking differences in the PEMDs for different alignment configurations, in particular large modifications in the high-energy electron yield and different high-energy cutoffs for backscattered electrons. By rotating the molecular axis with respect to the probe mid-IR laser polarization, we showed that the underlying structure of the Π-shaped HOMO orbital, in particular its nodal plane along the internuclear axis, strongly affected the ionization efficiency, the return probability and the rescattering probability. Electron ejection along the internuclear axis is expected to be strongly suppressed, leading to a modified electron wavepacket in the continuum. The position of the high-energy cutoff for backscattered electrons for parallel alignment could be attributed to an enhanced rescattering probability at the third revisit whereas rescattering at the first revisit is highly unprobable, which was recently confirmed by first simulations [291]. Due to the nodal plane imprint in the continuum electron wavepacket, an initial transverse momentum component is introduced which causes the electrons to miss the parent ion upon their first revisit. However, due to the Coulomb field of the cation, refocussing of the electron trajectories occurs which leads to an increased probability for rescattering at the third revisit. Direct comparison between different alignment configurations in terms of normalized difference momentum maps corroborated these findings, where in addition to strong modifications in the rescattering plateau $>2\,U_p$ also differences in the low-energy region $<2\,U_p$ were observed. In this momentum region the effect of the nodal plane for parallel alignment manifested itself

in a strong depletion of the signal along the laser polarization and a maximized yield at angles close to 45 °, in accordance with MO-ADK simulations. In the low-energy region $<2\,U_p$, further structures were observed, in particular the fork structure and holographic interference patterns. Comparison of these structures for different alignment distributions showed in the case of parallel alignment, besides an attenuated yield of rescattered electrons, that also the yield of forward scattered electrons, which form the fork structure and the inner spider structure, was weaker.

At last, we examined the dependence of the holographic interference pattern in the primary spider structure on the wavelength and the peak intensity of the probe laser and on the alignment configuration. In agreement with earlier work [292], we found that the fringe spacing in the interfrence pattern depends on the wavelength, which defines the travel time of the electron in the continuum from the time of ionization until rescattering, and only weakly on the intensity in the high-intensity regime with $\gamma \ll 1$. For different alignment configurations the same fringe spacing was observed with the lowest contrast for parallel alignment due to the smaller yield of forward scattered electrons compared to pependicular alignment.

In summary, our measurements revealed a strong dependence of the measured PEMDs on the alignment of the internuclear axis with respect to the laser polarization of the ionizing laser. Our explanation attributed the observed effects to the nodal plane imprint of the underlying molecular orbital on the continuum electron wavepacket, resulting in an substantial initial transverse momentum component and as a consequence in a modified return and rescattering probability. Structure retrieval in LIED experiments is based on the QRS theory, in which it is assumed that the structure of the electron continuum wavepacket is washed out during its propagation and, hence, treated as a plane wave. This approach is well justified when molecules are randomly oriented and the resulting measurements are averaged over all these orientations, since the effect of the nodal plane is smeared out and the wavefront of the electron wavepacket is almost flat at the time of rescattering, since it broadens substantially during its propagation in the laser field. However, when a molecule with a nodal plane in the molecular orbital, from which the electrons are released, is aligned along the laser polarization, the nodal plane imprint on the continuum electron wavepacket structure leads to major differences in the observed PEMDs and, hence, cannot be longer neglected. We claim therefore that the QRS model no longer provides a proper model for structure retrieval in these cases and it needs to be modified such as to account for the initial electron continuum wavepacket structure.

So far, the atomic spatial resolution of the LIED method was mainly employed to image static structures. However, it is particularly interesting to explore the full potential of this imaging method to observe time-resolved dynamics in molecules. In this respect, two follow-up experiments are planned. The first is on the indole-water cluster, where the dissociation of the water molecule from the indole-water cluster will be investigated, which is currently ongoing. The second experiment was already attempted during this thesis and regards the time-resolved measurement of bending dynamics, induced in OCS. For this experiment, a short, 230 nm wavelength laser pulse is used to pump the molecule and excite it to the A' Renner-Teller component of the $^1\Delta$ and the $A''\Sigma^-$ states. These

states are known to dissociate while the molecule is bending. The idea is to extract from LIED measurements simultaneously as a function of the delay time, the bond-angle and the bond-distances. This experiment involves the control and exact timing of two alignment laser pulses with 800 nm wavelength, the creation of a 230 nm wavelength pulse to excite the molecules, which is realized by second harmonic generation from 800 nm to 400 nm, second harmonic generation from 1200 nm to 600 nm and then mixing of 400 nm and 600 nm to generate the required 230 nm. Finally all these pulses have to be spatially and temporally collinearly overlapped with the 2.3 µm ionizing laser pulse. We already succeeded in setting up the experiment, creating all the required colors and to spatially and temporally overlap them in the VMIS, except for the 230 nm beam. Unfortunately, it turned out that the excitation laser pulse could not be properly focused. The problem was that the laser beam profile was not optimal and far from a low order Gaussian TEM mode, which after all the frequency mixing resulted in a beam profile that could not be focused enough to obtain the required peak intensities. The experimental setup is currently being optimized by cleaning the beam profile with a hollow-core fiber and using a beam stabilization system. The experiment is planned to start in the near future.

Appendices

A Calculation of Expectation Values

The degree of orientation is usually characterized through the expectation values $\langle \cos\theta_{Ji} \rangle$ and the degree of alignment through the expectation values $\langle \cos^2\theta_{Ji} \rangle$, where θ_{Ji} is the angle between the principal axis i in the molecule-fixed frame (MFF) and the cartesian axis J in the laboratory-fixed frame (LFF). Another observable of interest for direct comparison with experiment is $\langle \cos^2\theta_{2D} \rangle$, where the angle θ_{2D} is the polar angle in the 2D detector plane. It will be shown that these expectation values can be expressed in an analytical form by employing angular momentum algebra, suitable for direct numerical evaluation.

A.1. General Considerations

The MFF and the LFF are connected by a rotation about the three Euler angles (θ, ϕ, χ). This rotation can be described in terms of the rotation matrix $R(\theta, \phi, \chi)$ [127] whose entries are

$$R(\theta,\phi,\chi) = \begin{pmatrix} \cos\theta_{Xx} & \cos\theta_{Yx} & \cos\theta_{Zx} \\ \cos\theta_{Xy} & \cos\theta_{Yy} & \cos\theta_{Zy} \\ \cos\theta_{Xz} & \cos\theta_{Yz} & \cos\theta_{Zz} \end{pmatrix}, \tag{A.1}$$

i. e., the direction cosines $\Phi_{Ji} = \cos\theta_{Ji}$. The angles θ_{Ji} are thereby related to the Euler angles as follows:

$$\begin{aligned}
\cos\theta_{Xx} &= \cos\phi\cos\theta\cos\chi - \sin\phi\sin\chi, \\
\cos\theta_{Yx} &= \sin\phi\cos\theta\cos\chi + \cos\phi\sin\chi, \\
\cos\theta_{Zx} &= -\sin\theta\cos\chi, \\
\cos\theta_{Xy} &= -\cos\phi\cos\theta\sin\chi - \sin\phi\cos\chi, \\
\cos\theta_{Yy} &= -\sin\phi\cos\theta\sin\chi + \cos\phi\cos\chi, \\
\cos\theta_{Zy} &= \sin\theta\sin\chi, \\
\cos\theta_{Xz} &= \cos\phi\sin\theta, \\
\cos\theta_{Yz} &= \sin\phi\sin\theta, \\
\cos\theta_{Zz} &= \cos\theta.
\end{aligned}$$

Since $R(\theta, \phi, \chi)$ is an orthogonal matrix, the squared elements of each row and of each column add up to 1 such that only two entries in every row or column need to be known.

In the following we will concentrate on the calculation of the $\cos\theta_{Zz}$ expectation value, which is used to describe the alignment of the most polarizable axis of the molecule with respect to the major polarizability axis of the alignment laser. The other expectation values can be calculated in a similar way. The expectation values of interest are then

expressed in 3D as

$$\langle JKM|\cos\theta|JKM\rangle = \int_0^{2\pi}\int_0^{2\pi}\int_0^{\pi} \Psi^*_{JKM}\,\cos\theta\,\Psi_{JKM}\sin\theta \mathrm{d}\theta\mathrm{d}\phi\mathrm{d}\chi \tag{A.2}$$

and

$$\langle JKM|\cos^2\theta|JKM\rangle = \int_0^{2\pi}\int_0^{2\pi}\int_0^{\pi} \Psi^*_{JKM}\,\cos^2\theta\,\Psi_{JKM}\sin\theta \mathrm{d}\theta\mathrm{d}\phi\mathrm{d}\chi\,. \tag{A.3}$$

The degree of alignment in 2D is accordingly computed through substitution of $\cos\theta$ with $\cos\theta_{2\mathrm{D}}$, whereas the degree of orientation in 2D is typically characterized through the ratio $N_{\mathrm{up}}/N_{\mathrm{total}}$, where N_{up} is the yield measured in the upper half plane of the recorded ion-momentum distributions and $N_{\mathrm{total}} = N_{\mathrm{up}} + N_{\mathrm{down}}$ the total yield measured on the detector. The rotational wavefunctions $\Psi_{JKM}(\theta,\phi,\chi)$ in (A.2) and (A.3) are assumed to be normalized to unity in the following and the integration is carried out over the volume element of the Euler angles. The symmetric top eigenstates, expressed in the basis of Euler angles $\Omega = (\theta,\phi,\chi)$, are the Wigner D-functions and given by [127]

$$\langle\Omega|JKM\rangle = \left[\frac{2J+1}{8\pi^2}\right]^{1/2}\mathcal{D}^{*J}_{M,K}(\theta,\phi,\chi) = (-1)^{M-K}\left[\frac{2J+1}{8\pi^2}\right]^{1/2}\mathcal{D}^{J}_{-M,-K}(\theta,\phi,\chi). \tag{A.4}$$

The eigenfunctions of asymmetric top rotors cannot be cast in analytical form and are usually expanded in the basis of symmetric rotor states. For $K = 0$, i. e., $\chi = 0$, the Wigner D-functions reduce to the spherical harmonics, which are the eigenfunctions of linear rotors. Thus, a description of the expectation values in terms of Wigner D-functions suffices to describe the alignment and orientation of all types of rotating tops.

The relation between the Wigner D-functions and their complex conjugate is given by

$$\mathcal{D}^{*J}_{M,K}(\Omega) = (-1)^{M-K}\mathcal{D}^{J}_{-M,-K}(\Omega)\,. \tag{A.5}$$

We note that

$$\mathcal{D}^{J}_{M,K=0}(\theta,\phi,\chi=0) = \sqrt{\frac{4\pi}{2J+1}}\,Y^{*J}_{M}(\theta,\phi)\,, \tag{A.6}$$

relating the Wigner D-functions to the spherical harmonics, and

$$\mathcal{D}^{J}_{M=0,K=0}(\theta,\phi=0,\chi=0) = P_J(\cos\theta)\,, \tag{A.7}$$

relating the Wigner D-functions to the Legendre polynomials. The Wigner D-functions form a basis and satisfy the orthonormality relation

$$\int_0^{2\pi}\int_0^{2\pi}\int_0^{\pi}\mathcal{D}^{*J}_{M,K}(\theta,\phi,\chi)\mathcal{D}^{J'}_{M',K'}(\theta,\phi,\chi)\sin\theta\mathrm{d}\theta\mathrm{d}\phi\mathrm{d}\chi = \frac{8\pi^2}{2J+1}\delta_{JJ'}\delta_{MM'}\delta_{KK'}\,. \tag{A.8}$$

In addition, useful relations exist expressing the integral over three Wigner D-functions

in terms of Wigner 3j-symbols. These so-called Gaunt coefficients read

$$\int \mathcal{D}^{J1}_{M1,K1}(\Omega)\mathcal{D}^{J2}_{M2,K2}(\Omega)\mathcal{D}^{J3}_{M3,K3}(\Omega)\mathrm{d}\Omega = 8\pi^2 \begin{pmatrix} J_1 & J_2 & J_3 \\ M_1 & M_2 & M_3 \end{pmatrix} \begin{pmatrix} J_1 & J_2 & J_3 \\ K_1 & K_2 & K_3 \end{pmatrix} . \quad \text{(A.9)}$$

The possibility to express the integrals in (A.9) in terms of Wigner 3j-symbols is very useful, because the latter obey simple symmetry rules, which directly lead to the selection rules. For most combinations of the quantum numbers J, K, M the integrals are zero (exactly zero) and only few have to be calculated, thus greatly simplifying the computation of expectation values. Important symmetry rules are

$$\begin{pmatrix} J_1 & J_2 & J_3 \\ M_1 & M_2 & M_3 \end{pmatrix} = 0 \qquad \text{if } M_1 + M_2 \neq M_3 \,, \quad \text{(A.10)}$$

which leads to the selection rule $\Delta M = 0$ for linearly polarized light, i. e., that the magnetic quantum number is conserved. In addition, the relation

$$|J_1 - J_2| \leq J_3 \leq |J_1 + J_2| \quad \text{(A.11)}$$

must hold. Using the cyclic property of the 3j-symbols, a symmetric permutation results in

$$\begin{pmatrix} J_1 & J_2 & J_3 \\ M_1 & M_2 & M_3 \end{pmatrix} = \begin{pmatrix} J_2 & J_3 & J_1 \\ M_2 & M_3 & M_1 \end{pmatrix} = \begin{pmatrix} J_3 & J_1 & J_2 \\ M_3 & M_1 & M_2 \end{pmatrix} , \quad \text{(A.12)}$$

wheras an odd permutation leads to a sign change

$$\begin{pmatrix} J_1 & J_2 & J_3 \\ M_1 & M_2 & M_3 \end{pmatrix} = (-1)^{J_1+J_2+J_3} \begin{pmatrix} J_1 & J_3 & J_2 \\ M_1 & M_3 & M_2 \end{pmatrix} . \quad \text{(A.13)}$$

Finally, the sum of the angular momenta J in the upper row of the 3j-symbols has to be an integer number, otherwise the 3j-symbols vanish. The last requirement is always satisfied when considering molecular rotation since the angular momenta J themselves are integer numbers. For the special case $M_1 = M_2 = M_3 = 0$, the sum has to be an even integer number.

The aforementioned relations indicate that a description of the operators $\cos\theta$ and $\cos^2\theta$ in terms of Wigner D-functions is useful, since the expectation values can then be calculated using relation (A.9). Expressing the orientation and alignment operators in terms of Wigner D-functions is straightforward considering that

$$Y^0_1(\theta,\phi) = \frac{1}{2}\sqrt{\frac{3}{\pi}}\cos\theta = \sqrt{\frac{3}{4\pi}}\mathcal{D}^1_{0,0}(\theta,\phi,\chi) \,, \quad \text{(A.14)}$$

which leads directly to

$$\cos\theta = \mathcal{D}^1_{0,0}(\theta,\phi,\chi) \,, \quad \text{(A.15)}$$

and for the alignment operator

$$Y_2^0(\theta,\phi) = \frac{1}{4}\sqrt{\frac{5}{\pi}}(3\cos^2\theta - 1) = \sqrt{\frac{5}{4\pi}}\mathcal{D}^2_{0,0}(\theta,\phi,\chi)\,, \tag{A.16}$$

which leads directly to

$$\cos^2\theta = \frac{2}{3}\mathcal{D}^2_{0,0}(\theta,\phi,\chi) + \frac{1}{3}\,. \tag{A.17}$$

More on angular momentum algebra and detailed derivations of the above-stated relations can be found in [127].

A.2. 3D Expectation Values

Employing all the tools and the relations, presented in the section before, in particular (A.4), (A.5), (A.8), (A.9) and (A.17), one can express the degree of alignment in (A.3) as

$$\begin{aligned}\langle\cos^2\theta\rangle &= \frac{\sqrt{(2J+1)(2J'+1)}}{8\pi^2}\int \mathcal{D}^{J'}_{M',K'}(\theta,\phi,\chi)\left(\frac{2}{3}\mathcal{D}^2_{0,0}(\theta,\phi,\chi)+\frac{1}{3}\right)\mathcal{D}^{*J}_{M,K}(\theta,\phi,\chi)\mathrm{d}\Omega \\ &= \frac{2}{3}(-1)^{M-K}\sqrt{(2J+1)(2J'+1)}\begin{pmatrix}J' & 2 & J\\ M' & 0 & -M\end{pmatrix}\begin{pmatrix}J' & 2 & J\\ K' & 0 & -K\end{pmatrix} + \frac{1}{3}\delta_{JJ'}\delta_{MM'}\delta_{KK'}\,.\end{aligned} \tag{A.18}$$

For a linear molecule with $K = 0$, this simplifies to

$$\langle\cos^2\theta\rangle = \frac{2}{3}(-1)^{M}\sqrt{(2J+1)(2J'+1)}\begin{pmatrix}J' & 2 & J\\ M' & 0 & -M\end{pmatrix}\begin{pmatrix}J' & 2 & J\\ 0 & 0 & 0\end{pmatrix} + \frac{1}{3}\delta_{JJ'}\delta_{MM'}\,. \tag{A.19}$$

Analogously, for the degree of orientation in (A.2) one obtains

$$\begin{aligned}\langle\cos\theta\rangle &= \frac{\sqrt{(2J+1)(2J'+1)}}{8\pi^2}\int \mathcal{D}^{*J}_{M,K}(\theta,\phi,\chi)\mathcal{D}^1_{0,0}(\theta,\phi,\chi)\mathcal{D}^{J'}_{M',K'}(\theta,\phi,\chi)\mathrm{d}\Omega \\ &= (-1)^{M-K}\sqrt{(2J+1)(2J'+1)}\begin{pmatrix}J & 1 & J'\\ -M & 0 & M'\end{pmatrix}\begin{pmatrix}J & 1 & J'\\ -K & 0 & K'\end{pmatrix}\,.\end{aligned} \tag{A.20}$$

A.3. 2D Expectation Values

The calculation of the degree of alignment in 2D is not so straightforward, because the $\cos\theta_{2\mathrm{D}}$ operator can not be directly expressed in terms of Wigner D-functions. This problem can be circumvented by considering the relation between $\cos^2\theta$ and $\cos\theta_{2\mathrm{D}}$ [230]. A general vector $\vec{r}$, expressed in spherical coordinates, has a z-component $r\cos\theta$. A

projection of $\vec{r}$ onto a plane, the $y-z$ plane for example, yields the relation

$$\cos^2\theta_{2D} = \frac{\cos^2\theta}{\cos^2\theta + \sin^2\theta\sin^2\phi}\,, \tag{A.21}$$

which can be easily derived utilizing the inner product. If the alignment laser is linearly polarized, the projections onto the $x-z$ and the $y-z$ planes lead to the same matrix elements. In order to keep the derivation general, we substitute $\langle\cos^2\theta_{2D}\rangle$ by some general observable $\mathcal{A}$ and expand it in the basis of Wigner D-functions as

$$\mathcal{A} = \sum_{J,M,K}\sqrt{\frac{2J+1}{8\pi^2}}a^J_{M,K}\mathcal{D}^{*J}_{M,K}(\Omega)\,, \tag{A.22}$$

where the coefficients $a^J_{M,K}$ must be determined. Using the orthonormality relation (A.8), the coefficients can be expressed as

$$a^J_{M,K} = \sqrt{\frac{2J+1}{8\pi^2}}\int\mathcal{D}^J_{M,K}(\Omega)\mathcal{A}\mathrm{d}\Omega\,, \tag{A.23}$$

which can be computed through numerical integration. The advantage of this method, compared to a direct numerical integration of all expectation values, is that the number of integrals to be solved is greatly reduced. Furthermore, the coefficients have to be calculated only once and can be reused whenever needed. The expectation value can then be expressed in the form

$$\begin{aligned}\langle J'K'M'|\mathcal{A}|JKM\rangle = (-1)^{M-K}\sqrt{(2J+1)(2J'+1)}\sum_{J''=0}^{\infty}\sum_{M''=-J''}^{J''}\sum_{K''=-J''}^{J''}a^{J''}_{M'',K''}\\ (-1)^{M''-K''}\sqrt{\frac{2J''+1}{8\pi^2}}\begin{pmatrix}J & J' & J''\\ -K & K' & -K''\end{pmatrix}\begin{pmatrix}J & J' & J''\\ -M & M' & -M''\end{pmatrix},\end{aligned} \tag{A.24}$$

where the identities (A.9), (A.13) and the fact that $(-1)^{2(J+J'+J'')}$ is always even were used.

Turning back to the specific observable $\cos^2\theta_{2D}$ in (A.21) and assuming a linearly polarized alignment laser pulse interacting with a linear or symmetric top molecule for simplicity, (A.24) can be further simplified through symmetry considerations. First of all we note that $\cos^2\theta_{2D}$ does not depend on χ, hence χ is a cyclic coordinate and $K''=0$ in (A.24). Furthermore, for linear polarization, $K=K'$ and $M=M'$ must hold in (A.24). From the symmetries of the 3j-symbols, this results in $M''=0$ in (A.24), leaving only one sum over J''. Since $\cos^2\theta_{2D}$ is an even function, all coefficients with odd J'' are zero.

With this one arrives at the final expression

$$\frac{\langle J'KM|\cos^2\theta_{2D}|JKM\rangle}{\sqrt{(2J+1)(2J'+1)}} = \frac{(-1)^{M-K}}{4\pi^{3/2}} \sum_{J''=0}^{\infty} a_{J''}\sqrt{2J''+1} \begin{pmatrix} J & J' & J'' \\ -K & K & 0 \end{pmatrix} \begin{pmatrix} J & J' & J'' \\ -M & M & 0 \end{pmatrix}. \tag{A.25}$$

The matrix elements need to be calculated only once for all combinations of J, J', M, K, i. e., all rotational states included in the computational basis. The same analysis can be carried out for asymmetric top rotors and for elliptical polarization by considering all relevant symmetries and good quantum numbers, yielding slightly more complex expressions than (A.25). The first 200 coefficients $a_{J''}$, multiplied by $\frac{\sqrt{2J+1}}{4\pi^{3/2}}$, are shown

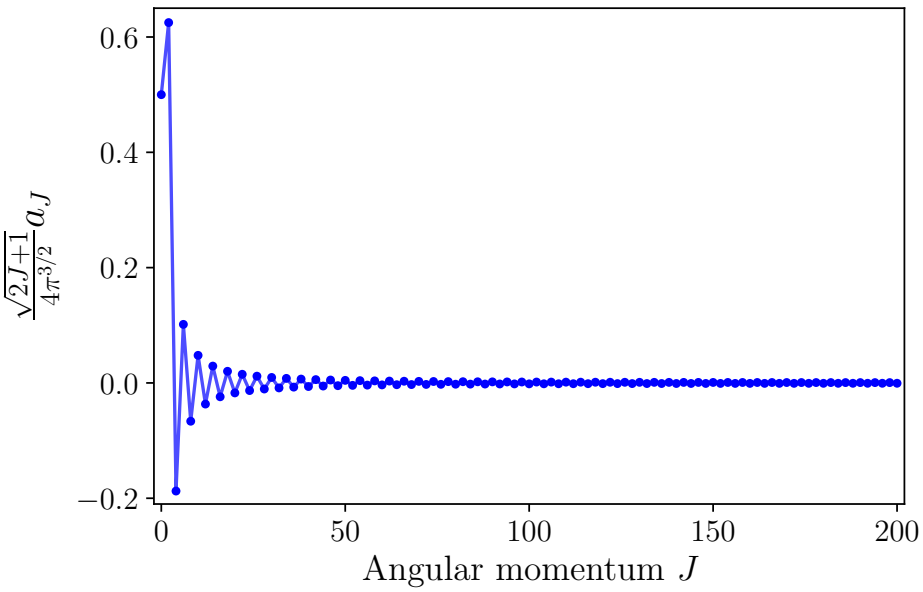

Figure A.1.: The first 200 expansion coefficients of $\cos^2\theta_{2D}$ in the basis of Wigner D-functions. Only non-zero coefficients for even J are shown, multiplied by $\frac{\sqrt{2J+1}}{4\pi^{3/2}}$.

in Figure A.1. The expansion converges fast and typically it suffices to include the first 50 to 100 coefficients in calculations. The coefficients, multiplied by the factor $\frac{\sqrt{2J+1}}{4\pi^{3/2}}$, are shown in Figure A.1. For an isotropic distribution the expected value of 0.5 is retrieved. Further details about the calculation of 2D expectation values, following the method presented above, can be found in [230].

When field-free alignment is employed, a coherent rotational wavepacket $\Psi(\theta, \phi, \chi, t)$ is formed. The field-free degree of alignment of such a wavepacket can be easily computed as

$$\langle\Psi(\theta,\phi,\chi,t)|\cos^2\theta_{2D}|\Psi(\theta,\phi,\chi,t)\rangle = \sum_{J,J'} c_J^*(t)c_{J'}(t)S_{J,J',M,K}\,, \tag{A.26}$$

with $S_{J,J',M,K}$ being the matrix containing the computed matrix elements and the c_J being the complex coefficients obtained from solving the TDSE.

For the comparison between experiment and theory in chapter 4 and chapter 6, another approach was followed to compute the required expectation values. First, the TDSE was solved for each state in the initial state distribution, which provided the time-dependent complex coefficients of all rotational states in each individual rotational wavepacket. The rotational density for each of these wavepackets was then computed for each timestep as a function of the Euler angles (θ, ϕ, χ). In chapter 6, the rotational density was computed individually for every hydrogen and carbon atom in indole. Subsequently, the rotational densities were projected onto a plane using a Monte-Carlo sampling method based on a metropolis algorithm. The Euler angles were randomly sampled and counts on the detector generated according to their detection probability, given by the value of the rotational density at the particular Euler angles. This procedure was followed for two main reasons. First, the Monte-Carlo simulation mimics the actual experiment and in this sense constitutes a computational experiment. The resulting 2D projected images can be directly compared to the experimental data and analyzed in the same way, i. e., the same observables can be extracted and compared. Finally, the method allows to easily extend the model and to include for example angle-dependent ionization probabilities and radial distributions, as presented in chapter 4.

B Molecular Data

Throughout this thesis three different molecules have been investigated, carbonyl sulfide (OCS), iodobenzene (IB) and indole. In this chapter, the main molecular properties and their values that were used in calculations are listed for these molecules.

B.1. Carbonyl Sulfide (OCS)

Carbonyl sulfide is a linear molecule composed of the three atoms oxygen, carbon and sulfur. Its equilibrium structure is schematically illustrated in Figure B.1 in a ball-and-stick model. Its properties are listed in table B.1.

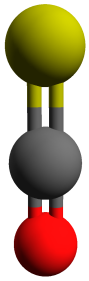

Figure B.1.: Schematic view of linear OCS molecule in a ball-and-stick model.

Molecular Property	Value	Reference
Chemical formula	OCS or COS	[298]
CAS registry number	463-58-1	[298]
Molecular weight	60.075 u	[298]
Rotational constant B_0	6081.492 439(134) MHz	[299]
Centrifugal distortion constant D_0	1.301 789(150) kHz	[299]
Ionization potential I_p	11.185(2) eV	[300]
Dipole moment	0.71519(3) D	[299]
Polarizability anisotropy	4.04(17) $Å^3$	[301]
O-C equilibrium bond length	115.43(10) pm	[299]
C-S equilibrium bond length	156.28(10) pm	[299]

Table B.1.: Molecular properties of carbonyl sulfide (OCS).

B.2. Iodobenzene (IB)

Iodobenzene is a planar asymmetric top rotor with its atomic constitutents being carbon, hydrogen and iodine. Its equilibrium structure is shown in a ball-and-stick model in Figure B.2 and its properties are listed in table B.2. Its polarizability tensor is diagonal in the principal axis system of inertia.

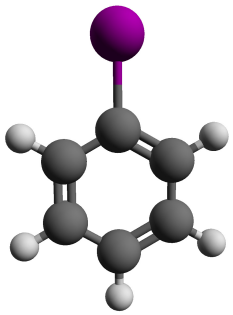

Figure B.2.: Schematic view of planar asymmetric top rotor iodobenzene in a ball-and-stick model.

Molecular Property	Value	Reference
Chemical formula	C_6H_5I	[298]
CAS registry number	591-50-4	[298]
Molecular weight	204.0084 u	[298]
Rotational constant A	5671.89(73) MHz	[302]
Rotational constant B	750.416(2) MHz	[302]
Rotational constant C	662.627(1) MHz	[302]
Dipole moment	1.625 D	[303]
Polarizability tensor entry α_{zz}	21.5 Å^3	[236]
Polarizability tensor entry α_{yy}	15.3 Å^3	[236]
Polarizability tensor entry α_{xx}	10.2 Å^3	[236]

Table B.2.: Molecular properties of iodobenzene (IB).

B.3. Indole

Indole is a planar asymmetric top rotor with its atomic constitutents being carbon, hydrogen and nitrogen. Its polarizability tensor is not diagonal in the principal axis system of inertia with the most polarizable axis forming an angle of 2.75 ° with respect to the a-axis. Its equilibrium structure is shown in a ball-and-stick model in Figure B.3 and its properties are listed in table B.3.

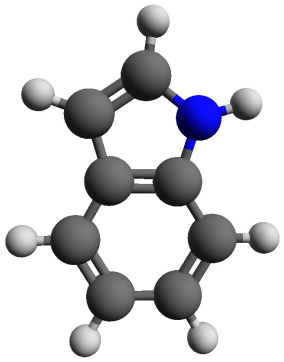

Figure B.3.: Schematic view of planar asymmetric top rotor indole in a ball-and-stick model.

Molecular Property	Value	Reference/Computation Method
Chemical formula	C_8H_7N	[298]
CAS registry number	120-72-9	[298]
Molecular weight	117.1479 u	[298]
Rotational constant A	3877.8366(64) MHz	[304]
Rotational constant B	1636.0461(48) MHz	[304]
Rotational constant C	1150.0900(19) MHz	[304]
Dipole moment component μ_z	1.36(3) D	[305]
Dipole moment component μ_x	1.59(12) D	[305]
Polarizability tensor entry α_{zz}	19.0572 Å^3	CCSD/aug-cc-pVTZ
Polarizability tensor entry α_{yy}	14.6608 Å^3	CCSD/aug-cc-pVTZ
Polarizability tensor entry α_{xx}	8.2546 Å^3	CCSD/aug-cc-pVTZ
Polarizability tensor entry α_{zy}	0.2182 Å^3	CCSD/aug-cc-pVTZ

Table B.3.: Molecular properties of indole.

C Detector Calibration

In order to calibrate the velocity map imaging spectrometer (VMIS), photoelectron momentum distributions (PEMDs) of OCS, Neon, Argon and Xenon were recorded for wavelengths of 400 nm and 800 nm of the ionizing laser. The measured angularly-resolved momentum distributions show clear above-threshold ionization (ATI) rings, equally spaced by one photon energy. These peaks were used to calibrate the detector and to convert from momentum measured in pixel to momentum measured in atomic units.

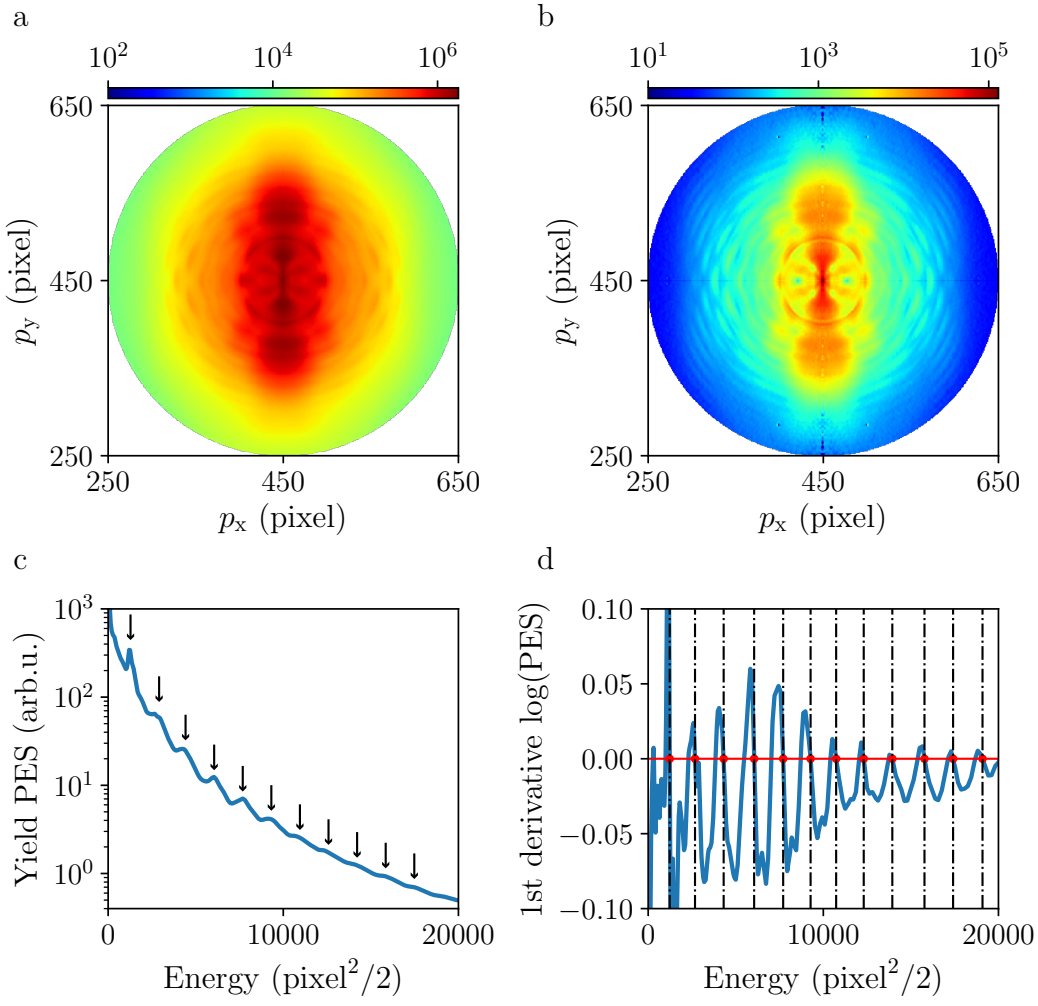

Figure C.1.: Photoelectron momentum distribution of Neon, ionized by a 400 nm laser pulse, with clear ATI structures being observed. **a** 2D PEMD of Neon, ionized by a 400 nm pulse, **b** central slice through 3D Abel-inverted PEMD, **c** angularly-integrated kinetic-energy spectrum **d** first derivative of the logarithm of the kinetic-energy spectrum, shown in **c**. The zeros determine the extrema, with the red dots showing the exact position of the maxima corresponding to the ATI peaks.

In Figure C.1 a-b, the measured 2D and the central slice through the 3D Abel-inverted PEMDs are shown for Neon, ionized at a wavelength of 400 nm. In Figure C.1 c, the angularly-integrated photoelectron spectrum (PES) is shown as a function of kinetic energy, measured in pixel^2/2. The rough positions of the ATI peaks are indicated by black arrows. In Figure C.1 d, the first derivative of the logarithm of the PES is plotted with red dots indicating the exact position of the zeros corresponding to maxima in the PES. The zeros corresponding to minima are not marked. For better visibility also black dashed lines were plotted to point out the exact position of the maxima in the PES, i. e., the ATI peaks.

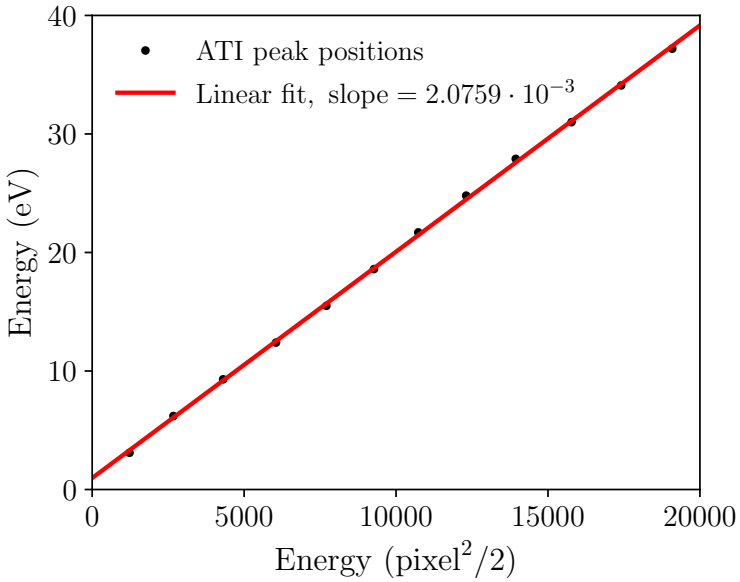

Figure C.2.: Detector calibration of velocity map imaging spectrometer (VMIS) employing ATI of Neon at 400 nm. The slope of the fitted line determines the scaling factor to convert from momentum in pixel to momentum or energy in atomic units.

Successive ATI peaks differ by exactly one photon energy, which for a wavelength of 400 nm amounts to 3.1 eV. In Figure C.2, the photon energy is plotted as a function of the ATI peak positions that were determined as the zeros of the first derivative of the PES. A line, determined through linear regression, was fitted through the data points and a slope of $2.0759 \cdot 10^{-3}$ obtained, i. e., the energy scaling factor. From the slope the conversion factor to convert momentum in pixel to momentum in atomic units can be determined through the relation

$$p[\text{a.u.}] = \sqrt{2E[a.u.]} \mathrel{\widehat{=}} \sqrt{\frac{\text{slope} \times \text{voltage}}{\text{Hartree}}} \times \text{pixel} \tag{C.1}$$

where E is the photoelectron kinetic energy in atomic units, voltage is the voltage applied at the repeller electrode and measured in kV, and 1 Hartree = 27.211 396 eV, corresponding to 1 atomic unit of energy. The measurement shown in Figure C.1 a was obtained for a repeller voltage of 3.1 eV. Therefore, the scaling factor has to be

normalized to 1 kV. In this way the final detector calibration of

$$p[\text{a.u.}] \mathrel{\widehat{=}} \sqrt{\frac{6.89 \cdot 10^{-4} \times \text{voltage}}{\text{Hartree}}} \times \text{pixel} \tag{C.2}$$

was obtained. ATI spectra were regularly recorded during the experiments and it was checked that the energy scaling factor increased linearly with the repeller voltage, such that equation (C.1) is valid. The average over all ATI calibration measurements yielded a scaling factor of $6.9 \cdot 10^{-4}$, which was used throughout this thesis.

Bibliography

[1] Y.-P. Chang, D. A. Horke, S. Trippel, and J. Küpper, "Spatially-controlled complex molecules and their applications," Int. Rev. Phys. Chem. **34**, 557–590 (2015), arXiv:1505.05632 [physics] .

[2] I. Hargittai and M. Hargittai, *Stereochemical Applications of Gas-Phase Electron Diffraction* (VCH Verlagsgesellschaft, Weinheim, Germany, 1988).

[3] M. Chergui and A. H. Zewail, "Electron and x-ray methods of ultrafast structural dynamics: Advances and applications," ChemPhysChem **10**, 28–43 (2009).

[4] A. L. Robinson, "Electron microscope inventors share nobel physics prize," Science **234**, 821–822 (1986).

[5] E. Callaway, "The revolution will not be crystallized: a new method sweeps through structural biology," Nature **525**, 172–174 (2015).

[6] P. B. Corkum and F. Krausz, "Attosecond science," Nat. Phys. **3**, 381–387 (2007).

[7] J. P. Gordon, H. J. Zeiger, and C. H. Townes, "The Maser - new type of microwave amplifier, frequency standard, and spectrometer," Phys. Rev. **99**, 1264–1274 (1955).

[8] T. Maiman, "Stimulated optical radiation in ruby," Nature **187**, 493–494 (1960).

[9] A. H. Zewail, "Femtochemistry: Atomic-scale dynamics of the chemical bond," J. Phys. Chem. A **104**, 5660–5694 (2000).

[10] A. H. Zewail, "Femtochemistry. Past, present, and future," Pure & Appl. Chem. **72**, 2219–2231 (2000).

[11] Pellegrini, C., "The history of x-ray free-electron lasers," Eur. Phys. J. H **37**, 659–708 (2012).

[12] A. Barty, J. Küpper, and H. N. Chapman, "Molecular imaging using x-ray free-electron lasers," Annu. Rev. Phys. Chem. **64**, 415–435 (2013).

[13] K. J. Gaffney and H. N. Chapman, "Imaging atomic structure and dynamics with ultrafast x-ray scattering," Science **316**, 1444–1448 (2007).

[14] J. Küpper, S. Stern, L. Holmegaard, F. Filsinger, A. Rouzée, A. Rudenko, P. Johnsson, A. V. Martin, M. Adolph, A. Aquila, S. Bajt, A. Barty, C. Bostedt, J. Bozek, C. Caleman, R. Coffee, N. Coppola, T. Delmas, S. Epp, B. Erk, L. Foucar, T. Gorkhover, L. Gumprecht, A. Hartmann, R. Hartmann, G. Hauser, P. Holl, A. Hömke, N. Kimmel, F. Krasniqi, K.-U. Kühnel, J. Maurer, M. Messerschmidt, R. Moshammer, C. Reich, B. Rudek, R. Santra, I. Schlichting, C. Schmidt, S. Schorb, J. Schulz, H. Soltau, J. C. H. Spence, D. Starodub, L. Strüder, J. Thøgersen, M. J. J. Vrakking, G. Weidenspointner, T. A. White, C. Wunderer, G. Meijer, J. Ullrich, H. Stapelfeldt, D. Rolles, and H. N. Chapman, "X-ray diffraction from isolated and strongly aligned gas-phase molecules with a free-electron laser," Phys. Rev. Lett. **112**, 083002 (2014), arXiv:1307.4577 [physics] .

[15] H. N. Chapman, A. Barty, M. J. Bogan, S. Boutet, S. Frank, S. P. Hau-Riege, S. Marchesini, B. W. Woods, S. Bajt, W. H. Benner, L. W. A., E. Plönjes, M. Kuhlmann, R. Treusch, S. Düsterer, T. Tschentscher, J. R. Schneider, E. Spiller,

T. Möller, C. Bostedt, M. Hoener, D. A. Shapiro, K. O. Hodgson, D. van der Spoel, F. Burmeister, M. Bergh, C. Caleman, G. Huldt, M. M. Seibert, F. R. N. C. Maia, R. W. Lee, A. Szöke, N. Timneanu, and J. Hajdu, "Femtosecond diffractive imaging with a soft-x-ray free-electron laser," Nat. Phys. **2**, 839–843 (2006).

[16] H. N. Chapman and K. A. Nugent, "Coherent lensless x-ray imaging," Nat. Photon. **4**, 833–839 (2010).

[17] S. Stern, L. Holmegaard, F. Filsinger, A. Rouzée, A. Rudenko, P. Johnsson, A. V. Martin, A. Barty, C. Bostedt, J. D. Bozek, R. N. Coffee, S. Epp, B. Erk, L. Foucar, R. Hartmann, N. Kimmel, K.-U. Kühnel, J. Maurer, M. Messerschmidt, B. Rudek, D. G. Starodub, J. Thøgersen, G. Weidenspointner, T. A. White, H. Stapelfeldt, D. Rolles, H. N. Chapman, and J. Küpper, "Toward atomic resolution diffractive imaging of isolated molecules with x-ray free-electron lasers," Faraday Disc. **171**, 393 (2014), arXiv:1403.2553 [physics] .

[18] H. N. Chapman, "Imaging beyond the limits," in *Biology with FELs: Toward the Molecular Movie* (Lawrence Berkeley National Laboratory, Berkeley, CA 94720, USA, 2011).

[19] C. M. Günther, B. Pfau, R. Mitzner, B. Siemer, S. Roling, H. Zacharias, O. Kutz, I. Rudolph, D. Schondelmaier, R. Treusch, and S. Eisebitt, "Sequential femtosecond x-ray imaging," Nature Photonics **5**, 99–102 (2011).

[20] R. J. D. Miller, R. Ernstorfer, M. Harb, M. Gao, C. T. Hebeisen, H. Jean-Ruel, C. Lu, G. Moriena, and G. Sciaini, "'making the molecular movie': first frames," Acta Crystallogr A **66**, 137–156 (2010).

[21] M. M. Seibert, T. Ekeberg, F. R. N. C. Maia, M. Svenda, J. Andreasson, O. Jönsson, D. Odić, B. Iwan, A. Rocker, D. Westphal, M. Hantke, D. P. Deponte, A. Barty, J. Schulz, L. Gumprecht, N. Coppola, A. Aquila, M. Liang, T. A. White, A. Martin, C. Caleman, S. Stern, C. Abergel, V. Seltzer, J.-M. Claverie, C. Bostedt, J. D. Bozek, S. Boutet, A. A. Miahnahri, M. Messerschmidt, J. Krzywinski, G. Williams, K. O. Hodgson, M. J. Bogan, C. Y. Hampton, R. G. Sierra, D. Starodub, I. Andersson, S. Bajt, M. Barthelmess, J. C. H. Spence, P. Fromme, U. Weierstall, R. Kirian, M. Hunter, R. B. Doak, S. Marchesini, S. P. Hau-Riege, M. Frank, R. L. Shoeman, L. Lomb, S. W. Epp, R. Hartmann, D. Rolles, A. Rudenko, C. Schmidt, L. Foucar, N. Kimmel, P. Holl, B. Rudek, B. Erk, A. Hömke, C. Reich, D. Pietschner, G. Weidenspointner, L. Strüder, G. Hauser, H. Gorke, J. Ullrich, I. Schlichting, S. Herrmann, G. Schaller, F. Schopper, H. Soltau, K.-U. Kühnel, R. Andritschke, C.-D. Schröter, F. Krasniqi, M. Bott, S. Schorb, D. Rupp, M. Adolph, T. Gorkhover, H. Hirsemann, G. Potdevin, H. Graafsma, B. Nilsson, H. N. Chapman, and J. Hajdu, "Single mimivirus particles intercepted and imaged with an x-ray laser," Nature **470**, 78 (2011).

[22] R. Neutze, R. Wouts, D. van der Spoel, E. Weckert, and J. Hajdu, "Potential for biomolecular imaging with femtosecond X-ray pulses," Nature **406**, 752–757 (2000).

[23] Z. Huang and K. J. Kim, "Review of x-ray free-electron laser theory," Phys. Rev. ST Accel. Beams **10**, 1–26 (2007).

[24] N. L. M. Müller, S. Trippel, K. Długołęcki, and J. Küpper, "Electron gun for

diffraction experiments on controlled molecules," J. Phys. B **48**, 244001 (2015), arXiv:1507.02530 [physics] .

[25] J. Yang, J. Beck, C. J. Uiterwaal, and M. Centurion, "Imaging of alignment and structural changes of carbon disulfide molecules using ultrafast electron diffraction," Nat. Commun. **6**, 8172 (2015).

[26] J. Yang, M. Guehr, X. Shen, R. Li, T. Vecchione, R. Coffee, J. Corbett, A. Fry, N. Hartmann, C. Hast, K. Hegazy, K. Jobe, I. Makasyuk, J. Robinson, M. S. Robinson, S. Vetter, S. Weathersby, C. Yoneda, X. Wang, and M. Centurion, "Diffractive imaging of coherent nuclear motion in isolated molecules," Phys. Rev. Lett. **117**, 153002 (2016).

[27] S. P. Weathersby, G. Brown, M. Centurion, T. F. Chase, R. Coffee, J. Corbett, J. P. Eichner, J. C. Frisch, A. R. Fry, M. Gühr, N. Hartmann, C. Hast, R. Hettel, R. K. Jobe, E. N. Jongewaard, J. R. Lewandowski, R. K. Li, A. M. Lindenberg, I. Makasyuk, J. E. May, D. McCormick, M. N. Nguyen, A. H. Reid, X. Shen, K. Sokolowski-Tinten, T. Vecchione, S. L. Vetter, J. Wu, J. Yang, H. A. Dürr, and X. J. Wang, "Mega-electron-volt ultrafast electron diffraction at SLAC National Accelerator Laboratory," Rev. Sci. Instrum. **86**, 073702 (2015).

[28] H. Stapelfeldt, E. Constant, H. Sakai, and P. B. Corkum, "Time-resolved coulomb explosion imaging: A method to measure structure and dynamics of molecular nuclear wave packets," Phys. Rev. A **58**, 426–433 (1998).

[29] F. Légaré, K. F. Lee, I. V. Litvinyuk, P. W. Dooley, A. D. Bandrauk, D. M. Villeneuve, and P. B. Corkum, "Imaging the time-dependent structure of a molecule as it undergoes dynamics," Phys. Rev. A **72**, 052717 (2005).

[30] P. M. Paul, E. S. Toma, P. Breger, G. Mullot, F. Augé, P. Balcou, H. G. Muller, and P. Agostini, "Observation of a train of attosecond pulses from high harmonic generation," Science **292**, 1689–1692 (2001).

[31] M. Hentschel, R. Kienberger, C. Spielmann, G. A. Reider, N. Milosevic, T. Brabec, P. Corkum, U. Heinzmann, M. Drescher, and F. Krausz, "Attosecond metrology," Nature **414**, 509–513 (2001).

[32] C. Kleine, M. Ekimova, G. Goldsztejn, S. Raabe, C. Strüber, J. Ludwig, S. Yarlagadda, S. Eisebitt, M. J. J. Vrakking, T. Elsaesser, E. T. J. Nibbering, and A. Rouzée, "Soft x-ray absorption spectroscopy of aqueous solutions using a table-top femtosecond soft x-ray source," J. Phys. Chem. Lett. **10**, 52–58 (2019).

[33] J. Xu, C. I. Blaga, P. Agostini, and L. F. DiMauro, "Time-resolved molecular imaging," J. Phys. B **49**, 112001 (2016).

[34] T. Zuo, A. D. Bandrauk, and P. B. Corkum, "Laser-induced electron diffraction: a new tool for probing ultrafast molecular dynamics," Chem. Phys. Lett. **259**, 313–320 (1996).

[35] M. G. Pullen, B. Wolter, A.-T. Le, M. Baudisch, M. Hemmer, A. Senftleben, C. D. Schroter, J. Ullrich, R. Moshammer, C. D. Lin, and J. Biegert, "Imaging an aligned polyatomic molecule with laser-induced electron diffraction," Nat. Commun. **6**, 7262 (2015).

[36] C. I. Blaga, J. Xu, A. D. DiChiara, E. Sistrunk, K. Zhang, P. Agostini, T. A.

Miller, L. F. DiMauro, and C. D. Lin, "Imaging ultrafast molecular dynamics with laser-induced electron diffraction," Nature **483**, 194–197 (2012).

[37] M. Okunishi, T. Morishita, G. Prümper, K. Shimada, C. D. Lin, S. Watanabe, and K. Ueda, "Experimental retrieval of target structure information from laser-induced rescattered photoelectron momentum distributions," Phys. Rev. Lett. **100**, 143001 (2008).

[38] J. Xu, C. I. Blaga, A. D. DiChiara, E. Sistrunk, K. Zhang, Z. Chen, A.-T. Le, T. Morishita, C. D. Lin, P. Agostini, and L. F. DiMauro, "Laser-induced electron diffraction for probing rare gas atoms," Phys. Rev. Lett. **109**, 233002 (2012).

[39] J. Xu, C. I. Blaga, K. Zhang, Y. H. Lai, C. D. Lin, T. A. Miller, P. Agostini, and L. F. DiMauro, "Diffraction using laser-driven broadband electron wave packets," Nat. Commun. **5**, 4635 (2014).

[40] M. Meckel, D. Comtois, D. Zeidler, A. Staudte, D. Pavičić, H. C. Bandulet, H. Pépin, J. C. Kieffer, R. Dörner, D. M. Villeneuve, and P. B. Corkum, "Laser-induced electron tunneling and diffraction," Science **320**, 1478–1482 (2008).

[41] Y. Ito, R. Carranza, M. Okunishi, R. R. Lucchese, and K. Ueda, "Extraction of geometrical structure of ethylene molecules by laser-induced electron diffraction combined with ab initio scattering calculations," Phys. Rev. A **96**, 053414 (2017).

[42] Y. Ito, C. Wang, A.-T. Le, M. Okunishi, D. Ding, C. D. Lin, and K. Ueda, "Extracting conformational structure information of benzene molecules via laser-induced electron diffraction," Struct. Dyn. **3**, 034303 (2016).

[43] B. Wolter, M. G. Pullen, A. T. Le, M. Baudisch, K. Doblhoff-Dier, A. Senftleben, M. Hemmer, C. D. Schroter, J. Ullrich, T. Pfeifer, R. Moshammer, S. Gräfe, O. Vendrell, C. D. Lin, and J. Biegert, "Ultrafast electron diffraction imaging of bond breaking in di-ionized acetylene," Science **354**, 308–312 (2016).

[44] U. Even, "Pulsed supersonic beams from high pressure source: Simulation results and experimental measurements," Adv. Chem. **2014**, 636042 (2014).

[45] G. Scoles, ed., *Atomic and molecular beam methods*, vol. 1 of [187] (1988).

[46] M. Hillenkamp, S. Keinan, and U. Even, "Condensation limited cooling in supersonic expansions," J. Chem. Phys. **118**, 8699–8705 (2003).

[47] U. Even, J. Jortner, D. Noy, N. Lavie, and N. Cossart-Magos, "Cooling of large molecules below 1 K and He clusters formation," J. Chem. Phys. **112**, 8068–8071 (2000).

[48] W. Christen, K. Rademann, and U. Even, "Supersonic beams at high particle densities: Model description beyond the ideal gas approximation," J. Phys. Chem. A **114**, 11189–11201 (2010).

[49] W. Gerlach and O. Stern, "Der experimentelle Nachweis der Richtungsquantelung im Magnetfeld," Z. Phys. **9**, 349–352 (1922).

[50] S. Y. T. van de Meerakker, H. L. Bethlem, and G. Meijer, "Taming molecular beams," Nat. Phys. **4**, 595 (2008).

[51] H. L. Bethlem, G. Berden, and G. Meijer, "Decelerating neutral dipolar molecules," Phys. Rev. Lett. **83**, 1558–1561 (1999).

[52] D. Auerbach, E. E. A. Bromberg, and L. Wharton, "Alternate-gradient focusing of molecular beams," J. Chem. Phys. **45**, 2160 (1966).

[53] H. L. Bethlem, A. J. A. van Roij, R. T. Jongma, and G. Meijer, "Alternate gradient focusing and deceleration of a molecular beam," Phys. Rev. Lett. **88**, 133003 (2002).

[54] H. L. Bethlem, M. R. Tarbutt, J. Küpper, D. Carty, K. Wohlfart, E. A. Hinds, and G. Meijer, "Alternating gradient focusing and deceleration of polar molecules," J. Phys. B **39**, R263–R291 (2006), arXiv:0604020 [physics] .

[55] J. J. Gilijamse, S. Hoekstra, S. Y. T. van de Meerakker, G. C. Groenenboom, and G. Meijer, "Near-threshold inelastic collisions using molecular beams with a tunable velocity," Science **313**, 1617–1620 (2006).

[56] J. van Veldhoven, J. Küpper, H. L. Bethlem, B. Sartakov, A. J. A. van Roij, and G. Meijer, "Decelerated molecular beams for high-resolution spectroscopy: The hyperfine structure of $^{15}ND_3$," Eur. Phys. J. D **31**, 337–349 (2004).

[57] E. R. Hudson, H. J. Lewandowski, B. C. Sawyer, and J. Ye, "Cold molecule spectroscopy for constraining the evolution of the fine structure constant," Phys. Rev. Lett. **96**, 143004 (2006).

[58] H. L. Bethlem, G. Berden, F. M. H. Crompvoets, R. T. Jongma, A. J. A. van Roij, and G. Meijer, "Electrostatic trapping of ammonia molecules," Nature **406**, 491–494 (2000).

[59] H. L. Bethlem, F. M. H. Crompvoets, R. T. Jongma, S. Y. T. van de Meerakker, and G. Meijer, "Deceleration and trapping of ammonia using time-varying electric fields," Phys. Rev. A **65**, 053416 (2002).

[60] J. J. Gilijamse, S. Hoekstra, S. A. Meek, M. Metsälä, S. Y. T. v. de Meerakker, G. Meijer, and G. C. Groenenboom, "The radiative lifetime of metastable CO (a $^3\Pi$, v=0)," J. Chem. Phys. **127**, 221102 (2007).

[61] J. S. Kienitz, K. Długołęcki, S. Trippel, and J. Küpper, "Improved spatial separation of neutral molecules," J. Chem. Phys. **147**, 024304 (2017), arXiv:1704.08912 [physics] .

[62] J. H. Nielsen, P. Simesen, C. Z. Bisgaard, H. Stapelfeldt, F. Filsinger, B. Friedrich, G. Meijer, and J. Küpper, "Stark-selected beam of ground-state OCS molecules characterized by revivals of impulsive alignment," Phys. Chem. Chem. Phys. **13**, 18971–18975 (2011), arXiv:1105.2413 [physics] .

[63] L. D. Carr, D. DeMille, R. V. Krems, and J. Ye, "Cold and ultracold molecules: science, technology and applications," New J. Phys. **11**, 055049 (2009).

[64] T. P. Rakitzis, A. J. van den Brom, and M. H. M. Janssen, "Directional dynamics in the photodissociation of oriented molecules," Science **303**, 1852–1854 (2004).

[65] P. R. Brooks and E. M. Jones, "Reactive scattering of K atoms from oriented CH_3I molecules," J. Chem. Phys. **45**, 3449 (1966).

[66] D. Pavičić, K. F. Lee, D. M. Rayner, P. B. Corkum, and D. M. Villeneuve, "Direct measurement of the angular dependence of ionization for N_2, O_2, and CO_2 in intense laser fields," Phys. Rev. Lett. **98**, 243001 (2007).

[67] R. Boll, D. Anielski, C. Bostedt, J. D. Bozek, L. Christensen, R. Coffee, S. De, P. Decleva, S. W. Epp, B. Erk, L. Foucar, F. Krasniqi, J. Küpper, A. Rouzée, B. Rudek, A. Rudenko, S. Schorb, H. Stapelfeldt, M. Stener, S. Stern, S. Techert, S. Trippel, M. J. J. Vrakking, J. Ullrich, and D. Rolles, "Femtosecond photoelectron

diffraction on laser-aligned molecules: Towards time-resolved imaging of molecular structure," Phys. Rev. A **88**, 061402(R) (2013).

[68] F. Filsinger, G. Meijer, H. Stapelfeldt, H. Chapman, and J. Küpper, "State- and conformer-selected beams of aligned and oriented molecules for ultrafast diffraction studies," Phys. Chem. Chem. Phys. **13**, 2076–2087 (2011), arXiv:1009.0871 [physics] .

[69] P. Reckenthaeler, M. Centurion, W. Fuss, S. A. Trushin, F. Krausz, and E. E. Fill, "Time-resolved electron diffraction from selectively aligned molecules," Phys. Rev. Lett. **102**, 213001 (2009).

[70] H. Stapelfeldt and T. Seideman, "Colloquium: Aligning molecules with strong laser pulses," Rev. Mod. Phys. **75**, 543–557 (2003).

[71] P. R. Brooks, "Reactions of oriented molecules," Science **193**, 11 (1976).

[72] D. H. Parker and R. B. Bernstein, "Oriented molecule beams via the electrostatic hexapole - preparation, characterization, and reactive scattering," Annu. Rev. Phys. Chem. **40**, 561–595 (1989).

[73] H. J. Loesch and A. Remscheid, "Brute force in molecular reaction dynamics: A novel technique for measuring steric effects," J. Chem. Phys. **93**, 4779 (1990).

[74] H. Loesch and J. Möller, "Reactive scattering from brute force oriented asymmetric top molecules: $K+C_6H_5I \rightarrow KI+C_6H_5$," J. Phys. Chem. A **101**, 7534–7543 (1997).

[75] B. Friedrich and D. R. Herschbach, "On the possibility of orienting rotationally cooled polar molecules in an electric field," Z. Phys. D **18**, 153–161 (1991).

[76] B. Friedrich and D. R. Herschbach, "Spatial orientation of molecules in strong electric fields and evidence for pendular states," Nature **353**, 412–414 (1991).

[77] J. Bulthuis, J. Möller, and H. J. Loesch, "Brute force orientation of asymmetric top molecules," J. Phys. Chem. A **101**, 7684–7690 (1997).

[78] B. Friedrich and D. Herschbach, "Alignment and trapping of molecules in intense laser fields," Phys. Rev. Lett. **74**, 4623–4626 (1995).

[79] T. Seideman, "Rotational excitation and molecular alignment in intense laser fields," J. Chem. Phys. **103**, 7887 (1995).

[80] J. Underwood, B. Sussman, and A. Stolow, "Field-free three dimensional molecular axis alignment," Phys. Rev. Lett. **94** (2005), 10.1103/PhysRevLett.94.143002.

[81] K. F. Lee, D. M. Villeneuve, P. B. Corkum, A. Stolow, and J. G. Underwood, "Field-free three-dimensional alignment of polyatomic molecules," Phys. Rev. Lett. **97**, 173001 (2006).

[82] A. Rouzee, S. Guerin, O. Faucher, and B. Lavorel, "Field-free molecular alignment of asymmetric top molecules using elliptically polarized laser pulses," Phys. Rev. A **77**, 043412 (2008).

[83] S. S. Viftrup, V. Kumarappan, S. Trippel, H. Stapelfeldt, E. Hamilton, and T. Seideman, "Holding and spinning molecules in space," Phys. Rev. Lett. **99**, 143602 (2007).

[84] B. Friedrich and D. Herschbach, "Polarization of molecules induced by intense nonresonant laser fields," J. Phys. Chem. **99**, 15686 (1995).

[85] W. Kim and P. M. Felker, "Spectroscopy of pendular states in optical-field-aligned species," J. Chem. Phys. **104**, 1147–1150 (1996).

[86] H. Sakai, C. P. Safvan, J. J. Larsen, K. M. Hilligsøe, K. Hald, and H. Stapelfeldt, "Controlling the alignment of neutral molecules by a strong laser field," J. Chem. Phys. **110**, 10235–10238 (1999).

[87] J. J. Larsen, H. Sakai, C. P. Safvan, I. Wendt-Larsen, and H. Stapelfeldt, "Aligning molecules with intense nonresonant laser fields," J. Chem. Phys. **111**, 7774 (1999).

[88] S. Trippel, J. Wiese, T. Mullins, and J. Küpper, "Communication: Strong laser alignment of solvent-solute aggregates in the gas-phase," J. Chem. Phys. **148**, 101103 (2018), arXiv:1801.08789 [physics] .

[89] T. Seideman, "On the dynamics of rotationally broad, spatially aligned wave packets," J. Chem. Phys. **115**, 5965 (2001).

[90] T. Seideman, "Revival structure of aligned rotational wave packets," Phys. Rev. Lett. **83**, 4971–4974 (1999).

[91] T. Seideman and E. Hamilton, "Nonadiabatic alignment by intense pulses. concepts, theory, and directions," Adv. Atom. Mol. Opt. Phys. **52**, 289–329 (2005).

[92] F. Rosca-Pruna and M. J. J. Vrakking, "Experimental observation of revival structures in picosecond laser-induced alignment of I_2," Phys. Rev. Lett. **87**, 153902 (2001).

[93] A. Rouzee, S. Guerin, V. Boudon, B. Lavorel, and O. Faucher, "Field-free one-dimensional alignment of ethylene molecule," Phys. Rev. A **73**, 033418–9 (2006).

[94] C. Z. Bisgaard, S. S. Viftrup, and H. Stapelfeldt, "Alignment enhancement of a symmetric top molecule by two short laser pulses," Phys. Rev. A **73**, 053410 (2006).

[95] C. Bisgaard, M. Poulsen, E. Péronne, S. Viftrup, and H. Stapelfeldt, "Observation of enhanced field-free molecular alignment by two laser pulses," Phys. Rev. Lett. **92**, 173004 (2004).

[96] M. Leibscher, I. Averbukh, and H. Rabitz, "Molecular alignment by trains of short laser pulses," Phys. Rev. Lett. **90**, 213001 (2003).

[97] J. P. Cryan, P. H. Bucksbaum, and R. N. Coffee, "Field-free alignment in repetitively kicked nitrogen gas," Phys. Rev. A **80**, 063412 (2009).

[98] K. Lee, I. Litvinyuk, P. Dooley, M. Spanner, D. Villeneuve, and P. Corkum, "Two-pulse alignment of molecules," J. Phys. B **37**, L43–L48 (2004).

[99] M. J. J. Vrakking and S. Stolte, "Coherent control of molecular orientation," Chem. Phys. Lett. **271**, 209–215 (1997).

[100] S. S. Viftrup, V. Kumarappan, L. Holmegaard, C. Z. Bisgaard, H. Stapelfeldt, M. Artamonov, E. Hamilton, and T. Seideman, "Controlling the rotation of asymmetric top molecules by the combination of a long and a short laser pulse," Phys. Rev. A **79**, 023404 (2009).

[101] M. D. Poulsen, T. Ejdrup, H. Stapelfeldt, E. Hamilton, and T. Seideman, "Alignment enhancement by the combination of a short and a long laser pulse," Physical Review A **73**, 033405 (2006).

[102] J. Underwood, M. Spanner, M. Ivanov, J. Mottershead, B. Sussman, and A. Stolow, "Switched wave packets: A route to nonperturbative quantum control," Phys. Rev. Lett. **90** (2003), 10.1103/PhysRevLett.90.223001.

[103] A. Rouzée, E. Hertz, B. Lavorel, and O. Faucher, "Towards the adaptive optimization of field-free molecular alignment," J. Phys. B **41**, 074002 (2008).

[104] R. S. Judson and H. Rabitz, "Teaching lasers to control molecules," Phys. Rev. Lett. **68**, 1500–1503 (1992).

[105] A. Rouzee, A. Gijsbertsen, O. Ghafur, O. M. Shir, T. Baeck, S. Stolte, and M. J. J. Vrakking, "Optimization of laser field-free orientation of a state-selected no molecular sample," New J. Phys. **11**, 105040 (2009).

[106] O. Ghafur, A. Rouzée, A. Gijsbertsen, W. K. Siu, S. Stolte, and M. J. J. Vrakking, "Impulsive orientation and alignment of quantum-state-selected NO molecules," Nat. Phys. **5**, 289–293 (2009).

[107] I. Nevo, L. Holmegaard, J. H. Nielsen, J. L. Hansen, H. Stapelfeldt, F. Filsinger, G. Meijer, and J. Küpper, "Laser-induced 3D alignment and orientation of quantum state-selected molecules," Phys. Chem. Chem. Phys. **11**, 9912–9918 (2009), arXiv:0906.2971 [physics] .

[108] L. Holmegaard, J. H. Nielsen, I. Nevo, H. Stapelfeldt, F. Filsinger, J. Küpper, and G. Meijer, "Laser-induced alignment and orientation of quantum-state-selected large molecules," Phys. Rev. Lett. **102**, 023001 (2009), arXiv:0810.2307 [physics] .

[109] F. Filsinger, J. Küpper, G. Meijer, L. Holmegaard, J. H. Nielsen, I. Nevo, J. L. Hansen, and H. Stapelfeldt, "Quantum-state selection, alignment, and orientation of large molecules using static electric and laser fields," J. Chem. Phys. **131**, 064309 (2009), arXiv:0903.5413 [physics] .

[110] S. Trippel, T. Mullins, N. L. M. Müller, J. S. Kienitz, J. J. Omiste, H. Stapelfeldt, R. González-Férez, and J. Küpper, "Strongly driven quantum pendulum of the carbonyl sulfide molecule," Phys. Rev. A **89**, 051401(R) (2014), arXiv:1401.6897 [quant-ph] .

[111] S. Trippel, T. Mullins, N. L. M. Müller, J. S. Kienitz, R. González-Férez, and J. Küpper, "Two-state wave packet for strong field-free molecular orientation," Phys. Rev. Lett. **114**, 103003 (2015), arXiv:1409.2836 [physics] .

[112] B. Friedrich and D. Herschbach, "Enhanced orientation of polar molecules by combined electrostatic and nonresonant induced dipole forces," J. Chem. Phys. **111**, 6157 (1999).

[113] B. Friedrich and D. Herschbach, "Manipulating molecules via combined static and laser fields," J. Phys. Chem. A **103**, 10280–10288 (1999).

[114] L. Cai, J. Marango, and B. Friedrich, "Time-Dependent Alignment and Orientation of Molecules in Combined Electrostatic and Pulsed Nonresonant Laser Fields," Phys. Rev. Lett. **86**, 775–778 (2001).

[115] J. J. Omiste, M. Gaerttner, P. Schmelcher, R. González-Férez, L. Holmegaard, J. H. Nielsen, H. Stapelfeldt, and J. Küpper, "Theoretical description of adiabatic laser alignment and mixed-field orientation: the need for a non-adiabatic model," Phys. Chem. Chem. Phys. **13**, 18815–18824 (2011), arXiv:1105.0534 [physics] .

[116] J. H. Nielsen, H. Stapelfeldt, J. Küpper, B. Friedrich, J. J. Omiste, and R. González-Férez, "Making the best of mixed-field orientation of polar molecules: A recipe for achieving adiabatic dynamics in an electrostatic field combined with laser pulses," Phys. Rev. Lett. **108**, 193001 (2012), arXiv:1204.2685 [physics] .

[117] J. S. Kienitz, S. Trippel, T. Mullins, K. Długołęcki, R. González-Férez, and J. Küpper, "Adiabatic mixed-field orientation of ground-state-selected carbonyl

sulfide molecules," Chem. Phys. Chem. **17**, 3740–3746 (2016), arXiv:1607.05615 [physics] .

[118] J. Ullrich, R. Moshammer, R. Dörner, O. Jagutzki, V. Mergel, H. Schmidt-Böcking, and L. Spielberger, "Recoil-ion momentum spectroscopy," J. Phys. B **30**, 2917–2974 (1997).

[119] J. Ullrich, R. Moshammer, A. Dorn, R. Dörner, L. P. H. Schmidt, and H. Schmidt-Böcking, "Recoil-ion and electron momentum spectroscopy: reaction-microscopes," Rep. Prog. Phys. **66**, 1463–1545 (2003).

[120] T. Arion and U. Hergenhahn, "Coincidence spectroscopy: Past, present and perspectives," J. Electron. Spectrosc. Relat. Phenom. **200**, 222–231 (2015).

[121] P. Morin, M. Simon, C. Miron, N. Leclercq, and D. L. Hansen, "Electron-ion spectroscopy: a probe of molecular dynamics," J. Electron. Spectrosc. Relat. Phenom. **93**, 49–60 (1998).

[122] B. Wolter, M. G. Pullen, M. Baudisch, M. Sclafani, M. Hemmer, A. Senftleben, C. D. Schröter, J. Ullrich, R. Moshammer, and J. Biegert, "Strong-field physics with mid-IR fields," Phys. Rev. X **5**, 021034 (2015).

[123] D. M. Bishop, "Molecular vibrational and rotational motion in static and dynamic electric fields," Rev. Mod. Phys. **62**, 343–374 (1990).

[124] A. T. J. B. Eppink and D. H. Parker, "Velocity map imaging of ions and electrons using electrostatic lenses: Application in photoelectron and photofragment ion imaging of molecular oxygen," Rev. Sci. Instrum. **68**, 3477–3484 (1997).

[125] J. L. Hansen, J. J. Omiste, J. H. Nielsen, D. Pentlehner, J. Küpper, R. González-Férez, and H. Stapelfeldt, "Mixed-field orientation of molecules without rotational symmetry," J. Chem. Phys. **139**, 234313 (2013), arXiv:1308.1216 [physics] .

[126] W. Gordy and R. L. Cook, *Microwave Molecular Spectra*, 3rd ed. (John Wiley & Sons, New York, NY, USA, 1984).

[127] R. N. Zare, *Angular Momentum* (John Wiley & Sons, New York, NY, USA, 1988).

[128] J. Stark, "Beobachtungen über den effekt des elektrischen feldes auf spektrallinien. i. quereffekt," Ann. Phys. **348**, 965–982 (1914).

[129] Y.-P. Chang, F. Filsinger, B. Sartakov, and J. Küpper, "CMIstark: Python package for the stark-effect calculation and symmetry classification of linear, symmetric and asymmetric top wavefunctions in dc electric fields," Comp. Phys. Comm. **185**, 339–349 (2014), arXiv:1308.4076 [physics] .

[130] S. Trippel, M. Johny, T. Kierspel, J. Onvlee, H. Bieker, H. Ye, T. Mullins, L. Gumprecht, K. Długołęcki, and J. Küpper, "Knife edge skimming for improved separation of molecular species by the deflector," Rev. Sci. Instrum. **89**, 096110 (2018), arXiv:1802.04053 [physics] .

[131] D. A. Horke, Y.-P. Chang, K. Długołęcki, and J. Küpper, "Separating para and ortho water," Angew. Chem. Int. Ed. **53**, 11965–11968 (2014), arXiv:1407.2056 [physics] .

[132] A. Monmayrant, S. Weber, and B. Chatel, "A newcomer's guide to ultrashort pulse shaping and characterization," J. Phys. B **43**, 103001 (2010).

[133] A. M. Weiner, D. E. Leaird, J. S. Patel, and J. R. Wullert, "Programmable

femtosecond pulse shaping by use of a multielement liquid-crystal phase modulator," Opt. Lett. **15**, 326–328 (1990).

[134] A. M. Weiner, "Femtosecond pulse shaping using spatial light modulators," Rev. Sci. Instrum. **71**, 1929–1960 (2000).

[135] A. M. Weiner, "Ultrafast optical pulse shaping: A tutorial review," Opt. Comm. **284**, 3669–3692 (2011).

[136] B. Friedrich, D. P. Pullman, and D. R. Herschbach, "Alignment and orientation of rotationally cool molecules," J. Chem. Phys. **95**, 8118–8129 (1991).

[137] V. Makhija, X. Ren, and V. Kumarappan, "Metric for three-dimensional alignment of molecules," Phys. Rev. A **85**, 033425 (2012).

[138] V. Dribinski, A. Ossadtchi, V. A. Mandelshtam, and H. Reisler, "Reconstruction of Abel-transformable images: The Gaussian basis-set expansion Abel transform method," Rev. Sci. Instrum. **73**, 2634 (2002).

[139] A. Messiah, *Quantum mechanics* (North-Holland, 1965).

[140] S. Ramakrishna and T. Seideman, "Rotational wave-packet imaging of molecules," Phys. Rev. A **87**, 023411 (2013).

[141] P. R. Bunker and P. Jensen, *Fundamentals of Molecular Symmetry*, Series in Chemical Physics (Institute of Physics Publishing, Bristol, UK, 2005).

[142] P. W. Dooley, I. V. Litvinyuk, K. F. Lee, D. M. Rayner, M. Spanner, D. M. Villeneuve, and P. B. Corkum, "Direct imaging of rotational wave-packet dynamics of diatomic molecules," Phys. Rev. A **68**, 023406 (2003).

[143] P. W. Joireman, L. L. Connell, S. M. Ohline, and P. M. Felker, "Characterization of asymmetry transients in rotational coherence spectroscopy," J. Chem. Phys. **96**, 4118–4130 (1992).

[144] E. Peronne, M. Poulsen, C. Bisgaard, H. Stapelfeldt, and T. Seideman, "Nonadiabatic alignment of asymmetric top molecules: Field-free alignment of iodobenzene," Phys. Rev. Lett. **91**, 04300 (2003).

[145] L. Holmegaard, S. S. Viftrup, V. Kumarappan, C. Z. Bisgaard, H. Stapelfeldt, E. Hamilton, and T. Seideman, "Control of rotational wave-packet dynamics in asymmetric top molecules," Phys. Rev. A **75**, 051403 (2007).

[146] S. Pabst and R. Santra, "Alignment of asymmetric-top molecules using multiple-pulse trains," Phys. Rev. A **81**, 065401 (2010).

[147] X. Ren, V. Makhija, and V. Kumarappan, "Multipulse three-dimensional alignment of asymmetric top molecules," Phys. Rev. Lett. **112**, 173602 (2014).

[148] S. Pabst, "Atomic and molecular dynamics triggered by ultrashort light pulses on the atto- to picosecond time scale," Eur. Phys. J. Special Topics **221**, 1–71 (2013).

[149] Y. Ohshima and H. Hasegawa, "Coherent rotational excitation by intense nonresonant laser fields," Int. Rev. Phys. Chem. **29**, 619–663 (2010).

[150] S. Guérin, "Strategies for efficient field-free molecular alignment and its control," J. Mod. Opt. **55**, 3193–3201 (2008).

[151] D. M. Villeneuve, S. Aseyev, A. Avery, and P. B. Corkum, "Using frequency-domain manipulation of stretched femtosecond laser pulses to create fast rise and fall times on picosecond pulses," Applied Physics B **74**, S157 – S161 (2002).

[152] J. J. Omiste and R. González-Férez, "Nonadiabatic effects in long-pulse mixed-field orientation of a linear polar molecule," Phys. Rev. A **86**, 043437 (2012).

[153] J. J. Omiste and R. González-Férez, "Rotational dynamics of an asymmetric-top molecule in parallel electric and nonresonant laser fields," Phys. Rev. A **88**, 033416 (2013).

[154] J. J. Omiste and R. González-Férez, "Theoretical description of mixed-field orientation of asymmetric top molecules: a time-dependent study," Phys. Rev. A **94**, 063408 (2016), arXiv:1610.01284 [physics] .

[155] J. J. Omiste, R. González-Férez, and P. Schmelcher, "Rotational spectrum of asymmetric top molecules in combined static and laser fields," J. Chem. Phys. **135**, 064310 (2011), arXiv:1106.1586 [physics] .

[156] C. Leforestier, R. H. Bisseling, C. Cerjan, M. D. Feit, R. Friesner, A. Guldberg, A. Hammerich, G. Jolicard, W. Karrlein, H.-D. Meyer, N. Lipkin, O. Roncero, and R. Kosloff, "A comparison of different propagation schemes for the time dependent Schrödinger equation," J. Comput. Phys. **94**, 59–80 (1991).

[157] M. Beck, A. Jäckle, G. Worth, and H.-D. Meyer, "The multiconfiguration time-dependent-Hartree (MCTDH) method: a highly efficient algorithm for propagating wavepackets," Phys. Rep. **324**, 1–105 (2000).

[158] A. Owens and A. Yachmenev, "RichMol: A general variational approach for rovibrational molecular dynamics in external electric fields," J. Chem. Phys. **148**, 124102 (2018).

[159] S. N. Yurchenko, W. Thiel, and P. Jensen, "Theoretical ROVibrational energies (TROVE): A robust numerical approach to the calculation of rovibrational energies for polyatomic molecules," J. Mol. Spectrosc. **245**, 126–140 (2007).

[160] R. B. Sidje, "Expokit: a software package for computing matrix exponentials," ACM Trans. Math. Soft. **24**, 130–156 (1998).

[161] H.-P. Schwefel, *Evolution and Optimum Seeking*, The Sixth Generation Computer Technology Series (John Wiley & Sons, New York, NY, USA, 1993).

[162] R. Storn and K. Price, "Differential evolution – a simple and efficient heuristic for global optimization over continuous spaces," J. Glob. Opt. **11**, 341–359 (1997).

[163] F.-A. Fortin, F.-M. De Rainville, M.-A. G. Gardner, M. Parizeau, and C. Gagné, "Deap: Evolutionary algorithms made easy," J. Mach. Learn. Res. **13**, 2171–2175 (2012).

[164] T. Bäck, *Evolutionary Algorithms in Theory and Practice: Evolution Strategies, Evolutionary Programming, Genetic Algorithms* (Oxford University Press, Inc., New York, NY, USA, 1996).

[165] P. Lambropoulos, "Topics on multiphoton processes in atoms," (Adv. Phys., 1976) pp. 87 – 164.

[166] W. Becker, F. Grasbon, R. Kopold, D. B. Milošević, G. G. Paulus, and H. Walther, "Above-threshold ionization: From classical features to quantum effects," Adv. Atom. Mol. Opt. Phys. **48**, 35–98 (2002).

[167] Z. Chen, T. Morishita, A.-T. Le, M. Wickenhauser, X. M. Tong, and C. D. Lin, "Analysis of two-dimensional photoelectron momentum spectra and the effect of

the long-range coulomb potential in single ionization of atoms by intense lasers," Phys. Rev. A **74**, 053405 (2006).

[168] D. G. Arbó, K. I. Dimitriou, E. Persson, and J. Burgdörfer, "Sub-Poissonian angular momentum distribution near threshold in atomic ionization by short laser pulses," Phys. Rev. A **78**, 1418 (2008).

[169] C. Z. Bisgaard and L. B. Madsen, "Tunneling ionization of atoms," Am. J. Phys. **72**, 249–254 (2004).

[170] M. V. Ammosov, N. B. Delone, and V. P. Krainov, "Tunnel ionization of complex atoms and of atomic ions in an alternating electromagnetic field," Soviet Physics - JETP **64**, 1191–1194 (1986).

[171] L. Keldysh, "Ionization in the field of a strong electromagnetic wave," J. Exp. Theor. Phys. **20**, 1307–1314 (1965).

[172] F. H. M. Faisal, "Multiple absorption of laser photons by atoms," J. Phys. B **6**, L89 (1973).

[173] H. R. Reiss, "Effect of an intense electromagnetic field on a weakly bound system," Phys. Rev. A **22**, 1786–1813 (1980).

[174] S. V. Popruzhenko, "Keldysh theory of strong field ionization: history, applications, difficulties and perspectives," J. Phys. B **47**, 204001 (2014).

[175] M. Y. Ivanov, M. Spanner, and O. Smirnova, "Anatomy of strong field ionization," J. Mod. Opt. **52**, 165–184 (2005).

[176] K. C. Kulander, K. J. Schafer, and J. L. Krause, "Dynamics of short-pulse excitation, ionization and harmonic conversion," in *Super-Intense Laser-Atom Physics*, Nato Science Series B: Physics, Vol. 316, edited by A. L'Huillier, B. Piraux, and K. Rzazewski (Plenum Press, New York, 1993) pp. 95–110.

[177] P. B. Corkum, "Plasma perspective on strong-field multiphoton ionization," Phys. Rev. Lett. **71**, 1994–1997 (1993).

[178] G. G. Paulus, W. Becker, W. Nicklich, and H. Walther, "Rescattering effects in above threshold ionization: a classical model," J. Phys. B **27**, L703–L708 (1994).

[179] A. Trabattoni, S. Trippel, U. D. Giovannini, J. F. Olivieri, J. Wiese, T. Mullins, J. Onvlee, S.-K. Son, A. R. Biagio Frusteri, and J. Küpper, "Setting the clock of photoelectron emission through molecular alignment," (2018), arXiv:1802.06622 [physics] .

[180] Z. Chen, A.-T. Le, T. Morishita, and C. D. Lin, "Quantitative rescattering theory for laser-induced high-energy plateau photoelectron spectra," Phys. Rev. A **79**, 033409 (2009).

[181] T. Morishita, A.-T. Le, Z. Chen, and C. D. Lin, "Accurate retrieval of structural information from laser-induced photoelectron and high-order harmonic spectra by few-cycle laser pulses," Phys. Rev. Lett. **100**, 013903 (2008).

[182] C. D. Lin, A.-T. Le, Z. Chen, T. Morishita, and R. Lucchese, "Strong-field rescattering physics - self-imaging of a molecule by its own electrons," J. Phys. B **43**, 122001 (2010).

[183] R. Bonham and M. Fink, *High Energy Electron Scattering* (Van Nostrand Reinhold Company, 1974).

[184] C. D. Lin, A.-T. Le, C. Jin, and H. Wei, *Attosecond and Strong-Field Physics: Principles and Applications* (Cambridge University Press, 2018).

[185] J. Als-Nielsen and D. McMorrow, *Elements of Modern X-ray Physics* (John Wiley & Sons, Chichester, West Sussex, United Kingdom, 2001).

[186] P. Colosimo, G. Doumy, C. I. Blaga, J. Wheeler, C. Hauri, F. Catoire, J. Tate, R. Chirla, A. M. March, G. G. Paulus, H. G. Muller, P. Agostini, and L. F. DiMauro, "Scaling strong-field interactions towards the classical limit," Nat. Phys. **4**, 386–389 (2008).

[187] G. Scoles, ed., *Atomic and molecular beam methods*, Vol. 1 (Oxford University Press, New York, NY, USA, 1988).

[188] D. H. Levy, "The spectroscopy of very cold gases," Science **214**, 263–269 (1981).

[189] A. A. Ischenko, P. M. Weber, and R. J. D. Miller, "Capturing chemistry in action with electrons: Realization of atomically resolved reaction dynamics," Chem. Rev. **117**, 11066–11124 (2017).

[190] K. Ayyer, O. M. Yefanov, D. Oberthür, S. Roy-Chowdhury, L. Galli, V. Mariani, S. Basu, J. Coe, C. E. Conrad, R. Fromme, A. Schaffer, K. Dörner, D. James, C. Kupitz, M. Metz, G. Nelson, P. L. Xavier, K. R. Beyerlein, M. Schmidt, I. Sarrou, J. C. H. Spence, U. Weierstall, T. A. White, J.-H. Yang, Y. Zhao, M. Liang, A. Aquila, M. S. Hunter, J. S. Robinson, J. E. Koglin, S. Boutet, P. Fromme, A. Barty, and H. N. Chapman, "Macromolecular diffractive imaging using imperfect crystals," Nature **530**, 202–206 (2016).

[191] C. J. Hensley, J. Yang, and M. Centurion, "Imaging of isolated molecules with ultrafast electron pulses," Phys. Rev. Lett. **109**, 133202 (2012).

[192] K. Pande, C. D. M. Hutchison, G. Groenhof, A. Aquila, J. S. Robinson, J. Tenboer, S. Basu, S. Boutet, D. P. DePonte, M. Liang, T. A. White, N. A. Zatsepin, O. Yefanov, D. Morozov, D. Oberthuer, C. Gati, G. Subramanian, D. James, Y. Zhao, J. Koralek, J. Brayshaw, C. Kupitz, C. Conrad, S. Roy-Chowdhury, J. D. Coe, M. Metz, P. L. Xavier, T. D. Grant, J. E. Koglin, G. Ketawala, R. Fromme, V. Šrajer, R. Henning, J. C. H. Spence, A. Ourmazd, P. Schwander, U. Weierstall, M. Frank, P. Fromme, A. Barty, H. N. Chapman, K. Moffat, J. J. van Thor, and M. Schmidt, "Femtosecond structural dynamics drives the trans/cis isomerization in photoactive yellow protein," Science **352**, 725–729 (2016).

[193] P. M. Felker, J. S. Baskin, and A. H. Zewail, "Rephasing of collisionless molecular rotational coherence in large molecules," J. Phys. Chem. **90**, 724–728 (1986).

[194] K. Mizuse, K. Kitano, H. Hasegawa, and Y. Ohshima, "Quantum unidirectional rotation directly imaged with molecules," Science Advances **1**, e1400185 (2015).

[195] C. Marceau, V. Makhija, D. Platzer, A. Y. Naumov, P. B. Corkum, A. Stolow, D. M. Villeneuve, and P. Hockett, "Molecular frame reconstruction using time-domain photoionization interferometry," Phys. Rev. Lett. **119**, 083401 (2017).

[196] J. Yang, M. Guehr, T. Vecchione, M. S. Robinson, R. Li, N. Hartmann, X. Shen, R. Coffee, J. Corbett, A. Fry, K. Gaffney, T. Gorkhover, C. Hast, K. Jobe, I. Makasyuk, A. Reid, J. Robinson, S. Vetter, F. Wang, S. Weathersby, C. Yoneda, M. Centurion, and X. Wang, "Diffractive imaging of a rotational wavepacket

in nitrogen molecules with femtosecond megaelectronvolt electron pulses," Nat. Commun. **7**, 11232 (2016).

[197] P. M. Felker, "Rotational coherence spectroscopy: studies of the geometries of large gas-phase species by picosecond time-domain methods," J. Phys. Chem. **96**, 7844–7857 (1992).

[198] C. Riehn, "High-resolution pump-probe rotational coherence spectroscopy - rotational constants and structure of ground and electronically excited states of large molecular systems," Chem. Phys. **283**, 297–329 (2002).

[199] K. Lee, D. Villeneuve, P. Corkum, and E. Shapiro, "Phase control of rotational wave packets and quantum information," Phys. Rev. Lett. **93**, 233601 (2004).

[200] A. S. Mouritzen and K. Mølmer, "Quantum state tomography of molecular rotation," J. Chem. Phys. **124**, 244311 (2006).

[201] H. Hasegawa and Y. Ohshima, "Quantum state reconstruction of a rotational wave packet created by a nonresonant intense femtosecond laser field," Phys. Rev. Lett. **101**, 053002 (2008).

[202] M. Berry, I. Marzoli, and W. Schleich, "Quantum carpets, carpets of light," Phys. World **14**, 39–46 (2001).

[203] S. Guérin, A. Rouzée, and E. Hertz, "Ultimate field-free molecular alignment by combined adiabatic-impulsive field design," Phys. Rev. A **77**, 041404 (2008).

[204] M. Pitzer, M. Kunitski, A. S. Johnson, T. Jahnke, H. Sann, F. Sturm, L. P. H. Schmidt, H. Schmidt-Böcking, R. Dörner, J. Stohner, J. Kiedrowski, M. Reggelin, S. Marquardt, A. Schießer, R. Berger, and M. S. Schöffler, "Direct determination of absolute molecular stereochemistry in gas phase by Coulomb explosion imaging," Science **341**, 1096–1100 (2013).

[205] L. Christensen, J. H. Nielsen, C. B. Brandt, C. B. Madsen, L. B. Madsen, C. S. Slater, A. Lauer, M. Brouard, M. P. Johansson, B. Shepperson, and H. Stapelfeldt, "Dynamic stark control of torsional motion by a pair of laser pulses," Phys. Rev. Lett. **113**, 073005 (2014).

[206] A. Owens, A. Yachmenev, S. N. Yurchenko, and J. Küpper, "Climbing the Rotational Ladder to Chirality," Phys. Rev. Lett. **121**, 193201 (2018), arXiv:1802.07803 [physics] .

[207] E. W. Kuipers, M. G. Tenner, A. Kleyn, and S. Stolte, "Observation of steric effects in gas-surface scattering," Nature **334**, 420–422 (1988).

[208] J. Itatani, J. Levesque, D. Zeidler, H. Niikura, H. Pépin, J. C. Kieffer, P. B. Corkum, and D. M. Villeneuve, "Tomographic imaging of molecular orbitals," Nature **432**, 867–871 (2004).

[209] L. Holmegaard, J. L. Hansen, L. Kalhøj, S. L. Kragh, H. Stapelfeldt, F. Filsinger, J. Küpper, G. Meijer, D. Dimitrovski, M. Abu-samha, C. P. J. Martiny, and L. B. Madsen, "Photoelectron angular distributions from strong-field ionization of oriented molecules," Nat. Phys. **6**, 428 (2010), arXiv:1003.4634 [physics] .

[210] S. J. Weber, M. Oppermann, and J. P. Marangos, "Role of rotational wave packets in strong field experiments," Phys. Rev. Lett. **111**, 263601 (2013).

[211] H. Rabitz, R. de Vivie-Riedle, M. Motzkus, and K. Kompa, "Chemistry – whither the future of controlling quantum phenomena?" Science **288**, 824–828 (2000).

[212] C. Brif, R. Chakrabarti, and H. Rabitz, "Control of quantum phenomena: past, present and future," New J. Phys. **12**, 075008 (2010).

[213] T. Brixner and G. Gerber, "Quantum control of gas-phase and liquid-phase femtochemistry," Chem. Phys. Chem. **4**, 418–438 (2003).

[214] M. Renard, E. Hertz, B. Lavorel, and O. Faucher, "Controlling ground-state rotational dynamics of molecules by shaped femtosecond laser pulses," Phys. Rev. A **69**, 043401 (2004).

[215] M. Renard, E. Hertz, S. Guérin, H. R. Jauslin, B. Lavorel, and O. Faucher, "Control of field-free molecular alignment by phase-shaped laser pulses," Phys. Rev. A **72**, 025401 (2005).

[216] C. Horn, M. Wollenhaupt, M. Krug, T. Baumert, R. de Nalda, and L. Bañares, "Adaptive control of molecular alignment," Phys. Rev. A **73**, 031401 (2006).

[217] T. Suzuki, Y. Sugawara, S. Minemoto, and H. Sakai, "Optimal control of nonadiabatic alignment of rotationally cold n_2 molecules with the feedback of degree of alignment," Phys. Rev. Lett. **100**, 033603 (2008).

[218] A. Stolow, "Applications of wavepacket methodology," Phil. Trans. R. Soc. A **356**, 345–362 (1998).

[219] J. R. R. Verlet, V. G. Stavros, R. S. Minns, and H. H. Fielding, "Controlling the radial dynamics of Rydberg wavepackets in Xe using phase-locked optical pulse sequences," J. Phys. B **36**, 3683 (2003).

[220] F. Calegari, D. Ayuso, A. Trabattoni, L. Belshaw, S. De Camillis, S. Anumula, F. Frassetto, L. Poletto, A. Palacios, P. Decleva, J. B. Greenwood, F. Martín, and M. Nisoli, "Ultrafast electron dynamics in phenylalanine initiated by attosecond pulses," Science **346**, 336–339 (2014).

[221] Z.-C. Yan and T. Seideman, "Photomanipulation of external molecular modes: A time-dependent self-consistent-field approach," J. Chem. Phys. **111**, 4113–4120 (1999).

[222] B. J. Sussman, J. G. Underwood, R. Lausten, M. Y. Ivanov, and A. Stolow, "Quantum control via the dynamic Stark effect: Application to switched rotational wave packets and molecular axis alignment," Phys. Rev. A **73**, 053403 (2006).

[223] A. J. Alcock, P. B. Corkum, and D. J. James, "A fast scalable switching technique for high–power CO_2 laser radiation," Appl. Phys. Lett. **27**, 680–682 (1975).

[224] A. Goban, S. Minemoto, and H. Sakai, "Laser-field-free molecular orientation," Phys. Rev. Lett. **101**, 013001 (2008).

[225] J. H. Mun, D. Takei, S. Minemoto, and H. Sakai, "Laser-field-free orientation of state-selected asymmetric top molecules," Phys. Rev. A **89**, 051402 (2014).

[226] D. Takei, J. H. Mun, S. Minemoto, and H. Sakai, "Laser-field-free three-dimensional molecular orientation," Phys. Rev. A **94**, 013401 (2016).

[227] S. Trippel, T. Mullins, N. L. M. Müller, J. S. Kienitz, K. Długołęcki, and J. Küpper, "Strongly aligned and oriented molecular samples at a kHz repetition rate," Mol. Phys. **111**, 1738 (2013), arXiv:1301.1826 [physics] .

[228] B. Shepperson, A. S. Chatterley, L. Christiansen, A. A. Søndergaard, and H. Stapelfeldt, "Observation of rotational revivals for iodine molecules in helium droplets using a near-adiabatic laser pulse," Phys. Rev. A **97**, 013427 (2018).

[229] B. Shepperson, A. A. Søndergaard, L. Christiansen, J. Kaczmarczyk, R. E. Zillich, M. Lemeshko, and H. Stapelfeldt, "Laser-Induced Rotation of Iodine Molecules in Helium Nanodroplets: Revivals and Breaking Free," Phys. Rev. Lett. **118**, 203203 (2017).

[230] A. A. Søndergaard, B. Shepperson, and H. Stapelfeldt, "Nonadiabatic laser-induced alignment of molecules: Reconstructing $\langle \cos^2 \theta \rangle$ directly from $\langle \cos^2 \theta_{2d} \rangle$ by Fourier analysis," J. Chem. Phys. **147**, 013905 (2017).

[231] L. V. Thesing, J. Küpper, and R. González-Férez, "Time-dependent analysis of the mixed-field orientation of molecules without rotational symmetry," J. Chem. Phys. **146**, 244304 (2017), arXiv:1705.03225 [physics.chem-ph] .

[232] T. Kierspel, J. Wiese, T. Mullins, J. Robinson, A. Aquila, A. Barty, R. Bean, R. Boll, S. Boutet, P. Bucksbaum, H. N. Chapman, L. Christensen, A. Fry, M. Hunter, J. E. Koglin, M. Liang, V. Mariani, A. Morgan, A. Natan, V. Petrovic, D. Rolles, A. Rudenko, K. Schnorr, H. Stapelfeldt, S. Stern, J. Thøgersen, C. H. Yoon, F. Wang, S. Trippel, and J. Küpper, "Strongly aligned molecules at free-electron lasers," J. Phys. B **48**, 204002 (2015), arXiv:1506.03650 [physics] .

[233] A. Chatterley, B. Sheperson, and H. Stapelfeldt, "Three-dimensional molecular alignment inside helium nanodroplets," Phys. Rev. Lett. **119**, 073202 (2017).

[234] V. Loriot, P. Tzallas, E. P. Benis, E. Hertz, B. Lavorel, D. Charalambidis, and O. Faucher, "Laser-induced field-free alignment of the OCS molecule," J. Phys. B **40**, 2503 (2007).

[235] M. Di Fraia, P. Finetti, R. Richter, K. C. Prince, J. Wiese, M. Devetta, M. Negro, C. Vozzi, A. G. Ciriolo, A. Pusala, A. Demidovich, M. B. Danailov, E. T. Karamatskos, S. Trippel, J. Kupper, and C. Callegari, "Impulsive laser-induced alignment of OCS molecules at FERMI," Phys. Chem. Chem. Phys. **19**, 19733–19739 (2017).

[236] M. D. Poulsen, E. Peronne, H. Stapelfeldt, C. Z. Bisgaard, S. Viftrup, E. Hamilton, and T. Seideman, "Nonadiabatic alignment of asymmetric top molecules: Rotational revivals," J. Chem. Phys. **121**, 783–791 (2004).

[237] X. Ren, V. Makhija, and V. Kumarappan, "Measurement of field-free alignment of jet-cooled molecules by nonresonant femtosecond degenerate four-wave mixing," Phys. Rev. A **85**, 033405 (2012).

[238] M. Poulsen, E. Skovsen, and H. Stapelfeldt, "Photodissociation of laser aligned iodobenzene: Towards selective photoexcitation," J. Chem. Phys. **117**, 2097–2102 (2002).

[239] M. Tsubouchi, B. J. Whitaker, L. Wang, H. Kohguchi, and T. Suzuki, "Photoelectron Imaging on Time-Dependent Molecular Alignment Created by a Femtosecond Laser Pulse," Phys. Rev. Lett. **86**, 4500–4503 (2001).

[240] J.-H. Mun, *Laser-field-free and field-free orientation of state-selected molecules*, Ph.D. thesis, University of Tokyo (2015).

[241] R. Torres, N. Kajumba, J. G. Underwood, J. S. Robinson, S. Baker, J. W. G. Tisch, R. de Nalda, W. A. Bryan, R. Velotta, C. Altucci, I. C. E. Turcu, and J. P. Marangos, "Probing orbital structure of polyatomic molecules by high-order harmonic generation," Phys. Rev. Lett. **98**, 203007 (2007).

[242] S. G. Walt, B. N. Ram, M. Atala, N. I. Shvetsov-Shilovski, A. von Conta, D. Baykusheva, M. Lein, and H. J. Wörner, "Dynamics of valence-shell electrons and nuclei probed by strong-field holography and rescattering," Nat. Commun. **8**, 15651 (2017).

[243] M. Meckel, A. Staudte, S. Patchkovskii, D. M. Villeneuve, P. B. Corkum, R. Dörner, and M. Spanner, "Signatures of the continuum electron phase in molecular strong-field photoelectron holography," Nat. Phys. **10**, 594–600 (2014).

[244] C. Vozzi, M. Negro, F. Calegari, G. Sansone, M. Nisoli, S. De Silvestri, and S. Stagira, "Generalized molecular orbital tomography," Nat. Phys. **7**, 822–826 (2011).

[245] F. Rosca-Pruna and M. J. J. Vrakking, "Revival structures in picosecond laser-induced alignemnt of I_2 molecules. ii. numerical modeling," J. Chem. Phys. **116**, 6579 (2002).

[246] E. T. Karamatskos, S. Raabe, T. Mullins, A. Trabattoni, P. Stammer, G. Goldsztejn, R. R. Johansen, K. Długołęcki, H. Stapelfeldt, M. J. J. Vrakking, S. Trippel, A. Rouzée, and J. Küpper, "Molecular movie of ultrafast coherent rotational dynamics," (2018), arXiv:1807.01034 .

[247] A. Chatterley, E. T. Karamatskos, C. Schouder, L. Christiansen, A. V. Jörgensen, T. Mullins, J. Küpper, and H. Stapelfeldt, "Switched wave packets with spectrally truncated chirped pulses," J. Chem. Phys. **148**, 221105 (2018).

[248] T. Brinck, J. Murray, and P. Politzer, "Polarizability and volume," J. Chem. Phys. **98**, 4305–4306 (1993).

[249] M. Amin, H. Samy, and J. Küpper, "Robust and accurate computational estimation of the polarizability tensors of macromolecules," J. Phys. Chem. Lett. (2019), 10.1021/acs.jpclett.9b00963, arXiv:1904.02504 [physics] .

[250] H. Niikura, F. Legare, R. Hasbani, A. D. Bandrauk, M. Y. Ivanov, D. M. Villeneuve, and P. B. Corkum, "Sub-laser-cycle electron pulses for probing molecular dynamics," Nature **417**, 917–922 (2002).

[251] A. M. Weiner, D. E. Leaird, J. S. Patel, and J. R. Wullert, "Programmable shaping of femtosecond optical pulses by use of 128-element liquid crystal phase modulator," IEEE Journal of Quantum Electronics **28**, 908–920 (1992).

[252] E. Kukk, H. Myllynen, K. Nagaya, S. Wada, J. D. Bozek, T. Takanashi, D. You, A. Niozu, K. Kooser, T. Gaumnitz, E. Pelimanni, M. Berholts, S. Granroth, N. Yokono, H. Fukuzawa, C. Miron, and K. Ueda, "Coulomb implosion of tetrabromothiophene observed under multiphoton ionization by free-electron-laser soft-x-ray pulses," Phys. Rev. A **99**, 023411 (2019).

[253] T. Kierspel, C. Bomme, M. Di Fraia, J. Wiese, D. Anielski, S. Bari, R. Boll, B. Erk, J. S. Kienitz, N. L. M. Müller, D. Rolles, J. Viefhaus, S. Trippel, and J. Küpper, "Photophysics of indole upon x-ray absorption," Phys. Chem. Chem. Phys. **20**, 20205 (2018), arXiv:1802.02964 [physics] .

[254] D. Popova-Gorelova, J. Küpper, and R. Santra, "Imaging electron dynamics with time- and angle-resolved photoelectron spectroscopy," Phys. Rev. A **94**, 013412 (2016).

[255] C. Kang, T. M. Korter, and D. W. Pratt, "Experimental measurement of the

induced dipole moment of an isolated molecule in its ground and electronically excited states: Indole and indole–H_2O," J. Chem. Phys. **122**, 174301 (2005).

[256] T. H. Dunning, "Gaussian basis sets for use in correlated molecular calculations. I. The atoms boron through neon and hydrogen," J. Chem. Phys. **90**, 1007 (1989).

[257] R. A. Kendall, T. H. Dunning, Jr., and R. J. Harrison, "Electron affinities of the first-row atoms revisited. Systematic basis sets and wave functions," J. Chem. Phys. **96**, 6796–6806 (1992).

[258] K. Aidas, C. Angeli, K. L. Bak, V. Bakken, R. Bast, L. Boman, O. Christiansen, R. Cimiraglia, S. Coriani, P. Dahle, E. K. Dalskov, U. Ekström, T. Enevoldsen, J. J. Eriksen, P. Ettenhuber, B. Fernández, L. Ferrighi, H. Fliegl, L. Frediani, K. Hald, A. Halkier, C. Hättig, H. Heiberg, T. Helgaker, A. C. Hennum, H. Hettema, E. Hjertenæs, S. Høst, I.-M. Høyvik, M. F. Iozzi, B. Jansík, H. J. Aa. Jensen, D. Jonsson, P. Jørgensen, J. Kauczor, S. Kirpekar, T. Kjærgaard, W. Klopper, S. Knecht, R. Kobayashi, H. Koch, J. Kongsted, A. Krapp, K. Kristensen, A. Ligabue, O. B. Lutnæs, J. I. Melo, K. V. Mikkelsen, R. H. Myhre, C. Neiss, C. B. Nielsen, P. Norman, J. Olsen, J. M. H. Olsen, A. Osted, M. J. Packer, F. Pawlowski, T. B. Pedersen, P. F. Provasi, S. Reine, Z. Rinkevicius, T. A. Ruden, K. Ruud, V. V. Rybkin, P. Sałek, C. C. M. Samson, A. S. de Merás, T. Saue, S. P. A. Sauer, B. Schimmelpfennig, K. Sneskov, A. H. Steindal, K. O. Sylvester-Hvid, P. R. Taylor, A. M. Teale, E. I. Tellgren, D. P. Tew, A. J. Thorvaldsen, L. Thøgersen, O. Vahtras, M. A. Watson, D. J. D. Wilson, M. Ziolkowski, and H. Ågren, "The Dalton quantum chemistry program system," WIREs Comput. Mol. Sci. **4**, 269–284 (2014).

[259] N. Tajima, "Analytical formula for numerical evaluations of the wigner rotation matrices at high spins," Phys. Rev. C **91**, 014320 (2015).

[260] J. M. Glownia, A. Natan, J. P. Cryan, R. Hartsock, M. Kozina, M. P. Minitti, S. Nelson, J. Robinson, T. Sato, T. van Driel, G. Welch, C. Weninger, D. Zhu, and P. H. Bucksbaum, "Self-referenced coherent diffraction x-ray movie of ångstrom- and femtosecond-scale atomic motion," Phys. Rev. Lett. **117**, 153003 (2016), arXiv:1608.03039 [physics] .

[261] M. Spanner, O. Smirnova, P. B. Corkum, and M. Y. Ivanov, "Reading diffraction images in strong field ionization of diatomic molecules," J. Phys. B **37**, L243–L250 (2004).

[262] M. Brouard, A. V. Green, F. Quadrini, and C. Vallance, "Photodissociation dynamics of ocs at 248nm: The s(d21) atomic angular momentum polarization," J. Chem. Phys. **127**, 084304 (2007).

[263] T. Suzuki, H. Katayanagi, S. Nanbu, and M. Aoyagi, "Nonadiabatic bending dissociation in 16 valence electron system OCS," J. Chem. Phys. **109**, 5778–5794 (1998).

[264] N. Sivakumar, I. Burak, W. Y. Cheung, P. L. Houston, and J. W. Hepburn, "State-resolved photofragmentation of carbonyl sulfide (OCS) monomers and clusters," J. Phys. Chem. **89**, 3609–3611 (1985), https://doi.org/10.1021/j100263a008 .

[265] J. H. Sanderson, T. R. J. Goodworth, A. El-Zein, W. A. Bryan, W. R. Newell, A. J. Langley, and P. F. Taday, "Coulombic and pre-coulombic geometry evolution of

carbonyl sulfide in an intense femtosecond laser pulse, determined by momentum imaging," Phys. Rev. A **65**, 043403 (2002).

[266] F. Salvat, A. Jablonski, and C. Powell, "ELSEPA - Dirac partial-wave calculation of elastic scattering of electrons and positrons by atoms, positive ions and molecules," Comp. Phys. Comm. **165**, 157–190 (2005).

[267] T. W. Dakin, W. E. Good, and D. K. Coles, "Bond distances in OCS from microwave absorption lines," Phys. Rev. **71**, 640–641 (1947).

[268] N. Teschmit, D. A. Horke, and J. Küpper, "Spatially separating the conformers of the dipeptide Ac-Phe-Cys-NH_2," Angew. Chem. Int. Ed. **57**, 13775–13779 (2018), arXiv:1805.12396 [physics] .

[269] J. Xu, Z. Chen, A.-T. Le, and C. D. Lin, "Self-imaging of molecules from diffraction spectra by laser-induced rescattering electrons," Phys. Rev. A **82**, 033403 (2010).

[270] W. C. Fon, K. A. Berrington, P. G. Burke, and A. Hibbert, "The elastic scattering of electrons from inert gases. III. Argon," J. Phys. B **16**, 307 (1983).

[271] W. C. Fon, K. A. Berrington, and A. Hibbert, "The elastic scattering of electrons from inert gases. IV. Krypton," J. Phys. B **17**, 3279–3294 (1984).

[272] H. Murai, Y. Ishijima, T. Mitsumura, Y. Sakamoto, H. Kato, M. Hoshino, F. Blanco, G. Garcia, P. Limao-Vieira, M. J. Brunger, S. J. Buckman, and H. Tanaka, "A comprehensive and comparative study of elastic electron scattering from OCS and CS_2 in the energy region from 1.2 to 200 eV," J. Chem. Phys. **138**, 054302 (2013).

[273] S. E. Michelin, T. Kroin, I. Iga, M. G. P. Homem, H. S. Miglio, and M. T. Lee, "Elastic and total cross sections for electron-carbonyl sulfide collisions," J. Phys. B **33**, 3293 (2000).

[274] F. Schell, T. Bredtmann, C.-P. Schulz, S. Patchkovskii, M. J. J. Vrakking, and J. Mikosch, "Molecular orbital imprint in laser-driven electron recollision," Science Advances **4**, eaap8148 (2018).

[275] F. Krečinić, P. Wopperer, B. Frusteri, F. Brauße, J.-G. Brisset, U. De Giovannini, A. Rubio, A. Rouzée, and M. J. J. Vrakking, "Multiple-orbital effects in laser-induced electron diffraction of aligned molecules," Phys. Rev. A **98**, 041401 (2018).

[276] G. Bilalbegovic, "Carbonyl sulphide under strong laser field: time-dependent density functional theory," Eur. Phys. J. D **49**, 43–49 (2008).

[277] A. Rouzée, Y. Huismans, F. Kelkensberg, A. Smolkowska, J. H. Jungmann, A. Gijsbertsen, W. K. Siu, G. Gademann, A. Hundertmark, P. Johnsson, and M. J. J. Vrakking, "Molecular movies from molecular frame photoelectron angular distribution (mf-pad) measurements," in *Ultrafast Phenomena in Molecular Sciences: Femtosecond Physics and Chemistry*, edited by R. de Nalda and L. Bañares (Springer International Publishing, Cham, 2014) pp. 1–24.

[278] J. L. Hansen, L. Holmegaard, J. H. Nielsen, D. Stapelfeldt, H.and Dimitrovski, and L. B. Madsen, "Orientation-dependent ionization yields from strong-field ionization of fixed-in-space linear and asymmetric top molecules," Journal of Physics B-Atomic Molecular and Optical Physics **45**, 015101 (2011).

[279] R. Johansen, K. G. Bay, L. Christensen, J. Thøgersen, D. Dimitrovski, L. B. Madsen, and H. Stapelfeldt, "Alignment-dependent strong-field ionization yields of carbonyl

sulfide molecules induced by mid-infrared laser pulses," J. Phys. B **49**, 205601 (2016).

[280] C. Wu, H. Zhang, H. Yang, Q. Gong, D. Song, and H. Su, "Tunneling ionization of carbon dioxide from lower-lying orbitals," Phys. Rev. A **83**, 033410 (2011).

[281] J. Mikosch, A. E. Boguslavskiy, I. Wilkinson, M. Spanner, S. Patchkovskii, and A. Stolow, "Channel- and angle-resolved above threshold ionization in the molecular frame," Phys. Rev. Lett. **110**, 023004 (2013).

[282] Y. Huismans, A. Rouzee, A. Gijsbertsen, J. H. Jungmann, A. S. Smolkowska, P. S. W. M. Logman, F. Lepine, C. Cauchy, S. Zamith, T. Marchenko, J. M. Bakker, G. Berden, B. Redlich, A. F. G. Van Der Meer, H. G. Muller, W. Vermin, K. J. Schafer, M. Spanner, M. Y. Ivanov, O. Smirnova, D. Bauer, S. V. Popruzhenko, and M. J. J. Vrakking, "Time-resolved holography with photoelectrons," Science **331**, 61–64 (2011).

[283] X.-B. Bian and A. D. Bandrauk, "Attosecond time-resolved imaging of molecular structure by photoelectron holography," Phys. Rev. Lett. **108**, 263003 (2012).

[284] D. D. Hickstein, P. Ranitovic, S. Witte, X.-M. Tong, Y. Huismans, P. Arpin, X. Zhou, K. E. Keister, C. W. Hogle, B. Zhang, C. Ding, P. Johnsson, N. Toshima, M. J. J. Vrakking, M. M. Murnane, and H. C. Kapteyn, "Direct visualization of laser-driven electron multiple scattering and tunneling distance in strong-field ionization," Phys. Rev. Lett. **109**, 073004 (2012).

[285] M. Abu-samha and L. B. Madsen, "Theory of strong-field ionization of aligned CO_2," Phys. Rev. A **80**, 023401 (2009).

[286] V. Kumarappan, L. Holmegaard, C. Martiny, C. B. Madsen, T. K. Kjeldsen, S. S. Viftrup, L. B. Madsen, and H. Stapelfeldt, "Multiphoton electron angular distributions from laser-aligned CS_2 molecules," Phys. Rev. Lett. **100**, 093006 (2008).

[287] R. Murray, M. Spanner, S. Patchkovskii, and M. Y. Ivanov, "Tunnel ionization of molecules and orbital imaging," Phys. Rev. Lett. **106**, 173001 (2011).

[288] M. Lein, "Antibonding molecular orbitals under the influence of elliptically polarized intense light," J. Phys. B **36**, L155 (2003).

[289] M. Möller, F. Meyer, A. M. Sayler, G. G. Paulus, M. F. Kling, B. E. Schmidt, W. Becker, and D. B. Milošević, "Off-axis low-energy structures in above-threshold ionization," Phys. Rev. A **90**, 023412 (2014).

[290] E. Hasović, M. Busuladžić, A. Gazibegović-Busuladžić, D. B. Milošević, and W. Becker, "Simulation of above-threshold ionization experiments using the strong-field approximation," Laser Phys. **17**, 376–389 (2007).

[291] J. Wiese, Dissertation, Universität Hamburg, Hamburg, Germany (2019).

[292] Y. Huismans, A. Gijsbertsen, A. S. Smolkowska, J. H. Jungmann, A. Rouzée, P. S. W. M. Logman, F. Lépine, C. Cauchy, S. Zamith, T. Marchenko, J. M. Bakker, G. Berden, B. Redlich, A. F. G. van der Meer, M. Y. Ivanov, T.-M. Yan, D. Bauer, O. Smirnova, and M. J. J. Vrakking, "Scaling laws for photoelectron holography in the midinfrared wavelength regime," Phys. Rev. Lett. **109**, 013002 (2012).

[293] X.-B. Bian, Y. Huismans, O. Smirnova, K.-J. Yuan, M. J. J. Vrakking, and

A. D. Bandrauk, "Subcycle interference dynamics of time-resolved photoelectron holography with midinfrared laser pulses," Phys. Rev. A **84**, 043420 (2011).

[294] T. Marchenko, Y. Huismans, K. J. Schafer, and M. J. J. Vrakking, "Criteria for the observation of strong-field photoelectron holography," Phys. Rev. A **84**, 053427 (2011).

[295] H. Liu, Y. Liu, L. Fu, G. Xin, D. Ye, J. Liu, X. T. He, Y. Yang, X. Liu, Y. Deng, C. Wu, and Q. Gong, "Low yield of near-zero-momentum electrons and partial atomic stabilization in strong-field tunneling ionization," Phys. Rev. Lett. **109**, 093001 (2012).

[296] Y. Deng, Y. Liu, X. Liu, H. Liu, Y. Yang, C. Wu, and Q. Gong, "Differential study on molecular suppressed ionization in intense linearly and circularly polarized laser fields," Phys. Rev. A **84**, 065405 (2011).

[297] M. Li, X. Sun, X. Xie, Y. Shao, Y. Deng, C. Qu, Q. Gong, and Y. Liu, "Revealing backward rescattering photoelectron interference of molecules in strong infrared laser fields," Sci. Rep. **5**, 8519 (2015).

[298] P. J. Linstrom and W. G. Mallard, eds., *NIST Chemistry WebBook, NIST Standard Reference Database Number 69* (National Institute of Standards and Technology, Gaithersburg MD, 20899, 2017).

[299] A. G. Maki, "Microwave spectra of molecules of astrophysical interest vi. carbonyl sulfide and hydrogen cyanide," Journal of Physical and Chemical Reference Data **3**, 221–244 (1974).

[300] L. S. Wang, J. E. Reutt, Y. T. Lee, and D. A. Shirley, "High-resolution UV photoelectron-spectroscopy of CO_2^+, COS^+ and CS_2^+ using supersonic molecular-beams," J. Electron. Spectrosc. Relat. Phenom. **47**, 167–186 (1988).

[301] D. S. Elliott and J. F. Ward, "Polarizability anisotropies of CO_2, N_2O, and OCS from measurements of the intensity-dependent refractive index in gases," Phys. Rev. Lett. **46**, 317–320 (1981).

[302] A. Mirri and W. Caminati, "Quadrupole hyperfine structure in the rotational spectrum of iodobenzene," Chem. Phys. Lett. **8**, 409 – 412 (1971).

[303] O. Dorosh, E. Białkowska-Jaworska, Z. Kisiel, and L. Pszczółkowski, "New measurements and global analysis of rotational spectra of Cl-, Br-, and I-benzene: Spectroscopic constants and electric dipole moments," J. Mol. Spectrosc. **246**, 228–232 (2007).

[304] R. D. Suenram, F. J. Lovas, and G. T. Fraser, "Microwave-spectrum and n-14 quadrupole coupling-constants of indole," J. Mol. Spectrosc. **127**, 472–480 (1988).

[305] W. Caminati and S. Di Bernardo, "Microwave spectrum and amino hydrogen location in indole," J. Mol. Struct. **240**, 253 (1990).

Acknowledgements

Many people have contributed to this work and supported me in one or another way in the course of this thesis and I am deeply grateful to all of them.

First of all I want to thank my supervisor Jochen Küpper for all the help that he provided and the opportunity to conduct my thesis in the Controlled Molecule Imaging group (CMI) at the Center for Free-Electron Laser Science (CFEL). I thank him for his active participation and support in all projects, be it the scientific input in the form of valuable ideas, critical analysis of results, or ideas how to improve the experiments, the data analysis or the manuscript writing. Besides his scientific help, I want to thank him for his great support during difficult personal times that came up during my thesis.

I want to cordially thank Arnaud Rouzée, our collaborator in the DFG priority program QUTIF. Most of the experiments presented in this thesis were conducted under his lead at the MBI in Berlin in his laboratory. I benefitted much from his incredible experimental skills, the discussions on physics we had from which I gained a deeper understanding of the topic and also for the nice time and the Berlin beamtimes. It was fun to work with you!

Furthermore I want to thank the group leader of the 'Imaging Chemical Dynamics' team and the kHz lab in Hamburg, Sebastian Trippel. His valuable help was always of high importance and helped to solve several problems that arose during the beamtimes. I thank Terry Mullins for being Terry Mullins. We had endless scientific discussions which due to his unique manner were always fun and fruitful. I want to thank my co-supervisor Robin Santra for his help, his interest in my work and his support during our supervisor meetings. Moreover, I want to thank Henrik Stapelfeldt, Rasmus Johansen and Adam Simon Chatterley from Aarhus for a nice and fruitful collaboration and their support in many aspects.

There are many more people that contributed to this work, either through actively participating in the experiments, through discussions that helped to clarify uncertain aspects, through help with numerical issues in simulations and during the data analysis and of course for having a nice time! These are in particular, Andrey Yachmenev, the group leader of the CMI theory team, for his help with simulations, Joss Wiese for many discussions and constructive comments on the interpretation of results, Thomas Kierspel for help of all sorts and a nice beamtime at FERMI, Karol Długołęcki for planning, designing and helping to set up the molecular beam machine, in particular the deflector part, Jolijn Onvlee and Helen Bieker for help with deflection profiles and the simulation thereof, Andrea Trabattoni for discussions and experimental support in the LIED experiments, and Rosario González-Férez and Linda Thesing for their help and discussions on theoretical and numerical aspects of the work.

Furthermore, I want to thank Marc Vrakking for his support of our beamtimes at the MBI, Philipp Stammer, Sebastian Raabe and Gildas Goldsztejn, with whom most of the measurements were conducted, often in continuous mode and during night shifts. I want to thank Steve Aplin, Adrian Pagel, Vitaliy Dodonov and Frank Schluenzen for their IT support with the hardware, the software and the high-performance computing cluster Maxwell. I want to thank Michele DiFraia and Carlo Callegari for a nice collaboration and the common beamtime at FERMI.

Before ending, I want to thank all of my coworkers for the nice time we had together during this last 4 years.

At last, I want to thank in particular my family that supported me during the whole time. I thank my mother Karin Karamatskos, my sister Antonia Karamatskou, my brother Alexander Karamatskos and my wife Eleftheria Filippaki for their support, cordial, mental, intellectual and material.

Finally, I thank my father Nikolaos Karamatskos, who passed away after my first year and whom we miss painfully. I owe him more than I can express. This thesis is dedicated to him.

Acronyms

ADK	Ammosov-Delone-Krainov model
ATI	above-threshold ionization
IB	iodobenzene
CCD	charge-coupled device
CEI	Coulomb-explosion imaging
CFEL	Center for Free-Electron Laser Science
DCS	differential cross section
DOA	degree of alignment
EA	evolutionary algorithm
FEL	free-electron laser
FWHM	full width at half maximum
GED	gas-phase electron diffraction
HATI	high-energy above-threshold ionization
HE-TOPAS	high-energy tunable optical parametric amplification system
HHG	high harmonic generation
HOMO	highest occupied molecular orbital
IAM	independent-atom model
IP	ionization potential
LFF	laboratory-fixed frame
LIED	laser-induced electron diffraction
MBI	Max-Born Institute
MCP	multi-channel plate
MCF	molecular contrast factor
MFF	molecule-fixed frame
MF-ARPES	molecular-frame angularly-resolved photoelectron spectroscopy
OCS	carbonyl sulfide
MFPAD	molecular-frame photoelectron angular distribution
PEMD	photoelectron momentum distribution
PES	photoelectron spectrum
QRS	quantitative rescattering theory
SFA	strong-field approximation
SFI	strong-field ionization
SFPH	strong-field photoelectron holography
SLM	spatial light modulator
STCP	spectrally truncated chirped pulse
TDSE	time-dependent Schrödinger equation
TOF	time-of-flight
UED	ultrafast electron diffraction
VMIS	velocity map imaging spectrometer

List of Figures

List of publications

Publications related to this thesis

2019 *Creating and characterising strong three-dimensional field-free alignment of complex molecules*
T. Mullins, **E. T. Karamatskos**, J. Wiese, J. Onvlee , A. Yachmenev, A. Rouzée, S. Trippel, and J. Küpper
in preparation (2019)

2019 *Molecular movie of ultrafast coherent rotational dynamics of OCS*
E. T. Karamatskos, S. Raabe, T. Mullins, A. Trabattoni, P. Stammer, G. Goldsztejn, R. R. Johansen, K. Dlugolęcki, H. Stapelfeldt, M.J.J. Vrakking, S. Trippel, A. Rouzée, and J. Küpper
Nature Communications **10**, 3364 (2019), *arxiv*:1807.01034

2019 *Atomic-resolution imaging of carbonyl sulfide by laser-induced electron diffraction*
E. T. Karamatskos, G. Goldsztejn, S. Raabe, P. Stammer, T. Mullins, A. Trabattoni, R. R. Johansen, H. Stapelfeldt, S. Trippel, M. J.J. Vrakking, J. Küpper and A. Rouzée
The Journal of Chemical Physics **150**, 244301 (2019), *arXiv*:1905.03541

2018 *Communication: Switched wave packets with spectrally truncated chirped pulses*
A. S. Chatterley, **E. T. Karamatskos**, C. Schouder, L. Christiansen, A. V. Jørgensen, T. Mullins, J. Küpper and H. Stapelfeldt
The Journal of Chemical Physics **148**, 221105 (2018), *arXiv*:1803.03953

2017 *Impulsive laser-induced alignment of OCS molecules at FERMI*
M. Di Fraia, P. Finetti, R. Richter, K. C. Prince, J. Wiese, M. Devetta, M. Negro, C. Vozzi, A. G. Ciriolo, A. Pusala, A. Demidovich, M. B. Danailov, **E. T. Karamatskos**, S. Trippel, J. Küpper, and C. Callegari
Physical Chemistry Chemical Physics **19**, 19733-19739 (2017), *arXiv*:1808.07281

Other publications

2016 *Two-electron processes in multiple ionization under strong soft-x-ray radiation*
M. Ilchen, **E. T. Karamatskos**, D. Markellos, S. Bakhtiarzadeh, A. J. Rafipoor, T. J. Kelly, N. Walsh, J. T. Costello, P. O'Keeffe, N. Gerken, M. Martins, P. Lambropoulos, and M. Meyer
Phys. Rev. A **94**, 013413 (2016)

2015 *Stability and Tunneling Dynamics of a Dark-Bright Soliton Pair in a Harmonic Trap*
E. T. Karamatskos, J. Stockhofe, P.G. Kevrekidis, P. Schmelcher
Phys. Rev. A **91**, 043637 (2015), *arXiv*:1411.3957

2014 *Time-Dependent Density-Functional Theory of Strong-Field Ionization of Atoms under Soft X-Rays*
A. Crawford-Uranga, U. De Giovannini, E. Räsänen, M. J. T. Oliveira, D. J. Mowbray, G. M. Nikolopoulos, **E. T. Karamatskos**, D. Markellos, P. Lambropoulos, S. Kurth, and A. Rubio
Phys. Rev. A **90**, 033412 (2014), *arXiv*:1408.6067

2013 *Multiple ionization of argon under 123 eV FEL radiation and the creation of 3s-hollow ions*
E. T. Karamatskos, D Markellos and P Lambropoulos
J. Phys. B: At. Mol. Opt. Phys. **46**, 164011 (2013)